UNIVERSITAT DE BARCELONA

Synthesis, Characterization and Deposition on Surfaces of Curcuminoids-based Systems

Raúl Díaz Torres

FACULTAT DE QUÍMICA

DEPARTAMENT DE QUÍMICA INORGÀNICA I ORGÀNICA

SECCIÓ DE QUÍMICA INORGÀNICA

Programa de Doctorat de **Química Orgànica**

Synthesis, Characterization and Deposition on Surfaces of Curcuminoids-based Systems

RAÚL DÍAZ TORRES

Director: Dra. Núria Aliaga Alcalde, Institut de Ciència de Materials de Barcelona (ICMAB-CSIC).

Tutor: Dr. Eliseo Ruiz Sabín, Departament de Química Inorgànica i Orgànica (Secció de Química Inorgànica) de la Facultat de Química de la Universitat de Barcelona.

NÚRIA ALIAGA ALCALDE, Professora ICREA de l'Institut de Ciència de Materials de Barcelona (ICMAB-CSIC)

CERTIFICA: que el treball titulat *Synthesis, Characterization and Deposition on Surfaces of Curcuminoids-based systems,* presentat per **Raúl Díaz Torres** per aspirar al grau de Doctor en Química, s'ha realitzat sota la seva direcció a l'Institut de Ciència de Materials de Barcelona (ICMAB-CSIC)

Barcelona, juny del 2018

ICREA Prof. Núria Aliaga Alcalde

ELISEO RUIZ SABÍN, Catedràtic del Departament de Química Inorgànica i Orgànica (Secció de Química Inorgànica) de la Facultat de Química de la Universitat de Barcelona

CERTIFICA: que ha estat el tutor responsable dels estudis de doctorat de **Raúl Díaz Torres** dins del programa de doctorat de Química Orgànica, impartit pel Departament de Química Inorgànica i Orgànica (Secció de Química Inorgànica) de la Facultat de Química de la Universitat de Barcelona.

Barcelona, juny del 2018

Prof. Eliseo Ruiz Sabin

A mis padres y
a mi hermano

Estoy entre aquellos que piensan que la ciencia tiene una gran belleza.
Un científico en su laboratorio no es sólo un técnico, es también un niño colocado
ante los fenómenos naturales que lo impresionan como un cuento de hadas.

Marie Curie. *El porvenir de la cultura.*

List of Abbreviations

CCMoids	Curcuminoids
SMM	Single-Molecule magnet
^{1}H NMR	Proton nuclear magnetic resonance
zfs	Zero field splitting
SQUID	Superconducting quantum interference device
HFEPR	High field electron paramagnetic resonance
QTM	Quantum tunneling of magnetization
HOMO	Highest occupied molecular orbital
LUMO	Lowest unoccupied molecular orbital
CHEF	Chelation enhanced fluorescence
CHQF	Chelation quenched fluorescence
IR	Infrared spectroscopy
MALDI	Matrix assisted laser desorption/ionization
XPS	X-ray photoelectron spectroscopy
UPS	Ultraviolet photoelectron spectroscopy
AFM	Atomic force microscopy
CASSCF	Complete active space self-consistent field
HOPG	Highly oriented pyrolytic graphite
PES	Photoemission spectroscopy
DOS	Density of the states
SCM	Single-Chain magnet
TIP	Temperature independent paramagnetism
DHB	2,5-Dihydroxybenzoic acid
STM	Scanning tunneling microscope
BJ	Break junctions

MCBJ	Mechanically controlled break junctions
EM	Electromigration
FET	Field-effect transistor
CD	Circular dichroism
SET	Single-electron transfer
FLG	Few layer graphene
DFT	Density functional theory
MLG	Multi-layer graphene
PMMA	Poly(methyl methacrylate)
SAMs	Self-assembled monolayers
μ-CP	Microcontact printing
PDMS	Polydimethylsiloxane
IM	Imidazole
CDI	1,1'-Carbonyldiimidazole
TPEDA	N-[3-(Trimethoxysilyl)propyl]ethylendiamine
Fc	Ferrocene
CD	Cyclodextrin
CB[n]	Cucurbit[n]uril
CV	Cyclic voltammetry
DPV	Differential pulse voltammetry
SW	Squarewave voltammetry
OPVs	Organic photovoltaics
ICT	Intramolecular charge transfer
P3HT	Poly(3-hexylthiophene-2,5-diyl)
$PC_{61}BM$	Phenyl-C61-butyric acid methyl ester
CB	Chlorobenzene
DB	Dichlorobenzene

Abstract

Nanoscience and Nanotechnology have become research areas that promote the design and fabrication of novel devices with a number of different applications with the aim of satisfying the growing demand of the society regarding technological advances. The breakthrough in some of these subjects directly associates with the development of specific molecular systems with new and advanced features, applicable toward the development, at the nanoscale, of efficient materials that could act as molecular switches or active components in memory devices, transistors or sensors, among others.

In this regard, promising molecular-based systems, to be applicable in these fields, are the so-called Curcuminoids (CCMoids). These molecules can present versatile structures, displaying always (i) a conjugated chain of seven carbon atoms, which confers the molecules with reasonable conductive properties; (ii) a β-diketone group located in the middle of the chain, that opens the possibility of coordinating with metallic centers, and (iii) two aromatic groups, located on both sides of the molecules that add fluorescent, redox active and optical properties, among others.

The main goal of this thesis rest on the design and synthesis of new CCMoids that can be applied in different areas of nanoscience. Thus, different modifications on their structure were carried out in order to achieve interesting properties.

The results obtained in this work have been grouped in five different sections; corresponding each one to a different area. This way:

(1) Molecular Magnetism: the first section is focused on the search of systems which display interesting magnetic properties, especially systems with single molecule magnet behavior. Thus, magneto-structural studies were performed by the synthesis of several coordination compounds using magnetic metallic centers (Co^{II} and Ni^{II}) coordinate with a CCMoid ligand called 9Accm. In addition, a study of the influence of the paramagnetic centers on the fluorescent properties derived from the CCMoid ligand was also performed together with deposition studies on HOPG (highly oriented pyrolytic graphite).

(2) Molecular Electronic: the second section focuses on the study of the electronic transport of a new CCMoid system within a three terminal nanodevice containing few layer graphene (FLG) electrodes. This study centers in the improvement of the conductive properties of a previously measured CCMoid system, in which 9Accm was used as a nanowire in a molecular transistor by π-π stacking interactions with the graphene electrodes. The new CCMoid

contains an elongated conjugated skeleton that improves the anchoring properties of the final system with the FLG electrodes.

(3) Molecular Sensors: the third section is based on the immobilization of fluorescent CCMoids on surfaces and their used as chemical sensors for boron ions. The immobilization was carried out on functionalized SiO_2 surfaces by the use of the Microcontact printing technique (μ-CP) that allowed the creation of fluorescent micropatterns on the surfaces. In addition, studies regarding the coordination of boron to the CCMoids attached on the surfaces and the effect in their fluorescent properties was performed to explore they as chemical sensors.

(4) Molecular Host-Guest Chemistry: the fourth section is focused on the fabrication of supramolecular host-guest systems based on CCMoids. In the first part, a study of the CCMoid acting as a guest was performed. In this case, a novel CCMoid molecule that contain a ferrocene group is inserted in different host cavities (cyclodextrin and cucurbituril). This study was performed in solution and on Au surfaces. On the other hand, the synthesis of another CCMoid was carried out to be used as a host, being the main ligand in the formation of molecular cages.

(5) Molecular Donor/Acceptor Chemistry: the fifth section is based on the study of the donor/acceptor properties of additional CCMoids with the idea of using them as components of organic photovoltaics cells (OPVs). For this study, the synthesis of two families of CCMoids with acceptor and donor moieties on the sides of the molecules was performed, and additional variations on their structure were achieved to assess their influence on the optical and electronic properties of the systems.

CONTENTS

General remarks

The results presented in this thesis are divided in five sections. This classification bases on the different subjects that have been addressed, all of them related to the area of nanoscience. Thus, the sections disclose: Molecular Magnetism (Section I), Molecular Electronics (Section II), Molecular Sensors (Section III), Molecular Host-Guest Chemistry (Section IV) and Molecular Donor-Acceptor Chemistry (Section V). Each section contains a separated Introductory block, with the goal of providing qualitative information of the explored topic. However, all of them have in common the use of curcuminoid molecules (CCMoids) and therefore, here a brief introduction regarding CCMoids is provided.

Curcumin (CCM) and Curcuminoids (CCMoids)

Curcumin (Figure 1) is a natural pigment and the main component of the turmeric acid found in the Curcuma Longa plant, which is commonly known as curcuma. For many years, this natural product has been widely used in gastronomy, being one of the main components of curry, and traditional medicine, functioning as anti-inflammatory[1] and antioxidant[2,3]. Lately, CCM greatest importance resides in its medical and biological properties[4,5] as anticancer agent[6,7] and preventive medicine[8]. Despite this, its poor bioavailability and solubility in water have limited its use regarding the subjects just mentioned.[9]

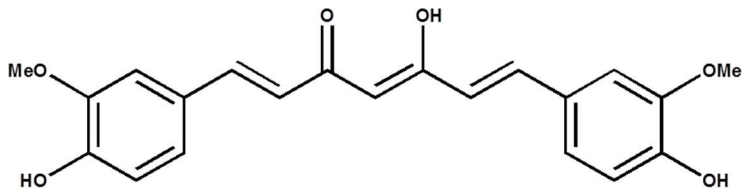

Figure 1: Representation of the curcumin.

CCM can be extracted directly from the rhizomes of the Curcuma Longa, but also can be synthesized, existing in the literature several synthetic methods that allow purity and good yields. The latest, together with the desire of improving the biological activity of CCM have triggered the appearance of an extensive family of molecules that present similar structures to CCM, called CURCUMINOIDS (CCMoids).

CCM and CCMoids are organic molecules that contain two aromatic groups connected by a conjugated chain of seven carbon atoms that contain a β-diketone moiety in the middle. The versatile chemistry that allows the achievement of CCMoids has risen the interest, of the scientific community in additional fields as nanoscience and nanotechnology. Nevertheless, it is important to emphasize that still more than 90 % of the published work of CCM/CCMoids belongs to biological fields and related.

The general objective of this thesis is the synthesis, characterization and study of properties, toward future applications in nanoscience, of new CCMoids, taking advantage of the versatile chemistry mentioned before.

Synthetic route

CCM was first isolated from the plants in 1815, by Vogel and Pelletier,[10] and synthetized few years later by Lampe (in 1918).[11] There, the proposed synthetic route consisted in five steps and the yield was very low. It was not until 1964, when the group of Pabon developed a new synthetic method based on a single-pot reaction for the synthesis of CCM that later was easily adapted toward the synthesis of CCMoids.[12]

Currently, this synthetic method is the commonly used and, also the one followed in this thesis because it provides high yields and allows the synthesis of a large variety of CCMoids.

The synthetic route (Figure 2) is based on the formation of a boron compound using acetylacetonate (acac). The objective of the boron-intermediate system is to avoid Knoevenagel reactions in the central carbon. Then, a boronic ester is added, mostly to remove the water produced in the condensation reaction.[13] Subsequently, the aromatic aldehyde and the n-butylamine are added, the latest acts as a catalyst by deprotonating the methyl of the acac. Finally, the boron compound formed hydrolyses under mild acidic conditions and the CCMoid can be isolated (Mechanism Annex A.I.1).

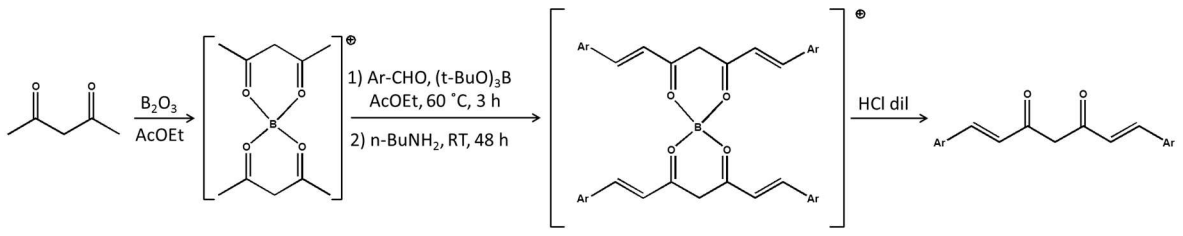

Figure 2: Pabon's method showing the general steps for the synthesis of CCMoids.

This methodology allows the synthesis of a large variety of CCMoids with different aromatic groups by varying the corresponding aldehyde, obtaining high yields in most of the cases. On the other

hand, their great versatility allows their derivation in more complex molecules by the creation of new generations where a part from the aromatic groups, additional moieties can be included in these molecules (see below).

Structural correlation between design and application in CCMoids

In order to synthesize new CCMoids, there are four different positions within the molecules that can be varied. In this thesis, we will refer to these positions as head, body, arms and leg (Figure 3). The modification of the lateral positions corresponding to the arms (aromatic groups enclosed in red square, Figure 3) could give rises to different properties such as electrochemistry, fluorescence,[14] etc. In the case of the conjugated chain (Figure 3, remarked in yellow) the number of carbon in the skeleton can be varied modifying for example the final conductivity properties.[15] The modification of β-diketone (Figure 3, ellipsoid in blue) allows the possibility of adding coordination to different metallic centers forming coordination systems (0D, 1D, etc.) In the latest, the coordination compound can combine the properties derived from the ligand (CCMoid) and those coming from the metallic center (magnetic,[16] electrochemical,[17] optical,[17] etc). Finally, the functionalization of the central part of the molecule (Figure 3, green rectangle) with specific functional groups will allow the immobilization of the molecules on surfaces and/or the addition of new functional groups (e.g. ferrocene moieties).

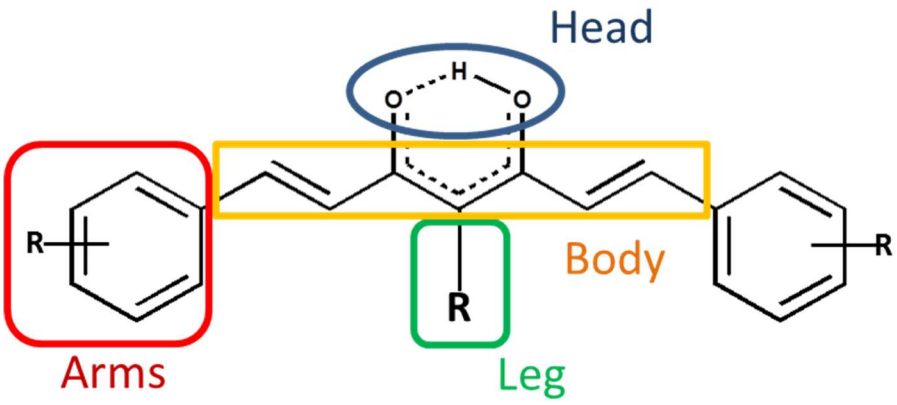

Figure 3: Scheme of the different part of a CCMoid

The following table shows the different modifications explored in the present thesis.

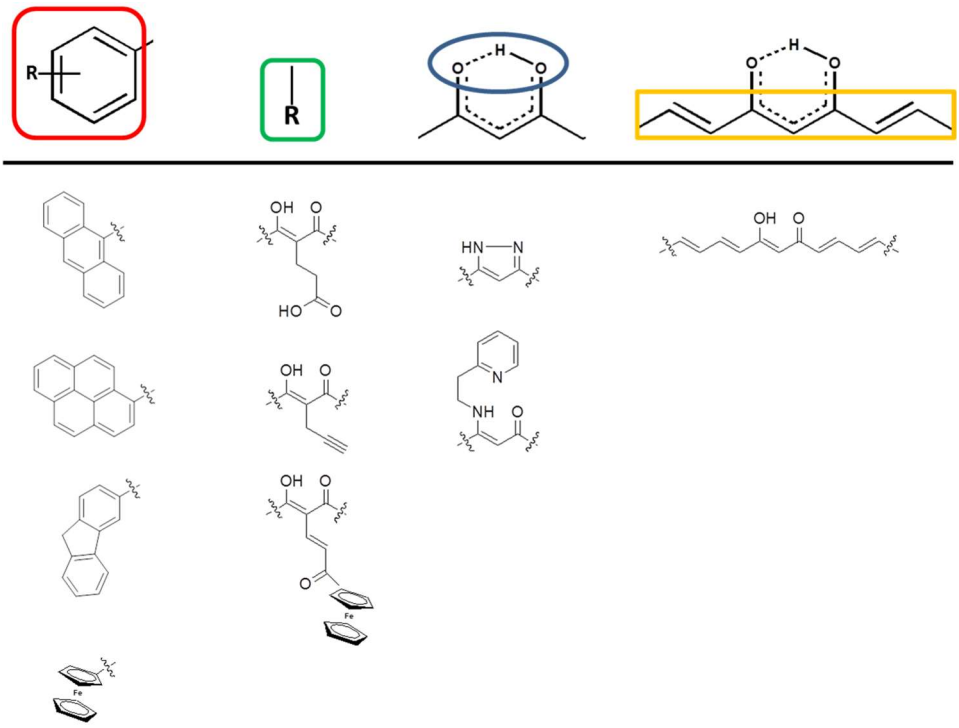

Figure 4: Different modifications performed for the CCMoids.

References

[1] M. A. Khan, R. El-Khatib, K. D. Rainsford, M. W. Whitehouse, *Bioorg. Chem.* **2012**, *40*, 30–38.

[2] R. Ciochina, C. Savella, B. Cote, D. Chang, D. Rao, *Drug Dev. Res.* **2014**, *75*, 88–96.

[3] Y. M. Sun, H. Y. Zhang, D. Z. Chen, C. B. Liu, *Org. Lett.* **2002**, *4*, 2909–2911.

[4] K. M. Nelson, J. L. Dahlin, J. Bisson, J. Graham, G. F. Pauli, M. A. Walters, *J. Med. Chem.* **2017**, *60*, 1620–1637.

[5] K. I. Priyadarsini, *Molecules* **2014**, *19*, 20091–20112.

[6] R. A. Sharma, A. J. Gescher, W. P. Steward, *Eur. J. Cancer* **2005**, *41*, 1955–1968.

[7] F. Harris, L. Pierpoint, *Med. Res. Rev.* **2012**, *29*, 1292–1327.

[8] H. Hatcher, R. Planalp, J. Cho, F. M. Torti, S. V. Torti, *Cell. Mol. Life Sci.* **2008**, *65*, 1631–1652.

[9] P. Anand, A. B. Kunnumakkara, R. A. Newman, B. B. Aggarwal, P. Anand, A. B. Kunnumakkara, R. A. Newman, *Mol. Pharmacol.* **2007**, *4*, 807–818.

[10] Vogel, Pelletier, *J. Pharm.* **1815**, 289.

[11] V. Lampe, *Berichte der Dtsch. Chem. Gesellschaft* **1918**, *51*, 1347–1355.

[12] H. J. Pabon, *Recl. Trav. Chim. Pays-Bas* **1964**, 379.

[13] H. Steinberg, D. L. Hunter, *Ind. Eng. Chem.* **1957**, *49*, 174–181.

[14] N. Aliaga-Alcalde, L. Rodríguez, M. Ferbinteanu, P. Höfer, T. Weyhermüller, *Inorg. Chem.* **2012**, *51*, 864–873.

[15] E. Burzurí, J. O. Island, R. Díaz-Torres, A. Fursina, A. González-Campo, O. Roubeau, S. J. Teat, N. Aliaga-Alcalde, E. Ruiz, H. S. J. Van Der Zant, *ACS Nano* **2016**, *10*, 2521–2527.

[16] M. Menelaou, F. Ouharrou, L. Rodríguez, O. Roubeau, S. J. Teat, N. Aliaga-Alcalde, *Chem. - A Eur. J.* **2012**, *18*, 11545–11549.

[17] A. Felouat, A. D'Aléo, F. Fages, *J. Org. Chem.* **2013**, *78*, 4446–4455.

SECTION I:

MOLECULAR MAGNETISM

Molecular Magnetism

1.1 Introduction

Coordination Chemistry and Molecular Magnetism

The development of the Coordination Chemistry has allowed the achievement of new and interesting materials, from a structural point of view and also from the great physical properties that can present. The combination of a versatile organic ligand together with the diverse properties of a metallic center give rises to the formation of coordination compounds presenting molecular functional properties.[1–4] Specifically, the relationship between the coordination chemistry and molecular magnetism (once the metal contains unpaired electrons) has become more and more important, due to the formation of magnetic molecules which can be used for information storage as it is the case of Single Molecule Magnets (SMMs).[5–7]

Along the years, the correlation between magnetic measurements and structural parameters has been extensively studied giving rise to a deep understanding of the factors and reasons that provide a variety of magnetic answers (ferromagnetism, ferrimagnetism, etc.)

Among all the possible molecular-based systems, small coordination compounds (mononuclear compounds) are of great interest because they present clear magnetic behavior allowing a better understanding of the materials and magnetic properties.

In the relationship between the metallic center and the ligands coordinated, the metal can provide redox, magnetic and/or luminescence properties.[8–10] This, together with the properties derivate from the organic molecule/s (ligand/s), that can be similar to the ones described for the metal center, allows the creation of multifunctional systems, where both properties are in synergy present in an individual molecule. [11]

For a global understanding, the reliable characterization of the performance of such entities not only in the solid state and solution but also on surfaces is mandatory.[12,13]

Therefore, our efforts are directly focused toward the integration of mononuclear functional coordination compounds in the field of molecular magnetism emphasizing both, the properties of the metal center but also the organic ligand attached to it.

In this section, the organic ligand selected is a CCMoid ligand called 9Accm (Figure I.1). Here, 9Accm coordinates with different paramagnetic 3d metal centers (Co^{II} and Ni^{II}). This way, the final coordination compounds exhibit fluorescence and magnetic properties. Related to the last one, our research group has a special interest in the development of systems that have slow relaxation of the magnetization. Apart from the magnetic and fluorescence studies, the stability of the systems in solution was explored by the use of paramagnetic ^{1}H NMR technique. Moreover, the ligand 9Accm is

a great candidate to attach, by π-π stacking, on carbon-based surface. Thus, the affinity and robustness of the final compounds were studied on surfaces.

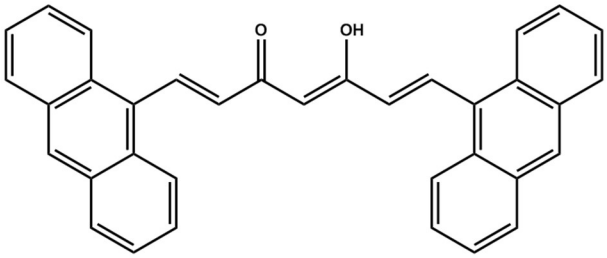

Figure I.1: Scheme of the 9Accm.

From Molecular Magnetism to Single Molecule Magnets

Nowadays, magnetic materials occupy a crucial role in our daily lives, since they are forming part of most of technological devices including those for communication and of information storage.[5–7] Traditionally, this demand has been satisfied by materials formed by heterometallic rare earth ions ($SmCo_5$) and magnetic nanoparticles (Fe_3O_4) using the top-down approach.[14] In these systems, each piece of information (hence, a bit) corresponds to one magnetic domain with a size of several nanometers, able of keeping the magnetization without the presence of an external magnetic field.

On the other hand, from the bottom-up approach,[15] a relative extensive family of small molecules, polynuclear and mononuclear compounds, so-called single molecule magnets (SMMs) exhibit also the phenomenon of slow relaxation of the magnetization, leading to magnetic hysteresis phenomena below a critical temperature (blocking temperature).[16] This bistable behavior is similar to that described above, but being inherent to unique molecules, where the size in average is only of few nanometer; SMMs can be seen as reliable successors of the magnetic materials used nowadays for the technological applications and information storage.

Although a growing impulse exists toward the miniaturization of technology,[17] one of the most important drawbacks for the implementation of SMMs is their blocking temperature (below which the systems keep their magnetization), in general very low (below 10 K). Their real application is also a challenge because the systems must present robustness (against decomposition because of high temperatures, solvents, humidity, etc.) and low cost preparation. Nevertheless, the studies of these systems in order to overcome these problems have generated a remarkable interest and factors as the blocking temperatures are being resolved thanks to molecular design.[18,19]

Single Molecule Magnets (SMMs)

The main feature of the single molecule magnets, as it was mentioned, is that present slow magnetic relaxation processes, inherent in each molecule of the sample, which gives rise to magnetic hysteresis.[5–7] This fact arises from the existence of two ground states of different magnetization +Ms and –Ms separated by an energy barrier (Figure I.2). Therefore, this energy barrier limits the interconversion (keeps the magnetization) in the absence of an external magnetic field (detailed explanation can be found in Annex 1.1).

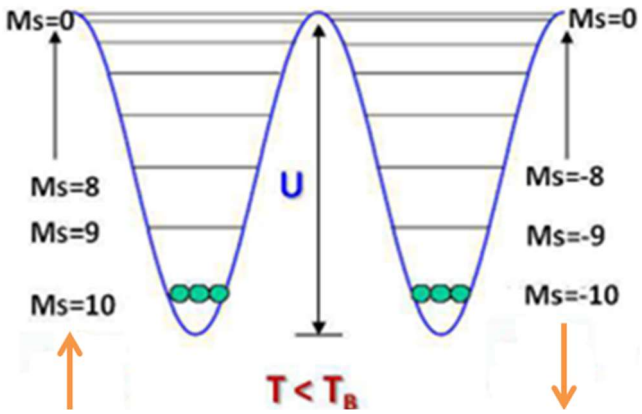

Figure I.2: Double-well potential and energy levels of Mn_{12} (S = 10, D < 0)

The height of the energy barrier (U) is given by the spin ground state (S) and the magnetic anisotropy.

$$U = S^2 |D| \qquad \text{(S = total spin for an integer molecular system)} \qquad (1)$$

$$U = (S^2 - 1/4) |D| \qquad \text{(S = total spin for a half-integer molecular system)} \qquad (2)$$

The magnitude of the magnetic anisotropy is the sum of an axial (parameter D, associated to the magnetic anisotropy in the direction of the external magnetic field applied) and rhombic (parameter E, perpendicular to it) magnetic distortions.

In addition, there are two paths for the magnetization of the molecule to relax: (i) on one side, systems could relax overcoming the energy barrier though an activated thermal mechanism, and here three additional processes can be found: Direct, Orbach and Raman (extent definition could be found in Annex 1.2). In this case, a part from the value of S, the biggest the axial magnetic anisotropy (D), the biggest the energy barrier is. On the other side, the molecular magnetization could relax by crossing the energy barrier, the so-called tunneling process. The molecular origin of these systems

gives rise to a process of quantum nature. In this case, the relaxation process is very fast and relates to the rhombic magnetic anisotropy parameter (E). This promotes the mixture of $\pm M_S$ levels on both sides of the barrier allowing the resonant transition (Figure I.3).

Therefore, the design of suitable SMMs rest on the ability of synthesized new systems with large spin ground state (S) and large axial magnetic anisotropy (D) values to increase the blocking temperature and as small as possible rhombic parameter (E) to avoid the relaxation tunneling process.

In addition, elusion of quantum tunneling processes can be achieved by the application of an external magnetic field (H_{DC}).[20] Thus, the energy of the states is modified (breaking resonance). However, depending on the values of the external field new levels of +Ms and –Ms of different spin numbers could present the same energy, giving rise to quantum tunneling again (Figure I.3, orange).

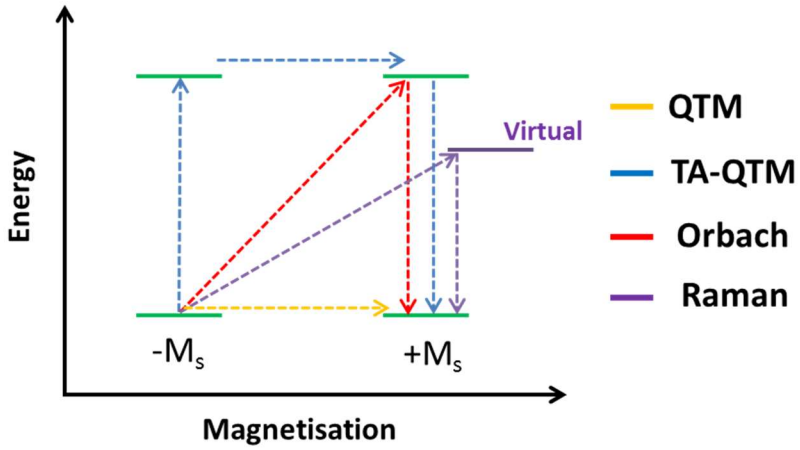

Figure I.3: Schematic representation of possible paths for the relaxation of a SMM. Green lines represent the spin states; purple lines the virtual states where Raman relaxation occurs. Color legend: yellow (fundamental state tunnel effect), blue (thermally assisted tunnel effect), red (Orbach relaxation) and purple (Raman relaxation).

From SMMs to Mononuclear SMMs

Since the discovery of the SMM systems, there has been a clear evolution from the scientist community in the approach taken toward the design of SMMs, in order to improve their magnetic properties (blocking temperature).

The first molecule discovered that exhibited molecular magnet behavior was a Mn_{12} cluster published by Gatteschi *et al.* in 1993.[16] This finding defined the first strategy to follow in the design

of SMMs, which was based on systems that present high nuclearity (polynuclear compounds) where their magnetic nuclei were coupled mainly by ferromagnetic interactions, to obtain high spin values.

Despite of the efforts made in this direction, it was barely possible to overcome the blocking temperature corresponding to the Mn_{12} (T_B = 3.5 K). For more than a decade the molecular design was based in combinatorial chemistry but the results were not better than those found for Mn_{12}. The second best polynuclear compound that presented a slightly higher energy barrier was a Mn_6 compound published by Professor Brechin in 2007,[21] with a T_B of 4.5 K.

This strategy, where systems with high spin values would result in more efficient SMMs was losing relevance mostly because, despite of having a high spin ground state (S), these systems showed low axial magnetic anisotropy (D) values.

Magnetic anisotropy can be defined as the preferred alignment of the magnetic moment along a specific direction (the so-called easy magnetization axis). Therefore, the reason for obtaining low values of (D) in polynuclear systems can be considered structural, since as the nuclearity is increases, it becomes more difficult to control the mutual alignment of the individual ions of the axis of the molecule, that normally cancel each others. A clear example can be observed in the Mn_{84} compound published by G. Christou *et al.*[22], where the energy barrier and blocking temperature obtained (E_a = 12 cm^{-1}, T_B= 1.5 K) were lower due to the present of a small anisotropy in its ground state.

This fact has promoted to look for alternative synthetic pathways, focusing on the anisotropic parameter (D).[23] The understanding and control of D becomes difficult with the use of polynuclear compounds. Instead, single ion systems present unique values of D avoiding the problem of cancellation of the anisotropy. This new strategy gave rise to mononuclear single molecule magnets (also called briefly in the literature single ion magnets, SIMs) with the use of metal centers from the d and f blocks of the periodic table.

The first mononuclear SMM appeared in 2003,[24] published by Ishikawa's group, where a mononuclear compound of terbium, with formula (*n*-Bu_4N)[$TbPc_2$] (Pc = Phthalocyanine), presented a SMM behavior with a high value of magnetic anisotropy (due to the typical strong spin-orbit contribution present in most of 4f metal ions) and an energy barrier of E_a = 230 cm^{-1}, overcoming significantly the value of the previous polynuclear compounds.

In addition, in 2010, J. Long group's published the first mononuclear SMM based on a 3d metal ion.[25] Their Fe^{II} compound presented an energy barrier of E_a = 42 cm^{-1} and a magnetic anisotropy of D = - 39.6 cm^{-1}.

Following this new strategy last year, it appeared a linear Dy compound from the group of Chilton that presents an energy barrier record of E_a = 1277 cm^{-1} and a blocking temperature of T_B = 60 K.[18,19] These high values are due to the low coordination numbers that reduce the splitting of 4f orbitals.

Overall, there has been an evolution on the approach in the design of the molecular magnets. Initially, this design was based mainly on serendipitous synthetic procedures toward the synthesis of polynuclear compounds with ferromagnetic interactions obtaining high spin (S) values. Then, mononuclear SMMs became more relevant, having improved magnetic properties and simple structures that allowed a better control of their synthesis. The latest present a S finite value, depending on the number of unpaired electrons achieved by their oxidation state, where the tuning of the magnetic properties depends mainly on the control of the zero-field splitting (zfs).[23] This, relates in great manner to the coordination number and nature of the ligands surrounding the metal center, therefore to the crystal field effects. In this regard, mononuclear Co^{II} and Ni^{II} systems are important in the SMM field, where some of these compounds present great zfs values (D values) as it was shown. [26,27] This thesis concentrates in mononuclear SMMs.

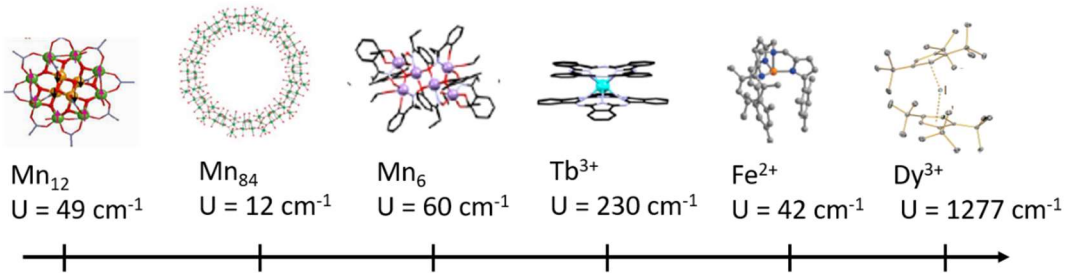

Figure I.4: Evolution timeline of different SMM discussed in the text

Magnetic Anisotropy

As it has been mentioned, the main feature of the SMMs is its slow relaxation of the magnetization, closely related to the magnetic anisotropy. Molecules which exhibit the latest are those that present a preferential direction of the magnetic moment (non-homogeneity at different direction of the field) and for that to happen spin-orbit coupling is necessary.[28]

High values of magnetic anisotropy are obtained when the ground state is degenerated (first-order spin-orbit coupling).[29] However, most compounds present distortions with respect to ideal geometries. Many of these distortions depend on steric reasons (the number, nature or bulkiness of the coordinated ligands, among others) and others due to electronic characteristics (for example Jahn-Teller effects).[30] These distortions give rise to the energy splitting of the ground state. Thus, magnetic anisotropy arises specifically from the coupling between this nondegenerate electronic state with excited states, both presenting the same multiplicity. This coupling, which corresponds to a second order spin-orbit coupling, it is well-known as zero field splitting (zfs) and it is quantify by the axial magnetic anisotropy (D).[28]

The axial anisotropy parameter (D) splits the S = n/2 levels into M_S states, where M_S = ± 0, 1, …, n/2, and M_S = ± 1/2, 3/2, …., n/2, for non-fractional S and fractional S values, respectively. Figure I.5 exemplifies the axial zfs.

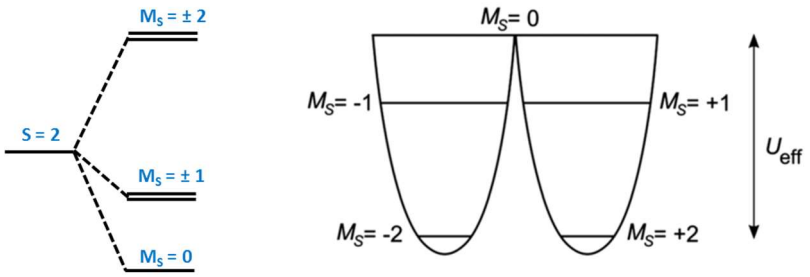

Figure I.5: Representation of the energy levels of the zero field splitting (left) and the double-well potential (right) for a S = 2 and D < 0.

Due to the large difference in energy between the ground state and the excited state, the resulting spin-orbit coupling and therefore, the anisotropy value, is usually small (reason for what the blocking temperature is still too small).

Therefore, several strategies have been developed in order to increase the magnetic anisotropy of the systems, for example: (i) the use of rare earth instead of 3d transition metal ions, since the first present large spin-orbit coupling values, and/or (ii) design of low-coordinated or ideal geometry in order to achieved nearly degenerated ground states which present first order spin-orbit coupling.

Magnetic Anisotropy: Experimental values

The study of the magnetic anisotropy parameters (D and E) is carried out by magnetic measurements using a SQUID (Superconducting Quantum Interference Devices) and/or electron paramagnetic resonance (EPR). As the order of the zero-field splitting is regularly of dozens of cm^{-1}, both techniques are able to study this phenomenon at low temperatures, since both acts only on the thermally populated terms (kT = 200 cm^{-1}).

To understand how both techniques work, it is important to explain first the electronic Zeeman effect. The electronic Zeeman effect produces the splitting of the energetic levels into states due to the application of the magnetic field. In the Figure I.6 shows the splitting of these states for an S = 2.

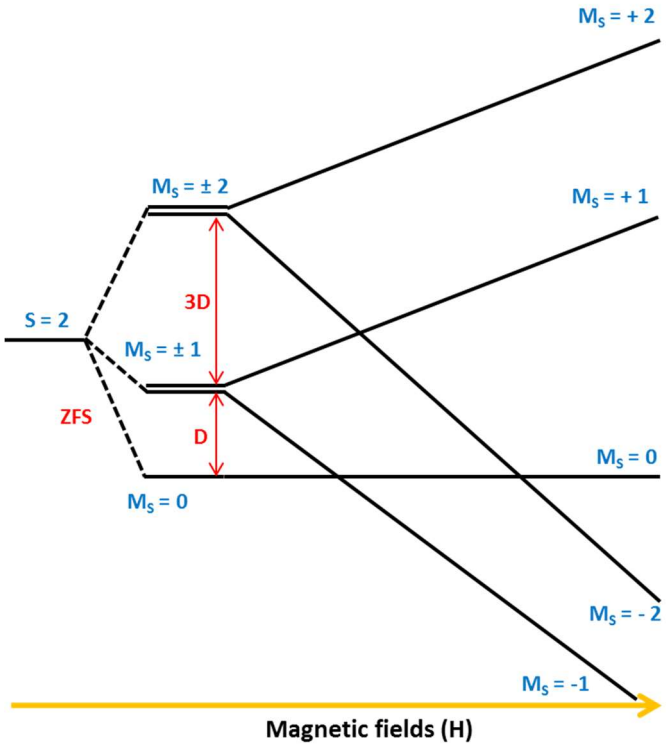

Figure I.6: Representation of the zero-field splitting (zfs) and Zeeman effect for a S = 2 a with significant D value.

Magnetic measurements

The magnetic measurements give us information about the population of these states. As seen in Figure I.6, the population of these states will be different due to the Boltzmann distribution. Within magnetic studies, measurements of: (i) magnetization versus temperature at different magnetic field and (ii) the magnetic susceptibility as a function of the temperature can be performed. Figure I.7 shows examples of both measures.

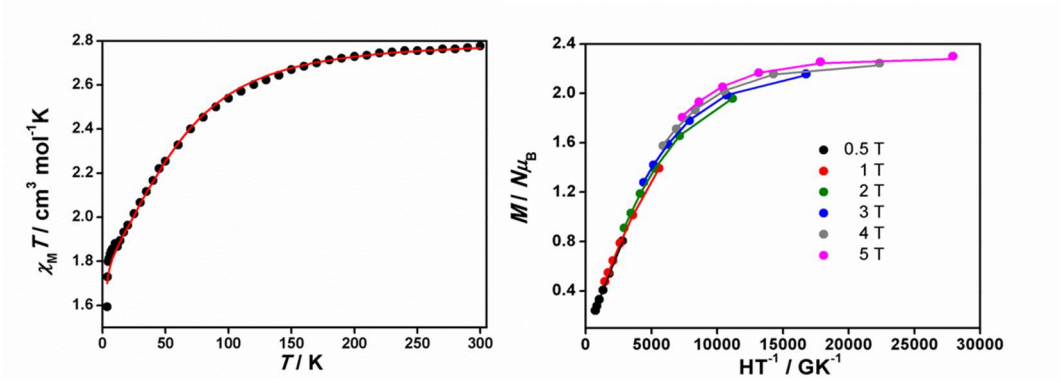

Figure I.7: Representation of $\chi_M T$ vs T (left) and M vs H / T at different temperature (right)

In the plot $\chi_M T$ vs T, at high temperatures the $\chi_M T$ exhibits values that can be mathematically related to magnetization and from that, to the magnetic moment of each molecule. As the temperature decreases, the values of the $\chi_M T$ temperature are maintained for a mononuclear system, although starts decreasing at lower temperatures due to the antiferromagnetic interactions with the neighboring molecules. At the lowest temperatures, an abrupt decreasing of the temperature is shown. At this range of temperature, the intermolecular interactions are stronger but also the spin-orbit contribution becomes relevant. The latest, as we will explain below, gives rise to the breaking of the degeneration states where only the ground state will be populated at low temperatures.

Magnetization measurements (M vs HT^{-1}) are performed at very low temperatures (in most of the cases in the range of 1.8 to 8 K) with the use of strong magnetic fields; this technique is one of the best for the study and quantification the zfs parameters (value and sign). At low fields, the magnetization shows low values since, apart from the ground state, other excited states are populated. As the magnetic field is increased, the states are more separated in energy (it will stabilize the ground state that is in the same direction of the magnetic field). Thus, at high magnetic fields, the separation may become optimal populating only the ground state, giving rise to magnetic saturation values. Compounds exhibiting high anisotropy values display split states before the application of any magnetic field (zero field splitting), therefore reaching the saturation value will be easier and the process presents low dependence with the magnetic field (superposition of the iso-field curves). In contrast, systems with low magnetic anisotropy values will present excited states closer in energy to the ground state and the process to reach saturation of the magnetization will present high dependence with the magnetic field (non-superposition of the iso-field curves).

In the practical side, systems with very small zfs parameters (below 0.1 cm^{-1}) will be not so precisely determined by the use of SQUID technique and the use of EPR is necessary.

EPR measurements

The EPR measurements will give us information about the energetic transitions between these states. As is shown in Figure I.6, when a magnetic field is applied the states are splitting. This difference in energy, and therefore different population of the states; for any given magnetic field there is an electronic radiation with energy E = hv (h = Planck constant and v = frequency of the applied radiation) that causes resonance between two M_S states, taking into consideration the "spectroscopic selection rules", $AM_S = \pm 1$ and $\Delta S = 0$.[31]

EPR measurements are performed with the use of a variable magnetic field (between 0 and 6 T) and a constant frequency. These frequencies are normally called bands and named with capital letters, the most used are X (9.5 GHz, 0.3 cm^{-1}) and Q (35 GHz, 1.16 cm^{-1}) bands.

Therefore, depending on the orbitallic component of the electron, which will vary according to the orbital in which is located, it will give rise to different frequencies (which implies a different g value compare to the free electron g = 2.00). The g value can be calculated from the formula (3):

$$g = \frac{h\nu}{\mu_B H} \qquad (3)$$

Figure I.8 shows a representation of the first derivative of the EPR spectra and Zeeman plots for S = 1 are shown for (i) isotropic system, D = 0 and (ii) anisotropic system D ≠ 0. In the first case, a single signal appears with g = 2.00 and the Zeeman plots are the same for the three directions of the magnetic field (x = y = z). In the second case, the anisotropy give rise to different Zeeman plots in the z direction (x = y ≠ z) and EPR signal splits into four ΔMs = 1 (red) and one ΔMs = 2 (blue). The last one should be forbidden according the spectroscopic selection rules. However, the anisotropy gives rise the mixing of Ms states allowing the transition.

As mentioned, EPR measurements is ideal for when the values of D are small; however, systems which presents big zfs parameters (D >> hv), present ΔMs = 1 transitions shift at high magnetic fields (H > 6 T) and therefore, a high-field EPR (HFEPR) instrument is needed.

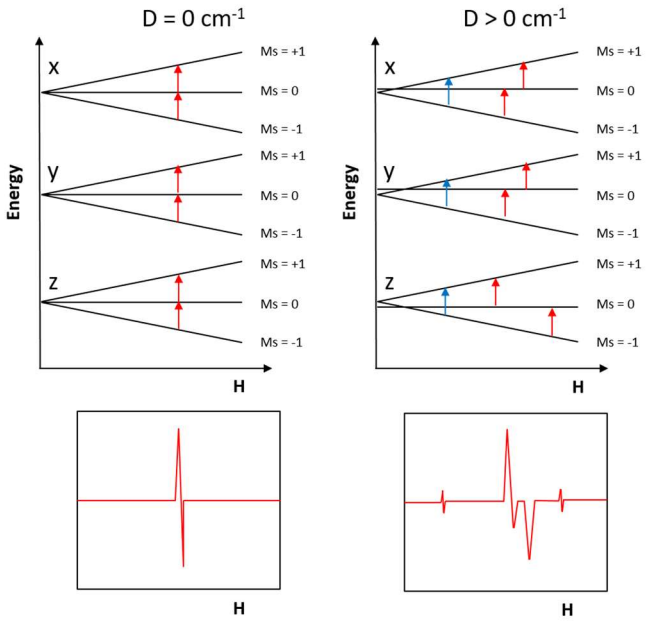

Figure I.8: Representation of the effect of the axial zero-field splitting on Zeeman plots and EPR spectra for an S = 1 state.

In part of the work presented here, HFEPR experiments were performed for the achievement of the D and E parameters. Fittings of the experimental measurements from the HFEPR experiment using correlation programs as for example PHI can provide the values of the anisotropic parameters.[32] In our case, such fittings were performed by our collaborators in Professors Hill's group. Further details will be shown in the chapter of mononuclear Ni^{II} systems.

In former times, from the values of the magnetic anisotropic parameters D and E were practically unpredictable and therefore the search of new systems which present high anisotropy parameter was based on serendipitous processes. However, as mentioned above, the use mononuclear SMMs, which are structurally simpler, has led to the creation of theoretical models,[33–35] in which these parameters can be predicted in function of structural and electronic factors of the paramagnetic centers under study. This fact is very relevant since allows the search of new systems with high magnetic anisotropic values based in a non-serendipitous methods and therefore the possibility of designing better SMMs.

Magnetic Anisotropy: Theoretical values approach

These studies have allowed the development of predictive theoretical models of the magnetic anisotropy,[33–35] relating the magnitude and sign of both parameters (D and E) with the electronic structure and coordination geometry of 3d metal centers.

The Hamiltonian equation that describes the terms of the zero field splitting is:

$$H = D\left(S_z^2 - \frac{1}{3}S^2\right) + E(S_x^2 - S_y^2) \quad (4)$$

where D corresponds to the axial zfs parameter, S corresponds to the spin operator and E rhombic zfs parameter. The parameters of magnetic anisotropy (D and E) are calculated from the elements of the diagonalization of the tensor D (equation 7).[36]

$$D = D_{zz} - \frac{D_{xx} + D_{yy}}{2} \quad (5)$$

$$E = \frac{D_{xx} - D_{yy}}{2} \quad (6)$$

$$D_{kl} = \frac{\zeta_{eff}^2}{4S^2} \sum_{i,p} \frac{\langle \varphi_i | l_k | \varphi_p \rangle \langle \varphi_p | l_l | \varphi_i \rangle}{\varepsilon_p - \varepsilon_i} - \frac{\zeta_{eff}^2}{4S^2} \sum_{p,a} \frac{\langle \varphi_p | l_k | \varphi_a \rangle \langle \varphi_a | l_l | \varphi_p \rangle}{\varepsilon_a - \varepsilon_p} \quad (7)$$

Where ζ_{eff} is the monoatomic spin-orbit coupling constant, l_k / l_l are the x, y, z components of the angular momentum operator and ε indicates the orbital molecular energy with the subscripts i, p or a, which indicate doubly occupied orbital, semi-occupied or empty orbital respectively.

The value and the sign of the parameter D (positive or negative) depend basically on (i) the nature of the orbitals involved and (ii) their difference in energy.

Small energy differences ($\delta = \varepsilon_a - \varepsilon_p$) will result in high D_{kl} values ($\varepsilon_a - \varepsilon_p$ is located in the denominator in the equation). The difference in energy will depend on the nature of the orbitals involved, it means, it will depend on the quantum number of spin (m_l) of the orbitals involved in the integral of the quantum moment operator (l_k, l_l), which are related to the magical pentagon (Figure I.9). This magical pentagon shows the allowed transition (± Δml = 0, 1).

Therefore, systems with presents transition that contain ± Δml = 0 (xz to yz or x^2-y^2 to xy) will show higher contribution from the operator L_z and consequently, the D_{zz} will be high. Hence, the factor D_{zz} will be larger than $(D_{xx} + D_{yy})/2$ and the parameter D will show negative D values.

In contrast, systems that present transitions that contain ± Δml = 1, show greater contributions of the L_y and L_x operators and therefore the values D_{xx} and D_{yy} will be elevated. Thus, the factor $(D_{xx} + D_{yy})/2$ will be larger than D_{zz} and the parameter D will show positive D values.

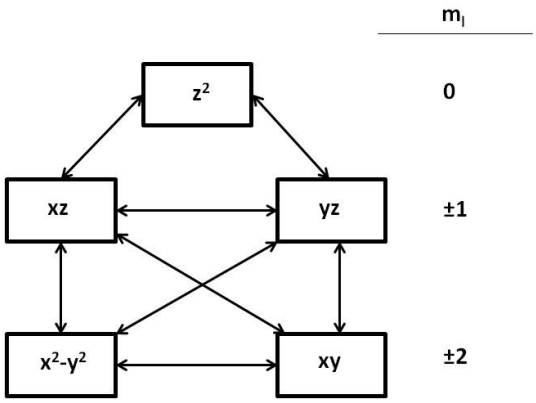

Figure I.9: Magic pentagon

Depending on the sign of the parameter D different Ms states will be stabilized; in the case of negative values, the ground state will be the highest Ms value and on the contrary, in the case of positive D values, the lowest Ms value (Figure I.10).

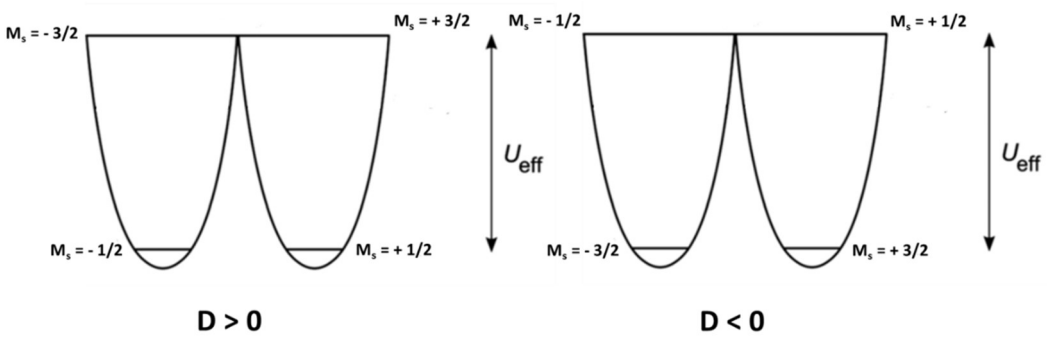

Figure I.10: Representation of double-well potential for D > 0 (left) and D < 0 (right) for an ideal S = 3/2 system.

Figure I.11 shows an example of the above explanation. In the case of Mn^{III} (d^4) compounds with octahedral symmetry, having axial elongation, the first excitation energy (δ) will correspond to the transition between the non-bonding orbital d_{xy} to the antibonding orbital d_{x2-y2}. This transition, in the magical pentagon, corresponds to (± Δml = 0), so the D_{zz} component will be great. These compounds contain excited states with very high energy, since the transition of the orbital d_{z2} (despite being lower in energy) is not allowed because ± Δml = 2. As a result, these systems will present small and negative values of D.

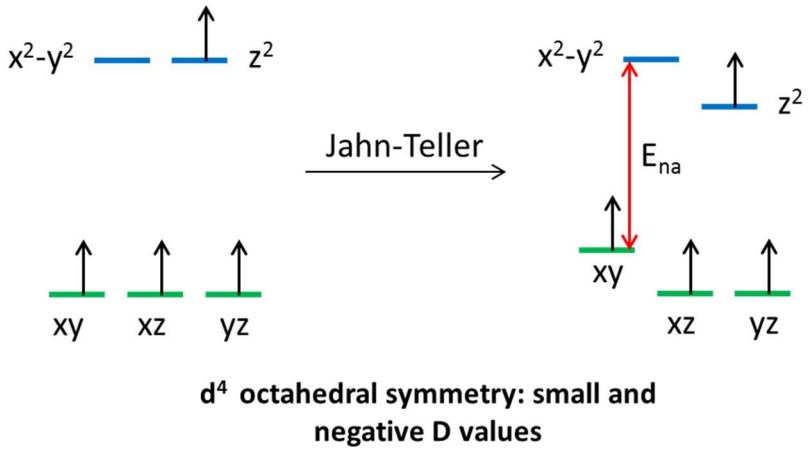

Figure I.11: Splitting of the d orbitals due to the Jahn-Teller effect for d^4-octahedral coordination and axial elongation. The energy difference is indicated by the red arrow.

The small energy difference, therefore high D values ($\delta = \varepsilon_a - \varepsilon_p$), will be achieved by small distortions caused in the ideal symmetry, originated by Jahn-Teller effects caused by the metal or by the distribution of the ligands coordinated to the metal center.

Identifying Single Molecule Magnets

The characterization of SMMs is carried out mainly by measurements of the magnetic susceptibility applying an alternating field (ac) at different frequencies to obtain information about the dynamic magnetization. This magnetic susceptibility (χ_{ac}) is separated into its two components ($\chi_{ac} = \chi_{ac}'$-i χ_{ac}''), where (χ_{ac}') is the real component, or in phase with the oscillating field, and (χ_{ac}'') is the imaginary component, or out of phase with the oscillating field.

In the case of systems which no exhibit SMMs behavior (fast magnetic relaxation) the magnetization of the molecule is able to follow the direction of the alternating magnetic field and there are not different values for the out-of-phase susceptibility (χ_{ac}''); on the contrary, in the case of SMMs, the presence of the thermal energy barrier caused the slow relaxation of the magnetization and therefore, the magnetization of the molecule are not able of following the oscillating direction of the applied magnetic field. This fact originates at a certain temperature, an increases of the signal corresponding to of out-of-phase susceptibility (χ_{ac}'') provide maxima in the χ_{ac}'' vs T curves and a dependence with the frequency (Figure I.12, left).

In addition, hysteresis cycle measurements can be also used to characterize SMMs, where the variation of the magnetization is measured by the application of an external cyclic magnetic field (-H + H) (Figure I.12, right). As it can be seen, jumps in the magnetization values are observed at certain magnetic fields. This phenomenon is attributed to tunneling effects.

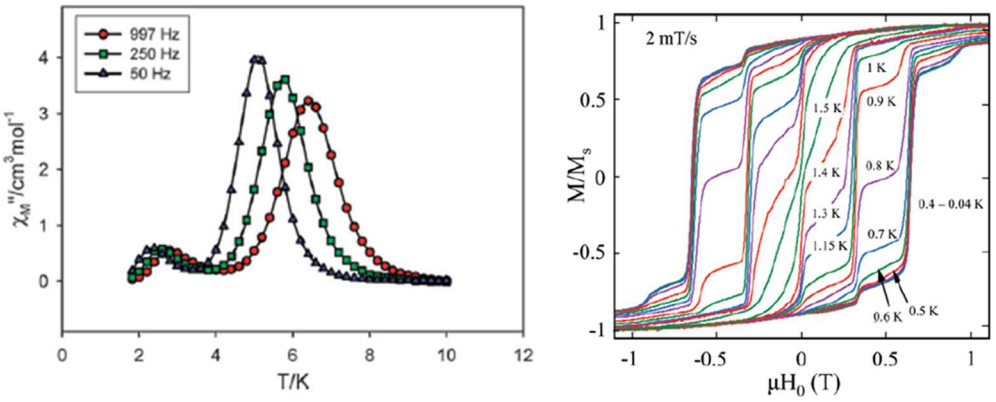

Figure I.12: Representation of χ_{AC}" vs T and different frequencies (left) and Hysteresis cycle (right) of Mn_{12}[37] Reprinted with permission from Copyright American Chemical Society.

Relaxation time calculations

The analysis of these measurements (χ_{ac}'' and χ_{ac}' vs T) allows the achievement of the relaxation time of the magnetization (τ) from the Debye equations.[38–40] These equations are used for systems that present a single relaxation process (a single value of τ). In that case, the representation of χ_{ac}'' vs χ_{ac}' (called as Argand diagram) will gives rise to semi-circled curves, where the frequency corresponding to the highest value (χ_{max}) relates to the relaxation time ($\omega^{-1} = \tau$) (Figure I.13).

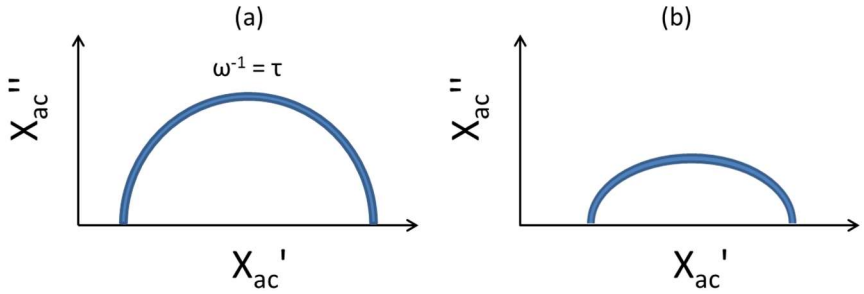

Figure I.13: Representation of Argand (left) and Cole-Cole (right)

On the other hand, when systems present more than one relaxation process, the representation will give a non-perfect semicircle. In that case, the equation of Cole-Cole is used, which is the Debye equations adding an α parameter (Annex 1.3). The α parameter presents values between ($0 < \alpha < 1$) that provide information about the different relaxation processes that are coexisting in the relaxation of magnetization. To obtain information of the distribution of these processes, a representation of the relaxation time versus the temperature (ln (τ) vs 1/T) will be performed. In the Figure I.14 it's possible to see the dependence temperature of the different processes.

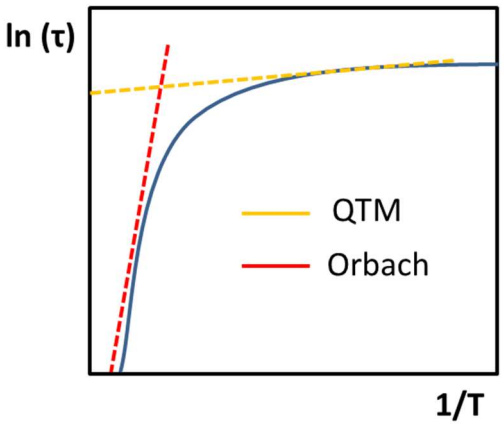

Figure I. 14: Representation of ln (τ) vs 1/T. Different dependence of relaxation time with the temperature is observed depending to the process responsible in the relaxation of the magnetization.

The process observed at high temperature corresponds to a thermal relaxation process which takes place overcoming the energy barrier (Orbach process). The linear dependence observed follows the Arrhenius equation. From this equation, the value of the energy barrier (U_{eff}) can be obtained.

$$\tau = \tau_0 \, e(-\frac{U_{eff}}{k_B T}) \qquad (8)$$

where U_{eff} is the effective energy barrier, k_B the Boltzman constant and τ_o a pre-exponential factor, which presents a value between 10^{-6} – 10^{-11} s.[5]

Multifunctional systems: Properties beyond Magnetism

Apart from the magnetic properties derived from the metal center, the combination of these properties with those from the organic matter, that will give rise to multifunctional systems, is a great challenge.

In this case, great efforts have been directed toward the design of coordination compounds where the magnetic properties derived from the metal, and the fluorescence properties derived from the organic ligand merge in the same molecule.

Apart from the fluorescence properties originate by the organic ligand, these systems can also provide affinity for certain substrates (eg.: graphite, see next chapter for further details). This fact would allow the study of how the systems organize on surfaces, as well as their stability toward their future inclusion as components in nanodevices. [41,42]

Fluorescence

Fluorescence can be defined as the process of light emission by molecules that are excited by electronic radiation. A molecule with “close shell” contains two electrons in the HOMO orbital (ground state, S_0) and the LUMO orbital reminds empty (excited state, S_1), as is represented in the Jablonski Diagram (Figure I.15)

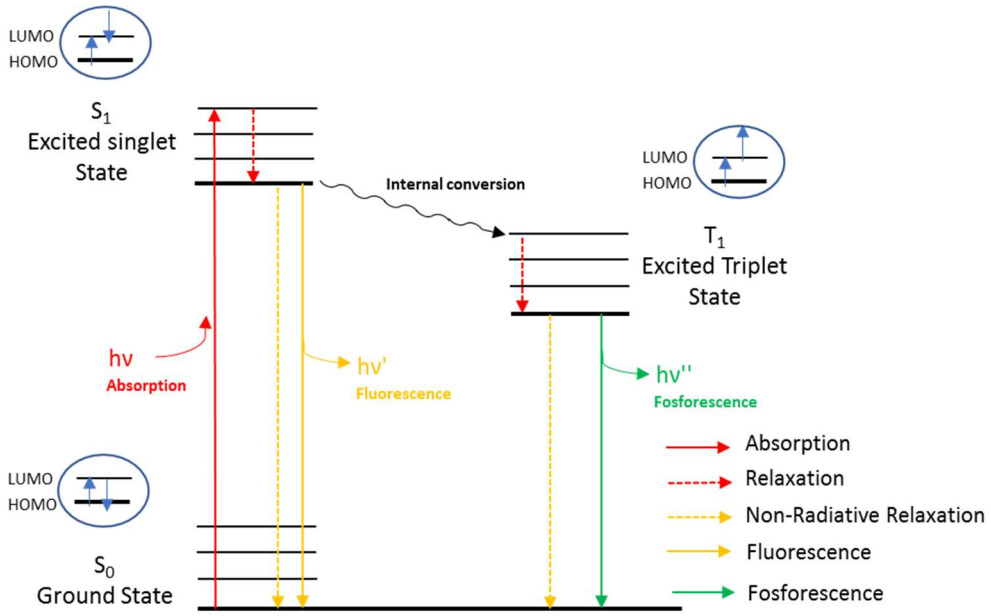

Figure I.15: Scheme of Jablonski diagram

By energy absorption (E = hv), the excited stated is reached and; it relaxes to the lowest vibrational state in the excited state. At this point there are two different ways for the molecule to release the energy and return to its ground state:

(i) Non-radiant relaxation, where the system reaches the basal state without emitting a phonon; only releasing the excess energy in the form of heat.

(ii) Luminescence relaxation where a phonon lower in energy hv', compare to the absorption, it is emitted. The shift to longer wavelengths is called Stokes shift. Luminescence processes can be from single excited states or through a crossing intersystem from a triplet excited state to the ground state, respectively. This thesis shows an example of the first.

One of the most attractive characteristics of the fluorescence is its inherent sensibility; for example, to the polarity of the solvent, pH, concentration, present of paramagnetic ions, etc.

In addition, depending on the nature of the chromophore, as it is in the case of aromatics rings (e.g.: anthracene) excimers species can be formed (supramolecular dimers where one of the molecules is excited and the other is in the ground state). These species exhibit broad fluorescence emissions shifted to lower energies compared to the isolated molecule (red shifts) and their formation is concentration dependent (Figure I.16).

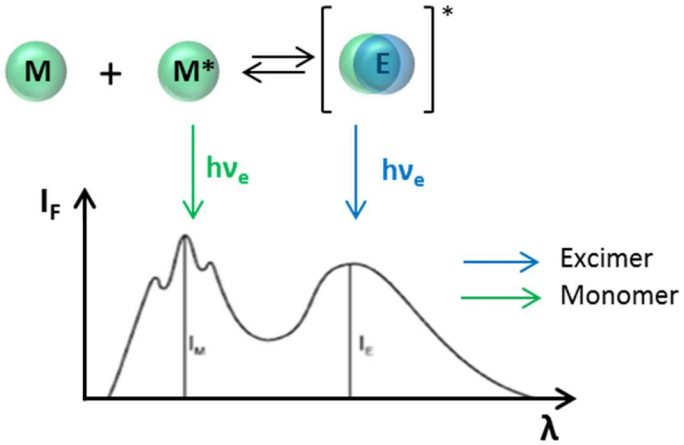

Figure I.16: Excimer formation with the corresponding monomer and excimer bands.

In relation to the presence of metal centers, depending on their nature two different effects can be observed: (i) on one hand, the coordination of diamagnetic metals leads to an increase of the fluorescence emission (QUEF, Chelation Enhanced Fluorescence), however the coordination of paramagnetic metals leads to a decrease of the emission (CHQF, Chelating Quenched Fluorescence).

This work shows the study of multifunctional materials that present magnetic and fluorescent properties and provides an overview of how one affects to the other toward future design.

Section classification

The results presented in this section are classified in three different chapters depending on the metallic center used and final structures:

(i) Mononuclear Co^{II} SMMs: systems based on CCMoid ligands (chapter I).

(ii) Mononuclear Ni^{II} compounds: systems based on CCMoid ligands (chapter II).

(iii) Coordination polymers based on Co^{II}/Ni^{II}-9Accm units (chapter III).

1.2 Chapter I: Mononuclear Co^{II} SMMs: systems based on CCMoid ligands

1.2.1 Introduction

Here in chapter I, the synthesis and characterization of two pseudo-octahedral mononuclear Co^{II}-compounds coordinated to a CCMoid ligand called 9Accm is described toward the creation of multifunctional systems. Among different metals, the choice of Co^{II} had as a purpose the synthesis of mononuclear compounds SMM properties, taking into account the inherent magnetic anisotropy (D) of such type of metal centers.[43] 9Accm was used to evaluate the effect of the magnetic center in the fluorescence of this free ligand and to study the affinity of the final molecules toward graphite surfaces.

Background

There is a limited number of mononuclear Co^{II} SMMs described in the literature. The first one was published in 2011 by T. Jurca *et al.*[44] with a $Co(NCS)_2$-bis(imino)pyridine formula exhibiting slow relaxation in the ac magnetic susceptibility experiments in the presence of an external magnetic field (dc). This compound presents a pyramidal geometry with a base square distorted where the center of Co^{II} was located above the basal plane. The same year, the group of Prof. Long published another mononuclear Co^{II} with tetrahedral geometry ($[Co(SPh)_4][Ph_4P]_2$).[45] This compound presented the peculiarity that it was not necessary to apply an external magnetic field (dc) to observe the slow relaxation. A following study presented a new Co^{II} system containing guanine derivatives as ligands with formula $[CoCl(3G)]^+$ (3G = guanine derivative).[46] In this case, the compound presents a distorted tetrahedral geometry, where a slow relaxation of the magnetization was observed despite of having a positive D sign (D = 12.7 cm^{-1}). This fact was relevant since, before that moment the behavior of SMM was restricted only to the values of negative axial magnetic anisotropy (D) and that originated a great interest for experimental and theoretical point of views. The following remarkable compound appears in 2012, with the publication of the first Co^{II} mononuclear with six coordination and formula *cis*-$[Co(dmphen)_2(NCS)_2]$.[47] This compound presents a large positive magnetic anisotropy (D = 98 cm^{-1}) with a distorted octahedral geometry. One of the latest compound published has been, in 2017, a mononuclear Co^{II} with coordination number two $[Co=N]^+$. This system presents the largest energy barrier record to date for any transition metal (U_{eff} = 413 cm^{-1}).[48]

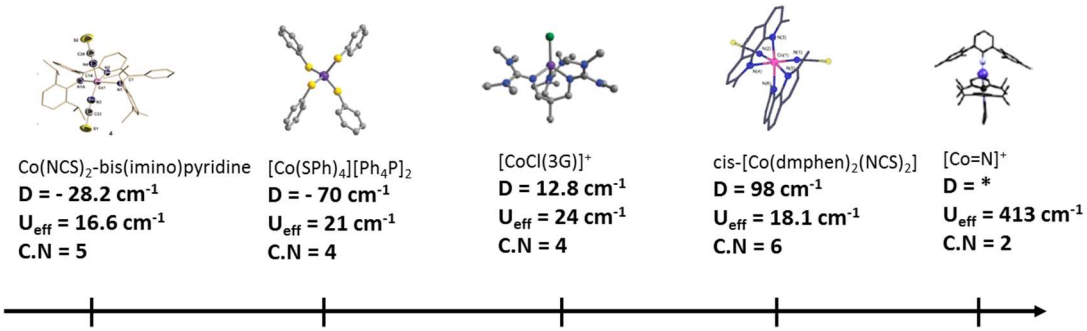

Figure 1.1.1: Evolution timeline of the different Co-SMMs discussed in the text.

Magnetic properties of mononuclear Co^{II} compounds

To have a better understanding of the magnetic behavior of cobalt systems and why the fascination of such systems, its electronic structure should be taken into account; details are shown schematically in Figure 1.1.2.

The excited states are located at 15000 cm^{-1} and above, therefore will not be populated even at room temperature, with the unique contribution of with the spin coupling and orbital moment of the mixture with ground terms which present same multiplicity (second order spin orbital contributions).

Mononuclear high spin Co^{II} systems (d^7) present a (4F) ground term. By the interaction of the crystalline field through coordination to the ligands, this term splits according their symmetry into two triplets ($^4T_{1g}$ and $^4T_{2g}$) and one singlet ($^4A_{2g}$), being the term $^4T_{1g}$ now the ground state. Thus, systems with an ideal octahedral structure will present an orbital degenerate ground state, exhibiting therefore a first-order spin-orbit coupling.

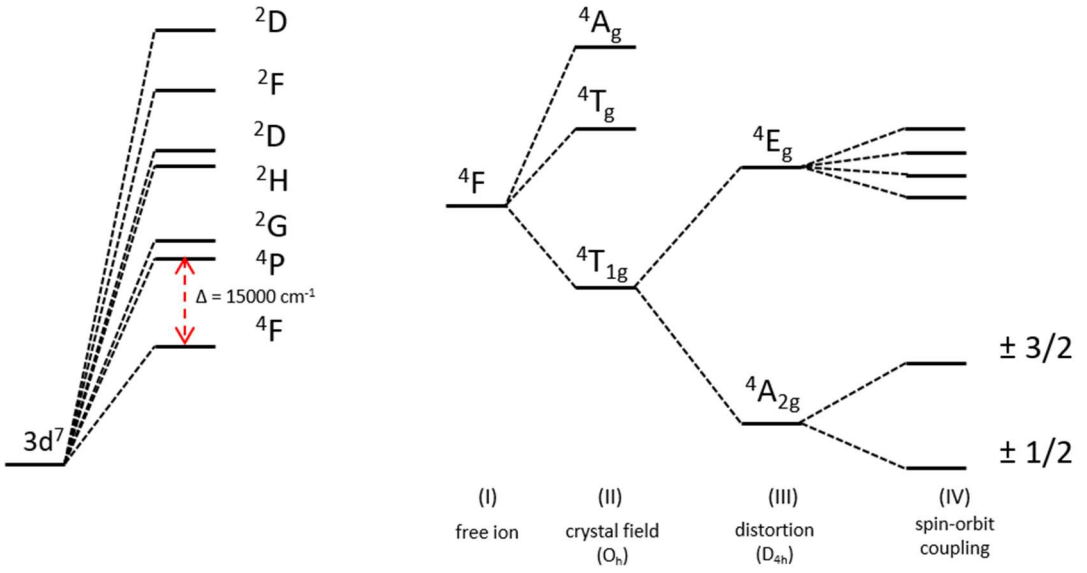

Figure 1.1.2: Scheme of (I) fundamental term for a free Co^{II} ion, (II) levels for an octahedral environment, (III) splitting of the fundamental triplet and excited states for an octahedral symmetry with axial distortion environment and (IV) second-order spin orbit coupling

However, most of the systems present distortions that cause the deviation from the ideal perfect O_h symmetry reducing the spin-orbit coupling. In the case of hexacoordinated Co^{II} compounds, some of the coordination geometries commonly present tetragonal distortions, giving place to axial elongations or compressions (D_{4h}) due to Jahn-Teller effects. This reduction of the symmetry produces the breakage of the degeneration of the ground state term $4T_{1g}$ in $^4A_{2g}$ and ^4E_g, both separated by Δ, which corresponds to the energy of stabilization of the crystalline field (Figure 1.1.3).

When the distortion is negative (Δ < 0), the system presents an axial compression and the ground state term corresponds to ^{4}Eg. In this case, the system will present first-order spin-orbit coupling and the behavior become more difficult. On the other hand, system which presents an axial elongation (Δ > 0), the ground state corresponds to a $^4A_{2g}$ singlet and the system will be considered as spin only S = 3/2 (Figure 1.1.3).

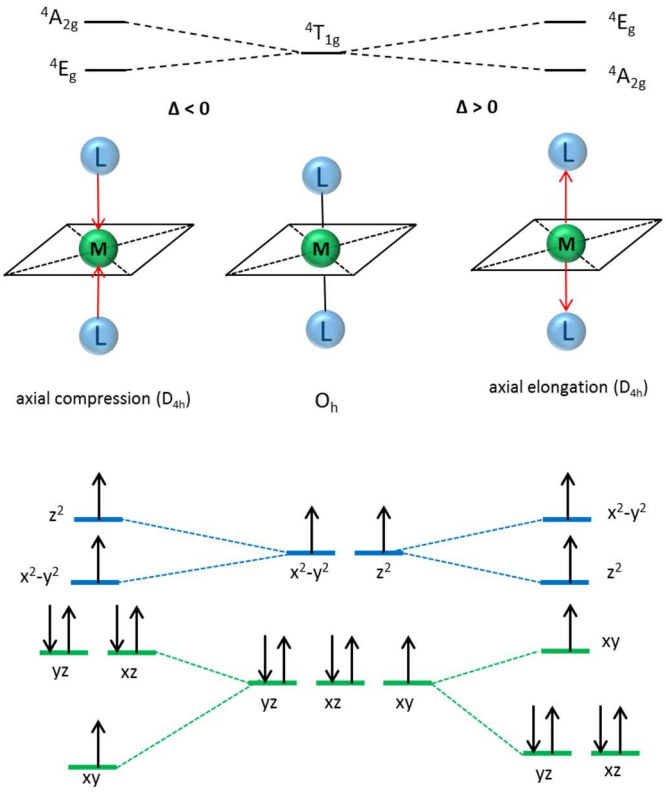

Figure 1.1.3: Scheme of octahedral environment symmetry and the evolution of the orbitals when an axial distortion is present.

This ground state $^4A_{2g}$ will exhibit a spin orbit contribution (zero field splitting) which evolves into the so-called Kramers doublet (± 3/2 and ± 1/2). Depending on the sign of the axial magnetic anisotropy (D), ± 3/2 or ± ½ will be stabilized. Compounds with D < 0, will present a ground state of ± 3/2 and with D > 0, will be of ± 1/2 (Figure I.10).

As it was shown before, the sign and the magnitude of the parameter D depend on the nature of the orbitals involved in the axial distortion.

In the case of Co^{II} (d^7) compounds with pseudo-octahedral symmetry, displaying an axial elongation (Figure 1.1.4), first excited energy (δ) will correspond to the transition between the orbitals d_{xz} or d_{yz} and the orbital d_{xy}. As the different of energy is small between them, huge values of D would be obtained. Related to the sign, it is possible to assign the transition by the use of the magical pentagon. As the transition correspond to (± Δml = 1), the D_{xx} or D_{yy} component will be great and therefore positive D values will be obtained.

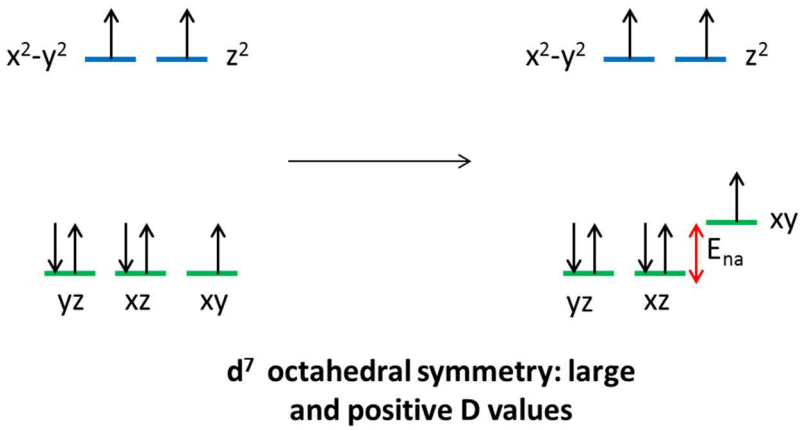

Figure 1.1.4: Splitting of the d orbitals due to Jahn-Teller effects for a d^7-octahedral coordination with an axial elongation. The energy difference is indicated by the red arrow

1.2.2 Objectives

In this chapter two octahedral mononuclear Co^{II} compounds were synthesized, each one having two 9Accm ligands but different pyridinic ligands, respectively. The different in the nature of the pyridinic groups in each compound led to different arrangements of the ligands (*trans* (1) / *cis* (2), see Figure 1.1.5) around the metallic center. This fact makes it possible to carry out a comparative study of both systems and the study of how the structural differences affect the luminescent properties, the stability of the systems in solution/on surfaces and the magnetic behavior, specially in the study of the slow magnetic relaxation. The compounds studied present the following formulae: **$[Co(9Accm)_2(py)_2]$ (1)** and **$[Co(9Accm)_2(2,2'\text{-bpy})]$ (2)** (where py = pyridine and 2,2'-bpy = 2,2'-bipyridine). Both systems present an octahedral distorted geometry, but the overall arrangement of the ligands is *trans* for compound **1** and *cis* for compound **2**, the latest forced, by the chelating nature of the bipyridine. The rich aromatic nature of 9Accm allows us the study of the luminescence properties (absorption/emission) of the coordination compounds and the assessment of the influence of the paramagnetic center on such property. On the other hand, this aromatic nature allows the immobilization of the systems on graphene surfaces by π-π interactions between the rings of the molecule (Figure 1.1.5) and the substrate. This point is very important for a possible future application as molecular devices and will be further exploited in section II.

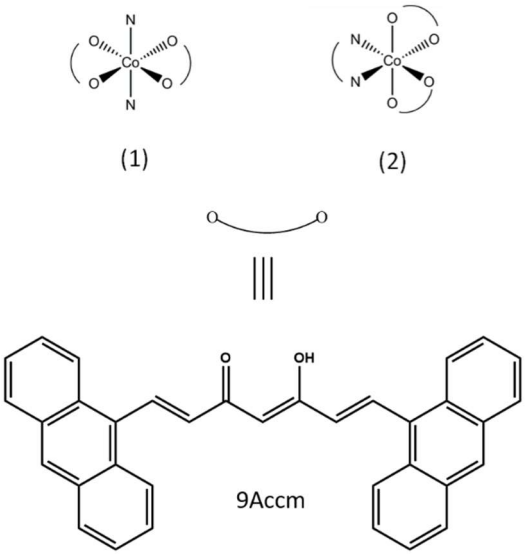

Figure 1.1.5: Visualization of the Co^{II} coordination environment for compound **(1)** *trans* and compound **(2)** *cis* (top). Structure of the ligand 9Accm (bottom).

1.2.3 Results and Discussion

1.2.3.1 Synthesis

The synthesis of the compounds $[Co(9Accm)_2(py)_2]$ **(1)** and $[Co(9Accm)_2(2,2'\text{-bpy})]$ **(2)** were carried out by the use of a microwave reactor (MW) using one equivalents of the metal and two equivalents of the CCMoid ligand, 9Accm. This technique allows us to increase the speed of the reactions with the benefits of higher yields in short periods of time together with high purity without unwanted cleaning procedures.[49] Despite being highly used in the field of organic chemistry,[49] its use has also spread in other fields of chemistry, reaching a prominent role even in the synthesis of coordination compounds due to the advantages mentioned before.[49] Within these reactions, the choice of solvent to perform the reaction is a crucial point, and especially in our systems, since it is the reason why we obtain different organization of 9Accm ligands around the Co^{II} metal center (when the solvent used is pyridine).

For compound **1**, pyridine was used as a co-ligand and as a solvent at the same time. The choice of pyridine as a solvent it was because has difference functions: (i) can acts as a base for deprotonating the ligand and (ii) can complete the coordination sphere of the central ion due to its high coordinating ability.[50] Since cobalt has a tendency to be hexacoordinated, the coordination of two

9Accm ligand and the two molecules of pyridine complete the coordination sphere. The final arrangement displays a *trans* disposition.

In a parallel way, the synthesis of a similar compound was carried out using 2,2'-bipyridine instead of pyridine. The nature of the first group is similar to the previous one, but the coordination mode in this case is through two nitrogen atoms that are side by side.

For compound **2** the synthesis was carried out using N,N-dimethylformamide (DMF) as a solvent. Despite its coordinating nature, in this case it will not coordinate with the metallic center due to the high stability provided by the chelate effect of the 2,2'-bipyridine. Thus, the 2,2'-bipyridine complete the coordination sphere of the Co^{II} together with two 9Accm ligands. Its bidentate nature leads to a *cis* disposition of all the ligands.

Therefore, two compounds similar in nature, but presenting a different arrangement of the ligands were synthesized.

Regarding standard characterization of the compounds, infrared spectroscopy (IR) is very useful because the reaction process can be followed since different bands are shifted compared to the free ligand 9Accm (Figure 1.1.6). In both compounds, common bands appear in the area 1600-1450 cm^{-1} corresponding to υ (C=O), υ (C=N) and υ (C=C). This area is shifted comparing with 9Accm due to the coordination of the Co^{II} center to the β-diketone moiety. In addition, another signal at 734 cm^{-1}, corresponding to the υ (CH) of the anthracene groups, shifted from the 9Accm (732 cm^{-1}). This band is usually used as a reference since there is always a slight shift in its value once the coordination with a metallic center has occurred. Apart from the similarities mentioned, there are significant changes between the two spectra. For compound **1** two peaks appear at 780 cm^{-1} and 697 cm^{-1}, corresponding to coordinated or pyridine-free molecules. Compound **2**, on the other hand, has a band at 765 cm^{-1} corresponding to the 2,2'-bipyridine group.[51]

Both systems were also studied using MALDI (Matrix-Assisted Laser Desorption/Ionization) (Annex 1.4). The two compounds show the existence of the $[Co(9Accm)_2]^+$ and $[Co(9Accm)_2]Na^+$ species with m/z values of 1010.3 and 1032.3, respectively. Apart from these signals, compound **2** includes a signal corresponding to $[Co(9Accm)(2,2'\text{-bpy})]^+$ at m/z 690.1.

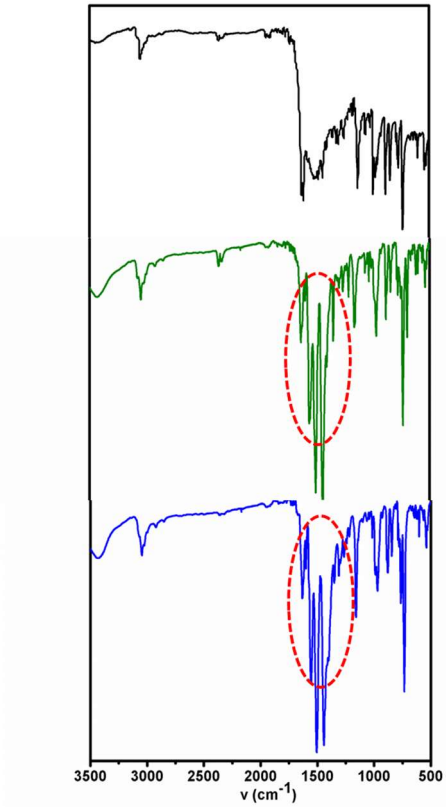

Figure 1.1.6: Comparison of the IR spectra of ligand 9Accm (black), compound **1** (green) and compound **2** (blue).

1.2.3.2 Crystal structures

Studies of single X-ray diffraction of **1** and **2** were carried out. This technique is important since it corroborated the disposition of the ligands for both compounds. The crystalline bond distances and angles of the molecular structures of the compounds **1** and **2** are described in Annex 1.5.

$[Co(9Accm)_2(py)_2]$ (1) crystallographic description

The compound **1** crystallizes in a space group P2 (1) / c. The central Co^{II} atom is coordinated to two pyridine ligands and also to two 9Accm ligands through their β-diketone groups. CCMoid ligands and pyridinic ligands present a *trans* arrangement giving rise to a hexacoordinated coordination compound as t is shown in Figure 1.1.7. The CCMoid ligands are located in the equatorial plane and are coordinated by the four oxygen atoms, whereas the pyridine ligands are arranged in the axial plane and are coordinated by the two nitrogen atoms, adopting the Co^{II} center a distorted O_h geometry.

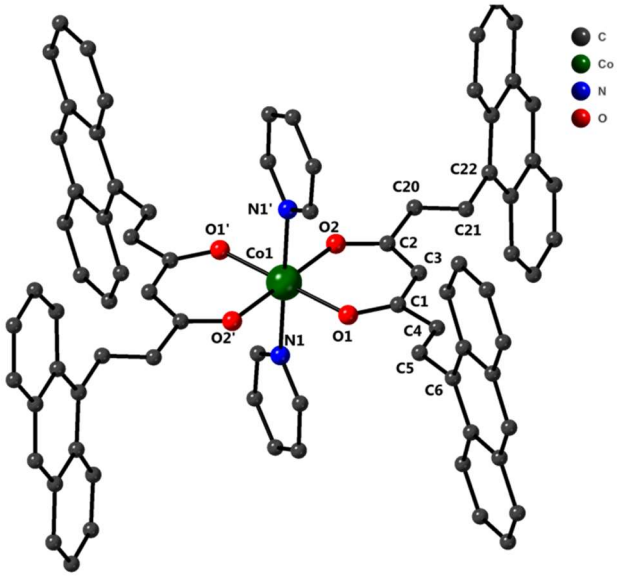

Figure 1.1.7: Representation of the molecular structure of compound **1** where the atoms of Co (green), O (red), N (blue) and C (gray) are shown. H atoms have been omitted to simplify the structure

The molecule shows two Co-O distances of 2.002 Å and 2.033 Å and one Co-N distance of 2.209 Å. These distances are in agreement with compounds in the literature that contain β-diketone ligands and pyridine groups coordinated to metallic Co^{II} centers.[52–56] No higher distances are found that could indicate the presence of Jahn-Teller effect. Theoretical studies were carried out confirming the no existence of this effects (however, expected for d^7 systems) due to the disposition of the occupied and semi-occupied orbitals and the fact of not having a homoleptic system.

The O(1)-Co(1)-O(2') (angle forming a six membered ring between the Co^{II} ion and the β-diketone) and a O(1)-Co(1)-O(1) angle values are of 90.13 ° and 89.97 °, respectively. These values deviate slightly from ideality due to the octahedral distortion caused by the different nature of the ligands. On the other hand, the angles corresponding to the diagonals of the octahedron (O(1)-Co(1)-O(1'), O(2)-Co(1)-O(2') and N(1)-Co(1)-N(1') are 180 ° by symmetry.

Basically, the coordinated 9Accm ligands display two alternating C-C values: C(1)-C(4), C(5)-C(6), C(2)-C(20) and C(21)-C(22) relate to the C-C single bond (1.400-1.486 Å) and on the other hand, C(4)-C(5) and C(20)-C(21) show characteristic C-C double bonds (1.311-1.315 Å). Such distances are found in related compounds.[57–60] The conjugated chains show different conformation in each side. In one side, the conformation is in a zig-zag and in the other side a boat-shape. This fact indicates the flexibility present in the conjugated chain and the diversity of its packing by comparing with the free ligand and reported compounds.[57–60] The C-C corresponding to the β-diketone group C(2)-C(3) and C(3)-C(1) show value of 1.400 and 1.404 Å, respectively. These values present intermediate distances

between double and single C-C confirming the resonant character of this group. The aromatic rings, anthracenes moieties of the 9Accm and the two pyridines molecules, are oriented perpendicularly to the skeleton of the conjugated chain (equatorial plane). This arrangement could be caused by supramolecular packing and/or steric hindrances.
Finally, it should be noted that no remarkable intermolecular interactions between neighboring compounds are found in the structure. The metal centers are certainly separated with distances $Co^{II}\cdots Co^{II}$ of 8.962 Å.

[Co(9Accm)$_2$(2,2'-bpy)] (2) crystallographic description

Compound **2** crystallizes in a space group P21/n with a solvent molecule of $CHCl_3$ which is omitted in the representation (Figure 1.1.8). The structure shows a similar compound as **1**, with the central ion bounded to two molecules of ligands 9Accm disposed in a *cis* arrangement and one molecule of 2,2'-bipyridine, now resulting in a C_{2v} ideal symmetry.

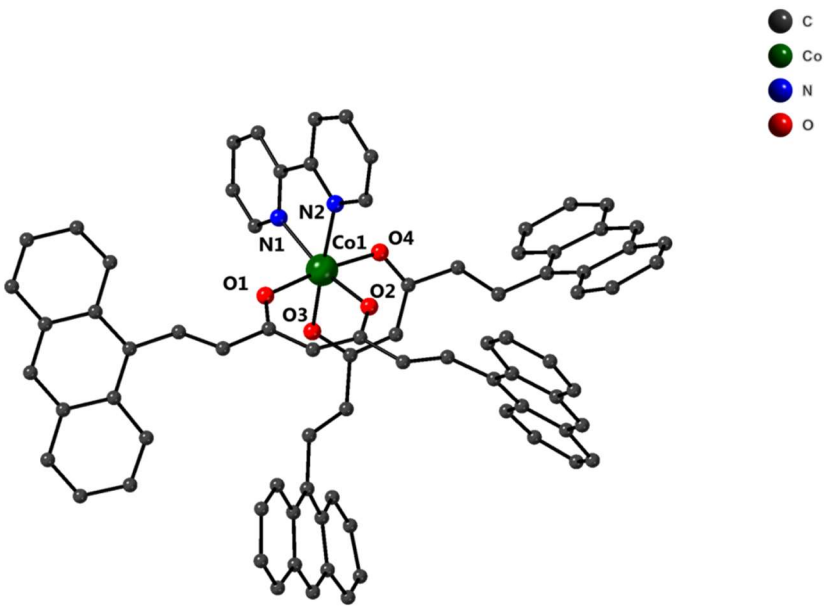

Figure 1.1. 8: Representation of the molecular structure of compound 2 where the atoms of Co (green), O (red), N (blue) and C (gray) are shown. H atoms have been omitted to simplify the structure

The distances around the metallic center, Co(1)-O(1) - Co(1)-O(2), Co(1)-O(4) - Co(1)-O(3) and Co(1)-N(1) - Co(1)-N(2) show values of 2.072 – 2.013 Å, 2.065 – 2.069 Å and 2.110 – 2.115 Å, respectively. These are very similar to those found for compound **1**. On the contrary, O-Co-N angles differ slightly with respect to 1. The angles corresponding to O(1)-Co(1)-O(4), O(3)-Co(1)-N(2) and O(2)-Co(1)-N(1) are 173.48 °, 174.37 ° and 167.38 °, respectively (for compound **1** were 180 °) showing higher deviation from an ideal octahedral structure. Similar C-C values as in the structure of **1** are found for

the C-C distances in both 9Accm ligands, with one of them presenting its two sides in zig-zag conformation meanwhile the other shows zig-zag and boat-shape conformations. The shortest $Co^{II}\cdots Co^{II}$ distance is 10.105 Å and no significant supramolecular interactions can be identified, except a short C-H···O contact of the lattice chloroform molecule with O3, at 2.269 Å.

From the study of crystal structures for both compounds it is important to note that the crystal structure of compound **2** deviates significantly more from the ideal octahedron geometry than compound **1**. This fact can be studied through the measurements of the angles around the metal center (Table 1.1.1). These distortions will present a great relevance in the magnetic behavior as we will see later.

	O1-Co-N1	O1-Co-O1'	O1-Co-O2	O1-Co-O2'	O2-Co-N1
Compound 1	90.06 ˚	180 ˚	90.13 ˚	89.87 ˚	88.52 ˚
Compound 2	95.55 ˚	173.52 ˚	88.21 ˚	87.86 ˚	91.16 ˚
Ideal O_h	90 ˚	180 ˚	90 ˚	90 ˚	90 ˚

Table 1.1. 1: O-Co-N angles of **1**, **2** and ideal O_h.

1.2.3.3 Characterization

The characterizations of the systems were carried out in different states: (i) solid state: by SQUID (Superconducting Quantum Interference Device); (ii) solution by UV-Vis, Fluorescence, Paramagnetic ^{1}H NMR and (iii) surface by XPS (X-ray Photoelectron Spectroscopy) and AFM (Atomic Force Microscopy).

1.2.3.3.1 Studies in solution

Nuclear Paramagnetic Resonance (^{1}H NMR)

The study of paramagnetic compounds by the use of ^{1}H NMR techniques is highly complex compared to those compounds with a diamagnetic nature. The presence of unpaired electrons in the metal centers generates an efficient additional relaxation path to the nuclei located near to the metal center. Consequently, these nuclei show higher relaxations speed (shorter relaxation times) and result in wider signals.[61]

However, metals such Fe^{III} low spin or Co^{II} with octahedral geometries, are considered suitable ions for their study by nuclear magnetic resonance due to their fast electronic relaxation (π_s= 10^{-11}- 10^{-13} s) compared with others metals.[62,63] Therefore, spectral features of "[Co(9Accm)$_2$]" systems are found sharp enough to use ^{1}H NMR as a diagnostic tool in solution. These studies allow better understanding of the paramagnetic effect, the stability and the influence of the geometry (*cis/trans*). To carry out this study, a part of the two compounds, additional four compounds **(3-6)** similar to **1** and **2** were synthesized and characterized by IR, EA and ESI (Figure 1.1.9). Two compounds with *trans*-arranged with formula: [Co(9Accm)$_2$(3,5-(CH$_3$)$_2$-py)$_2$] **(3)** and [Co(9Accm)$_2$(dmf)$_2$] **(4)** and two compounds with *cis*-arranged with formula: [Co(9Accm)$_2$(4,4'-(CH$_3$)$_2$-2,2'-bpy)$_2$] **(5)** and [Co(9Accm)$_2$(5,5'-(CH$_3$)$_2$-2,2'-bpy)$_2$] **(6)** were studied in solution gathering information about the nature of most of the peaks (Annex 1.6). The comparison of their spectra, together with the use of previous literature taking into account mononuclear Co^{II} systems containing acac (acetylacetonate) and pyridinic groups gave rise of the assignment of the peaks.[64–66]

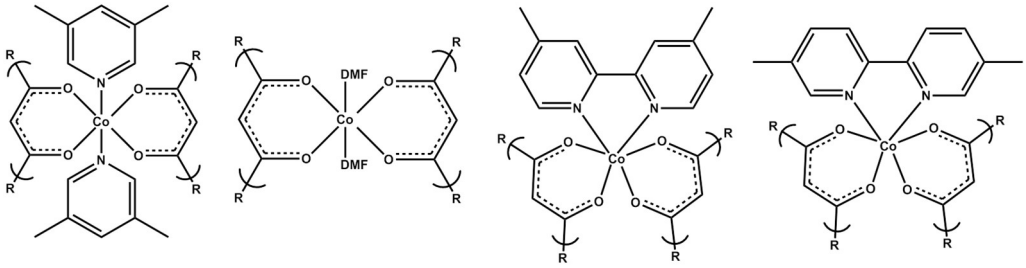

Figure 1.1. 9: Representation of [Co(9Accm)$_2$(3,5-(CH$_3$)$_2$-py)$_2$] **(3)**, [Co(9Accm)$_2$(dmf)$_2$] **(4),** [Co(9Accm)$_2$(4,4'-(CH$_3$)$_2$-2,2'-bpy)$_2$] **(5)** and [Co(9Accm)$_2$(5,5'-(CH$_3$)$_2$-2,2'-bpy)$_2$] **(6)**.

In the case of compound **3**, the choice of (3,5-(CH$_3$)$_2$-py) allows the assignment of the signal of the *meta*- position due to the presence of the methyl group in comparison with the pyridine group in compound **1**. In the case of compound **4**, as (dmf) does not contain aromatic nuclei, it allows the identification of the signals corresponding to the 9Accm groups.

On the other hand, the groups (4,4'-(CH$_3$)$_2$-2,2'-bpy) and (5,5'-(CH$_3$)$_2$-2,2'-bpy) corresponding to compound **5** and **6** respectively, allow us, in the case of pyridine, to assign the positions corresponding to *–meta* and *–para.*

For compound **1**, that displays an ideal D_{4h} symmetry, the number of peaks in the ^{1}H NMR were reduced to eight (taking into account the overlap of some of the signals, free rotation of the anthracene groups in solution and fast conformations that the 9Accm chain can experience), as if there was only one magnetically unique 9Accm and pyridine ligand as well.

In Figure 1.1.10 the spectrum corresponding to compound **1** made in $CDCl_3$ with a window from 0 to 75 ppm is shown. Depending on the shift of the signals, two differentiated regions could be observed: (i) a down-field region where two broad signals appear (38 and 63 ppm respectively) and (ii) an up-field region where six intense signals appear between 15 - 0 ppm.

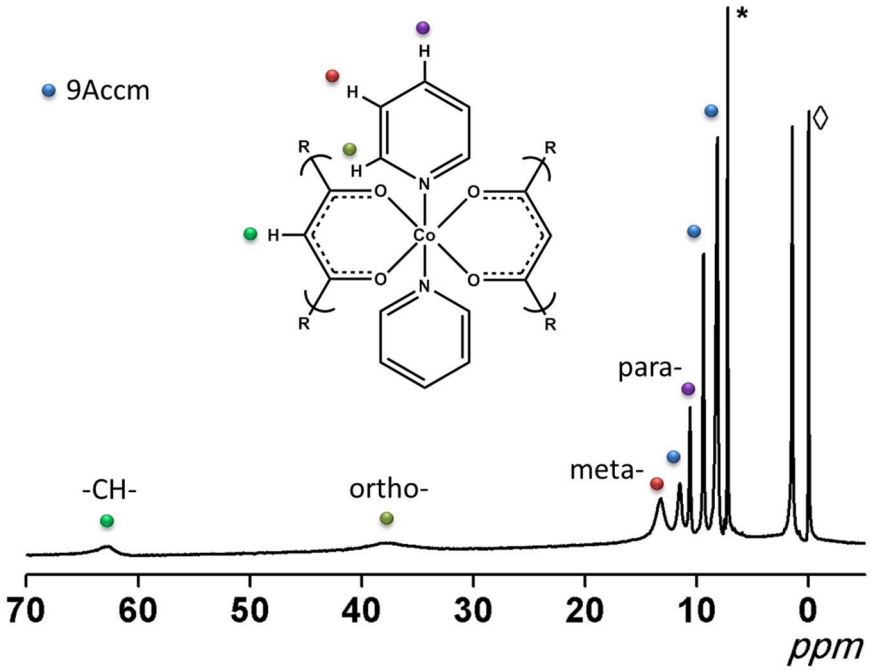

Figure 1.1. 10: ^1H NMR spectrum of **1** in $CDCl_3$ between -5 to 70 ppm. *CDCl3 and ◊TMS.

The position and shape of the down-field are related to closest proton to the Co^{II} center, being this: the methine -CH- from the 9Accm groups and the ones in ortho- from the two pyridine molecules. The assignments of these signals are based on previous literature[64–66] and the comparison between **1** with related compounds and compounds, **3** and **4**.

Based on this comparison, the signal at 63 ppm is assigned to the -CH- group of 9Accm because it is present in the three compounds; meanwhile the absence of the broad peak at 38 ppm in **4** proved a pyridinic origin.[67] The latest, together with two signals at 12.1 and 8.0 ppm, are attributed to the *ortho-*, *para-* and *meta-* positions of pyridine respectively. The rest of the signals located at high field (10 - 0 ppm) correspond to nuclei that are far from the metallic nucleus (less affected) and are attributed to the conjugated chain and anthracene groups.[68] The exact assignment for each nucleus could not be carried out, however they maintain their structure without varying in solution. The complete list of peaks for **1**, **3** and **4** is shown in Annex 1.7.

Figure 1.1.11 shows the spectrum corresponding to compound **2** in $CDCl_3$ within a window of -20 to 90 ppm. This compound displays an ideal C_{2v} symmetry and comes close to the expected, displaying

one type of 9Accm and four signals for the 2,2'-bpy (*ortho-, meta-, meta'*- and *para*- protons). The comparison between **2** and compounds **5** and **6**, together with the literature consulted[63,69] regarding Co^{II} systems (that contain 2,2'-bipyridine groups) made possible the assignment of the signals (Annex 1.7).

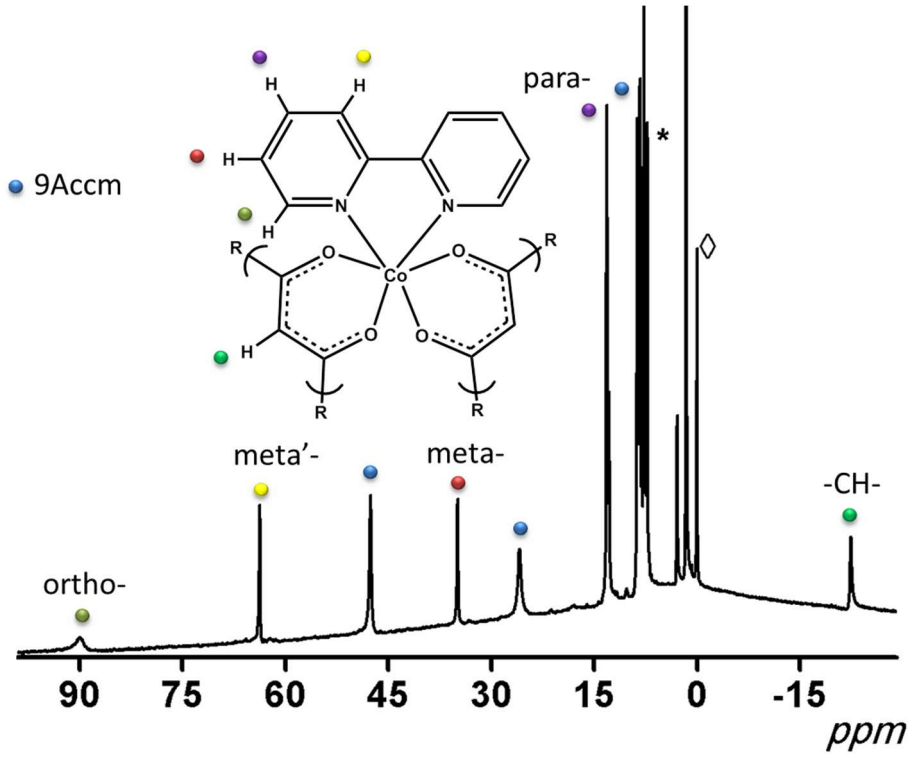

Figure 1.1.11: ^{1}H NMR spectrum of **2** in $CDCl_3$ between -25 to 95 ppm. *CDCl3 and ◊TMS.

In this case, compound **2** presents a richer downfield area exhibiting sharp peaks at 89.1, 63.0, 47.0, 34.6 and 25.7 ppm with an upfield region that goes from 13.0 to -22.3 ppm. Previous literature shows an usual *ortho-, meta'-, meta-,* and *para*- order (from downfield to upfield) for the proton resonance in Co^{II}-(2,2'-bpy) systems.[69] This, together with the study of **5** and **6** allow the assignation of the two downfield shifts, at 90 and 63 ppm, that correspond to the *ortho*- and *meta'*- protons from the 2,2'-bpy, since they are present in the three compounds. The following peaks at 47 ppm and 26 ppm, are present in the three compounds, corresponding to the protons from the conjugated chain of 9Accm. The following signal at 35 ppm correspond to the *meta*- position due to its absence in compound **6** (because its functionalization in that position). Similarly, the signal at 12 ppm can be attributed to para- position since it is absent in compound **5**. The rest of the signals between 13 and 7 ppm correspond to the anthracene groups of the CCMoid ligands. Furthermore, at upfields appears at -22 ppm a signal that, was initially assigned to the group 9Accm, however recent studies using Ni^{II} compounds (next chapter) have allowed to assign it specifically to the group -CH- of the

CCMoid. This region corresponds to nuclei which present exclusively a strong pseudocontact contribution. This contribution is directly proportional to the magnetic anisotropy of the metal, as a consequence of the coordination geometry and the presence of zefo field splitting (zfs). Comparing that signal with the signal of compound **1**, appears shift to upfields (63 ppm). Finally, spectra were measured at different times and their structure remains unchanged in solution.

Overall, the paramagnetic ^{1}H NMR studies of both systems provide information about (i) stability of the systems in solution by preserving their structure, (ii) flexibility of the conjugated chain and free rotation of the anthracene groups through the decrease of observed signals, (iii) show the great influence of the paramagnetic centers in the ligands by the difference shift between the methine peaks (-CH-) of compound **1** and **2** (being a difference on 16 ppm). Taking into account all the amassed information, ^{1}H NMR technique could be used now as a preliminary technique to predict the *cis/trans* arrangements of future compounds with the formula "[Co(9Accm)$_2$]" through the analysis of the shift of the -CH- signal from the coordinated CCMoid.

UV-Vis Absorption and Fluorescence studies

Previous studies performed in the group had corroborated the luminescence properties of the free ligand 9Accm,[58,59] due to its aromatic nature of the anthracene groups and the presence of the conjugated chain. Therefore, one of the objectives here was to study the influence of the paramagnetic center on the luminescent properties of both systems comparing their results with that of the free ligand, 9Accm. Thus, studies of UV-Visible and Fluorescence in solution were performed using CH_2Cl_2 and THF as solvents to study also the effect of the solvent on the luminescent properties (solvatochromic effect).[59]

The electronic spectra of **1**, **2** and the free ligand 9Accm with absorptions around 255 and 460 nm band regions are shown in Figure 1.1.12. The three systems present an intense band at the highest energies related to π-π* transitions (E(1) = 337000, E(2) = 331000 M^{-1} cm^{-1}). At lower energies, small and broad bands with maxima at 446 and 425 nm (E(1) = 47000 , E(2) = 57000 M^{-1} cm^{-1}) for compound **1** and **2**, respectively, associated to the CCMoid character π-π* were found. In that case, compare with the free ligand 9Accm (437 nm), the absorption band of compound **1** is slightly shifted to lower energies, in opposition to compound **2**, which is shifted toward higher energies, due to the coordination to the metal centers. A shoulder between 300-400 nm is sometimes observed with maxima features characteristic of the anthracene groups. These experiments were repeated with THF (Annex 1.8) to study solvatochromic effects. The lowest energy bands appeared at 426 and 424 for compound **1** and **2** respectively, indicating higher solvatochromic effects (hypsochromic shift) for **1** than **2**.

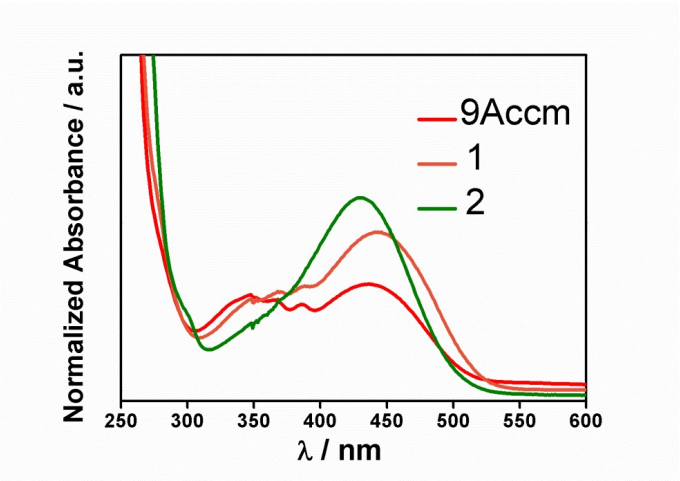

Figure 1.1.12: Comparison of the UV-Vis spectra of 9Accm (red), compound **1** (orange) and compound **2** (green) in CH_2Cl_2.

Figure 1.1.13 shows the fluorescence spectra of compounds **1** and **2** in THF when excited at 426 and 424 nm, respectively, showing a broad band at 553 and 555 nm, in that order. The observed changes are very close to the free ligand 9Accm (555 nm), which shows a similar behavior indicating, as expected, that the fluorescent nature of the two systems is directly related to the organic ligand. In both cases, the emission corresponds to the formation of excimers that can correspond to the intrinsic nature of the ligand, having only one of the anthracene groups in the molecule excited or *via* supramolecular interactions, through π-π stacking, between different molecules. Studies at lower concentration were performed in order to disfavor this interaction, but no significant changes in their emission were obtained.

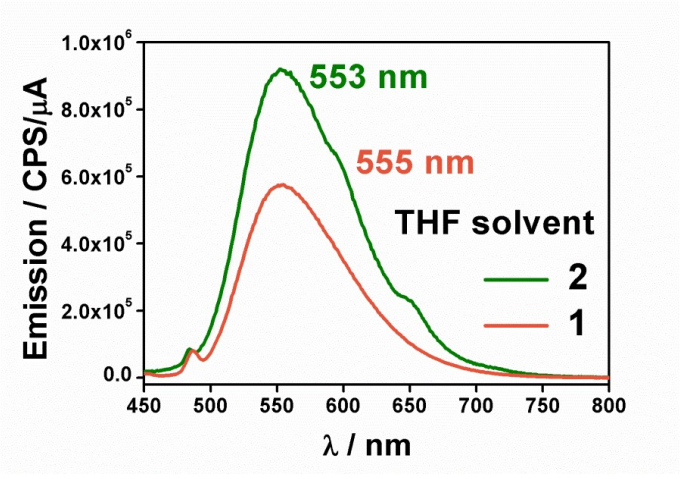

Figure 1.1.13: Comparison of the emission spectra of compounds **2** (green) and **1** (orange) in THF.

Solvatochromic studies were also carried out using CH_2Cl_2 as solvent to study the effect on fluorescence. Figure 1.1.14 shows the emission of compound **2** using CH_2Cl_2 and THF as solvents

(compound **1** is found in Annex 1.9). Comparing both emissions, a hypsochromic shift in THF compared to CH_2Cl_2 is observed, with a difference of around 50 nm between them. (THF, 555 nm; CH_2Cl_2, 600 nm) and both have a shift of 25 nm compared to free 9Accm (577 nm). On the other hand, in a qualitative way it can be observed that the intensity emission in THF is slightly higher. This may be because THF can facilitate fluorescent relaxation pathways to a greater extent.

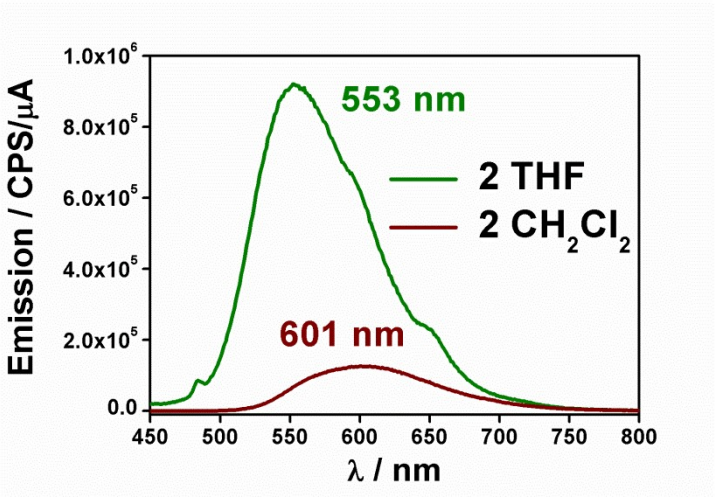

Figure 1.1. 14: Comparison of the emission spectra of compound **2** in THF (green) and CH_2Cl_2 (brown).

The fluorescence emissions of both compounds are dramatically lower than that from ligand 9Accm, which exhibited stronger fluorescence emission as we can see in Figure 1.1.15. This behavior is common due to the paramagnetic effect of the metallic center that normally acts as quenchers because it provides non-radiative alternative fluorescent relaxation pathways to the molecules.[60] Even so, as has been mentioned, this "quenching" does not become total since both have a reasonable emission, possibly caused by (i) a greater number of anthracene groups per molecule; (ii) free rotation in solution and (iii) because the distance between the metal center and these anthracene groups is relatively long (less paramagnetic influence).

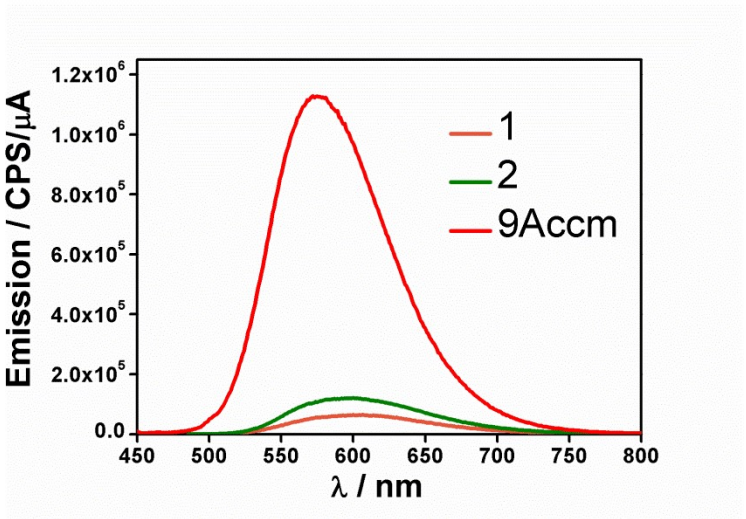

Figure 1.1. 15: Comparison of the emission spectra of compounds **1** (orange), **2** (green) and 9Accm (red) in THF.

To study the paramagnetic influence of the metallic center on the luminescence in a quantitative way, quantum performance studies of the fluorescence of the three compounds were carried out. This study was performed using an internal standard, which in this case was Fluorescein. The quantum yield (ϕ) of **1** (0.0010) was slightly smaller than **2** (0.0014); both presented one order of magnitude smaller than the free ligand 9Accm.[58]

1.2.3.3.2 Studies in the solid state

Magnetic studies

As it was mentioned in the introduction, mononuclear systems containing Co^{II} metal centers can exhibit very interesting magnetic properties, such as single molecular magnet (SMM) behavior due to their high anisotropy (zfs D parameter).[70–79]

In our case, compounds **1** and **2** filled up the requirements to become SMM candidates, and therefore magnetic susceptibility studies were measured on polycrystalline samples using dc and ac techniques at variable temperature. The dc magnetic studies are presented as $\chi_M T$ vs T, M/NμB vs H and M vs H/T. Finally, ac studies were carried out to study their possible behavior as SMMs measuring the alternating magnetic susceptibility (ac) applying oscillating magnetic fields, respectively. The results are presented as χ_{AC}'' vs T and χ_{AC}'' vs v. In both samples the values of the zero-field splitting (D), (E) and (g) were obtained by fitting the data $\chi_M T$ vs T and M vs H/T using the program PHI.[32]

Magnetic susceptibility and magnetization

The magnetic susceptibility of powder samples of compounds **1** and **2** were performed between 2 and 300 K, under a constant magnetic field of 0.03 T (from 2 to 30 K) and 0.5 T (from 30 to 300 K) (Figure 1.1.16). For the compound **1**, at 300 K, the $\chi_M T$ has a value of 2.77 cm^3 K mol^{-1}. This value is higher than that expected for a spin only system S = 3/2 ($\chi_M T$ = 1.875 cm^3 K mol^{-1}, g = 2.0) due to the orbital contribution of the Co^{II} center. These values are within the range typically observed for highly anisotropic Co^{II} ions with large spin-orbit coupling contribution. When the temperature decreases, the $\chi_M T$ decreases slightly to 100 K due to possible intermolecular antiferromagnetic interactions. The dependence on the temperature reflected by changes in the Boltzmann population is indicative of systems that present magnetic anisotropy. At lower temperatures, the temperature decreases sharply to reach a value of $\chi_M T$ of 1.59 cm^3 K mol^{-1} to 3 K. This value is expected for a ground Kramers doublet due to the second-order spin-orbit coupling.[70–79] The study of compound **2** was carried out under the same conditions and is represented in Figure 29 (right). As we can see, it has a behavior very similar to compound **1**. At 300 K, its maximum value of $\chi_M T$ is 2.87 cm^3 K mol^{-1} and decreases as the temperature decreases to a value of 1.64 cm^3 K mol^{-1} at 2 K.

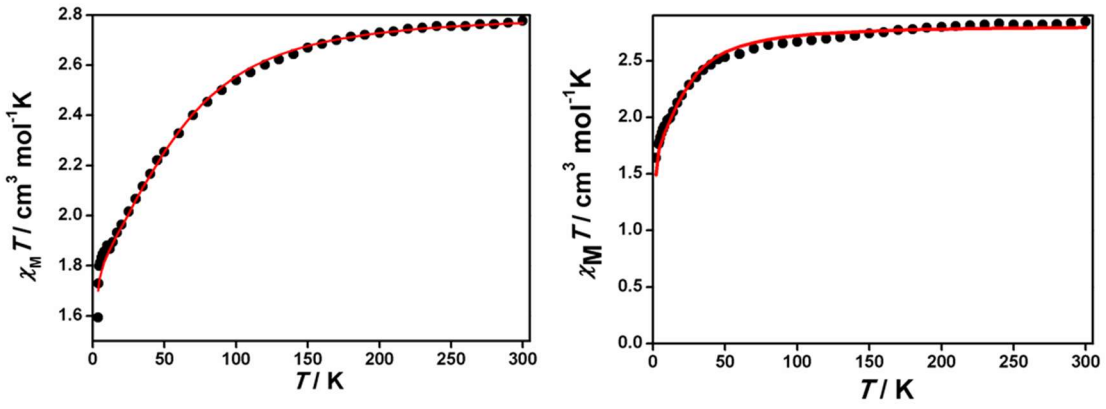

Figure 1.1. 16: Representation of $\chi_M T$ vs T for compounds **1** (left) and **2** (right). Experimental data are shown as dots and the resulting fitting as a red line.

Regarding the variation of the magnetization studies, two types of measurements were performed: (i) on one hand, the variation of the magnetization with the magnetic field ($M/N\mu_B$ vs H) until the magnetic saturation was reached (Figure 1.1.17, bottom) and (ii) on the other, the variation of the magnetization with the field at different temperatures (M vs H/T) (Figure 1.1.17, top). From this measurement and its fitting is possible to obtain the zero field splitting parameters (axial distortion (D) and rhombic (E) values). The first measurement ($M/N\mu_B$ vs H) was recorded applying an external magnetic field varying between 0 and 0.5 T at a constant temperature of 2 K. In both cases the same behavior was observed. As the magnetic field applied is increased, the magnetization of the sample

increases almost linearly since the population of the ground state is increasing. This behavior is truncated from higher magnetic fields where the saturation of the magnetization is reached and this takes a constant value of 2.13 and 2.29 µB for the compound **1** and **2**, respectively. This saturation indicates that the states are well separated and only the ground state is populated. The saturation values obtained are lower than expected for S = 3/2 (M/NµB = 3.0 µB, g = 2.0). Systems with positive D > 0 stabilize the ground state with low Ms values (Figure I.10), being in this case the Kramer doublet M_S = ½.

In relation to the second measurement (M vs H/T) it was performed under different external magnetic fields (between 0.5-5 T) and at a variable temperature between 1.8-6.8 K. In both cases, magnetic saturation was reached at the lowest temperatures and applying large fields (5 T). The small separation between different curves when different magnetic fields are applied is an indication of the presence of strong anisotropy (D values). As it was explained in the introduction, the presence of anisotropy produces the splitting of the Ms states before applying the external magnetic field (zero field splitting). This fact facilitates to reach saturation, being the process less dependent with the temperature.

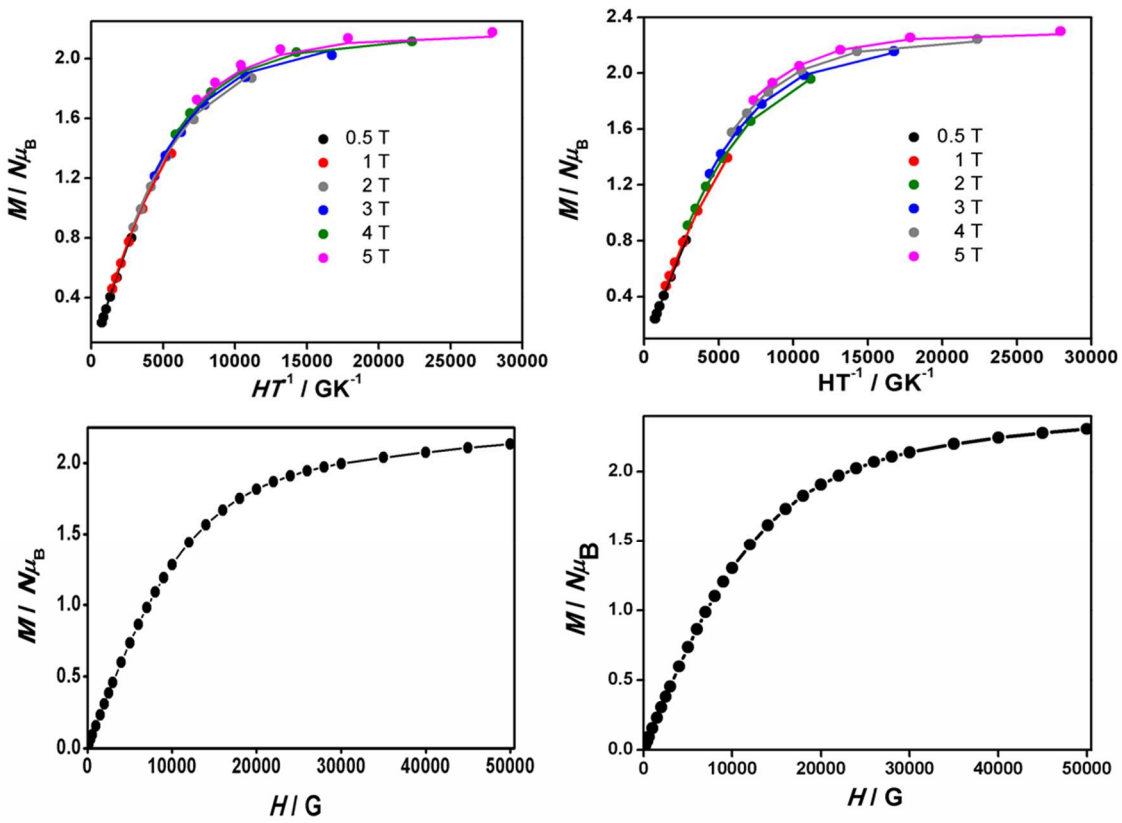

Figure 1.1. 17: Representation of M/Nµ$_B$ vs H/T for compounds **1** (left) and **2** (right) (up) and M/Nµ$_B$ vs H for compounds **1** (left) and **2** (right) (bottom). Experimental data are shown as dots and the resulting fitting as lines.

Calculation of parameters zfs: g, D, E

The calculations of the parameters were carried out by the simultaneous fitting of the experimental measurements of (M vs H/T) and (χ_MT vs T) by the diagonalization of the Hamiltonian spin matrix using the program PHI.[32] This program allows the correlation of experimental magnetic data from orbital degenerate systems using multiple sources (in our case M vs H/T and χ_MT vs T) in a simultaneous manner.

Following this procedure, for the compound **1** the values obtained were g = 2.26, D = 74.1 cm^{-1}, and E = 1.21 cm^{-1} and for the compound **2** g = 2.39, D = 24.1 cm^{-1} and E = -1.89 cm^{-1}. In the case of compound **1**, the high D value obtained, fits perfectly with the expected according to the analysis of M vs H/T previously described. This value is comparable with the highest value to date of D = 98 cm^{-1} published by Cano *et al.*[47] In the compound **2** the D value obtained is lower, and again it is in agreement with the behavior found in Figure 30, where the distances between the isofield are higher.

As it was mentioned in the introduction, the sign and value of the parameter D depends on the nature of the ground state and first excited states. Also it is important to emphasize that the smaller this distance is (δ), the higher the value of D.

Theoretical calculations by CASSCF of both compounds were also performed. These calculations showed the involved orbitals correspond to the transition between the d_{xz} or d_{yz} (ground state) and d_{xy} (first excited state). Figure 1.1.18 shows a representation of the orbitals. Furthermore, the energy different (δ) of these orbitals and the D and E values were also obtained by theoretical calculations. The results are shown in Table 1.1.2 together with those D and E values obtained by the experimental fitted.

Compound	D_{phi} (cm^{-1})	E_{phi} (cm^{-1})	g_{phi}	D_{calc} (cm^{-1})	E_{calc} (cm^{-1})	δ_{calc} (cm^{-1})
1	74.1	1.21	2.26	167.1	24.0	405
2	24.1	-1.89	2.39	71.6	7.8	775

Table 1.1.2: Values of D and E (all in cm^{-1}) for the S = 3/2 ground state of compounds **1** and **2** calculated with CASSCF. The last column gives the first excitation energy (δ)

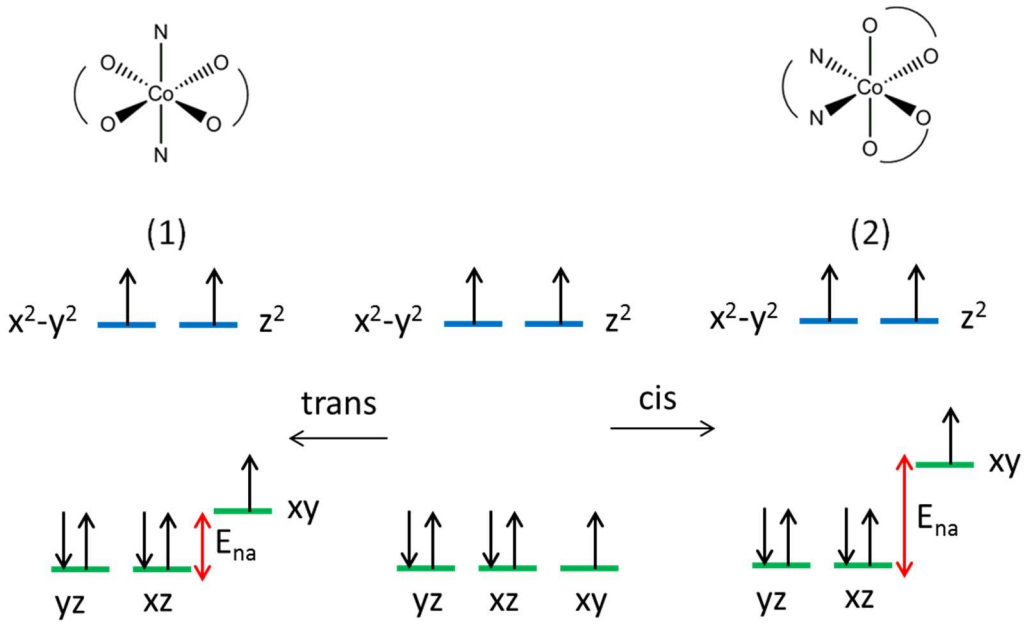

Figure 1.1.18: Representation of the d orbitals splitting due to the Jahn-Teller effect for compounds **1** (left) and **2** (right). The energy difference is indicated by the red arrow

As the table shows, the calculated values obtained for the parameter D from both compounds, like the experimental values, are positive. This fact is due to the nature of the orbitals involved. Taking into account the magic pentagon (Figure I.9), the transition in both cases (d_{xz}/d_{yx} to d_{xy}) corresponds to ± Δml = 1, therefore the values D_{xx} and D_{yy} will be elevated and the parameters show positive D values.

In relation to the magnitude of the values obtained for the parameter D, as it can be seen, compound **1** exhibits low energy differences (δ_{calc} = 405 cm^{-1}) compare to compound **2** (δ_{calc} = 775 cm^{-1}) and therefore, its value of D is higher (D = 167.1 cm^{-1}). This fact is in agreement with the crystal structure of both compounds. Compound **1** exhibited the smallest distortion from their octahedron geometry than compound **2** (Table 1.1.1).

In both cases, these energy separations are significantly small to the point that can be considered degenerated. This fact gives rise a relevant first-order orbital contribution that should be considered.

On the other hand, the parameter D and E calculated are significantly higher compare with the obtained from the fitting. This fact is expected since in the calculation the spin relaxation mechanism depending on the lattice is not taken into account. The different in energies are related to the Jahn-Teller effect which originates distortions, thus breaks the orbital degeneration (assuming perfect octahedral coordination).

The high D values for mononuclear compounds from the first transition series relate to the presence of excited states (without spin-orbit contribution) near in energy to the ground state.[33] The

presence of these excited states close in energy could be present in systems that show slightly deviation from ideal geometries due to the Jahn-Teller effect.

Single Molecule Magnet behavior: AC measurements

From the zero field splitting values, both compounds show the existence of large axial magnetic anisotropy and therefore were great candidates for exhibiting slow relaxation of magnetization as it has been already observed in other mononuclear pseudo-octahedral Co^{II} (high spin).[47]

To study the possible SMM behavior, measurements of magnetic susceptibility χ_{AC}'' were carried out, where the dynamic magnetic response is monitored by applying an oscillating magnetic field H_{AC} in order to detect the possibility of slow relaxation of the magnetization.

Magnetic susceptibility measurements were performed in the presence of an alternating magnetic field H_{AC} under the application of an external magnetic field H_{DC}. This external magnetic field allows us to break the degeneration of the states located on both sides of the barrier, reducing the interconversion of the magnetic moment through the barrier (quantum tunneling), thus favoring the retention of magnetization. Measurements were performed in the absence of the H_{DC} and no out-of-phase susceptibility signal χ_{AC}'' was observed.

Therefore, χ_{AC}'' measurements were first carried out for compounds **1** and **2** in an oscillating field frequencies range between 1-1488 Hz under an oscillating magnetic field H_{AC} = 0.0004 T at the constant temperature of 2 K, applying different external magnetic fields H_{DC} in order to find the optimal H_{DC} value where the signal corresponding to χ_{AC}'' is higher (Figure 1.1.19).

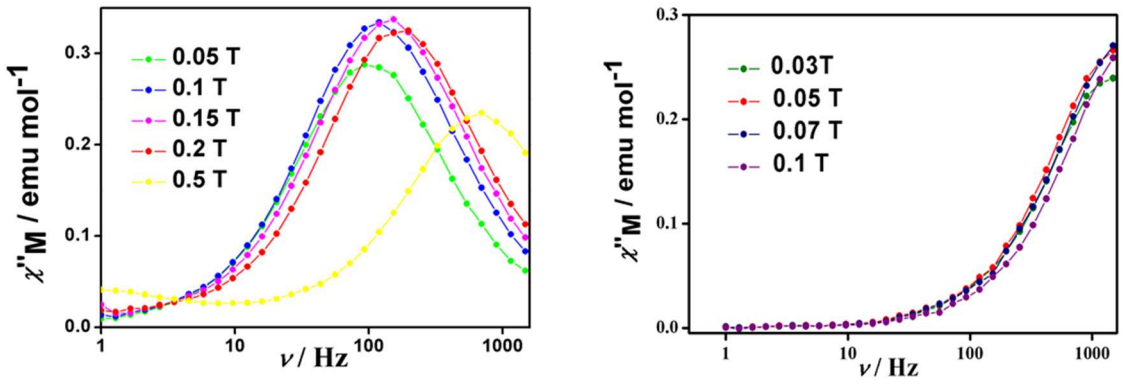

Figure 1.1.19: Representation χ_{AC}'' vs. ν at different magnetic fields H_{DC} of compound **1** (left) and compound **2** (right).

As the Figure 1.1.19 shows, the maximum of value χ_{AC}'' are obtained when an H_{DC} of 0.15 T and 0.07 T are applied for compounds **1** and **2**, in that order.

Once the H_{DC} magnetic fields are known, the χ_{AC}'' measurements are performed as a function of the oscillating field frequency using a wider range with values between 100 Hz and 10 kHz under an oscillating magnetic field, H_{AC} = 0.0004 T, at different temperatures (range of 1.9 K to 5 K) for the two compounds (Figure 1.1.20).

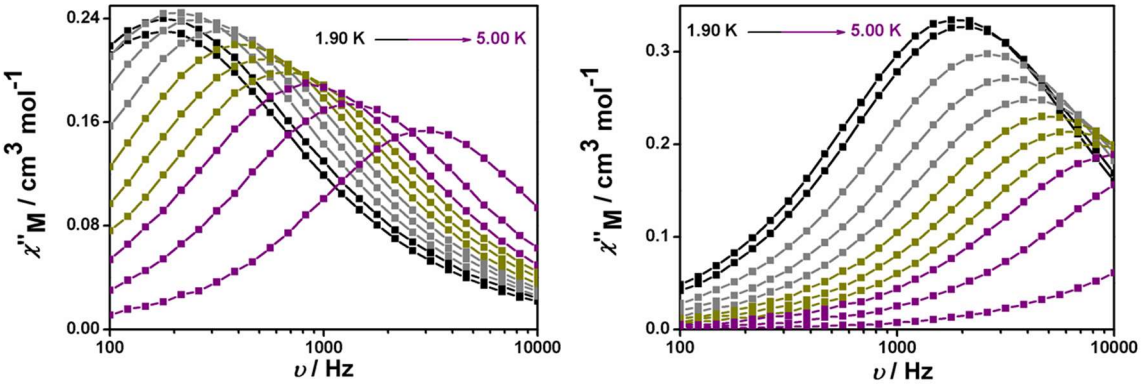

Figure 1.1.20: Frequency dependence of the χ_{AC}'' for compounds **1** (left) and **2** (right) under 1500 Oe and 700 Oe dc fields, respectively.

As Figure 1.1.20 shows, a clear dependence of the magnetic susceptibility in phase (χ_{AC}') (Annex 1.10) and out of phase (χ_{AC}'') with the frequency was observed in both compounds indicating that both systems exhibit SMM behavior. In the case of compound **1** the maximum is observed during all the temperature range indicating the impossibility to reverse the magnetic direction since it is not in phase with the oscillating magnetic field H_{AC}. For compound **2**, the behavior is significantly different because the presence of the maximum appears at lower temperatures. This behavior will be reflected later in a low value of the activation energy in comparison with the one found for compound **1**.

Calculation of relaxation times and activation energy.

Magnetic susceptibility χ_{AC}' and χ_{AC}'' values at different temperature were fitted by Debye equation (Figure 1.1.21) (Cole-Cole graphs, equation Annex 1.3) using the CCFit program.[80] From this fit, values of relaxation times (τ), X_T and X_S and the value of α, which indicates the distribution of the processes present for each temperature were achieved (Annex 1.11).

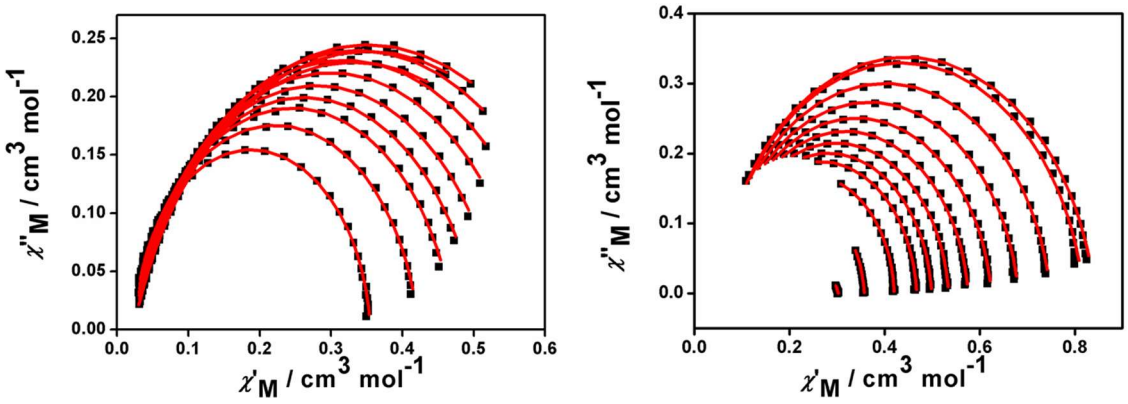

Figure 1.1.21: Cole-Cole plots of compounds **1** (left) and **2** (right) measured from 1.9 to 5 K under 1500 and 700 Oe dc fields. Experimental data are shown as dots and the resulting fitting as lines.

As the Figure 1.1.21 shows, compound **1** presents a more defined semi-circular shape, which would indicate a single relaxation process. However, the α values (α = 0.18-0.10) obtained indicates the presence of more than one relaxation mechanism. Compound **2**, presents a less defined semi-circular shape but similar α values (α = 0.1-0.038). Hence, it can be considered that both systems present more than one relaxation mechanism.

To determine the contribution of each relaxation mechanism and the energy barrier, the (τ^{-1}) vs T (Figure 1.1.22, right) and ln(τ) vs 1/T (Figure 1.1.22, left) are represented respectively.

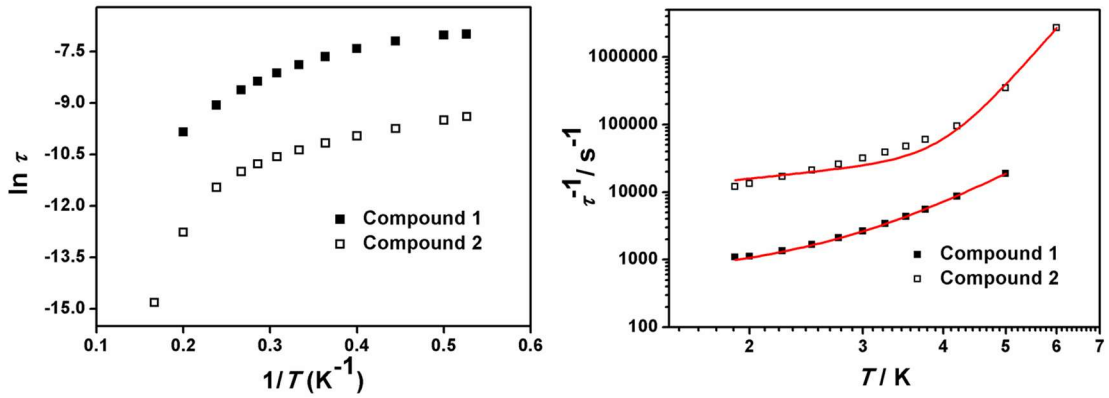

Figure 1.1. 22: Representation of ln (τ) vs 1 / T (left) and (τ^{-1}) vs T (right) of compounds **1** (■) and **2** (□) measured from 1.9 K to 5.0 K under 1500 and 700 Oe dc fields, respectively

In the graph ln (τ) vs 1/T, two different regions can be differentiated: (i) a first region at low temperatures where the dependence with temperature is noticeable but rather small. In this case the relaxation mechanism is dominates by Raman and Direct mechanisms (Annex 1.1). (ii) A second

region at high temperatures presents linear temperature dependence. Therefore, it is possible to consider that only the system relaxes through Orbach mechanism, due to the possibility of tunneling is discarded because there is no independent zone from the temperature. These data can be fitted by Arrhenius equation (Annex 1.12) and the energy barrier and relaxation time factor are obtained (Table 1.1.3).

Compound	τ_o (s^{-1})	U_{eff}(cm^{-1})
1	$9.8x10^{-6}$	7.7
2	$7.6x10^{-7}$	7.8

Table 1.1.3: Results of the fitted by Arrhenius

The values obtained from τ_o are similar with others molecular magnet systems. Related to the energy barrier, such U_{eff} values are significantly lower than those calculated $U = |D|S^2$. This fact indicates the existences of alternative relaxation processes.

In order to determine the contribution of each relaxation mechanism,[81] the data of (τ^{-1}) vs T (Figure 1.1.22, right) were fitted with the equation (9). This equation takes into account the four different mechanisms that rule the relaxation processes. However, in this case to facilitate the calculations, only two of them (Raman and Direct) are taking into account. The contribution corresponding to quantum tunneling effects is not relevant since no independent temperature zone is observed.[82] On the other hand, Orbach process is not possible because this mechanism has to take place through a "real" state. In both systems ab initio calculations were performed and indicated that the energy of the first excited state (E_n = 405 for **1** and 775 cm^{-1} for **2**) is situated significantly above in comparison to the calculated energy barrier (E_a = 7.8 cm^{-1}). The fit is represented in Figure 1.1.22 (right) and the values obtained in Table 1.1.4.

$$\tau^{-1} \approx A'T + CT^n \qquad (9)$$

Compound	A' (s^{-1} k^{-1})	C	n
1	447	1.8	5
2	6688	5.3	7.5

Table 1.1. 4: *Results of the contribution of each relaxation mechanism*

The obtained values were compared with others systems found in the literature (Annex 1.13, Table S1.7). A' values are similar in compound 1, whereas for compound 2 is an order of magnitude higher compare with others system in the literature.[81,83] In relation with C, both systems are comparable with other published Fe^{II} systems[81] but are higher to other Co^{II} systems.[81] Finally, n values are of the same order as other systems,[81,83] therefore indicates that direct and Raman mechanism are present.

It is important to stress the limited amount of information regarding these parameters in the literature and that some of these data has been collected in frozen solution, where the molecules are further away from each other decreasing the effect of intermolecular interactions. In our case, the samples were treated in the solid state. The bibliographic recompilation of such data would help to understand better the relation mechanism but at the moment we can only use the parameters in a comparative way.

1.2.3.3.3 Studies on surfaces

Atomic Force Microscopy (AFM)

The organization of functional molecules on surfaces is one of the current challenges due to their potential applications as active parts of nanodevices. There are different ways to locate molecules on surfaces depending on the nature of both, molecular system and substrate, and the objective of the deposition. In this chapter the method used was the simplest, where the molecules were dissolved in a solvent and deposited by spin coating. The interested was to see the affinity toward the chosen substrate as well as the study of robustness of the samples by the use of photoemission experiments.

For this reason, AFM experiments were performed after depositing compounds **1** and **2** in two different substrates: (i) on highly oriented pyrolytic graphite (HOPG) and (ii) on silicon wafers Si(100).

Therefore, in both substrates spin coating at 300 rpm for 30 seconds were used to add three drops of 10^{-5} M and 10^{-4} M solutions in CH_2Cl_2 with an interval of 10 seconds. This methodology provides a better homogeneous dispersion of the molecules on the surface. The topographies were carried out by atomic force microscopy (AFM) using "tapping" mode. Blanks were performed using exclusively the solvent CH_2Cl_2 under the same conditions.

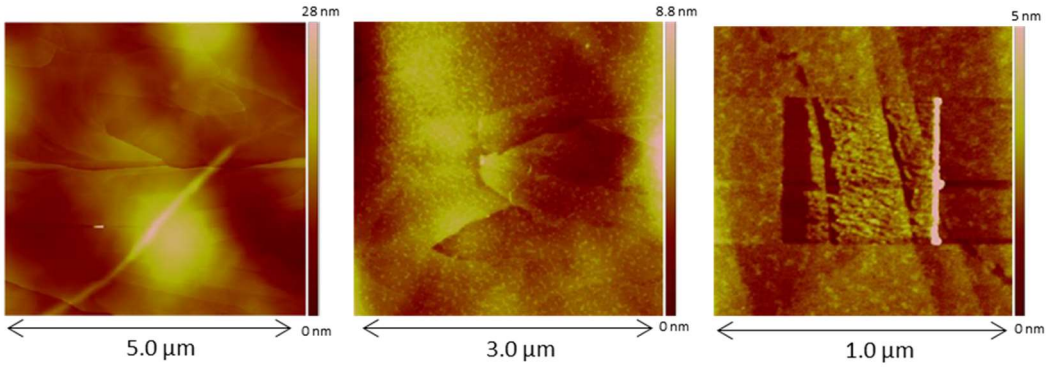

Figure 1.1. 23: AFM experiment to (I) blank, (II) tapping mode and (III) contact mode of compound **2**.

The experiments carried out on HOPG show the affinity of both compounds for the surface due to the π-π interactions of the anthracene groups of the molecule with the substrate, as described with other M-9Accm systems (M = 3d metal center) in the past.[60] Here it is important to mention that there is a competitive effect between the substrate (HOPG) and the intermolecular interaction among molecules due to the similar nature of the interactions. The effect of the solvent evaporation is another important point to take into account, where the final aggregation must be the sum of all these factors.

In Figure 1.1.23, the first image (left) corresponds to the blank made with CH_2Cl_2, where graphene terraces corresponding to the exfoliate process are observed. The second image corresponds to the deposition of compound **1**. As the images shows, multiple aggregations of the molecules distributed relatively homogeneously are observed. In the third image, a scratching process on the graphite surface was performed. There, the objective was the removal of the molecules scratching the surface using the tip (an accumulation is observed at the edge) leaving only the surfaces of graphite without molecules. Thereby, this measurement allows measuring the distances between the molecules and the substrate in a rather precise way. Compound **1** and compound **2** show heights of 1.0-1.2 and 1.2-1.6 nm respectively (Annex 1.13). These heights correspond to the stacking of approximately 1-2 molecules taking in account the distances from the crystal structures. Furthermore, increasing the number of drops added to the substrate, fully coated surfaces were achieved due to their high affinity with the substrate. These surfaces will be suitable for the emission studies as we will show below.

On the other hand, experiments with the same conditions were performed using Si(100) substrates. The images showed large aggregates caused by the evaporation of the solvent, making it impossible to obtain a homogeneously distributed surface due to the lack of affinity of the molecule with the substrate.

Photoemission Spectroscopy (PES)

Surface analyses were carried out using Photoemission Spectroscopy (PES) experiments. This technique allows us to analyze the energy of the electrons emitted by a solid when it is irradiated with X-rays (XPS), or UV-beam (UPS). The energy obtained provides qualitative and quantitative information about the: elemental composition, chemical state and also information about the molecular environment (oxidation state, molecular orbitals, etc).

X-ray photoelectron spectroscopy (XPS)

For the XPS experiments, samples were prepared by spin-coating using CH_2Cl_2 solutions of both compounds at 300 rpm on HOPG surfaces (previously exfoliated). The surfaces were quickly introduced into the vacuum system to avoid possible contamination and kept overnight under such conditions, later the surfaces were taken to the analysis chamber and exposed to an intense X-ray beam.

In the case of compound **2**, the results performing as described above shows the presence of spin-orbit splitting lines corresponding to N1s, C1s, O1s and Co2p with the characteristic form of the electronic configuration (Figure 1.1.24). Furthermore, stability studies were carried out by performing different spectra at different times obtaining the same result. However, experiments performed with compound **1** show an absence of the N signal and ambiguous results regarding the existence and oxidation state of the cobalt center. This fact indicates most probably the loss of the pyridine group/s during the deposition process; overall this process may affect the stability of **1** and for that the metal analysis provides ambiguous results. We concluded that this compound is less robust compare with compound **2** and pointed out the relevance that the methodology of deposition has toward the further use of molecules on surfaces.

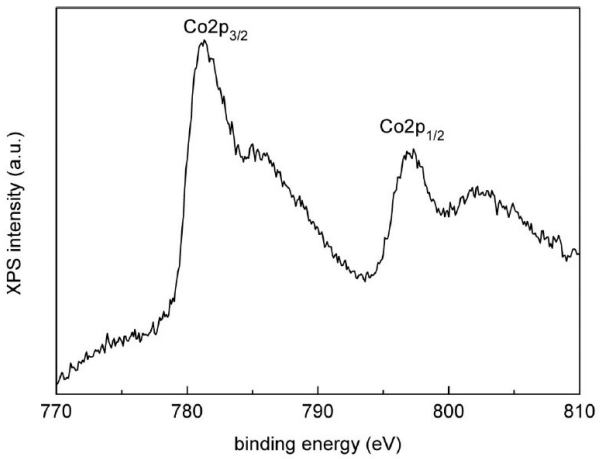

Figure 1.1. 24: XPS experiments of a film of compound 2 spin-coated on HOPG

Ultraviolet photoelectron spectroscopy (UPS)

The UV radiation energy used in the UPS (less energetic than XPS) assist in the location of electrons from the external levels of the molecules, specifically those located in the valence band. These external electrons provide information about the entire molecules instead of particular atoms as it happens for XPS. The following figure shows the spectra of the density of the states (DOS) of compound **2** (red) compared to its calculated spectrum (blue) by Gaussian code[84] with B3LYP functional[85] and the TZV basis[86] and the spectrum of the graphene substrate (black).

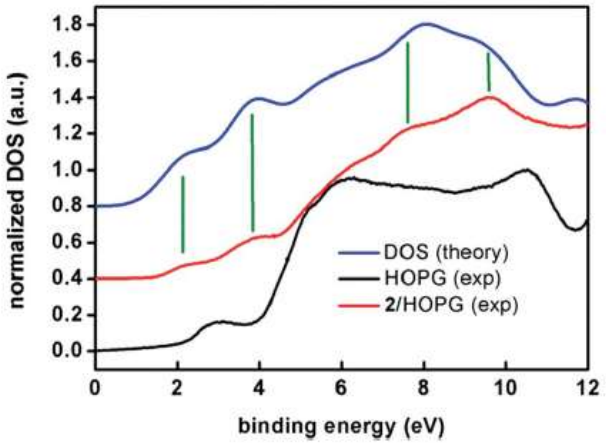

Figure 1.1. 25: Experimental UPS (Ultra-violet Photo-emission Spectroscopy) density of states of a spin-coated film of compound 2 on HOPG (red) and of a freshly cleaved HOPG Surface (black) compared to the DFT calculated (blue). The hig-resolution UPS spectra were acquired with pass energy of 5 eV in UHV and at room temperature. Binding energies are referred to the Fermi level of the system (E_F = 0 eV). Spectra have been normalized to their maxima and shifted in the vertical scale for clarity. The DFT calculated DOS spectrum has been shifted by 3.1 eV in order to level the HOMO. Vertical green lines have been included to guide the eye comparing experimental and calculated bands.

As the Figure 1.1.25 shows, the experimental signals fit well with the theoretical signals in their vast majority. Particularly, the first two signals observed at 2.1 and 3.8 eV correspond to the aromatic groups since they have a π-anthracene nature. The orbitals corresponding to the metal e_g and t_{2g} are located at higher binding energies. The wide signal at 6 eV is observed both in the experimental and theoretical parts, corresponding to the HOPG substrate. Overall, the UPS experiment agrees well with the conjugated and aromatic nature of the molecule where a huge art of the density of the states relates to the ligand.

1.2.4 Conclusions

In this chapter, two mononuclear systems of Co^{II}-CCMoids with formula $[Co(9Accm)_2(py)_2]$ **(1)** and $[Co(9Accm)_2(2,2'\text{-bpy})]$ **(2)** are presented. The synthesis of both systems was carried out through the use of microwave radiation, giving rise to high yields and purity. Structurally, both systems present pseudo-octahedral environments with two CCMoid 9Accm coordinated to the metallic center Co^{II} and two pyridine ligands, in the case of compound **1** and a 2,2'-bipyridine ligand in the case of compound **2**. The different nature of these latter ligands results in a different arrangement of the 9Accm ligand being *trans* disposition for the compound **1** and *cis* for the compound **2**.

Comparative studies of the two "isomers" have been carried out in solution, solid state and on surfaces. In relation with solution studies, paramagnetic ^1H NMR technique allowed the study of stability of the systems in solution (both systems remained unchanged in solution over the time). Four additional compounds were synthesized and characterized in a similar way toward the assignation of the signals for **1** and **2**. That study allowed also the use of this technique as a tool to predict the *cis/trans* arrangement of the Co-CCMoids systems analyzing the shift of the –CH- group corresponding to the coordinated 9Accm ligands. On the other hand, emission studies of both compounds were performed showing a moderate emission corresponding to the anthracenes groups of the 9Accm. Comparing with the free ligand 9Accm, the emission is partially quenched due to the presence of paramagnetic metal center for both compounds. Studies with different solvents were performed showing in both cases solvatochromic effects with similar quantum yields.

Related to solid state studies, magnetic studies using a SQUID were performed. Both systems show a SMM behavior although the application of an external magnetic field is needed. Particularly, compound **1** exhibits one of the highest values of positive D (D = + 74 cm^{-1}) found in the literature for mononuclear Co^{II} systems, while the value of compound **2** is (D = + 24 cm^{-1}). These studies were corroborated by theoretical calculations of D values (CASSCF / NEVPT2). This study showed a high D value corresponding to compound **1** due to the presence of unoccupied excited states closer to the ground state.

Finally, studies on surface were carried out by the deposition of both systems on HOPG and Si(100) substrates, respectively. In the case of AFM, both compounds showed images with the formation of aggregates in the HOPG substrate, indicating the good affinity of the compounds with the substrates due to π-π interactions. The height found relates to the stack of 1-2 molecules. On the other hand, XPS and UPS studies showed energy spectra corresponding to compound **2**. However, the same exact experiment with compound **1** did not show signals probably due to decomposition of **1**.

In summary, comparative study of both compounds were performed showing in some cases greater differences in the solid state experiments where for example they differ in great manner in the values of the zfs D parameters, in solution displaying significant shifts of -CH- group in the ^{1}H NMR and on surfaces where compound **2** show robustness that was not appreciated in **1**. On the other hand, their luminescence properties (UV-Visible and Fluorescence) were found similar.

1.3 Chapter II: Mononuclear Ni^{II} compounds: systems based on CCMoid ligands

1.3.1 Introduction

In the chapter II, the synthesis and characterization of five octahedral mononuclear Ni^{II}-CCMoid compounds are described. Fe^{II} and Co^{II} ions are commonly employed as sources of unpaired electrons, but Ni^{II} compounds are also particularly interesting in the area of SMMs due to the presence of a great magnetic anisotropy (D); they are frequently used as building blocks in the synthesis of polynuclear SMMs.[87,88] However, comparing with cobalt systems, fewer studies have been performed toward the study of the magnetic anisotropy of mononuclear Ni^{II} compounds to understand the origin of the factors that influence their axial anisotropy (zfs D parameter).

Focusing in mononuclear Ni^{II} systems, there is a reach structural literature with plenty of compounds exhibiting different geometries (linear, trigonal, tetrahedral, planar trigonal, trigonal bipyramid and octahedral).[89–92] Following the crystal field theory, depending on the geometry and therefore the disposition of the orbitals, the final systems may display an unquenched first-order orbital angular momentum, thus generating intrinsic magnetic anisotropy with significantly high values of D (approximately -530 cm^{-1}). This impressive number is in contrast to the energy barrier and blocking temperature found, which values are not that remarkable. Discussion of our findings in our magnetic studies and the factors that may interfere in the creation of SMM compounds are presented below.

Background

The first polynuclear nickel compound which exhibited molecular magnet behavior was published in 2001 by Winpenny *et al.*[93] This compound was a giant $\{Ni_{12}\}$ wheel that presented an S = 12 ground state and D = - 0.047 cm^{-1}, with a reported energetic barrier of U_{eff} = 9.6 K.

Following this publication, Christou's group published a molecular cube formed by four Ni^{II} with formula $[Ni(hmp)(ROH)Cl]_4$ (hmp = 2-hydroxymethylpyridine and R = CH_3, CH_2CH_3 or $CH_2CH_2C(CH_3)_3$), that displayed ferromagnetic couplings among the Ni^{II} centers exhibiting SMM behavior with a S = 4 ground state of a negative D = - 0.6 cm^{-1}.[94]

The first example of a mononuclear SMM Ni^{II} compound with trigonal bipyramid geometry corresponds to a compound published by Murrie *et al.*[95] in 2015 with formula $[Ni(MDABCO)_2Cl_3]ClO_4$ ($MDABCO^+$ = 1-methyl-4-aza-1-azoniabicyclo[2.2.2]octanium cation). The idea in the latest was to reduce structural distortions due to the Jahn-Teller effect by using large ligands located in the equatorial plane together with bulky and rigid ligands located in the axial plane. The decrease of the distortion leads to an orbital degeneration and therefore, to high values of axial anisotropy (D). In this case, the authors suggest values of D = - 535 cm^{-1} based on studies of HF-EPR with a corresponding values E = 0.18 cm^{-1} and $U_{eff/k}$ = 25 K.

In the case of pseudo-octahedral geometry, so far there is only one mononuclear Ni^{II} compound SMM published by Bôca in 2015.[96] This compounds presents a formula $[Ni(pydc)(pydm)]\cdot H_2O$ (pydc = pyridine-2,6-dicarboxylate, pydm = 2,6-bis(hydroxylmethyl)pyridine). In this case, as it is a pseudo-octahedral system, its orbital contribution is significantly quenched, which gives rise to values of magnetic axial anisotropy of a smaller order than in the previous case D = - 13.7 cm^{-1}, E = 0.07 cm^{-1} and a barrier of U_{eff} = 21.2 K.

Magnetic properties of mononuclear Ni^{II} compounds

Mononuclear high spin nickel (II) systems (d^8) present a (3F) ground term.

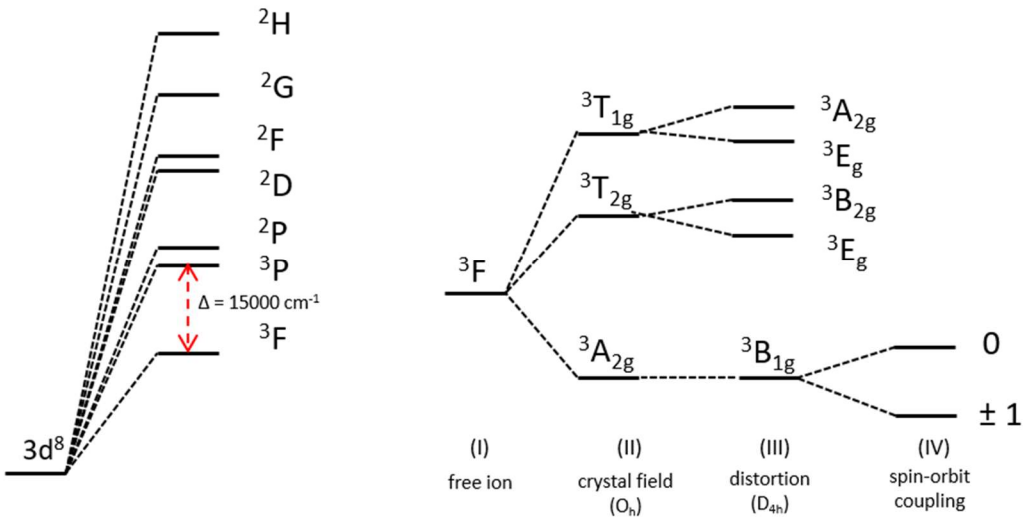

Figure 1.2.1: Scheme of (I) fundamental term for a free Ni^{II} ion, (II) levels for an octahedral environment, (III) splitting of the fundamental singlet and the excited states for an environment with octahedral symmetry with axial distortion and (IV) second-order spin orbit coupling

In the case of compounds with octahedral symmetry, the crystalline ligand field splits the ground term into three energy levels, giving rise to a single state $^3A_{2g}$ as the ground state and two triplet states $^3T_{2g}$ and $^3T_{1g}$. In principle, the magnetic behavior is expected to be dominated only by spin angular momentum; however, g values are in general slightly higher than expected. This fact is due to the presence of the first excited state, $^3T_{2g}$, which confers orbital contribution and presents the same value of spin multiplicity than the ground state, inducing a second-order spin-orbit coupling.

In systems with pseudo-octahedral symmetry displaying an axial elongation (Figure 1.2.2), the first excited state (δ) will correspond to the transition between the orbital d_{yz}, d_{xz} or d_{xy} and the orbital d_{z2}. As the difference in energy is large, low values of D would be expected.

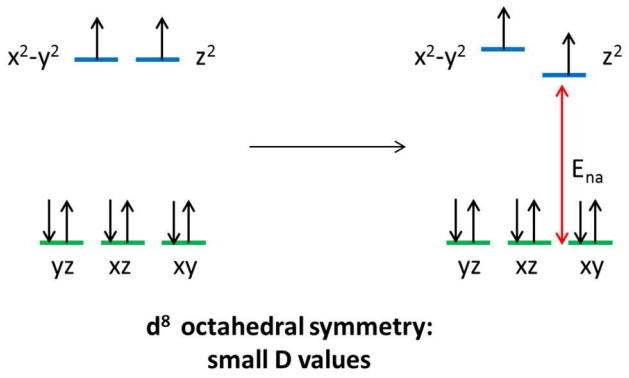

Figure 1.2.2: Splitting of the d orbitals due to the Jahn-Teller effect for d^8-octahedral coordination and axial elongation. The energy difference is indicated by the red arrow

In contrast, in the case of compounds with trigonal bipyramid symmetry, the d orbitals are disposed as shown the Figure 1.2.3. The degeneration between the orbital d_{xy} and d_{x2-y2} is broken due to Jahn-Teller distortions, which causes the presence of excited states near the ground state.[97] As it was mentioned in the introduction, this energy distance is inversely proportional to the parameter D, therefore high values of D will be obtained. The splitting energy of these two orbitals is directly related to the distortion of the geometry (high distortions provide low D values). In this way, Ni^{II} systems which present "trigonal bipyramid" with small distortions are perfect candidates to obtain system that display SMM behavior.

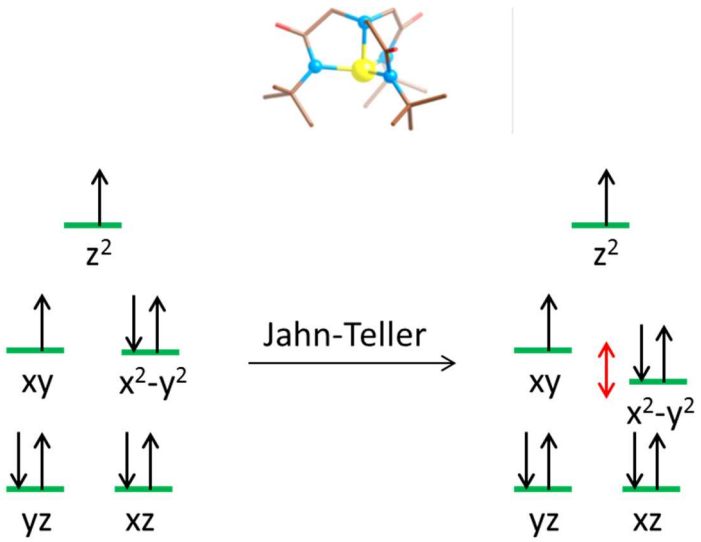

Figure 1.2.3: Splitting of the d orbitals due to the Jahn-Teller effect for d^8-trigonal bipyramid. The energy difference is indicated by the red arrow

1.3.2 Objectives

This chapter shows the synthesize and characterization of a family of five mononuclear octahedral compounds of Ni^{II}. Each system includes two 9Accm ligands and different pyridinic ligands: $[Ni(9Accm)_2(py)_2]$ **(7)**, $[Ni(9Accm)_2(2,2'\text{-bpy})]$ **(8)**, $[Ni(9Accm)_2(3\text{-picoline})_2]$ **(9)**, $[Ni(9Accm)_2(phen)]$ **(10)** and $[Ni(9Accm)_2(5,5'\text{-dimethyl-}2,2'\text{-bpy})]$ **(11)**. As in previous chapter, the different nature of these pyridinic moieties generates different arrangements of the ligands around the metallic center (hence, *cis/trans*). Again, a comparative study of luminescence properties of the systems in solution is shown. Regarding the metallic center, Ni^{II} and, despite not being a good candidate for SMMs as it was Co^{II}, magnetic studies were carried out for all the systems. In this case, the magnetic results are compared with those achieved by high field electronic paramagnetic resonance (HFEPR), being able to correlate these results with the structural differences of the systems.

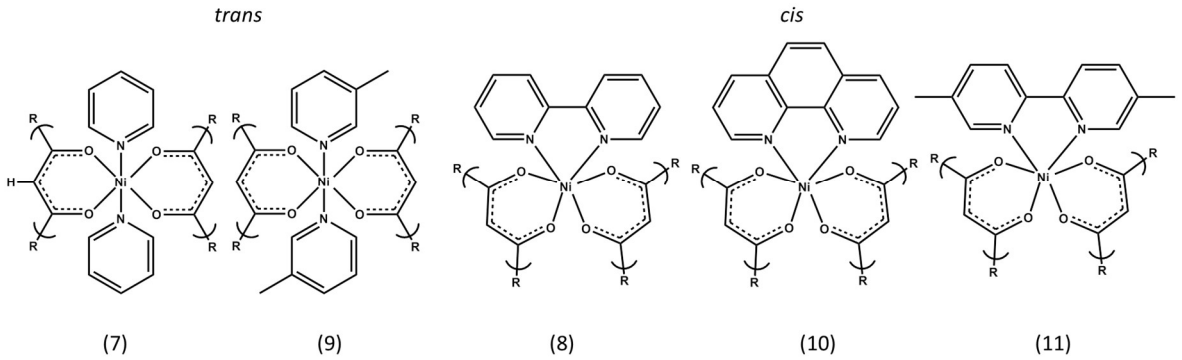

Figure 1.2.4: Visualization of the Ni^{II} coordination environment for compounds **7** and **9** (*trans*) and compounds **8**, **10** and **11** (*cis*).

1.3.3 Results and Discussion

1.3.3.1 Synthesis

Following the same procedure as the compounds described before, the synthesis of the Ni^{II}-CCMoids: $[Ni(9Accm)_2(py)_2]$ **(7)**, $[Ni(9Accm)_2(2,2'\text{-bpy})]$ **(8)**, $[Ni(9Accm)_2(3\text{-picoline})_2]$ **(9)**, $[Ni(9Accm)_2(phen)]$ **(10)** and $[Ni(9Accm)_2(5,5'\text{-dimethyl-}2,2'\text{-bpy})]$ **(11)** were carried out by the use of a microwave reactor (MW).

The synthesis of compound **7** and **9** was performed using pyridine and 3-picoline as solvents, respectively. In both cases, since they are nitrogenous bases, they are coordinated in a monodentate way to the metal center exhibiting both *trans* arrangements forming this way coordination compounds that display two pyridine/3-picoline ligands and two 9Accm ligands with pseudo-octahedral structures.[50]

In the case of compounds **8**, **10** and **11**, 2,2'-bipyridine, phenanthroline and 5,5'-dimethyl-2,2'-bipyridine were added in that order. These compounds were synthesized using DMF as a solvent; being bidentate systems and expecting to coordinate to the bipyridine groups and to two 9Accm groups as well, the sphere coordination is complete with no solvent molecules coordinated to the metallic center, where the systems exhibit *cis* arrangement with pseudo-octahedral structures.

A preliminary characterization was carried out using basic techniques such as Infrared Spectroscopy (IR) and Mass Spectrometry (MS). As the previous compounds (Figure 1.1.6), different bands in the area of 1600-1400 cm^{-1} corresponding to υ(C=O), υ(C=N) y υ(C=C) were found comparing with the free ligand 9Accm. Mass Spectrometry MALDI experiments were performing showing in all the compounds signals at 1009.3 m/z corresponding to the system $[Ni(9Accm)_2]^+$. In the case of compound 8, 10 and 11 a signal at 689.2, 713.2 and 717.2 m/z corresponding to [Ni(9Accm)(2,2'-bpy)]$^+$, [Ni(9Accm)(phen)]$^+$ and [Ni(9Accm)(5,5'-dimethyl-2,2'-bpy)]$^+$ is observed respectively (Annex 1.14).

1.3.3.2 Crystal structures

Crystal structures corresponding to compounds **7**, **8** and **9** were obtained. The crystalline bond distances and angles are described in Annex 1.15. For the rest of the compounds it was not possible to obtain crystalline structures.

$[Ni(9Accm)_2(py)_2]$ (7) crystallographic description

Compound **7** crystallizes with an extra molecule of pyridine as a solvent in a space group P-1. The mononuclear compound was formed by a Ni^{II} center which coordinates with two 9Accm molecules and two pyridine molecules. The organic pairs are arranged with *trans* disposition resulting in a distorted geometry D_{4h}. (Figure 1.2.5)

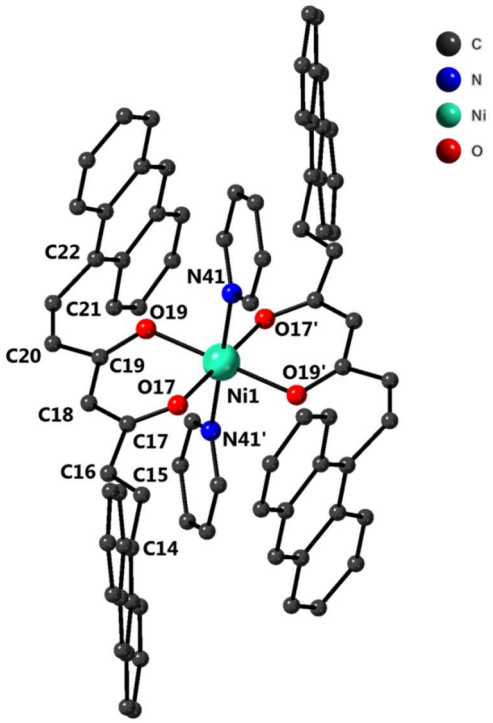

Figure 1.2.5: Representation of the molecular structure of compound **7** where the atoms of Ni (green), O (red), N (blue) and C (gray) are shown. H atoms have been omitted to simplify the structure

Two different Ni-O distances of 2.009 Å and 2.038 Å and one Ni-N distance of 2.087 Å were observed. These distances were similar to others reported systems.[98] Regarding the angles, for O(17)-Ni-O(19) and O(17)-Ni-O(19) were 89.78 and 90.22 ˚ respectively, while O(17)-Ni-O(17), O(19)-Ni-O(19) and N(41)-Ni-N(41) show angles of 180 ˚. The conjugated chain displayed two alternating C-C values: C(22)-C(21), C(20)-C(19), C(19)-C(18), C(17)-C(16) and C(15)-C(14) show characteristic C-C single bonds (1.411-1.479 Å) and C(21)-C(20) and C(16)-C(15) show characteristic double bond distances (between 1.311-1.335 Å). Interestingly, this conjugated skeleton showed different conformations on each side. One side displayed a zig-zag conformation meanwhile the other shows a boat-shape, indicating the high flexibility of the organic molecule. No hydrogen bonds were observed in the structure, however π stacking interactions are observed between the double bond corresponding to the organic chain and the rings corresponding to the anthracene groups. The shortest distances between $Ni^{II}\cdots Ni^{II}$ were 10.343 Å.

[Ni(9Accm)$_2$(2,2'-bpy)] (8) crystallographic description

Compound **8** crystallizes with a dichloromethane molecule of solvent in a space group P21/n. The structure was similar to that found for **7**, exhibiting a central Ni^{II} atom coordinated to two molecules of 9Accm arranged in a *cis* disposition and one molecule of 2,2'-bipyridine, providing an ideal C_{2V}

symmetry (Figure 1.2.6). The molecule shows Ni-O distances between 1.991 Å and 2.050 Å and Ni-N distances between 2.061 and 2.069 Å. These distances were similar to other systems in the literature.[98] On the other hand, the angles O-Ni-O, N-Ni-N and O-Ni-N differed slightly comparing with compound **7** (Annex 1.15). The conjugated chain showed similar distances than compound **2** [$Co(9Accm)_2(2,2'\text{-bpy})$], but in the case of their conformations, one of the 9Accm ligands presented two sides with zig-zag arrangements and the other 9Accm displays a zig-zag in one part of the molecule and a boat-shape in the other side. The shortest distances between $Ni^{II}\cdots Ni^{II}$ were 10.210 Å and no remarkable supramolecular interaction was observed.

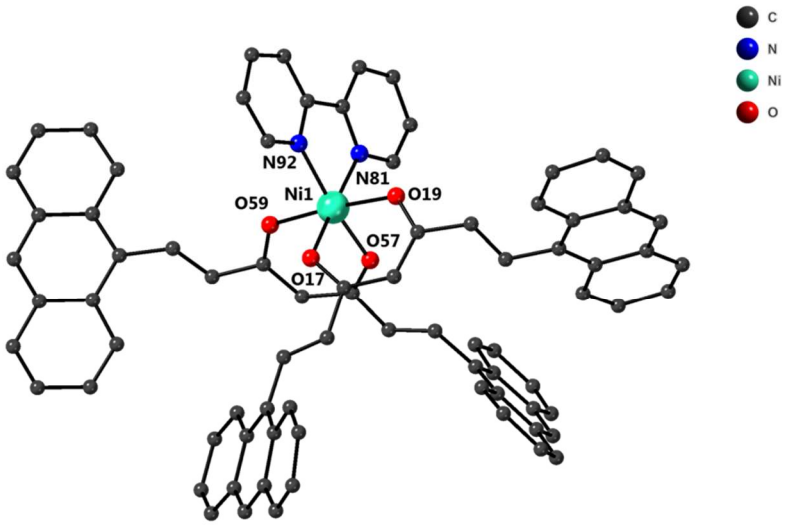

Figure 1.2.6: Representation of the molecular structure of compound **8** where the atoms of Ni (green), O (red), N (blue) and C (gray) are shown. H atoms have been omitted to simplify the structure

$[Ni(9Accm)_2(3\text{-picoline})_2]$ (9) crystallographic description

Compound **9** crystallizes with a molecule of dichloromethane as a solvent in a triclinic space group P-1. The structure was similar to compounds **1** and **7** because of the *trans* disposition of the 3-picoline and 9Accm molecules, respectively, where the metallic Ni^{II} center was coordinated to two molecules of each (Figure 1.2.7). As previous *trans* compounds this typical arrangement gave rise to a slightly distorted group of symmetry D_{4h}. The Ni-O distances presented values of 1.996 Å and 2.048 Å and the O-Ni-O angles show values of 89.07 ° and 90.93 ° similar to those found for **1** (see Table S.1.11). The distances presented in the conjugated chain and conformation were similar to those found for compound **7**. The shortest distances between $Ni^{II}\cdots Ni^{II}$ was of 10.475 Å and no relevant hydrogen

interactions were observed. However, there was a C-C stacking interaction between the ring corresponding to the 3-picoline group and the dichloromethane molecules at 3.586 Å.

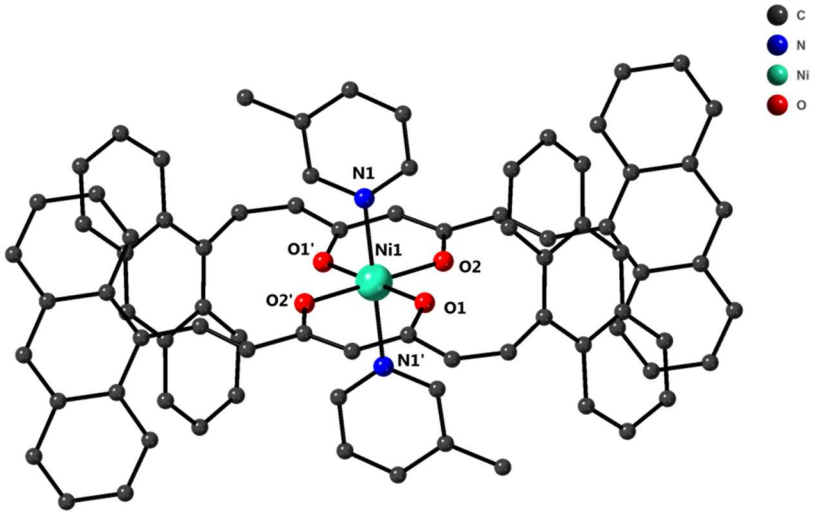

Figure 1.2.7: Representation of the molecular structure of compound **9** where the atoms of Ni (green), O (red), N (blue) and C (gray) are shown. H atoms have been omitted to simplify the structure

1.3.3.3 Characterization

The characterizations of the systems were carried out in different states: (i) in the solid state: by SQUID (Superconducting Quantum Interference Device) and measures of High Field Electronic Paramagnetic Resonance Spectroscopy (HFEPR) and (ii) in solution by Paramagnetic ^{1}H NMR.

1.3.3.3.1 Studies in solution

Nuclear Paramagnetic Resonance NMR

As it was mentioned, the electronic relaxation (fast relaxation of the electrons decreases the effect of the proton nuclei) depends on several factors such as: the nature of the metal ion, its oxidation state, geometry, etc. As general rule, those nuclei that contain different energies levels close to the ground state (either by spin-orbit coupling or zfs) will present non-excessively slow relaxation times and the paramagnetic ^{1}H NMR signals can be observed. For this reason, Co^{II} systems were able to characterize as it was shown in chapter I.[64–66]

In the case of Ni^{II} systems, the metal nature is less anisotropic, however it contains some anisotropy due to the second order spin-orbit coupling. For this reason, although exhibits lower relaxation times than Co^{II} (10^{-12} s for Ni and 10^{-11} s for Co), it is still considered a good candidate to provide defined signals by nuclear paramagnetic resonance.

As in previous chapter, the study of the stability in solution and the assignment of the signals were performed by the comparison of the spectra together with other similar systems found in the literature.[99–102] Thus, the ^{1}H NMR spectra of [Ni(9Accm)$_2$(py)$_2$] **(7)**, [Ni(9Accm)$_2$(2,2'-bpy)] **(8)**, [Ni(9Accm)$_2$(3-picoline)$_2$] **(9)**, [Ni(9Accm)$_2$(phen)] **(10)** and [Ni(9Accm)$_2$(5,5'-dimethyl-2,2'-bpy)] **(11)** were measured in $CDCl_3$.

cis compounds: [Ni(9Accm)$_2$(2,2'-bpy)] (8), [Ni(9Accm)$_2$(phen)] (10) y [Ni(9Accm)$_2$(5,5'-dimethyl-2,2'-bpy)] (11)

The three compounds display ideal C_{2V} symmetries which reduces the number of the peaks due to the equivalencies inside the organic groups (2,2'-bipyridine), (5,5'-dimethyl-2,2'-bpy), phenanthroline and 9Accm. Figures 1.2.8, 1.2.9 and 1.2.10 correspond to the spectra of compounds **8**, **10** and **11** respectively, and depending on the shift of the signals, two differentiated region can be observed: (i) a low-field region, here the *ortho* position of the pyridine groups should be present in all three systems. However, this signal was not possible to see in any cases due to the high contact contribution with the metal. This fact is also found in similar systems, where in the literature some compounds show wide and large shifts.[102] Therefore, compounds **8** and **11** exhibit their first signal in the low-field range at 58 ppm that corresponded to the *meta'* position of the pyridine group. This *meta'* position in compound **10**, (located in the central ring) exhibited a shift at 22 ppm. The signal corresponding to *meta* positions exhibited shifts at 39 and 40 ppm for compounds **8** and **10,** respectively (compound **11** is functionalized so this signal does not appear). The *para* position presented a shift at 14 ppm for compounds **8** and **11** and at 16 ppm for compound **10**.

On the other hand, related to the 9Accm ligand, three signals at 43, 38 and -13 ppm were present in the three compounds. The first two signals correspond to the two protons of the conjugated chain and the signal at -13 ppm corresponds to the –CH- group, similarly as it happened before in the case of the Co^{II} systems. Then, a number of signals appeared between 8 and 6 ppm, corresponding to the anthracene CCMoid groups. The complete list of peaks for 8, 10 and 11 is shown in Annex 1.16.

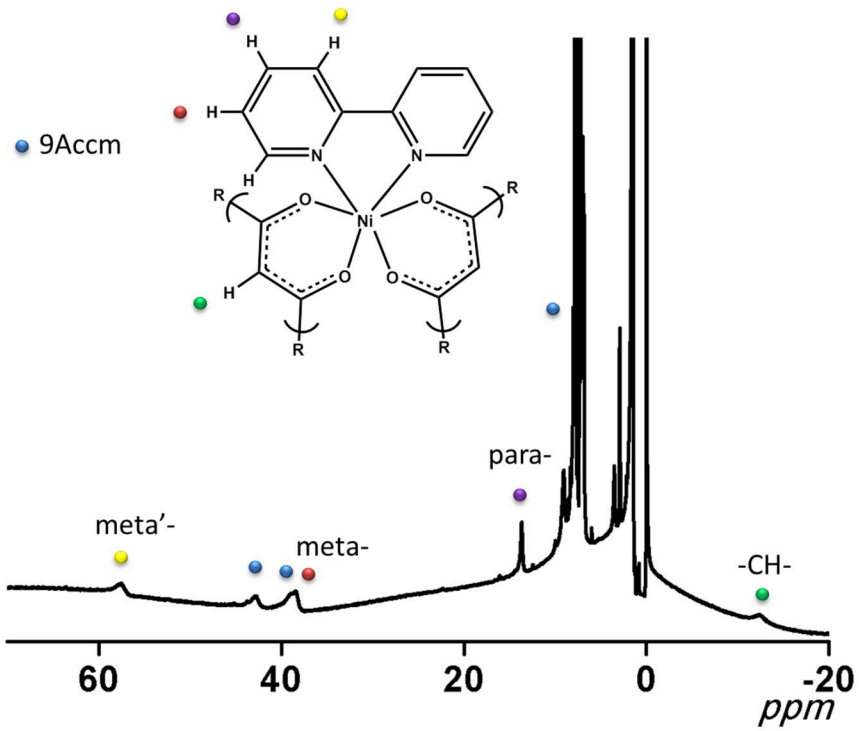

Figure 1.2.8: ^{1}H NMR spectrum of **8** in $CDCl_3$ between -20 to 70 ppm.

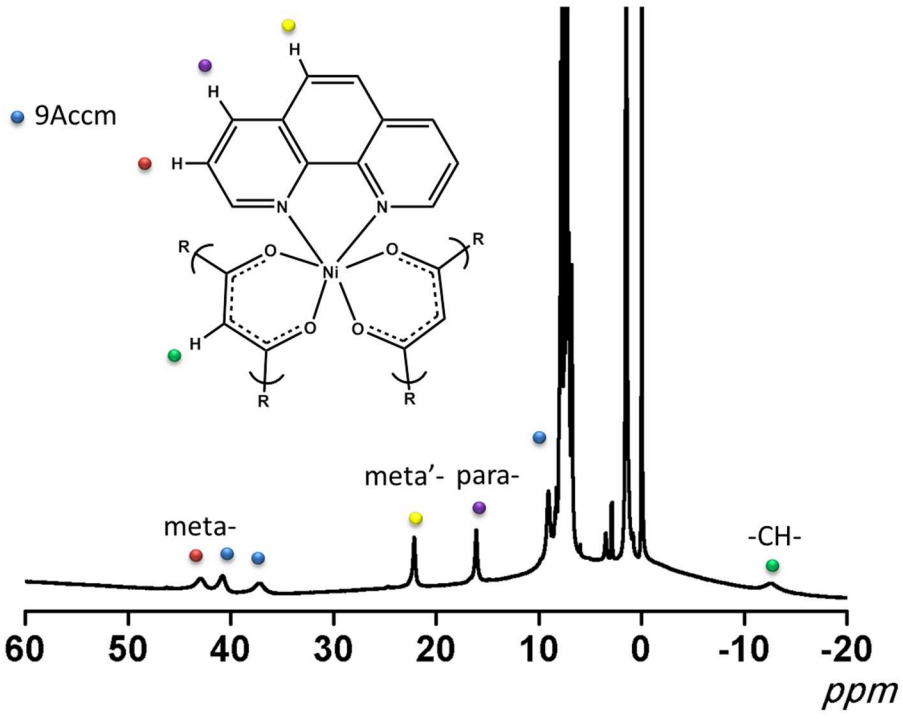

Figure 1.2.9: ^{1}H NMR spectrum of **10** in $CDCl_3$ between -25 to 60 ppm.

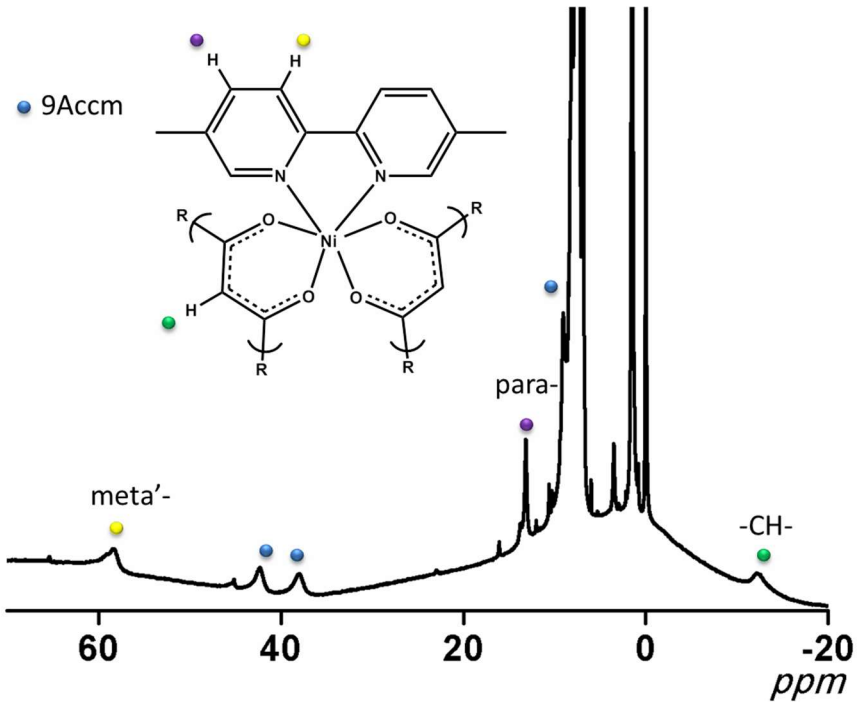

Figure 1.2.10: ^{1}H NMR spectrum of 11 in $CDCl_3$ between -20 to 70 ppm.

The comparison of the signals between the *cis* Co-CCMoids and Ni-CCMoids show similar shifts of the peaks corresponding to 9Accm and pyridine origin. In the case of [Ni(9Accm)$_2$(2,2'-bpy)], the *meta'*, *meta* and *para* positions show shifts at 58, 39 and 14 ppm, in that order, where in the case of the [Co(9Accm)$_2$(2,2'-bpy)] systems these appeared at 63, 35 and 12 ppm, respectively. The -CH- group corresponding to the 9Accm, showed shifts at -22 and -13 ppm for the Co^{II} and Ni^{II} systems, respectively. As mentioned before, the shifts in this area are proportional to the magnetic anisotropy of the metal. Thus, the results agree with the idea of cobalt systems presenting greater shifts.

trans compounds: [Ni(9Accm)$_2$(py)$_2$] (7) y [Ni(9Accm)$_2$(3-picoline)$_2$] (9)

For both compounds, the first signals in the low field area appeared at 43 ppm (Annex 1.17). One could assign this signal to the position *meta* of the pyridinic group, not having a CCMoid origin. In the case of the compound **9**, the signal had a lower intensity because on one side of the ring is functionalized in the *meta* position. The signal corresponding to the *ortho* position was not possible to be observed as it happened in the previous compounds.[99–102] Thus, the -CH- group, that normally is located at lower fields compared to the *ortho* position (for example in [Co(9Accm)$_2$] compounds in

previous chapter I), now it was not possible to be observed either. Finally, the signal corresponding to the *para* position appeared at 9 ppm in both cases.

In the case of compound **7** a signal at high fields with a shift of -15 ppm appeared, however, this signal is only characteristic for systems which present *cis* arrangement. This fact maybe is due to the presence of an equilibrium between *cis/trans* arrangements in the case of pyridines. Compound **9** did not present that signal, indicating that this equilibrium was not allowed due to steric hinderances.

On the other hand, compound $[Ni(9Accm)_2(dmf)_2]$ was synthesized as in the previous chapter, with the aim of identifying CCMoids signals. However, in this case the spectra showed a large number of signals, probably due to the different geometries that could be achieved by having *cis/trans* equilibria or different compounds (molecules containing different numbers of dmf groups attached).

UV-Vis Absorption and Fluorescence studies

Luminescent measurements were performed to study the effect of the coordination of paramagnetic center. Thus, UV-Visible and Fluorescence studies were carried out in solution using CH_2Cl_2. Further, experiments of the emission using different concentrations were performed to study the possible formation of excimers.

In general, the UV-Visible spectra of curcuminoids compounds containing 3d metal centers exhibit similar features.[59,60] Thus, this technique can be used as a fingerprint to characterize them. For that reason, it was expected to achieve spectra for the Ni^{II} CCMoid systems similar to those shown for Co^{II} CCMoid compounds described before, including the nature of their absorbance bands. For this reason, the description of their spectra is here obviated.

The absorption spectra corresponding to **7**, **8**, **9**, **10** and **11** compared to the free ligand (9Accm in red) are shown in the Figure 1.2.11. All systems presented (i) an intense absorption band at the highest energies (255 nm) and (ii) an additional transition between 420-440 nm. In the case of 9Accm, different transition at 350 nm of vibrionic nature corresponding to the anthracene groups were observed.

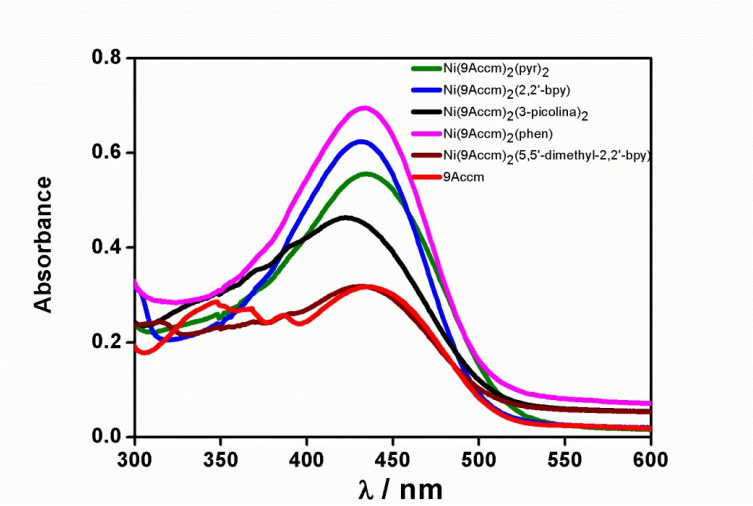

Figure 1.2.11: Comparison of the UV-Vis spectra of compounds **7** (green), **8** (blue), **9** (black), **10** (pink), **11** (Brown) and 9Accm (red) in CH_2Cl_2 (10^{-5} M).

Regarding the emission studies, it is expected a similar response as the Co^{II} compounds, since the fluorescence is mainly derived from the 9Accm ligand.[58] Thus, in this case our efforts were directed to carry out emission studies at different concentrations to observe their influence in the emission.

The emission spectra of compound **7** at two concentrations (10^{-4} M (red) and 10^{-6} M (blue)) using CH_2Cl_2 as solvent excited at 350 nm are shown in Figure 1.2.12 (the spectra of the rest of compounds are in Annex 1.19). Depending on the concentration, different emission bands were observed. In the case of the emission corresponding to 10^{-6} M (blue) two bands were also observed: (i) one at the highest energy (390 nm), corresponding to the anthracene groups and (ii) a second one between 540-640 nm with a maximum at 590 nm corresponding to the presence of excimers.[103] Excimers can be defined as supramolecular dimer structure where at least one of these molecules is in an excited electronic state, giving rise to emissions coming back to the ground state. This emission is always at lower energies compare with the monomers.[104] The presence of excimers in conjugated systems (pyrenes, anthracenes,…) has been highly studied due to the strong π-π stacking interactions. The formation of these excimers, therefore, is affected among others factors, by the numbers of monomers in the medium (the higher concentration, the higher probability of collisions and formation of excimers). In the case of the emission corresponding to the system at higher concentration 10^{-4} M, an increase of the band corresponding to the excimer was observed; meanwhile the signal corresponding to the monomer (anthracene) totally disappeared. Therefore, in the case of the system at 10^{-6} M and exciting at 350 nm, two different luminescence processes were present.

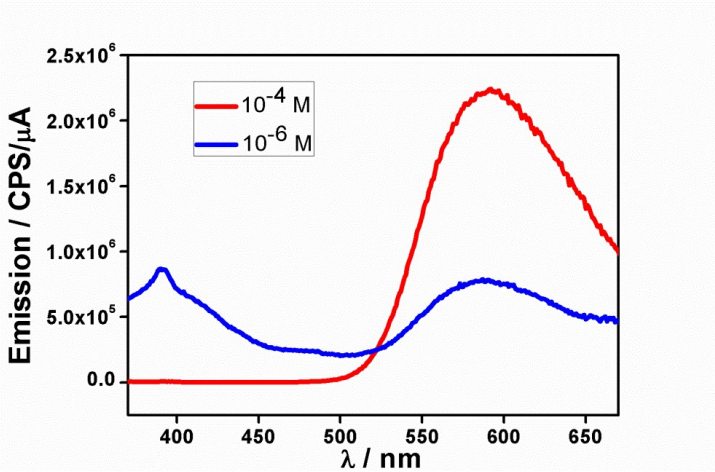

Figure 1.2. 12: Emission spectra of compound **7** at different concentration 10^{-4} M (red) and 10^{-6} M (blue) in CH_2Cl_2.

Figure 1.2.13 shows the influence of the paramagnetic coordination on the emission. Here, the emission of all the systems are shown when they were excited at 440 nm using a concentration of 10^{-5} M. As it is observed, all the emission corresponding to the coordination compounds present lower intensity bands than that of the free ligand 9Accm due to the CHQF effects. The comparison is qualitative because the absorbance values are different among all the systems, however it is still possible to observed that the free ligand provides the best emission results.

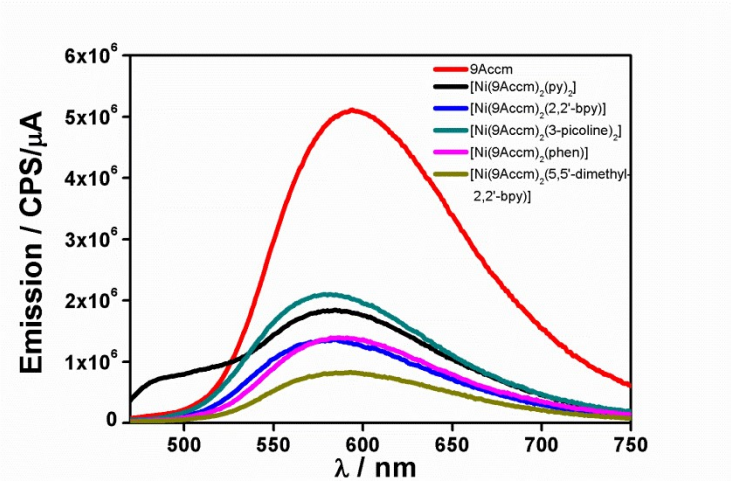

Figure 1.2.13: Comparison of the emission spectra of compounds **7** (black), **8** (blue), **9** (green), **10** (pink), **11** (ocher) and 9Accm (red) in THF.

1.3.3.3.2 Studies in the solid state

Magnetic studies

As it was mentioned in the introduction, Ni^{II} systems can exhibit relevant molecular magnet properties. Thus, studies based on magnetization and magnetic susceptibility were performed. The measurements were fitted using the program PHI[32] in order to obtain the values of g, E and D.

Magnetic susceptibility and magnetization

Magnetic susceptibility measurements of the compounds $[Ni(9Accm)_2(py)_2]$ **(7)**, $[Ni(9Accm)_2$(2,2'-bpy)] **(8)**, $[Ni(9Accm)_2$(3-picoline)$_2]$ **(9)**, $[Ni(9Accm)_2$(phen)] **(10)** and $[Ni(9Accm)_2$(5,5'-dimethyl-2,2'-bpy)] **(11)**, in a temperature range between 2-300 K under the application of a magnetic field of 0.03 (2-30 K) and 0.5 T (30-300 K) were performed, respectively. All the systems present similar magnetic behavior as it can be seen in the Figure 1.2.14. The values of $\chi_M T$ at room temperature for compound **7**, **8**, **9**, **10** and **11** correspond to 1.29, 1.40, 1.29, 1.38, and 1.31 cm^3 K mol^{-1}, in that order. These values are higher from the expected for an S = 1 system (take into account only the spin value, $\chi_M T$ = 0.99 cm^3 K mol^{-1}, g = 2.0), due to the existence of second order spin-orbit contributions. In all cases, when the temperature decreased, the value of the $\chi_M T$ decreased slightly (almost constant) until it reached a temperature of 9 K. Within this range, the systems followed the Curie-Weiss law as it's expected for Ni^{II} O_h. Below this temperature, a very pronounced decrease was observed in all the compounds until values between 0.88–0.67 cm^3 K mol^{-1} were reached. This decrease with the temperature is caused by the zero fields splitting and intermolecular interactions. The obtained values were similar to other mononuclear Ni^{II} reported in the literature.[105]

Magnetization measurements $M/N\beta$ vs H (Figure 1.2.14, inset) were performed under a variable magnetic field from 0 to 0.5 T at constant temperature of 2 K. The increasing of the magnetic field promotes the increase of the magnetization since the ground state population was increasing. This fact was truncated when the saturation values were reached (when all the spins are aligned with the field) and values of 1.94, 1.87, 1.85, 1.88, 2.01 were obtained for the **7**, **8**, **9**, **10** and **11**, respectively. These values are lower than those expected for a S = 1 ($M/N\beta$ = 2 μB, g = 2.0) due to the spin-orbit coupling of the second order present in Ni^{II}.

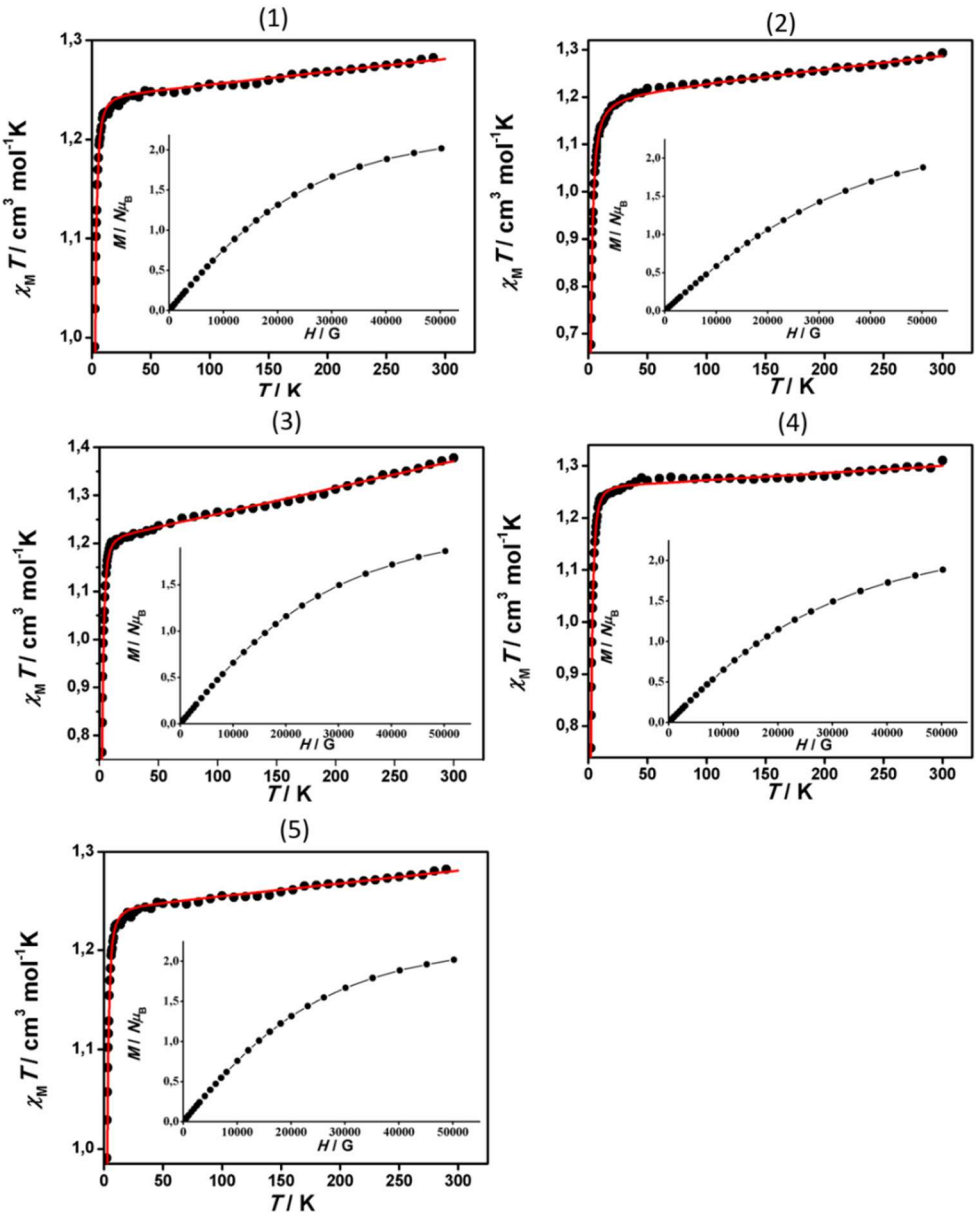

Figure 1.2. 14: Representation of χ_MT vs T and M vs H / T (inset) for compounds **7**, **8**, **9**, **10** and **11**. Experimental data are shown as dots and the resulting fitting as a red line.

On the other hand, magnetization measurements M vs H/T (Figure 1.2.15) were performed under an external magnetic field between 0.5 and 5 T at a variable temperature of 1.8-6.8 K. The curves at different magnetic field did not overlap, indicating the presence of certain anisotropy. Comparing the measurements obtained from the Co^{II}-systems, in this case the separation between the curves at different magnetic field was longer. This fact, indicated stronger dependence with temperature and external magnetic field, in the process to reach the saturated magnetization, caused by low D values. Therefore, these measurements indicated, in a qualitative manner, that the value of the magnetic

anisotropy of Ni^{II}- systems was going to be lower than those of the Co^{II}-systems studied in previous chapter.

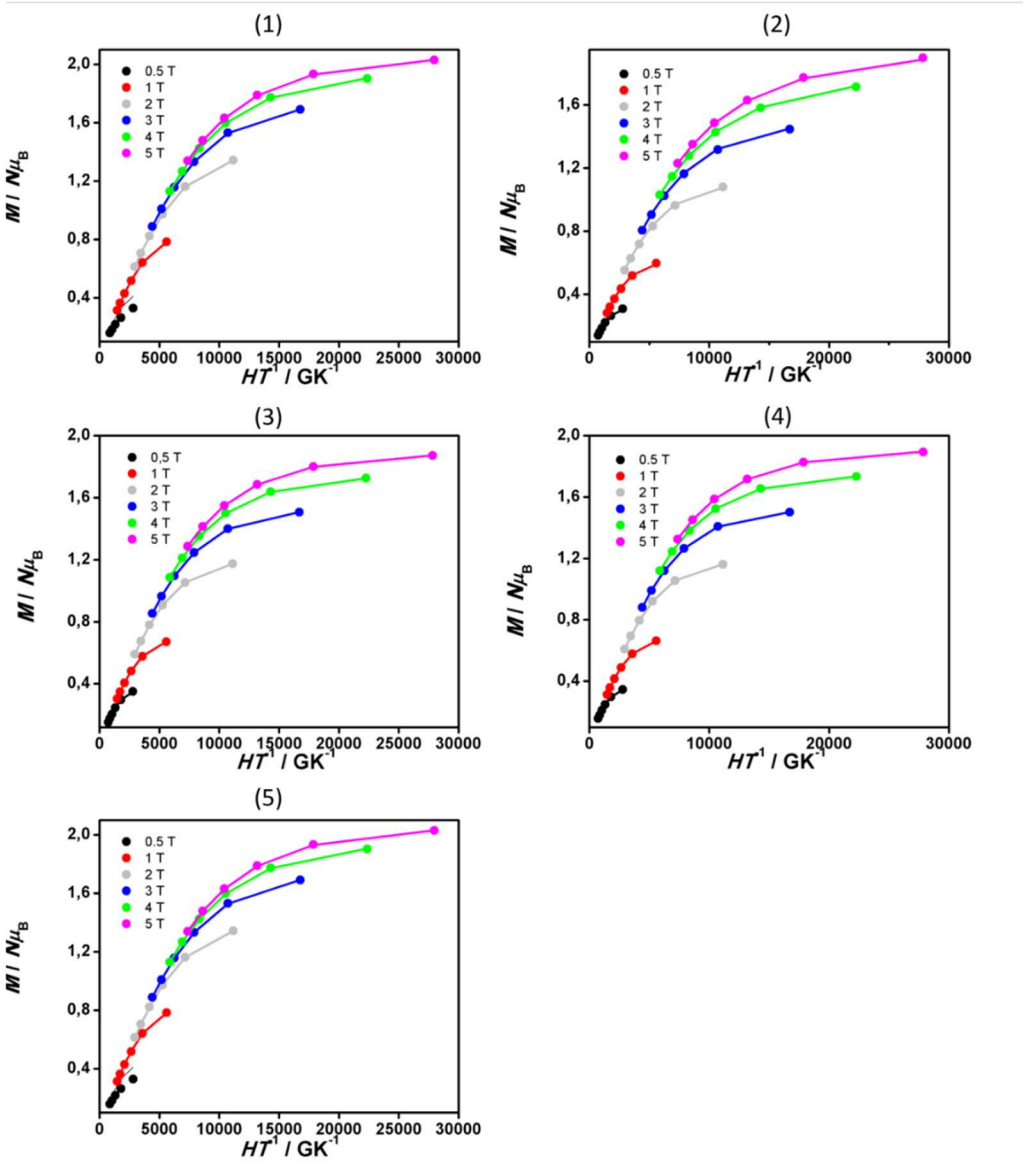

Figure 1.2.15: Representation of M/Nμ$_B$ vs H/T for compounds **7**, **8**, **9**, **10** and **11**. Experimental data are shown as dots and the resulting fitting as lines.

High Field Electron Paramagnetic Resonance (HFEPR)

The HFEPR measurements were performed by Prof. Steven Hill group at the Florida State University. The measurements were collected using a powder sample since the crystals achieved for all the compounds were tiny for single crystal measurements.

The measured compounds were [Ni(9Accm)$_2$(py)$_2$] **(7)**, [Ni(9Accm)$_2$(3-picoline)$_2$] **(9)**, [Ni(9Accm)$_2$(phen)] **(10)** and [Ni(9Accm)$_2$(5,5'-dimethyl-2,2'-bpy)] **(11)**.

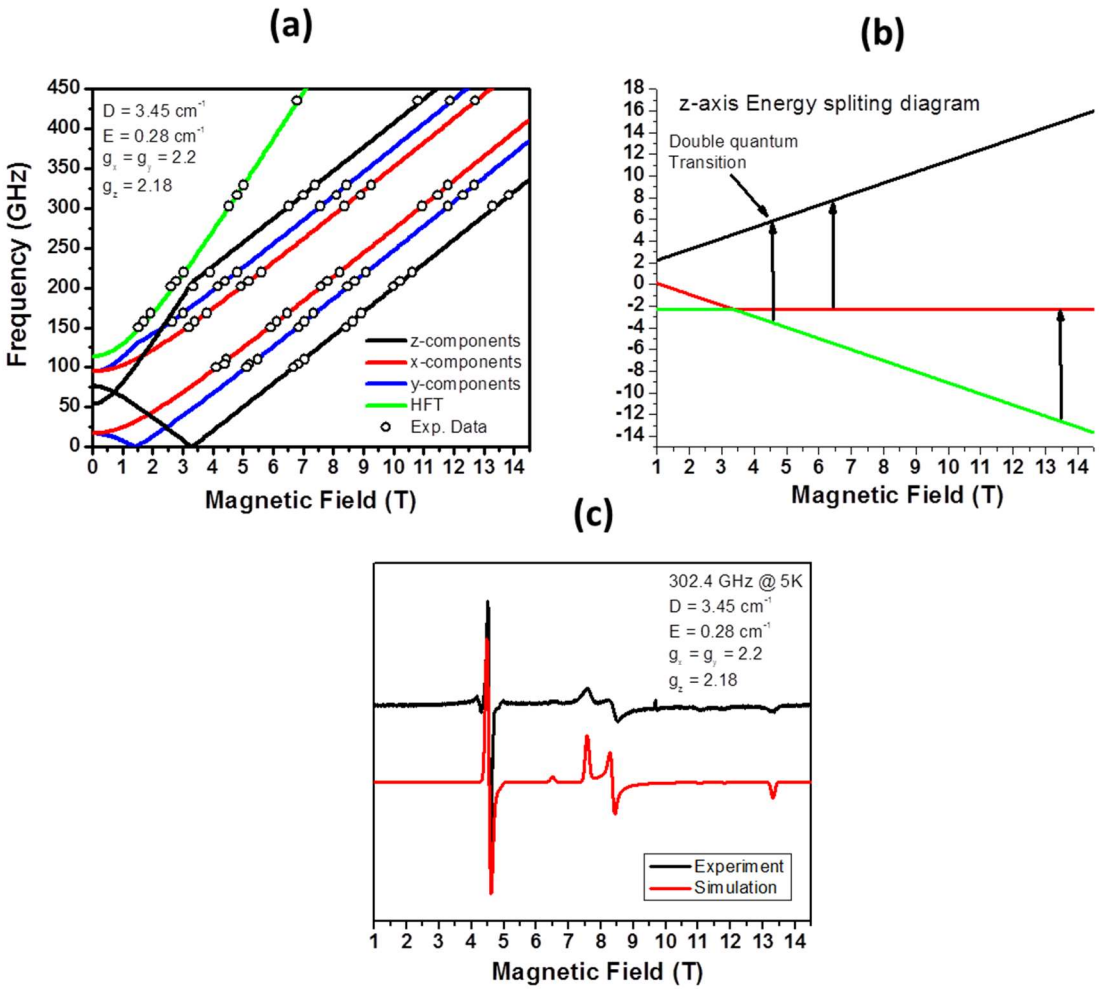

Figure 1.2.16: (a) Representation of frequency vs magnetic field. (b) Zeeman plots and (c) EPR spectra for compound **7**.

As example here, the graphs of Figure 1.2.16 (a) represents in solid black, red and blue lines simulations for the z, x and y components respectively of compound **7**, using the parameters sets listed in the top left corner of each plot. Black circles represent the experimental frequency dependent data (peak position). The solid green lines represent simulations for the single-quanta half-field transition. The high field transitions are dominated by the xy-plane because more of these components in the pellet will be oriented along the applied field.

The Ni^{II} compounds were all easy-plane type (D>0). The data were simulated employing a giant spin model with rigid S = 1. Interestingly, symmetry might explain the E-values (second-order rhombic Hamiltonian term). The cleanest spectra (transition peak for xyz were observed at nearly all frequencies) was obtained for the systems with a *trans* disposition. One might expect that this

compound would have the highest symmetry, and thus, the smallest E term. Table 1.2.1 provides the comparison between the data achieved by the use of our SQUID and the HFEPR results.

Calculation of parameters zfs: g, D, E

The experimental measurements of $\chi_M T$ vs T and M vs H/T were fitted by the diagonalization of the Hamiltonian spin matrix, using the program PHI.[32] The values of D, E and g obtained from fitted of the magnetic measurements (MAG) and high field electronic paramagnetic resonance (HFEPR) are shown in Table 1.2.1.

Sample	Compound	Arrangement	HFEPR g average	HFEPR D (cm^{-1})	HFEPR E (cm^{-1})	MAG g average	MAG D (cm^{-1})	MAG E (cm^{-1})
(7)	$[Ni(9Accm)_2(py)_2]$	*trans*	2.19	3.45	0.28	2.22	3.3	-0.07
(8)	$[Ni(9Accm)_2$(2,2'-bpy)]	*cis*	-	-	-	2.24	3.84	-0.53
(9)	$[Ni(9Accm)_2$(3-picoline)$_2$]	*trans*	2.18	3.47	0.73	2.19	3.60	-0.30
(10)	$[Ni(9Accm)_2$(phen)]	*cis*	2.17	4.50	0.93	2.19	4.26	0.81
(11)	$[Ni(9Accm)_2$(5,5'-dimethyl-2,2'-bpy)]	*cis*	2.17	3.80	0.83	2.23	4.56	1.03

Table 1.2.1: Comparison of the values of g, D (cm-1) and E (cm-1) obtained from HFEPR and magnetic measurements.

The values of g, D and E corresponding to magnetic and HFEPR measurements were very similar in all the compounds. For one side, the g values (2.19-2.23) indicated an orbital contribution comparable to the spin value (g = 2.00). These values were similar compare to others Ni^{II} systems found in the literature. On the other hand, contrary to cobalt compounds, in this case there was no difference in D values between systems with different disposition (*cis*/*trans*). According to the expected, these values are significantly lower due to the lower anisotropy present in the Ni^{II} center.[96]

Single Molecule Magnet behaviour: AC measurements

AC measurements were performed to study the possible single molecule magnet behavior in the systems. However, no dependence of the out of phase magnetic susceptibility (χ_{AC}") with the frequency was found even with the application of an external magnetic field. One of the reasons may be related to the low value of the D parameters found.

1.3.3.3.3 Studies on surface

X-ray photoelectron spectroscopy (XPS)

XPS experiments were carried out to study the stability of the compounds using the same conditions than in the previous chapter. Thus, to perform these studies, two compounds with different arrangements were selected: compounds **7** (*trans*) and **11** (*cis*).

As it can be seen in Figure 1.2.17, compound **11** displayed the presence of spin-orbit splitting lines corresponding to Ni2p and Ni1s, meanwhile for **7,** these peaks did not appear. The graph showed the same behavior as in the previous chapter, indicating the great robustness of systems displaying *cis* disposition *vs* the *trans* analogues.

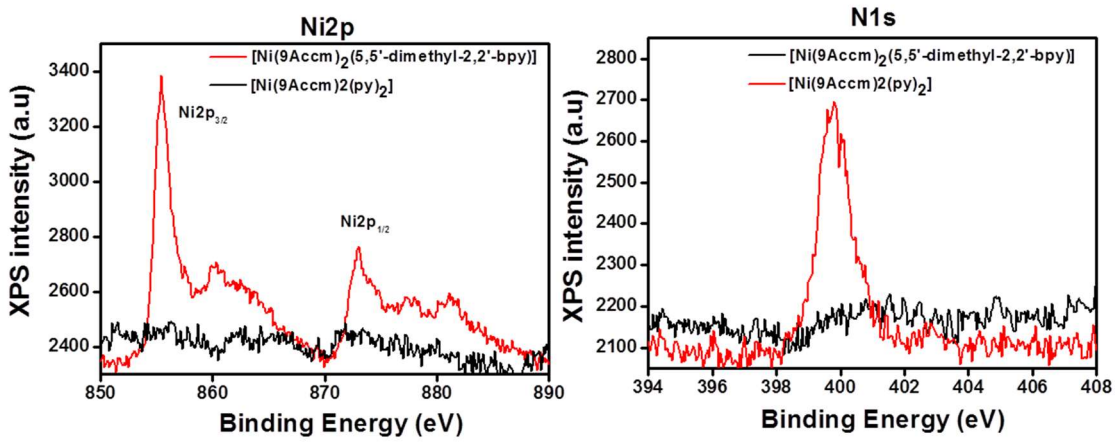

Figure 1.2.17: XPS experiments of a film of compound 7 (black) and 9 (red) spin-coated on HOPG

1.3.4 Conclusions

In this chapter, five mononuclear systems of Ni^{II}-CCMoids have been synthesized with formulae: [Ni(9Accm)$_2$(py)$_2$] **(7)**, [Ni(9Accm)$_2$(2,2'-bpy)] **(8)**, [Ni(9Accm)$_2$(3-picoline)$_2$] **(9)**, [Ni(9Accm)$_2$(phen)] **(10)** and [Ni(9Accm)$_2$(5,5'-dimethyl-2,2'-bpy)] **(11)**. As in the previous chapter, the synthesis was carried out by using the microwave reactor providing high yields and, in some cases, the achievement of monocrystalline samples directly from the MW tube was possible.

The systems were characterized in solution by paramagnetic ^{1}H NMR. The comparison of their spectra allowed the signal assignation of *cis*-arranged compounds. These compounds present a shift relatively similar to those found in cobalt compounds. In the case of Ni^{II} systems, the signal corresponding to -CH- group appears shifted to lower fields (-13 ppm) compared to analogous Co^{II}

systems (-22 ppm), probably due to the low value of the field splitting parameter D for the Ni^{II} systems. Related to the *trans*-arranged compounds, their assignment was not possible probably due to the labile nature of the pyridine groups attached to the Ni^{II} centers, which also affected the intensity and the number of signals. Furthermore, UV-Visible and Fluorescence studies were carried out in solution. UV-Vis spectra show a single absorption band around 420-400 nm, common for all the studied CCMoids. This absorption, as in the cobalt compounds, was very similar to the free ligand 9Accm. On the other hand, emission studies were performed at different concentration to analyze the formation of excimers. The spectra at low concentrations (10^{-6} M) show two emission mechanisms: (i) one band at higher energies (390 nm) corresponding to the anthracene groups (monomer) and (ii) one band at lower energies (590 nm) corresponding to the formation of excimers. By increasing the concentration (10^{-4} M), intermolecular interactions and therefore, the formation of excimers was favored. The spectra at this concentration showed only a single band at 590 nm (excimer formation), with higher intensity than that found for the lowest concentration.

The characterization in solid state was carried out by magnetic measurements to study the possible molecular magnet behavior. However, no signal dependence of the out of phase magnetic susceptibility (χ_{AC}") with the frequency was found in any of the compounds. This fact was due to nickel metal centers did not present high magnetic anisotropy ($D < 4\ cm^{-1}$). The values of g, D and E were obtained from the fitting of the magnetic measurements: M vs H/T and $\chi_M T$ vs T.

On the other hand, measurements by high field electronic paramagnetic spectroscopy (HFEPR) were performed and compared with those found by the use of an SQUID. The values were similar in both measurements, exhibiting lower values for the D parameters and small but rather important contributions for the E parameter.

1.4 Chapter III: Coordination polymers based on Co^{II}/Ni^{II}-9Accm units

1.4.1 Introduction

Chapters I and II show the studies performed with mononuclear Co and Ni species containing 9Accm as a ligand. There, a variety of units, with both metal centers, were conceived pointing out the structural diversity found by the use of 9Accm and additional pyridinic ligands. Magneto-structural correlations were performed by comparing the magnetic differences between mononuclear *cis*/*trans* Co/Ni systems. Here, the assembly of $M(9Accm)_2$ units by the use of bridging ligands toward the achievement of coordination polymers was explored. In addition, magnetic characterization, as before, was performed to analyze the effect of the bifunctional pyridinic groups on the final properties.

Together with SMMs, Single Chain Magnets (SCMs) are an additional family of nano-magnets formed by molecular based systems that display one dimension (1D).[106–108] They are composed by magnetically isolated chains that present slow relaxation of the magnetization.[109] The motivation behind the synthesis and study of SCMs is to provide a new approach to increase the blocking temperatures (normally very low for SMMs, as discussed in previous chapters) since the 1D organization in such materials is predicted to induce significant increase of the energy barrier.[110–113]

In SMM systems, as it was mentioned, the slow relaxation of the magnetization arises for each single system, through the combination of large spin ground state, S, and zero-field splitting parameter, D. However, in the case of the SCM, the slow magnetic relaxation is due to the interactions between repeating units along a well-isolated single chain. Thus, the slow magnetic relaxation arises from the combination of (i) a large uni-axial magnetic anisotropy (ii) strong intrachain magnetic interactions and (iii) very weak or negligible interchain magnetic interactions. A 1D chain system will be considered SCM only if presents these three conditions. Although several examples of SCM have been reported in the past,[110–113] the requirements mentioned restrict in great manner the development of these systems, so controlled methodologies to achieve SCMs are still a challenge. The most common strategy bases on:

(i) The use of appropriate bridge ligands that allow an effective magnetic interaction between anisotropic centers (Co^{II}, Ni^{II}, Mn^{III}, Fe^{II} and lanthanides) in the 1D chains.

(ii) The use of suitable diamagnetic spacers that give rise to magnetically isolated chains to reduce intermolecular interactions.

So far, the SCMs reported in the literature derived from 3d ions[114–116], mixed 3d-4f[117,118] and homometallic 4f[119] systems. As explained before, the existence of chains is mandatory but one most

stress that the appearance of intramolecular interactions among the paramagnetic centers as well. Figure 1.3.1 depicts both possibilities, taking into account two units in an ideal chain.

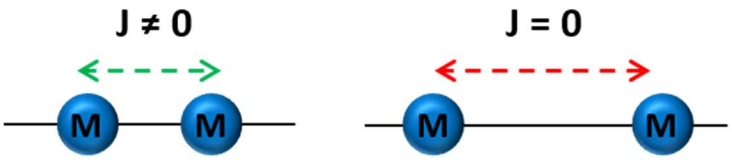

Figure 1.3.1: Scheme of molecular chain 1D with intrachain magnetic interaction (J ≠ 0) (left) and without magnetic interaction (J = 0) (right)

In the first class, usually ferromagnetic interactions between the metals on the same chain are present, resulting in a high total spin S (SCM behavior). In the second class, the M···M interactions are negligible (J=0); there, structurally the system can be described as a chain but, magnetically it could be considered as each unit is independent of the others, having a 1D SMM system.

1.4.2 Objectives

In this chapter, two coordination polymers, having Ni^{II} and Co^{II} ions respectively, were synthesized using 9Accm and 4,4'-bipyridine as ligands. This way, two systems with general formulae $[Co(9Accm)_2(4,4'\text{-bpy})]_n$ **(12)** and $[Ni(9Accm)_2(4,4'\text{-bpy})]_n$ **(13)** were achieved. In both compounds, the 9Accm ligands will be disposed in *trans*-disposition and the metallic centers connect through the 4,4'-bipyridine moieties, also in a *trans* arrangement, giving rise to two isostructural systems. Comparative studies of the two species were performed in solution, the solid state and by deposition on a surface. In the solid state, magnetic studies in both systems were pursued. Solution studies focused on their stability by performing ^1H NMR paramagnetic experiments together with the analysis of the luminescent properties. Finally, solid studies were performed using different substrates.

1.4.3 Results and Discussion

1.4.3.1 Synthesis

The syntheses of two coordination polymers compounds, $[Co(9Accm)_2(4,4'\text{-bpy})]_n$ **(12)** and $[Ni(9Accm)_2(4,4'\text{-bpy})]_n$ **(13)**, were carried out by two different methodologies: (i) solvothermal synthesis[120] and (ii) by the use of a microwave reactor (MW).[121] Advantages of the use of a microwave reactor have been already discussed in previous chapters. In the case of solvothermal methodology, the reactions were worked out at the boiling point of the solvent generating high pressure. The use of such conditions favors the solubility of the reagents and increases the capacity of the molecules to interact with each other and therefore coordination (giving rise sometimes to serendipitous structures). In principle, by controlling the decreasing of the temperature for example, the precipitation of the final species may be possible, giving rise to the formation of suitable crystals for X-ray diffraction analysis. Currently, this method is widely used to the formation of high dimensionality compounds such as MOFs (Metal Organic Frameworks).

As mentioned above, 4,4'-bipyridine was used as the linker between the coordination units toward the formation of 1D systems.[122] This ligand it is an ideal connector for 3d transition metals due to the following characteristics: (i) it presents two binding positions (N based) and (ii) exhibits a rigid structure being used to create pillar architectures, which can provide certain predictability of the final network geometries[122]. Depending on the nature of the coordination metal and the ligand, bipyridine moieties can give rise to monodimensional (1D) or three-dimensional (3D) structures. Here, all the systems present 1D arrangements, where coordination sphere of the Co^{II} and Ni^{II} contains two 9Accm ligands and two 4,4'-bipyridine.

A preliminary characterization was performed by Mass Spectrometry (MS) (Annex 1.20).

1.4.3.2 Crystal structures

The most relevant crystalline bond distances and angles of compounds **12** and **13** are described in Annex 1.21. The X-ray diffraction analysis of the two species showed that both are isostructural, so a general description has been made for both.

$[Co(9Accm)_2(4,4'\text{-bpy})]_n$ (12) and $[Ni(9Accm)_2(4,4'\text{-bpy})]_n$ (13) crystallographic description

Compounds **12** and **13** crystallize in the same space group C2/c. The crystal structures show hexacoordinated M^{II} centers (Co^{II} and Ni^{II} centers for **12** and **13**, respectively) attached to two 9Accm

ligands in the equatorial plane of the metal ion and two molecules of 4,4'-bipyridines bound in the axial plane, exhibiting distorted octahedral geometries in both cases. Figure 1.3.2 (bottom) shows an isolated fragment of the compound **12** and (top) a fragment corresponding to compound **13**.

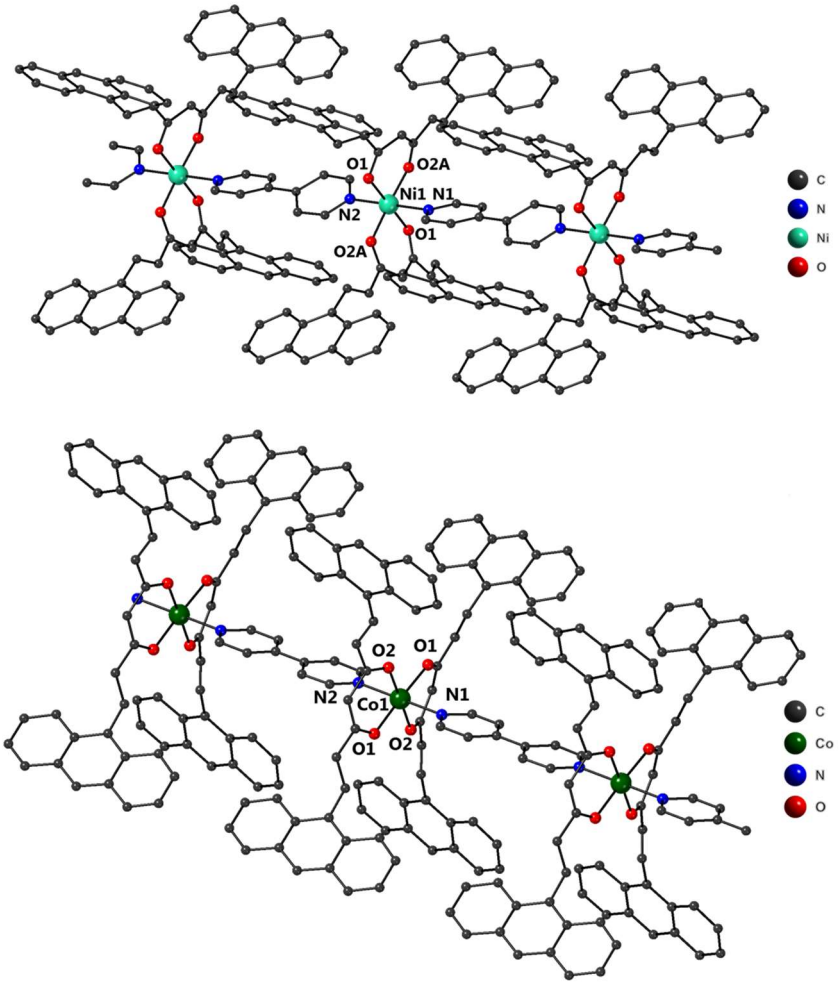

Figure 1.3.2: Representation of compounds **12** (bottom) and **13** (top) where the atoms of Co (green), Ni (turquoise), O (red), N (blue) and C (gray) are shown. H atoms have been omitted to simplify the structure

Distances related to the metallic center Co-O/Co-N (2.030-2.061 Å/ 2.137-2.147 Å) and Ni-O/Ni-N (2.000-2.042 Å/ 2.081-2.131 Å) are similar to the mononuclear systems showed previously. The pyridine groups corresponding to the 4,4'-bipyridine ligand acts as a bridge between the neighboring metal centers forming 1D chains. The aromatic group of the 4,4'-bipyridine are rotated avoiding coplanarity between the two rings within the ligand, with angles of 25.26 ° for compound **12** and 25.56 ° for compound **13**, respectively.

The linearity of the chain in both compounds is due to the *trans* arrangement of the conjugated nature of the 4,4'-bipyridine ligands Co-Co/Ni-Ni distances are 11.337 Å and 11.287 Å respectively. The conjugated chain of the 9Accm ligands displays two alternating C-C values as in the mononuclear compounds. Such skeletons, exhibit complete zig-zag conformations (this is mentioned because in the mononuclear system it was seen that some of them could present zig-zag but also boat shape conformations). The anthracene groups are arranged practically perpendicular to the chains. This disposition prevents intermolecular interactions among the chains, where the closest of the metal center distances is approximately of 13 Å. However, σ-π interactions between the anthracene groups and the neighboring chains were observed (Figure 1.3.3). No additional π-π or hydrogen bonding interactions were observed.

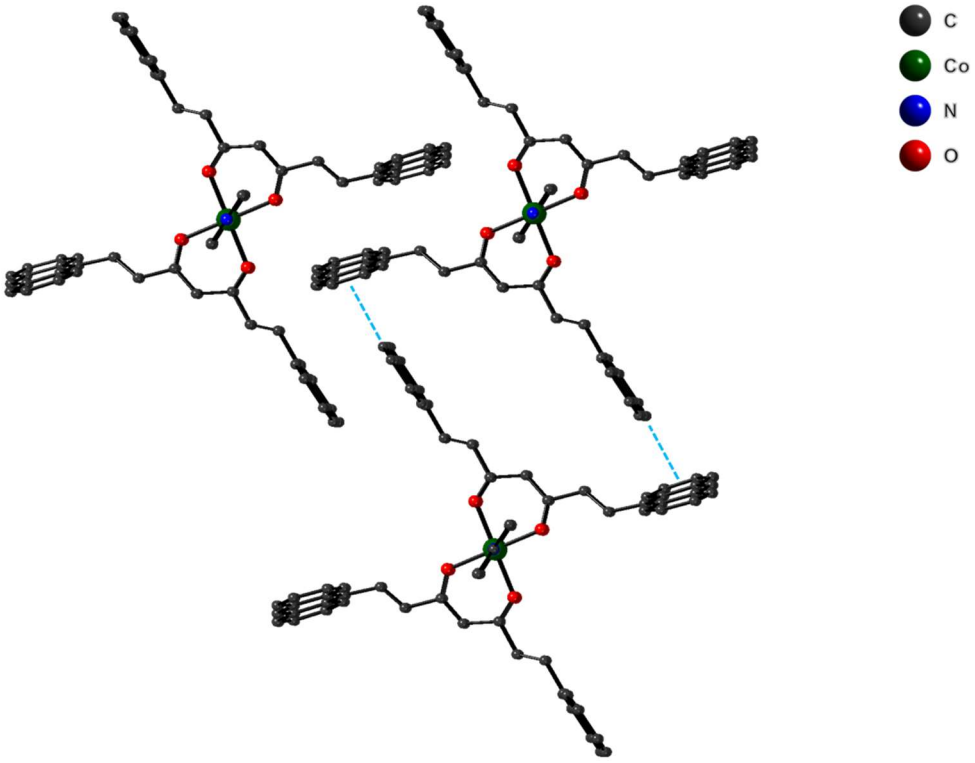

Figure 1.3.3: Representation of compound **12** emphasizing intermolecular interactions among different chains (light blue lines)

1.4.3.3 Characterization

As in the previous chapters, the characterizations were carried out in: (i) the solid state by means of a SQUID (Superconducting Quantum Interference Device) performing magnetic analyses of the

samples, (ii) in solution, by UV-Visible absorption and fluorescence experiments, and (iii) on surfaces with the assistance of AFM (Atomic Force Microscopy).

1.4.3.3.1.- Studies in solution

Nuclear Paramagnetic Resonance (^{1}H NMR)

Paramagnetic ^{1}H NMR studies of the two coordination polymers **12** and **13**, were performed in $CDCl_3$. As it was mentioned before, Co^{II} and Ni^{II} centers present slow nuclear relaxation;[123] taking into account the information amassed in previous chapters here such study was performed to analyze the stability of the chains in solution and the possible disposition of the 9Accm CCMoids in the structures.

$[Co(9Accm)_2(4,4'\text{-bpy})]_n$ (12)

Figure 1.3.4 shows the spectrum corresponding to compound **12**. As it happens with the mononuclear systems, the number of signals was reduced due to the symmetry (D_{4h}) and the free rotation of the anthracene groups. In the region between 70 to 20 ppm, a broad signal was observed at 61 ppm corresponding to the proton -CH- of the 9Accm. This shift is in agreement with the mononuclear system $[Co(9Accm)_2(py)_2]$, which show a similar shape and shift (63 ppm). This fact indicated that both systems presented the same distribution of the ligand (*trans*), as it was already confirmed by the analysis of the crystal structure. At higher fields, appeared a signal at 22 ppm corresponding to the *ortho* position of the 4,4'-bipyridine. In addition, two sharp peaks of pyridinic nature appeared at 10 and 9 ppm. These peaks may correspond to *meta* and *para* positions, although their assignment was not possible due to the presence of several nearby signals (from 8.7 to 7.5 ppm). To study the stability, additional spectra were performing after several hours where no modifications of their signals were observed, indicating that the system was stable under these conditions.

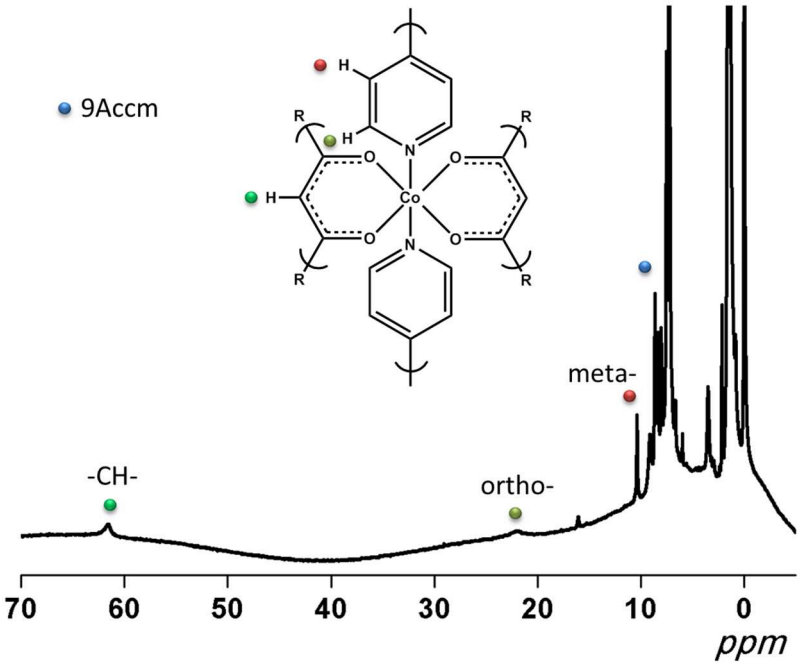

Figure 1.3.4: ^{1}H NMR spectrum of **12** in $CDCl_3$ between -5 to 70 ppm.

$[Ni(9Accm)_2(4,4'\text{-bpy})]_n$ (13)

Figure 1.3.5 shows the spectrum corresponding to compound **13** carried out under the same conditions as the one before. However, no paramagnetic signals were observed, with all the signals located at the diamagnetic region (between 10 and 0 ppm). This fact clearly indicated that the 1D system is not stable in such conditions.

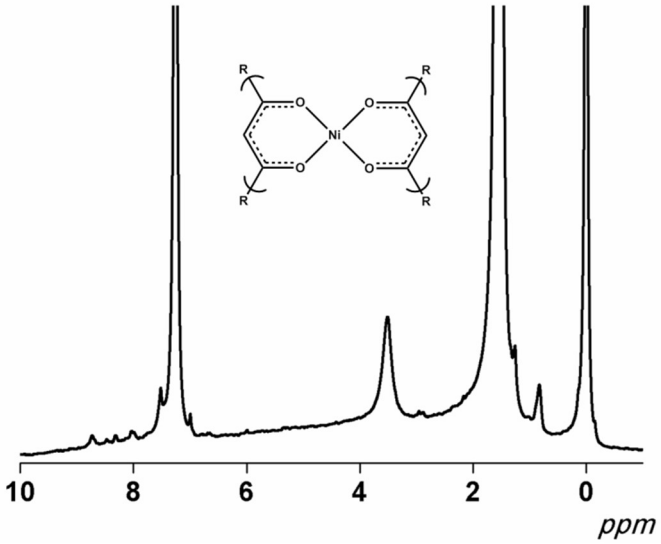

Figure 1.3.5: Paramagnetic ^1H NMR spectrum of **13** in $CDCl_3$.

A reasonable explanation for the signals observed between 0 and 10 ppm was the possibility of stabilizing $[Ni(9Accm)_2]$ unit, where Ni^{II} ions could adopt a square-planar geometry providing then a diamagnetic response. In order to corroborate this idea, additional NMR experiment was performed using C_5D_5N as a solvent. This solvent was chosen to analyze the possible coordination of the deuterated pyridine molecules to the new Ni units. Thus, the evolution of the system was carried out over time. Right after the sample was dissolved in C_5D_5N, the spectra began to exhibit paramagnetic signals (Figure 1.3.6). Two broad signals at 45 and -12 ppm were observed and several sharp signals in the range 9-7 ppm appeared as well. The shifts of these signals agree well with those observed for $[Ni(9Accm)_2(pyr)_2]$ in the previous chapter, corroborating thus, the pyridines coordination and the existence of square planar $Ni(9Accm)_2$ units in solution. As defined in the previous chapter, the signal located at 45 ppm corresponds to *-meta* position of the pyridine molecule, and the signal at -12 ppm (only present in the mononuclear Ni compounds that show a *cis* rearrangement of the ligand) maybe due to the existence of *cis*/*trans* equilibria. Even though the spectra remains constant over time, the detailed assignment of the signals is complicated because there may be different stable units with general formula: $[Ni(9Accm)_2(C_5D_5N)_n(H_2O)_m]$ (where n,m = 0, 1 or 2). The complete list of peaks for **12** and **13** is shown in Annex 1.22.

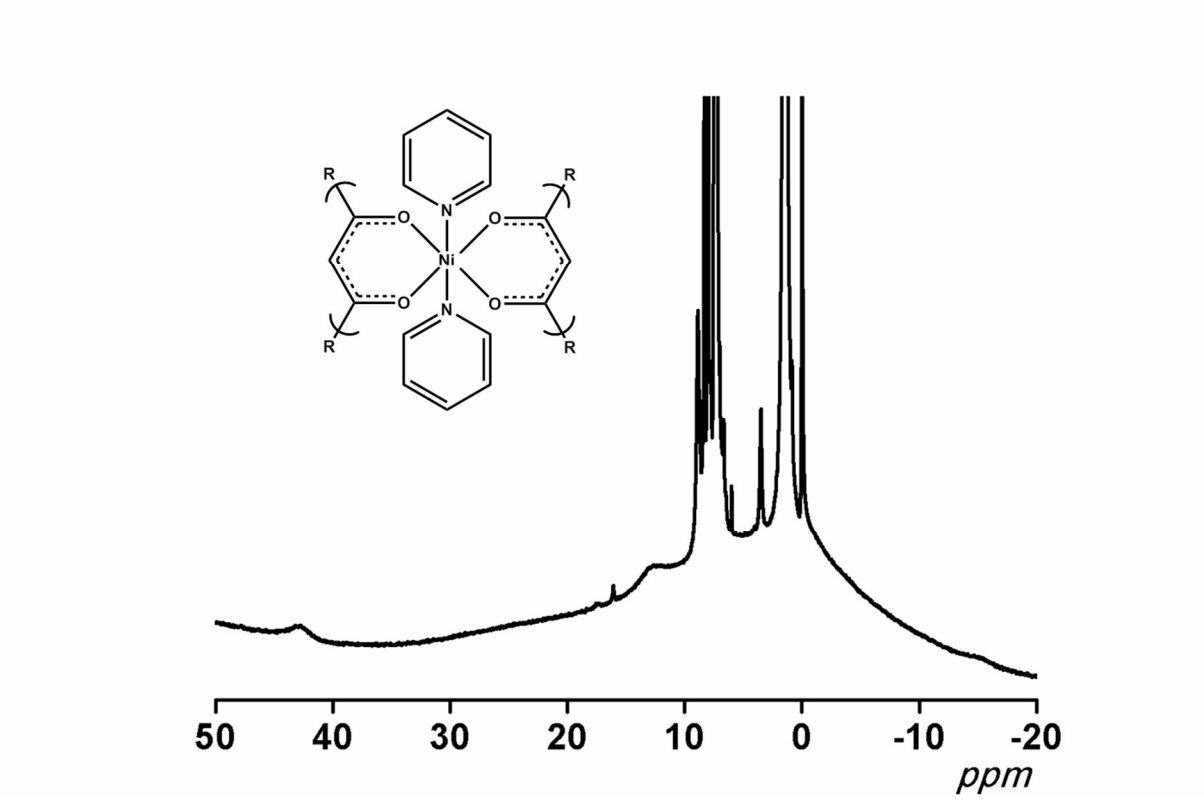

Figure 1.3.6: ^{1}H NMR spectrum of **13** in C_5D_5N between -20 to 50 ppm.

Therefore, the studies of both systems by paramagnetic ^{1}H NMR in solution gave rise to different behaviors. Compound **12** remained stable in solution since the spectra do not suffer modifications over time. In contrast, compound **13** had a tendency of dissociating in stable diamagnetic [Ni(9Accm)$_2$] units. These difference points out the stronger coordination of the Co^{II} centers to the neutral pyridinic units and the possibility of stabilizing Ni^{II} systems with a variety of coordination modes (with a number of geometries, from square planar to distorted O_h).

UV-Vis Absorption and Fluorescence studies

Further studies in solution, were performed exclusively with compound **12**, since compound **13** was not stable in solution.

The UV-Vis spectra of compound **12** was expect to present similar behavior as the Co^{II}-CCMoid mononuclear systems studied in chapter I. The spectra in CH_2Cl_2 (Figure 1.3.7, left) showed an intense band at 265 nm and two broad bands with similar intensity overlapped between 300-500 nm (Figure 1.3.7, inset).

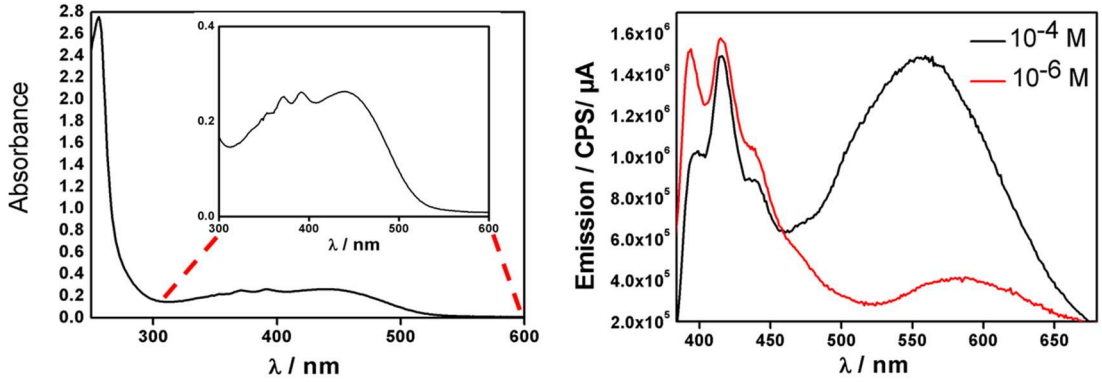

Figure 1.3.7: UV-Vis spectra of compound **12** (10^{-5} M) (left) and emission spectra of compound **12** at different concentration 10^{-4} M (black) and 10^{-6} M (red) in CH_2Cl_2.

Emission studies of **12** were performed at different concentrations (10^{-4} M, black) and (10^{-6} M, red) in CH_2Cl_2 when excited at 350 nm (Figure 1.3.7, right). The emission corresponding to the highest concentration show two different luminescence processes: (i) one signal appeared at high energies, centered at 405 nm, which split in into three signals with maxima between 390 and 450 nm. This signal corresponds to the anthracene groups exhibiting well-defined vibrionic bands. (ii) At low energies one wide signal between 500 and 650 nm with a maximum at 596 nm was observed corresponding to the formation of excimers.[103,104] This absorption band was not favored at low concentrations. In our case, as it was observed in the crystal structure, these intermolecular interactions could be given from the chain and the anthracene groups which interact though σ-π interactions and from the supramolecular interactions between anthracene groups and the 4,4'-bipyridine groups of the different chains.

Comparing the emission present in compound **12**, two different luminescence mechanisms were observed. In contrast, the emission corresponding to the free ligand 9Accm or mononuclear cobalt systems [$Co(9Accm)_2$] only shows one emission band corresponding to the excimer band. This fact may indicate that the chain of compound **12** difficult the interactions between the molecules and allows the emission corresponding to the anthracenes groups.

Finally, comparing with the free ligand 9Accm, the emission corresponding to the coordination polymer compounds decreases due to CHEQ effects, as it happens in previous mononuclear systems. (Figure 1.3.8).

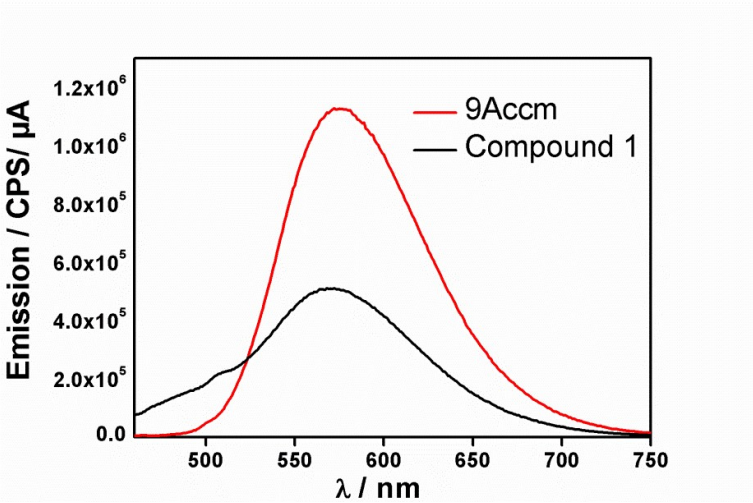

Figure 1.3.8: Comparison of the emission spectra of compound **12** (black) and 9Accm (red) in THF.

1.4.3.3.2 Studies in solid state

Magnetic studies

Compound **12** contains the $[Co(9Accm)_2]$ unit in a similar manner as compound **1** in chapter I, which exhibited the largest zfs value. Chapter II also shows a mononuclear compound of Ni^{II}, **7,** that presents the same distribution of the 9Accm ligand as here compound **13**. However, here, the $[M(9Accm)_2]$ units in **12** and **13**, are connected through 4,4'-bipyridine molecules.[124,125] Therefore, SQUID studies were performed with the aim of describing the effects of such a linker on the final magnetic behaviors.

Magnetic susceptibility and magnetization

$[Co(9Accm)_2(4,4'\text{-bpy})]_n$ (12)

The magnetic susceptibility of a powder sample of compound **12** was performed in a temperature range between 2 and 300 K, under a constant magnetic field of 0.03 T (from 2 to 30 K) and 0.5 T (from 30 to 300 K) (Figure 1.3.9). The $\chi_M T$ value at room temperature corresponded to 2.87 cm^3 mol^{-1} K. As in the mononuclear Co^{II}-CCMoids, this value was significantly higher than expected for a Co^{II} ion (1.875 cm^3 mol^{-1} K, g = 2.00) due to the spin-orbit coupling present in these metallic centers.[126] When the temperature decreased, the value decreased slightly to 2.63 cm^3 mol^{-1} K at 100 K. Below this temperature, a pronounced decrease of the values was observed that intensifies between 10

and 2 K, reaching a final value for the magnetic susceptibility of 1.23 cm^3 mol^{-1} K. Such decrease was due to the effect of zero field splitting, having more relevance at the lowest temperatures.

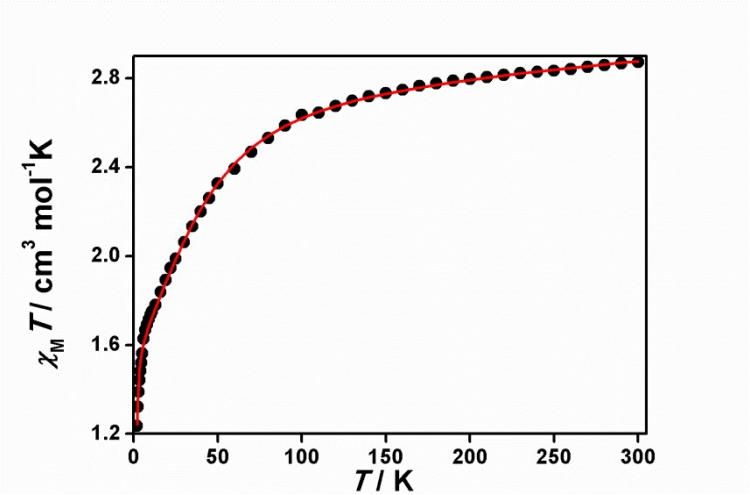

Figure 1.3.9: Representation of $\chi_M T$ vs T for compound **12.**

$M/N\mu_B$ vs H (Figure 1.3.10, right) measurements were performed at 2 K. The saturation of the magnetization appeared at a value close to 2 μ_B. This value is lower than the expected for S = 3/2 ($M/N\mu_B$ = 3.0 μ_B, g = 2.0), which indicated the existence of a significant orbital contribution, as before happened in the case of compound **1** (chapter I). In addition, measurements of M vs H/T were performed under external magnetic fields between 0.5-5 T at a variable temperature (1.8-6.8 K). As Figure 1.3.10 (left) shows, the curves at different magnetic field did not overlap, indicating the presence of anisotropy. As it happened in the mononuclear Co^{II}-systems, the different between the curves is small indicating a significant value of the magnetic anisotropy.

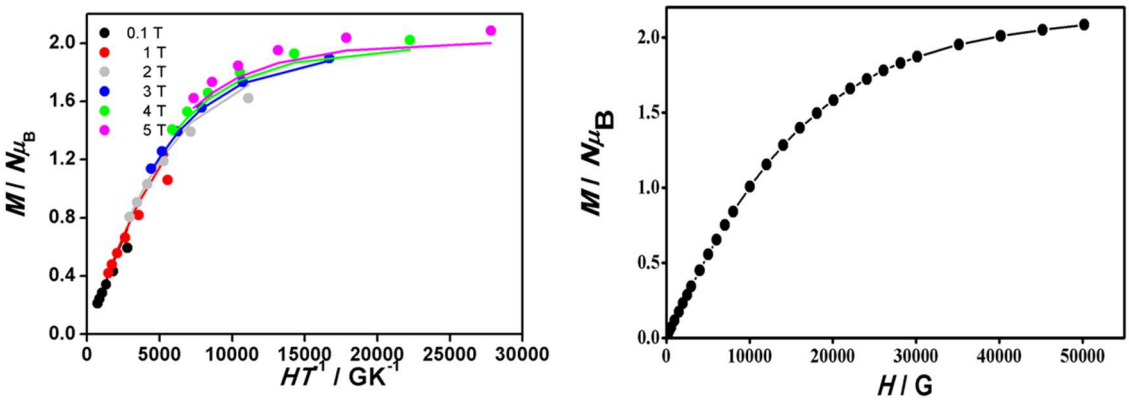

Figure 1.3.10: Representation of $M/N\mu_B$ vs H/T (left) and $M/N\mu_B$ vs H (right) for compound **12**. Experimental data are shown as dots and the resulting fitting as lines.

[Ni(9Accm)$_2$(4,4'-bpy)]$_n$ (13)

The magnetic measurements of the compound **13** were measured under the same conditions as in the previous case. The $\chi_M T$ value at room temperature corresponded to 1.28 cm^3 mol^{-1} K, being higher than expected for S = 1 (0.99 cm^3 mol^{-1} K, g = 2.00), due to the spin-orbit contribution of the metallic center. The $\chi_M T$ value decreased gradually to 1.09 cm^3 mol^{-1} K at 10 K. Below this temperature, a drastic decrease was observed reaching a value of 0.54 cm^3 mol^{-1} K at 2 K (Figure 1.3.11).

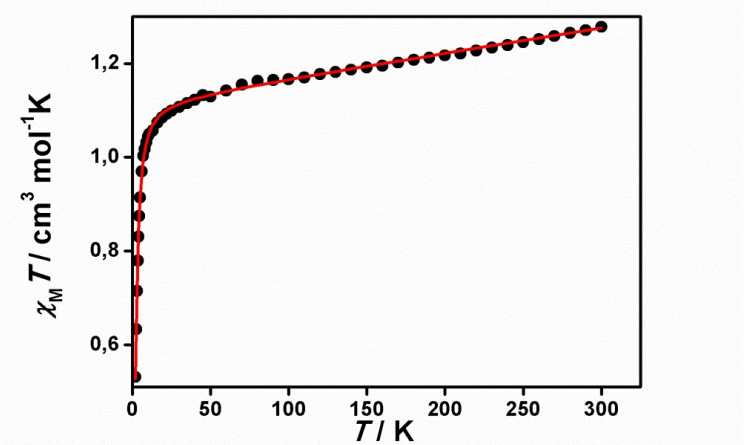

Figure 1.3.11: Representation of $\chi_M T$ vs T for compound **13**.

$M/N\mu_B$ vs H (Figure 1.3.12, right) measurements did not follow the ideal Brillouin curve expected for an S = 1 since the saturation was not reached even at the lowest temperatures. To reach saturation of the magnetization it would be necessary to apply higher fields and/or to proceed at even lower temperatures. This fact was indicative of small anisotropy values, as it was observed for the mononuclear related systems studied in chapter II.

Related to the M vs. H/T measurements (Figure 1.3.12, left), they show the presence of certain anisotropy since the curves at different magnetic field did not overlap, however the large different between them, corroborated again small anisotropy values.

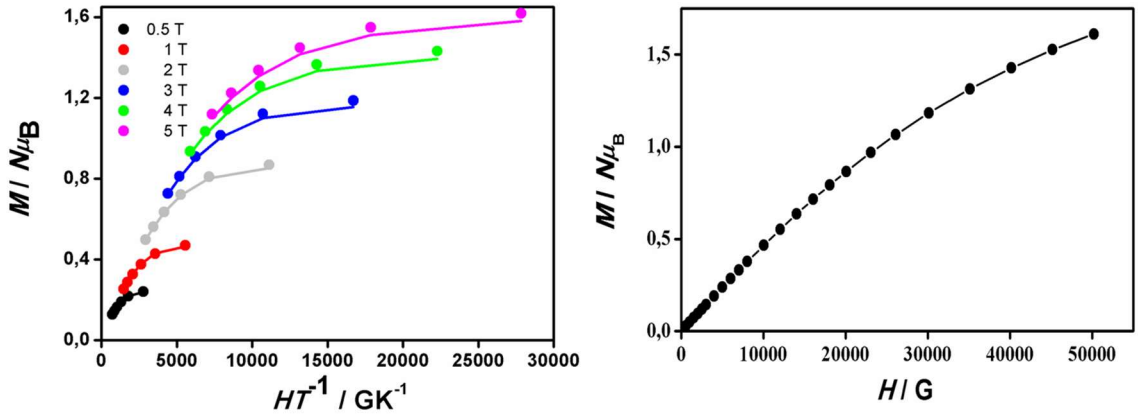

Figure 1.3.12: Representation of M/Nμ$_B$ vs H/T (left) and M/Nμ$_B$ vs H (right) for compound **13**. Experimental data are shown as dots and the resulting fitting as lines.

Fitting of the data

The magnetic measurements of compound **12** and **13** were fitted using the program PHI.[32] In a first approach, the fitting was carried out considering both systems as mononuclear systems, although their crystal structures show a 1D chain disposition. This was based on: (i) M/Nβ vs H and ln (χ_MT) vs 1/T measurements indicated significant spin-orbit contributions, which implied low Ising-like anisotropy. (ii) The data matched well with those found for the mononuclear family [M(9Accm)$_2$] mentioned in previous chapters, and (iii) the metals centers were connected through 4,4'-bipyridine molecules which provide weak/null antiferromagnetic interactions between metal centers.[124,125] The crystallographic data supported that idea where the two aromatic rings of the bipyridine moiety were twisted > 25 ° in both systems, **12** and **13**, thus hindering the magnetic coupling.

The fittings for both compounds were performed using the data of (M vs H/T) and (χ_MT vs T). Compound **12** showed values of g_{av}= 2.42, D= 44.3 cm^{-1}, E = 0.81 cm^{-1} and TIP = 546.10-6 cm^3 mol^{-1}. The high and positive value obtained for the parameter D agreed well with the values obtained for compound **1** in chapter I. In this case, D presented an intermediate value compared to previous mononuclear system (75 cm^{-1} for *trans* and 25 cm^{-1} for *cis*). This fact may indicate that the magnetic anisotropy could be affected by the small intramolecular interaction between the Co^{II} centers (through the 4,4'-bipyridine) and/or intermolecular interactions between the chains. Compound 13 show values of g_{av} = 2.12, D = 4.65 cm^{-1}, E = 0.71 cm^{-1}, TIP = 545.10-6 cm^3 mol^{-1} and ρ = 1.62 %. In this case, the parameter D values agreed with those obtained for the mononuclear systems as well.[127–130]

The comparison of the values obtained from both isostructural compounds show a higher value related to the parameter D corresponding to the compound **12** due to the presence of the Co^{II} metal center.[131]

Single Molecule Magnet behavior: AC measurements

Measurements of magnetic susceptibility were carried out by applying an alternating field in both compounds below 5 K in the presence and absence of an external dc magnetic field. However, only compound **12** exhibited ac magnetic susceptibility dependency with the frequency under the presence of an external field.

Therefore, a first measurement was performed applying different external magnetic fields, H_{DC} to find out the optimal (Annex 1.23). Once the optimal field was known (H_{DC} = 0.2 T), χ_{AC} measurements in phase (χ_{AC}') and out of phase (χ_{AC}'') were performed with a range of frequencies between 10-1488 Hz under a magnetic oscillating field H_{AC} = 0.0004 T at 2 K.

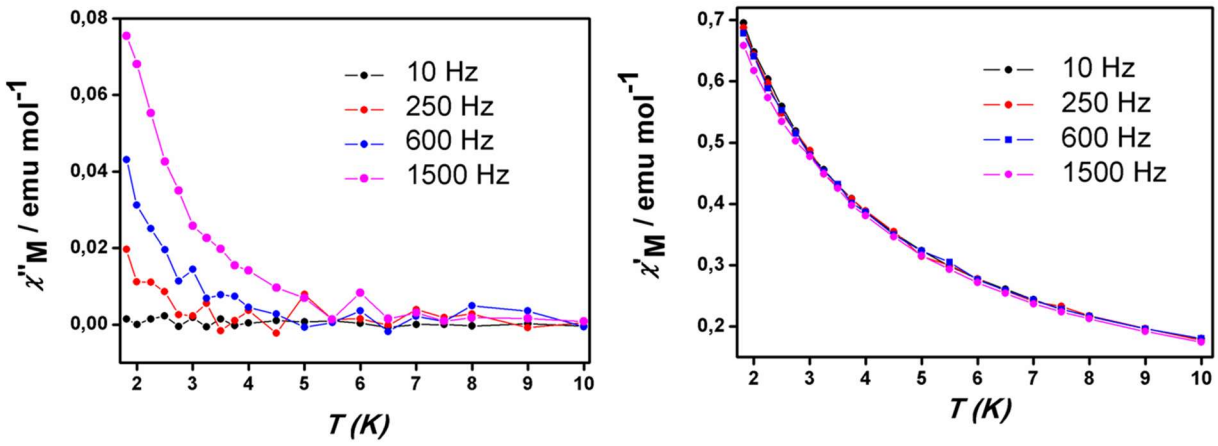

Figure 1.3.13: Frequency dependence of the χ_{AC}" vs T (left) and χ_{AC}' vs T (right) for compound **12** under 2000 Oe dc field.

As the Figure 1.3.13 shows, compound **12** exhibited slow relaxation of the magnetization presenting frequency dependence of the magnetic susceptibility in phase (χ_{AC}') and out of phase (χ_{AC}''). However, no maximum was observed above 2 K therefore was not possible to confirm the single magnet behavior (SMM). Further experiments should be carried out at low temperature/higher frequency or in solution (to isolate better the chains) to corroborate this behavior.

1.4.3.3.3 Studies on surfaces

Study of deposition on HOPG

AFM experiments were performed by depositing compound **12** on highly oriented pyrolytic graphite (HOPG). The main objective was to compare the structural differences obtained between the 1D chain compound **12** and the analogous mononuclear compound **1** $[Co(9Accm)_2(py)_2]$. Therefore, experiments were repeated under the same conditions as described in chapter I.

On the other hand, experiments at different concentration were also performed with the objective of analyzing the possibility of multilayers stacking on the substrate.

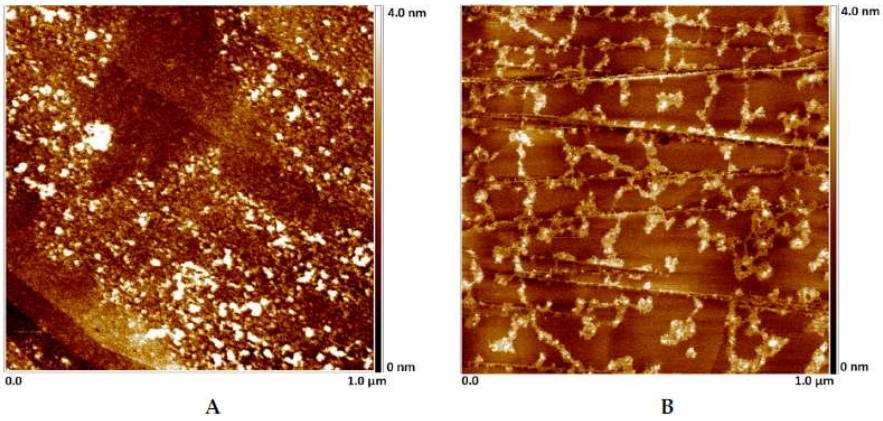

Figure 1.3.14: AFM images at different concentration of compound **12** in CH_2Cl_2: at 10^{-5} M (left) and 10^{-6} M (right).

As the Figure 1.3.14 shows, compound **12** exhibited a great affinity with the graphite surfaces probably due to the π-π stacking interactions between the anthracene groups and the substrate.[57,60] The experiment performed at high concentration (10^{-5} M, left) showed a surface completely covered. To analyze the number of layers and their heights, experiment by scratching the surface were carried out. (Annex 1.24). These experiments show an average height of 3.0 nm corresponding to a number of 2-3 units of **12** stacked on the substrate. The experiments were repeated at a lower concentration (10^{-6} M) and the images showed multiple aggregates with height around 1.4 and 2.0 nm corresponding to 1-2 stacked units of **12**. (Annex 1.24).

These measurements did not provide any specific information of the structure polymer present in the compound **12**. However, the obtained shape in the Figure 1.3.14 (B) differed in comparison to the AFM images obtained for the mononuclear compound (Figure 1.1.23). This may be due to a preferential disposition in the case of **12**, forced by the coordination of the different units of $[Co(9Accm)_2]$ through the 4,4'-bipyridine moieties.

1.4.4 Conclusions

In this chapter coordination polymer with formulae: $[Co(9Accm)_2(4,4'\text{-bpy})]_n$ **(12)** and $[Ni(9Accm)_2(4,4'\text{-bpy})]_n$ **(13)** have been synthesized. The synthesis of compound **13** was carried out using a microwave reactor meanwhile **12** was achieved using solvothermal methodology. In both cases 4,4'-bipyridine ligand was added. The nature and structural features of the latest gave rise to the arrangement in the form of 1D chains. The analysis of the crystal structures of **12** and **13** showed that they were isostructural, with two CCMoid ligands, 9Accm, arranged in a *trans* disposition. Both systems were characterized in solution by paramagnetic ^{1}H NMR. Regarding compound **12**, the shift of its signals were comparable to those expected for mononuclear $[Co(9Accm)_2]$ units arranged in *trans*-disposition as it was observed for compound **1** in chapter I. This, corroborated the *trans* arrangement of **12** in solution. In addition, stability studies showed that the compound was stable in $CDCl_3$ after time. Regarding compound **13**, its ^{1}H NMR spectrum showed purely diamagnetic nature. This fact was due the creation in solution of square planar systems with general formulae: $[Ni(9Accm)_2]$. To corroborate this fact, studies using deuterated pyridine as solvent (coordinating solvent), were performed, observing the appearance of paramagnetic signals. The shifts of these signals agreed well with the mononuclear $[Ni(9Accm)_2(pyr)_2]$ of chapter II, appearing some at high filed indicating the possible equilibrium between *cis*/*trans* conformations. UV-Vis studies in different solvents were carried out for compound **12**, obtaining a band around 300 nm, corresponding to the anthracene groups, and a second band at 440 nm common for all CCMoids. Fluorescence studies were also carried out, where experiments performed at different concentration evidenced the formation of excimers. Regarding the magnetic measurements, the fitting of the magnetic data of both systems were carried out considering the systems as independent mononuclear moieties, due to the low coupling existing between the metals through the 4,4'-bipyridine. This way, it was found a D = 44.3 cm^{-1} for the compound **12** and D = 4.65 for the compound **13**. In both systems, studies of the dynamics magnetization were carried out to analyze their possible SCM behavior. However, only compound **12** showed ac dependence of susceptibility at different frequency, although without maxima. Therefore, it can be confirmed that the system presents a slow relaxation of the magnetization, but future experiments have to be performed to analyze further the magnetic behavior. Finally, surface studies of compound **12** were carried out by AFM in order to compare with compound **1** from Chapter I. In this case, the images did not show a specific polymer structure, however a preferential disposition was observed.

1.5 Experimental part

CHAPTER I: Mononuclear Co^{II} SMMs: systems based on CCMoid ligands

(1) $[Co(9Accm)_2(py)_2]$

(2) $[Co(9Accm)_2(2,2'\text{-bpy})]$

(3) $[Co(9Accm)_2(3,5\text{-}(CH_3)_2\text{-py})_2$

(4) $[Co(9Accm)_2(dmf)_2]$

(5) $[Co(9Accm)_2(4,4'\text{-}(CH_3)_2\text{-}2,2'\text{-bpy})_2]$

(6) $[Co(9Accm)_2(5,5'\text{-}(CH_3)_2\text{-}2,2'\text{-bpy})_2]$

CHAPTER II: Mononuclear Ni^{II} compounds: systems based on CCMoid ligands

(7) $[Ni(9Accm)_2(py)_2]$

(8) $[Ni(9Accm)_2(2,2'\text{-bpy})]$

(9) $[Ni(9Accm)_2(3\text{-picoline})_2]$

(10) $[Ni(9Accm)_2(phen)]$

(11) $[Ni(9Accm)_2(5,5'\text{-dimethyl-}2,2'\text{-bpy})]$

CHAPTER III: Coordination polymers based on Co^{II}/Ni^{II}-9Accm units.

(12) $[Co(9Accm)_2(4,4'\text{-bpy})]_n$

(13) $[Ni(9Accm)_2(4,4'\text{-bpy})]_n$

CHAPTER I: Mononuclear Co^{II} SMMs: systems based on CCMoid ligands

Materials: All the reagents used in the work were used as they were received from the commercial company, without further purification.

Synthesis of $[Co(9Accm)_2(py)_2]$ (1)

In a microwave tube cobalt (II) acetate (0.026 g, 0.146 mmol), 9Accm (0.1g, 0.210 mmol) and pyridine (5 mL) were added. The mixture was heated by microwave radiation with permanent stirring; the parameters used limited the temperature to 140 °C meanwhile microwave energy of 15 W for 2 minutes was applied. The solution was heated up quickly and the system reached equilibrium when the maximum energy was applied at a constant temperature of 140 °C. After 2 minutes, the sample was cooled down to room temperature. The solution in the tube was stirred uncovered for a few more hours. Finally, an orange precipitate appeared **1**. The solid was filtered and washed with H_2O and Et_2O respectively to remove impurities and to dry. The total yield of the reaction was 83 %. The obtaining of crystal was possible through layers in pyridine and Et_2O.

KBr pellet IR (v/cm^{-1}): 3428b, 1632m, 1554s, 1504vs, 1441vs, 1349m, 1162s, 970m, 887m, 734vs, 444m. Elemental analysis calculated for $[Co(9Accm)_2(py)_2.0{,}5py]$ ($CoC_{82,5}O_4H_{58,5}N_{2,5}$): C, 82.02; H, 4.88; N, 2.9; and found: C, 81.91; H, 4.85; N, 3.00. MALDI$^+$ (DHB): m/z 1010.2 ($[Co(9Accm)_2]^+$)

Synthesis of $[Co(9Accm)_2(2,2'\text{-bpy})]$ (2)

The synthesis of compound **2** was carried out following the previous procedure, but using 2,2'-bpy (0.016 g, 0.142 mmol) instead of pyridine and DMF (5 mL) as the reaction solvent. Once the microwave reaction was complete, a precipitate appeared which was filtered and washed with H_2O and Et_2O; the final orange solid was characterized as $[Co(9Accm)_2(2,2'\text{-bpy})]$ **(2)**. The total yield of the reaction was 79%. The crystals were obtained by layering a solution of the sample in $CHCl_3$ with Et_2O.

KBr pellet IR (v/cm-1): 3439b, 1671m, 1630m, 1555s, 1506vs, 1442vs, 1348m, 1151s, 985m, 880m, 735vs, 443m. Elemental analysis calculated for $[Co(9Accm)_2(2,2'\text{-bpy})].0{,}3DMF$ ($CoC_{80,9}N_{2,3}O_{4,3}H_{56,1}$): C, 81.78; H, 4.76; N, 2.71; and found: C, 81.91; H, 4.85; N 3.00. MALDI$^+$ (DHB): m/z 690.1 ($[Co(9Accm)(2,2'\text{-bpy})]^+$), 1032.3 ($[Co(9Accm)_2]Na^+$).

Synthesis of $[Co(9Accm)_2(3,5\text{-}(CH_3)_2\text{-}py)_2$ (3)

The synthesis of compound **3** was carried out following the procedure of compound **1** but using in this case 3,5-$(CH_3)_2$-py)$_2$. The total yield of the reaction was 89%. No monocrystalline sample could be obtained.

KBr pellet IR (v/cm-1): 3419b, 3046b, 3021b, 3006b, 2920b, 1640m, 1566s, 1499vs, 1452m, 1408vs, 1348m, 1264s, 1161m, 968m, 881m, 790m, 736vs, 703m, 605m, 538m, 446m. Elemental analysis calculated for [Co(9Accm)2(3,5-$(CH_3)_2$-py)$_2$].0,3(3,5-$(CH_3)_2$-py).0,3H_2O ($C_{86,1}H_{67,3}CoN_{2,3}O_{4,3}$): C, 81.91; H, 5.80; N, 2.55; and found: C, 81.57; H, 5.48; N 2.63. MALDI$^+$ (m/z): 1010.3 ([Co(9Accm)$_2$]$^+$) and 1032.3 ([Co(9Accm)$_2$ + Na]$^+$).

Synthesis of [Co(9Accm)$_2$(dmf)$_2$] (4)

The synthesis of compound **4** was carried out following the procedure of compound **1**, but using in this case N,N-dimethylformamide (DMF). The total yield of the reaction was 93 %. No monocrystalline sample could be obtained.

KBr pellet IR (v/cm-1): 3426b, 3043b, 3021b, 2925b, 1652b, 1561m, 1504m, 1442m, 1405vs, 1378m, 1348m, 1262s, 1156m, 1096m, 970m, 881m, 844m, 792m, 733m, 671m, 602m, 538m, 444m. Elemental analysis calculated for [Co(9Accm)$_2$(dmf)$_2$].1DMF.0.5H2O ($C_{79}H_{68}CoN_3O_{7,5}$): C, 76.62; H, 5.53; N, 3.39 and found: C, 76.21; H, 5.38; N, 2.99. MALDI$^+$ (m/z): 1010.3 ([Co(9Accm)$_2$]$^+$) and 1032.3 ([Co(9Accm)$_2$ + Na]$^+$).

Synthesis of [Co(9Accm)$_2$(4,4'-$(CH_3)_2$-2,2'-bpy)$_2$] (5)

The synthesis of compound **5** was carried out following the procedure of compound **2**, but using in this case (4,4'-$(CH_3)_2$-2,2'-bpy)$_2$. The total yield of the reaction is 97 %. No monocrystalline sample could be obtained.

KBr pellet IR (v/cm-1): 3419b, 3048b, 3021b, 2915b, 1672b, 1615b, 1558m, 1506m, 1437m, 1408vs, 1348m, 1296s, 1168m, 1084m, 1044m, 968m, 874m, 842m, 736m, 622m, 602m, 528m. Elemental analysis calculated for [Co(9Accm)$_2$(4,4'-$(CH_3)_2$-2,2'-bpy)$_2$]0.4 (4,4'-$(CH_3)_2$-2,2'-bpy) ($C_{73,3}H_{60,8}CoN_{2,4}O_{4,4}$): C, 79,68; H, 5,55; N, 3,05, and found: C, 79.48; H, 5.25; N, 3.34. MALDI$^+$: 718.2 ([Co(9Accm)(4,4'-$(CH_3)_2$-2,2'-bpy)]$^+$) and 1032.3 ([Co(9Accm)$_2$+ Na]$^+$).

Synthesis of [Co(9Accm)$_2$(5,5'-$(CH_3)_2$-2,2'-bpy)$_2$] (6)

The synthesis of compound **6** was carried out following the procedure described for compound **2**, but using in this case (5,5'-$(CH_3)_2$-2,2'-bpy)$_2$. The total yield of the reaction was 86 %. No monocrystalline sample could be obtained.

KBr pellet IR IR (v/cm-1): 3426b, 3046b, 3024b, 2922b, 1672b, 1630b, 1558m, 1506m, 1437m, 1346m, 1161m, 985m, 968m, 879m, 847m, 782m, 736m, 605m, 538m. Elemental analysis calculated for $[Co(9Accm)_2(5,5'\text{-}(CH_3)_2\text{-}2,2'\text{-bpy})_2]$ ($C_{72}H_{58}CoN_2O_4$): C, 80.51; H, 5.44; N, 2.55, and found: C, 80.60; H, 5.04; N, 2.55. MALDI$^+$: 718.2 ($[Co(9Accm)(5,5'\text{-}(CH_3)_2\text{-}2,2'\text{-bpy})]^+$) and 1032.3 ($[Co(9Accm)_2+ Na]^+$).

CHAPTER II: Mononuclear Ni^{II} compounds: systems based on CCMoid ligands

Synthesis of $[Ni(9Accm)_2(py)_2]$ (7)

Nickel (II) acetate (0.026 g, 0.104 mmol), 9Accm (0.1 g, 0.210 mmol) and pyridine (5 mL) were added in a microwave tube. The mixture was heated by microwave radiation with permanent stirring at 140 °C for 2 minutes. After this, the sample was cooled down to room temperature. The solution was stirred uncovered for few more hours. Finally, a yellow precipitate was obtained. The solid was filtered and washed with H_2O and Et_2O respectively to remove impurities and to dry. The total yield of the reaction was 63 %. Crystals were obtained by layering a solution of the sample in CH_2Cl_2 with Et_2O.

KBr pellet IR (v/cm^{-1}): 3424b, 3046w, 2920w, 2846w, 1620m, 1555s, 1506s, 1450s, 1348m, 1259m, 1212m, 1163m, 990m, 973m, 889m, 844m, 753m, 731s, 694m, 624w, 540w, 451w. Elemental analysis calculated for $C_{80}H_{56}NiN_2O_4\cdot 0.5H_2O$ (1175,36 g·mol^{-1}): C 81.67; H 4.88; N 2.38 and found: C 81.62; H 4.78; N 2.32. MALDI$^+$ (DHB) (m/z): 533.0 ($[Ni_2(9Accm)_2]^{2+}$; 1009.3 ($[Ni(9Accm)_2]^+$; 1031.3 ($[Ni(9Accm)_2Na^+]$).

Synthesis of $[Ni(9Accm)_2(2,2'\text{-bpy})]$ (8)

The synthesis of compound **8** was carried out following previous procedure, but using nickel(II) acetate (0.026 g, 0.104 mmol), 9Accm (0.1 g, 0.210 mmol) and 2,2'-bipyridine (0.016 g, 0.102 mmol) in 5 mL of DMF. The total yield of the reaction was 76 %. The crystals were obtained by layering a solution of the sample in CH_2Cl_2 with Et_2O.

KBr pellet IR (v/cm^{-1}): 3426b, 3043w, 3019w, 2927w, 2848w, 1670s, 1630m, 1561s, 1546vs, 1435vs, 1346m, 1306m, 1151m, 970m, 889m, 763m, 731vs, 665w, 602w, 540w, 449w. Elemental analysis calculated for: $C_{80}H_{54}NiN_2O_4\cdot 2.1H_2O\cdot 0.5C_{10}H_8N_2$ (1280.40 g·mol^{-1}): C 79.66; H 4.91; N 3.28 and found: C 79.59; H 4.93; N 3.29. MALDI$^+$ (m/z): 689.2 ($[Ni(9Accm)(2,2'\text{-bpy})]^+$.

Synthesis of [Ni(9Accm)$_2$(3-picoline)$_2$] (9)

The synthesis of compound **9** was carried out following previous procedure described for **8**, but using nickel(II) acetate (0.026 g, 0.104 mmol), 9Accm (0.1 g, 0.210 mmol) and 5 mL of 3-picoline. The total yield of the reaction was 82 %. Crystals were obtained by layering a solution of the sample in CH_2Cl_2 with Et_2O.

KBr pellet IR (v/cm^{-1}): 3414b, 3043w, 3014w, 2917w, 1637m, 1568s, 1501s, 1450vs, 1403m, 1259m, 1343w, 1163m, 970m, 884m, 844m, 790m, 736s, 701m, 620w, 533w, 442w. Elemental analysis calculated for $C_{82}H_{60}NiN_2O_4 \cdot 0.9H_2O$ (1210.60 g·mol^{-1}): C 81.24; H 5.14; N 2.31 and found: C 81.15; H 4.99; N 2.41. MALDI$^+$ (m/z): 1031.3 ([Ni(9Accm)$_2$Na$^+$]).

Synthesis of [Ni(9Accm)$_2$(phen)] (10)

The synthesis of compound **10** was carried out following the procedure described for **8**, but using nickel(II) acetate (0.026 g, 0.104 mmol), 9Accm (0.1 g, 0.210 mmol) and 1,10-phenantroline (0.019 g, 0.102 mmol) in 5 mL of DMF. The total yield of the reaction was 84 %. No monocrystalline sample could be obtained.

KBr pellet IR (v/cm^{-1}): 3434b, 3048w, 3021w, 2944w, 2920w, 2856w, 1672s, 1630m, 1563vs, 1509vs, 1442vs, 1410s, 1348m, 1257w, 1153m, 1109w, 988m, 889w, 844m, 733s, 613w, 548w, 444w. Elemental analysis calculated for: $C_{82}H_{34}N_2NiO_4 \cdot 1.5H_2O \cdot 1.1C_3H_7NO$ (1277.23 g·mol−1): C 80.21, H 3.53, N 3.4 and found: C 81.3; H 4.63; N 2.33. MALDI$^+$ (m/z): 713.1 ([Ni(9Accm)(phen)]$^+$.

Synthesis of [Ni(9Accm)$_2$(5,5'-dimethyl-2,2'-bpy)] (11)

The synthesis of compound **11** was carried out following the procedure described for **8**, but using nickel(II) acetate (0.026 g, 0.104 mmol), 9Accm (0.1 g, 0.210 mmol) and 5,5'-dimethyl-2,2'-dipyridyl (0.019 g, 0.102 mmol) in 5 mL of DMF. The total yield of the reaction was 79 %. No monocrystalline sample could be obtained.

KBr pellet IR (v/cm^{-1}): 3426b, 3046w, 3028w, 2920w, 2860w, 1630m, 1558vs, 1506vs, 1442vs, 1348m, 1306w, 1264w, 1153m, 1044w, 973m, 881m, 844m, 733vs, 618w, 543w, 449w. Elemental analysis calculated for: $C_{82}H_{60}N_2NiO_4 \cdot 0.1H_2O$ (1196.19 g·mol−1): C 82.2; H 5.07; N 2.34 and found: C 82.1; H 4.88; N 2.19. MALDI$^+$ (m/z): 717.21 ([Ni(9Accm)(5,5'-dimethyl-2,2'-dipyridyl)]$^+$.

CHAPTER III: Coordination polymers based on Co^{II}/Ni^{II}-9Accm units.

Synthesis of $[Co(9Accm)_2(4,4'\text{-bpy})]_n$ (12)

The synthesis of system **12** was carried out adding $[Co(O_2CMe)_2 \cdot 4H_2O]$ (0.026 g, 0.104 mmol), 9Accm (0.1 g, 0.210 mmol) and 4,4'-bipyridine (0.016 g, 0.104 mmol) in DMF (5 mL) in a solvothermal vial. The mixture was kept in the oven at 143 ˚C for 2 days without stirring. Crystals were obtained directly from the vial. The total yield of the reaction was 88 %.

KBr pellet IR (v/cm^{-1}): 3394b, 3046w, 2922w, 2853w, 1630m, 1603m, 1548s, 1506s, 1440s, 1405s, 1348m, 1217m, 1158m, 975m, 889m, 842m, 807m, 733vs, 622m, 538w, 446w. Elemental analysis calculated for $C_{83}H_{57}CoN_2O_5 \cdot 0.3C_3H_7NO \cdot 1.3\ H_2O$ (1265.65 g·mol^{-1}): C 79.56; H 4.91; N 2.54 and found: C 79.48; H 4.86; 2.52. MALDI$^-$ (m/z): 1009.3 ($[Co(9Accm)_2]^-$).

Synthesis of $[Ni(9Accm)_2(4,4'\text{-bpy})]_n$ (13)

The synthesis of system **13** was performed following the amounts described for **12**, but using a microwave reactor (MW) instead of solvothermal methodology and a Ni source. The mixture was heated at 140 °C for 2 min. Crystals were obtained directly from the microwave tube. The total yield of the reaction was 78 %.

KBr pellet IR (v/cm^{-1}): 3426br, 3043w, 2964w, 2920w, 2843w, 1677w, 1625m, 1548s, 1504vs, 1447vs, 1410s, 1348m, 1212s, 1158m, 1109w, 968m, 879w, 839w, 812w, 726s, 617w, 543w, 449w. Elemental analysis calculated for $C_{80}H_{54}NiN_2O_4 \cdot 0.9H_2O$ (1182.56 g·mol^{-1}): C 81.17; H 4.76; N 2.36 and found: C 81.18; H 4.61; N 2.40. MALDI$^+$ (m/z): 533.0 ($[Ni_2(9Accm)_2]^{2+}$; 1031.3 ($[Ni(9Accm)_2Na^+]$).

1.6 References

[1] M. Verdaguer, V. Robert, in *Compr. Inorg. Chem. II*, Elsevier, **2013**, pp. 131–189.

[2] J. M. Clemente-Juan, E. Coronado, A. Gaita-Ariño, *Chem. Soc. Rev.* **2012**, *41*, 7464.

[3] E. Burzurí, R. Gaudenzi, H. S. J. van der Zant, *J. Phys. Condens. Matter* **2015**, *27*, 113202.

[4] W. Wernsdorfer, *Int. J. Nanotechnol.* **2010**, *7*, 497.

[5] M. Murrie, D. J. Price, *Annu. Reports Sect. "A" (Inorganic Chem.* **2007**, *103*, 20.

[6] D. Gatteschi, R. Sessoli, J. Villain, *Molecular Nanomagnets*, Oxford University Press, **2006**.

[7] D. Gatteschi, L. Bogani, A. Cornia, M. Mannini, L. Sorace, R. Sessoli, *Solid State Sci.* **2008**, *10*, 1701–1709.

[8] H. Hiraga, H. Miyasaka, K. Nakata, T. Kajiwara, S. Takaishi, Y. Oshima, H. Nojiri, M. Yamashita, *Inorg. Chem.* **2007**, *46*, 9661–9671.

[9] F. Pointillart, J. Jung, R. Berraud-Pache, B. Le Guennic, V. Dorcet, S. Golhen, O. Cador, O. Maury, Y. Guyot, S. Decurtins, et al., *Inorg. Chem.* **2015**, *54*, 5384–5397.

[10] F. Pointillart, B. le Guennic, O. Cador, O. Maury, L. Ouahab, *Acc. Chem. Res.* **2015**, *48*, 2834–2842.

[11] G. Kumar, R. Gupta, *Chem. Soc. Rev.* **2013**, *42*, 9403.

[12] J. Narayan, *Int. J. Nanotechnol.* **2012**, *9*, 914.

[13] S. J. van der Molen, J. Liao, T. Kudernac, J. S. Agustsson, L. Bernard, M. Calame, B. J. van Wees, B. L. Feringa, C. Schönenberger, *Nano Lett.* **2009**, *9*, 76–80.

[14] D. Mijatovic, J. C. T. Eijkel, A. van den Berg, *Lab Chip* **2005**, *5*, 492.

[15] W. Lu, C. M. Lieber, *Nat. Mater.* **2007**, *6*, 841–850.

[16] R. Sessoli, D. Gatteschi, A. Caneschi, M. A. Novak, *Nature* **1993**, *365*, 141–143.

[17] L. Bogani, W. Wernsdorfer, *Nat. Mater.* **2008**, *7*, 179–186.

[18] C. A. P. Goodwin, F. Ortu, D. Reta, N. F. Chilton, D. P. Mills, *Nature* **2017**, *548*, 439–442.

[19] F. S. Guo, B. M. Day, Y. C. Chen, M. L. Tong, A. Mansikkamäki, R. A. Layfield, *Angew. Chemie - Int. Ed.* **2017**, *56*, 11445–11449.

[20] D. Gatteschi, R. Sessoli, *Angew. Chemie-International Ed.* **2003**, *42*, 268–297.

[21] C. J. Milios, A. Vinslava, W. Wernsdorfer, S. Moggach, S. Parsons, S. P. Perlepes, G. Christou, E. K. Brechin, *J. Am. Chem. Soc.* **2007**, *129*, 2754–2755.

[22] A. J. Tasiopoulos, A. Vinslava, W. Wernsdorfer, K. A. Abboud, G. Christou, *Angew. Chemie - Int. Ed.* **2004**, *43*, 2117–2121.

[23] F. Neese, D. A. Pantazis, *Faraday Discuss.* **2011**, *148*, 229–238.

[24] N. Ishikawa, M. Sugita, T. Ishikawa, S. Y. Koshihara, Y. Kaizu, *J. Am. Chem. Soc.* **2003**, *125*, 8694–8695.

[25] D. E. Freedman, W. H. Harman, T. D. Harris, G. J. Long, C. J. Chang, J. R. Long, *J. Am. Chem. Soc.* **2010**, *132*, 1224–1225.

[26] G. A. Craig, M. Murrie, *Chem. Soc. Rev.* **2015**, *44*, 2135–2147.

[27] J. M. Frost, K. L. M. Harriman, M. Murugesu, *Chem. Sci.* **2016**, *7*, 2470–2491.

[28] R. Boča, *Coord. Chem. Rev.* **2004**, *248*, 757–815.

[29] A. A. B. Bleaney, *Electron Paramagnetic Resonance of Transition Ions*, Oxford, England: Oxford University Press, **1970**.

[30] I. B. Bersuker, *The Jahn-Teller Effect and Vibronic Interactions in Modern Chemistry*, Springer US, Boston, MA, **1984**.

[31] J. R. Gispert, *Coordination Chemistry*, Wiley-VCH Verlag GmbH & Co. KGaA, Weinheim, **2008**.

[32] N. F. Chilton, R. P. Anderson, L. D. Turner, A. Soncini, K. S. Murray, *J. Comput. Chem.* **2013**, *34*, 1164–1175.

[33] S. Gomez-Coca, E. Cremades, N. Aliaga-Alcalde, E. Ruiz, *J. Am. Chem. Soc.* **2013**, *135*, 7010–7018.

[34] J. Cirera, E. Ruiz, S. Alvarez, F. Neese, J. Kortus, *Chem. - A Eur. J.* **2009**, *15*, 4078–4087.

[35] S. Gómez-Coca, D. Aravena, R. Morales, E. Ruiz, *Coord. Chem. Rev.* **2015**, *289–290*, 379–392.

[36] F. Neese, E. I. Solomon, *In Magnetism to Materials*, **2003**.

[37] N. E. Chakov, M. Soler, W. Wernsdorfer, K. A. Abboud, G. Christou, *Inorg. Chem.* **2005**, *44*, 5304–5321.

[38] S. T. Bishay, *Egypt. J. Sol.* **2000**, *23*, 179–188.

[39] K. S. Cole, R. H. Cole, *J. Chem. Phys.* **1941**, *9*, 341–351.

[40] J. G. Powles, D. M. Heyes, G. Rickayzen, W. A. B. Evans, *J. Chem. Phys.* **2009**, *131*, 214509.

[41] M. L. Perrin, C. A. Martin, F. Prins, A. J. Shaikh, R. Eelkema, J. H. van Esch, J. M. van Ruitenbeek, H. S. J. van der Zant, D. Dulić, *Beilstein J. Nanotechnol.* **2011**, *2*, 714–719.

[42] F. Prins, M. Monrabal-Capilla, E. A. Osorio, E. Coronado, H. S. J. Van Der Zant, *Adv. Mater.* **2011**, *23*, 1545–1549.

[43] W. Sucksmith, J. E. Thompson, *Proc. R. Soc. A Math. Phys. Eng. Sci.* **1954**, *225*, 362–375.

[44] T. Jurca, A. Farghal, P. H. Lin, I. Korobkov, M. Murugesu, D. S. Richeson, *J. Am. Chem. Soc.* **2011**, *133*, 15814–15817.

[45] J. M. Zadrozny, J. R. Long, *J. Am. Chem. Soc.* **2011**, *133*, 20732–20734.

[46] J. M. Zadrozny, J. Liu, N. A. Piro, C. J. Chang, S. Hill, J. R. Long, *Chem. Commun.* **2012**, *48*, 3927.

[47] J. Vallejo, I. Castro, R. Ruiz-García, J. Cano, M. Julve, F. Lloret, G. De Munno, W. Wernsdorfer, E. Pardo, *J. Am. Chem. Soc.* **2012**, *134*, 15704–15707.

[48] X. N. Yao, J. Z. Du, Y. Q. Zhang, X. B. Leng, M. W. Yang, S. Da Jiang, Z. X. Wang, Z. W. Ouyang, L. Deng, B. W. Wang, et al., *J. Am. Chem. Soc.* **2017**, *139*, 373–380.

[49] C. J. Milios, A. Vinslava, A. G. Whittaker, S. Parsons, W. Wernsdorfer, G. Christou, S. P. Perlepes, E. K. Brechin, *Inorg. Chem.* **2006**, *45*, 5272–5274.

[50] N. R. Champness, *Dalt. Trans.* **2011**, *40*, 10311.

[51] K. Nakamoto, *Infrared and Raman Spectra of Inorganic and Coordination Compounds*, New York (N.Y.): Wiley, **1997**.

[52] E. C. Constable, C. E. Housecroft, T. Kulke, C. Lazzarini, E. R. Schofield, Y. Zimmermann, *J. Chem. Soc. Dalt. Trans.* **2001**, 2864–2871.

[53] T. B. Faust, P. G. Heath, C. A. Muryn, G. A. Timco, R. E. Winpenny, *Chem. Commun.* **2010**, *46*, 6258–6260.

[54] G. Aromi, A. S. Batsanov, P. Christian, M. Helliwell, O. Roubeau, G. A. Timco, R. E. P. Winpenny, *Dalt. Trans.* **2003**, 4466–4471.

[55] R. C. Elder, *Inorg. Chem.* **1968**, *7*, 1117–1123.

[56] E. Carolina Sañudo, T. B. Faust, C. A. Muryn, R. G. Pritchard, G. A. Timco, R. E. P. Winpenny, *Inorg. Chem.* **2009**, *48*, 9811–9818.

[57] M. Menelaou, F. Ouharrou, L. Rodríguez, O. Roubeau, S. J. Teat, N. Aliaga-Alcalde, *Chem. - A Eur. J.* **2012**, *18*, 11545–11549.

[58] N. Aliaga-Alcalde, P. Marqués-Gallego, M. Kraaijkamp, C. Herranz-Lancho, H. Den Dulk, H. Görner, O. Roubeau, S. J. Teat, T. Weyhermüller, J. Reedijk, *Inorg. Chem.* **2010**, *49*, 9655–9663.

[59] N. Aliaga-Alcalde, L. Rodríguez, *Inorganica Chim. Acta* **2012**, *380*, 187–193.

[60] N. Aliaga-Alcalde, L. Rodríguez, M. Ferbinteanu, P. Höfer, T. Weyhermüller, *Inorg. Chem.* **2012**, *51*, 864–873.

[61] N. Bloembergen, E. M. Purcell, R. V. Pound, *Phys. Rev.* **1948**, *73*, 679.

[62] J. A. Happe, R. L. Ward, *J. Chem. Phys.* **1963**, *39*, 1211–1218.

[63] W.-J. Wang, H.-H. Wei, *J. Chinese Chem. Soc.* **1978**, *25*, 185–194.

[64] K. Dimitrou, J. S. Sun, K. Folting, G. Christou, *Inorg. Chem.* **1995**, *34*, 4160–4166.

[65] J. A. Happe, R. L. Ward, *J. Chem. Phys.* **1963**, *39*, 1211–1218.

[66] W. Wang, H.-H. Wei, *J. Chinese Chem. Soc.* **1978**, *25*, 185–194.

[67] M. W. Wemple, H. L. Tsai, K. Folting, D. N. Hendrickson, G. Christou, *Inorg. Chem.* **1993**, *32*, 2025–2031.

[68] M. Mameli, V. Lippolis, C. Caltagirone, J. L. Capelo, O. N. Faza, C. Lodeiro, *Inorg. Chem.* **2010**, *49*, 8276–8286.

[69] M. L. Wicholas, R. S. Drago, *J. Am. Chem. Soc.* **1968**, *90*, 2196–2197.

[70] R. Boča, J. Miklovič, J. Titiš, *Inorg. Chem.* **2014**, *53*, 2367–2369.

[71] R. Ruamps, L. J. Batchelor, R. Guillot, G. Zakhia, A.-L. Barra, W. Wernsdorfer, N. Guihéry, T. Mallah, *Chem. Sci.* **2014**, *5*, 3418.

[72] F. Habib, I. Korobkov, M. Murugesu, *Dalt. Trans.* **2015**, *44*, 6368–6373.

[73] M. S. Fataftah, J. M. Zadrozny, D. M. Rogers, D. E. Freedman, *Inorg. Chem.* **2014**, *53*, 10716–10721.

[74] T. Jurca, A. Farghal, P. H. Lin, I. Korobkov, M. Murugesu, D. S. Richeson, *J. Am. Chem. Soc.* **2011**, *133*, 15814–15817.

[75] J. M. Zadrozny, J. R. Long, *J. Am. Chem. Soc.* **2011**, *133*, 20732–20734.

[76] J. Vallejo, I. Castro, R. Ruiz-García, J. Cano, M. Julve, F. Lloret, G. De Munno, W. Wernsdorfer, E. Pardo, *J. Am. Chem. Soc.* **2012**, *134*, 15704–15707.

[77] C. Plenk, J. Krause, E. Rentschler, *Eur. J. Inorg. Chem.* **2015**, *2015*, 370–374.

[78] Y.-Z. Zhang, S. Gómez-Coca, A. J. Brown, M. R. Saber, X. Zhang, K. R. Dunbar, *Chem. Sci.* **2016**, *7*, 6519–6527.

[79] F. Habib, O. R. Luca, V. Vieru, M. Shiddiq, I. Korobkov, S. I. Gorelsky, M. K. Takase, L. F. Chibotaru, S. Hill, R. H. Crabtree, et al., *Angew. Chemie - Int. Ed.* **2013**, *52*, 11290–11293.

[80] N. F. Chilton, *CC-FIT*, Copyright, **2014**.

[81] J. M. Zadrozny, M. Atanasov, A. M. Bryan, C.-Y. Lin, B. D. Rekken, P. P. Power, F. Neese, J. R. Long, *Chem. Sci.* **2013**, *4*, 125–138.

[82] S. Gómez-Coca, A. Urtizberea, E. Cremades, P. J. Alonso, A. Camón, E. Ruiz, F. Luis, *Nat. Commun.* **2014**, *5*, 1–8.

[83] X. C. Huang, C. Zhou, D. Shao, X. Y. Wang, *Inorg. Chem.* **2014**, *53*, 12671–12673.

[84] J. Fraxedas, S. García-Gil, S. Monturet, N. Lorente, I. Fernández-Torrente, K. J. Franke, J. I. Pascual, A. Vollmer, R. P. Blum, N. Koch, et al., *J. Phys. Chem. C* **2011**, *115*, 18640–18648.

[85] J. Fraxedas, J. Lee, I. Jiménez, R. Gago, M. Nieminen, P. Ordejón, E. Canadell, *Phys. Rev. B - Condens. Matter Mater. Phys.* **2003**, *68*, 1–11.

[86] F. Mavandadi, Å. Pilotti, *Drug Discov. Today* **2006**, *11*, 165–174.

[87] C. Cadiou, M. Murrie, C. Paulsen, V. Villar, W. Wernsdorfer, R. E. P. Winpenny, *Chem. Commun.* **2001**, 2666–2667.

[88] S. T. Ochsenbein, M. Murrie, E. Rusanov, H. Stoeckli-Evans, C. Sekine, H. U. Güdel, *Inorg. Chem.* **2002**, *41*, 5133–5140.

[89] R. Ruamps, R. Maurice, L. Batchelor, M. Boggio-Pasqua, R. Guillot, A. L. Barra, J. Liu, E.-E. Bendeif, S. Pillet, S. Hill, et al., *J. Am. Chem. Soc.* **2013**, *135*, 3017–3026.

[90] R. Ruamps, L. J. Batchelor, R. Maurice, N. Gogoi, P. Jiménez-Lozano, N. Guihéry, C. de Graaf, A.-L. Barra, J.-P. Sutter, T. Mallah, *Chem. - A Eur. J.* **2013**, *19*, 950–956.

[91] G. Rogez, J.-N. Rebilly, A.-L. Barra, L. Sorace, G. Blondin, N. Kirchner, M. Duran, J. van Slageren, S. Parsons, L. Ricard, et al., *Angew. Chemie Int. Ed.* **2005**, *44*, 1876–1879.

[92] J. Krzystek, J.-H. Park, M. W. Meisel, M. A. Hitchman, H. Stratemeier, L.-C. Brunel, J. Telser, *Inorg. Chem.* **2002**, *41*, 4478–4487.

[93] C. Cadiou, M. Murrie, C. Paulsen, V. Villar, W. Wernsdorfer, R. E. P. Winpenny, *Chem. Commun.* **2001**, 2666–2667.

[94] E.-C. Yang, W. Wernsdorfer, S. Hill, R. S. Edwards, M. Nakano, S. Maccagnano, L. N. Zakharov, A. L. Rheingold, G. Christou, D. N. Hendrickson, *Polyhedron* **2003**, *22*, 1727–1733.

[95] K. E. R. Marriott, L. Bhaskaran, C. Wilson, M. Medarde, S. T. Ochsenbein, S. Hill, M. Murrie, *Chem. Sci.* **2015**, *6*, 6823–6828.

[96] J. Miklovič, D. Valigura, R. Boča, J. Titiš, *Dalt. Trans.* **2015**, *44*, 12484–12487.

[97] S. Gómez-Coca, E. Cremades, N. Aliaga-Alcalde, E. Ruiz, *Inorg. Chem.* **2014**, *53*, 676–678.

[98] M. Boutebdja, A. Beghidja, C. Beghidja, *Acta Crystallogr. Sect. E Struct. Reports Online* **2013**, *69*, m131–m131.

[99] T. Yoshida, S. Kaizaki, *Inorg. Chem.* **1999**, *38*, 1054–1058.

[100] J. P. Rehmann, J. K. Barton, *Biochemistry* **1990**, *29*, 1710–1717.

[101] J. A. Happe, R. L. Ward, *J. Chem. Phys.* **1963**, *39*, 1211–1218.

[102] W. Wang, H.-H. Wei, *J. Chinese Chem. Soc.* **1978**, *25*, 185–194.

[103] B. D. Wagner, G. J. Mcmanus, B. Moulton, M. J. Zaworotko, **2002**, *5*, 2176–2177.

[104] Q. Yuan, T. Probes, P. Intermediate, D. Energy, **1975**.

[105] T. Yoshida, T. Suzuki, K. Kanamori, S. Kaizaki, *Inorg. Chem.* **1999**, *38*, 1059–1068.

[106] L. Bogani, A. Vindigni, R. Sessoli, D. Gatteschi, *J. Mater. Chem.* **2008**, *18*, 4750.

[107] W.-X. Zhang, R. Ishikawa, B. Breedlove, M. Yamashita, *RSC Adv.* **2013**, *3*, 3772.

[108] H. L. Sun, Z. M. Wang, S. Gao, *Coord. Chem. Rev.* **2010**, *254*, 1081–1100.

[109] R. J. Glauber, *J. Math. Phys.* **1963**, *4*, 294–307.

[110] T. Liu, Y. J. Zhang, S. Kanegawa, O. Sato, *J. Am. Chem. Soc.* **2010**, *132*, 8250–8251.

[111] S. Chorazy, R. Podgajny, W. Nitek, M. Rams, S. I. Ohkoshi, B. Sieklucka, *Cryst. Growth Des.* **2013**, *13*, 3036–3045.

[112] R. Clérac, H. Miyasaka, M. Yamashita, C. Coulon, *J. Am. Chem. Soc.* **2002**, *124*, 12837–12844.

[113] R. M. Wei, F. Cao, J. Li, L. Yang, Y. Han, X. L. Zhang, Z. Zhang, X. Y. Wang, Y. Song, *Sci. Rep.* **2016**, *6*, 1–8.

[114] a Caneschi, D. Gatteschi, N. Lalioti, R. Sessoli, L. Sorace, V. Tangoulis, a Vindigni, *Chem. Eur. J.* **2002**, *8*, 286–292.

[115] A. Amjad, G. Mínguez Espallargas, J. Liu, J. M. Clemente-Juan, E. Coronado, S. Hill, E. Del Barco, *Polyhedron* **2013**, *66*, 218–221.

[116] M. G. F. Vaz, R. A. A. Cassaro, H. Akpinar, J. A. Schlueter, P. M. Lahti, M. A. Novak, *Chem. - A Eur. J.* **2014**, *20*, 5460–5467.

[117] R. Gheorghe, A. M. Madalan, J.-P. Costes, W. Wernsdorfer, M. Andruh, *Dalt. Trans.* **2010**, *39*, 4734.

[118] D. Visinescu, A. M. Madalan, M. Andruh, C. Duhayon, J. P. Sutter, L. Ungur, W. Van Den Heuvel, L. F. Chibotaru, *Chem. - A Eur. J.* **2009**, *15*, 11808–11814.

[119] F. Luo, Z. Liao, Y. Song, H. Huang, X. Tian, G. Sun, Y. Zhu, Z.-Z. Yuan, M. Luo, S. Liu, et al., *Dalt. Trans.* **2011**, *40*, 12651.

[120] K. K. Gangu, S. Maddila, S. B. Mukkamala, S. B. Jonnalagadda, *ChemInform* **2016**, *47*, 4000.

[121] A. El-Faham, S. N. Khattab, H. A. Ghabbour, H. K. Fun, M. R. H. Siddiqui, *Chem. Cent. J.* **2014**, *8*, 1–10.

[122] K. Biradha, M. Sarkar, L. Rajput, *Chem. Commun.* **2006**, 4169–4179.

[123] K. E. Schwarzhans, *Angew. Chemie Int. Ed. English* **1970**, *9*, 946–953.

[124] P. Jensen, S. R. Batten, B. Moubaraki, K. S. Murray, *J. Chem. Soc., Dalt. Trans.* **2002**, *1*, 3712–3722.

[125] D. Aguilà, L. A. Barrios, O. Roubeau, S. J. Teat, G. Aromí, *Chem. Commun.* **2011**, *47*, 707–709.

[126] C. Plenk, J. Krause, E. Rentschler, *Eur. J. Inorg. Chem.* **2015**, *2015*, 370–374.

[127] J. Miklovič, D. Valigura, R. Boča, J. Titiš, *Dalt. Trans.* **2015**, *44*, 12484–12487.

[128] J. Paharová, J. Černák, R. Boča, Z. Žák, *Inorganica Chim. Acta* **2003**, *346*, 25–31.

[129] H. Miyasaka, A. Saitoh, S. Yanagida, C. Kachi-Terajima, K. I. Sugiura, M. Yamashita, *Inorganica Chim. Acta* **2005**, *358*, 3525–3535.

[130] H. Miyasaka, K. Mizushima, K. Sugiura, M. Yamashita, *Synth. Met.* **2003**, *137*, 1245–1246.

[131] M. Chen, H. Zhao, E. C. Sañudo, C. Sen Liu, M. Du, *Inorg. Chem.* **2016**, *55*, 3715–3717.

SECTION II:

MOLECULAR ELECTRONICS

Curcuminoids in three-terminal devices

2.1 Introduction

Molecular Electronics

The development of society has been always connected with the technological advances. Current technology, based on silicon devices,[1] tries to satisfy human needs where our continuous demand of energy requires faster devices with greater storage capacity and therefore, optimal miniaturization and assembly of the materials used to create them.

So far, these advances have been only possible by the development of sophisticated photolithographic techniques that allows the reduction of the devices through "top-down" strategies.[2] However, the physical, technological and economic limitations caused by the willing of further miniaturization are imminent.[1] The 10 nm design, using top-down methods, is a great challenge, where quantum phenomena become more important than the bulk properties of the materials; in addition, current leaks from electron tunneling prevent the good working of the systems.

Here, molecular electronics present putative alternatives to provide economical and effective devices.[3–5] The active components of the systems are based on "bottom-up" strategies; this provides advantages in terms of scaling down the devices and, due to the molecular components, a huge variability of molecular-based systems can be obtained taking into account the possibility of designing molecules with specific properties (optics, magnetics, mechanics, etc.)[6] giving rise to the development of new technologies with advanced applications.

However, these new strategies required still of fundamental studies and are not ready to substitute current technologies. This fact points out the necessity of understanding the factors that dominate and influence molecular electronic transport. Hence, in order to improve the devices, is mandatory the establishment of correlation between the molecular structure and the conductive transport properties of the physical systems.[3]

Techniques for the measurement of single molecules

The development of advanced techniques to measure the electron transport at the nano-scale using single molecules has been crucial in the progress of the molecular electronic field. To perform transport studies, these techniques have to contain at least two electrodes (as in diodes) or three (as transistors) separated by few nanometers.

Currently, the most used techniques are: (i) Scanning Tunneling Microscopy (STM)[7] and Break Junction technique (BJ)[8]. (Figure 2.1).

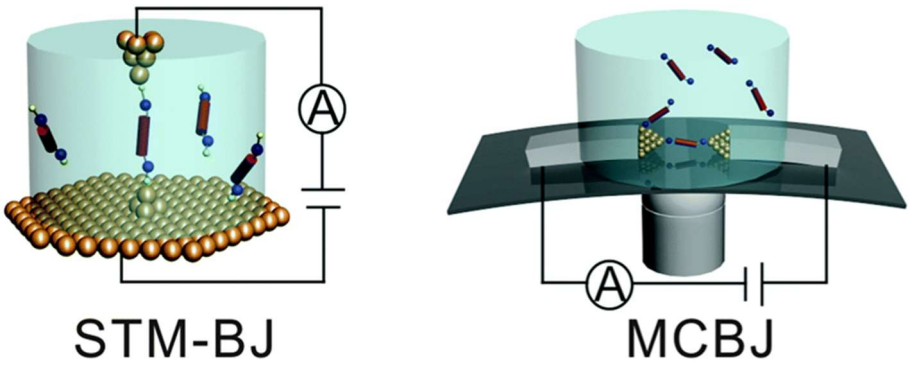

Figure 2.1: Representation of a Scanning Tunneling Microscope (left) and Break Junction (right) techniques. Reprinted with permission from Copyright Royal Society of Chemistry.

STM is a technique which makes use of a phenomenon of tunneling electrons to map the positions of individual atoms in a surface and allowing the analysis of their electrical properties by the use of a tip that acts as an electrode.

On the other hand, the BJ technique consists of two electrodes separated by a very thin gap. The gap generation can be done physically, which corresponds to the technical Mechanical Controlled Break Junction (MCBJ). In this case, a metal thin wire is place on a substrate with piezoelectric properties. The gap is generated by the application of current which give rise to the progressively curved of the piezoelectric substrate until the wire breaks leaving a space of few nm. Then, the molecule can be trapped between the two electrodes and the action can be repeated in a control manner. In fact, STM and MCBJ techniques allow statistics, where the measurement of molecules can be repeated thousands of times. In this regard both techniques are the most used to gather general information of molecular systems when gold is used as the material to build up the electrodes.

This section emphasizes the break junction technique and describes the use of Electromigration (EM) to achieve a nano-gap between electrodes that will allow the measurement of the electronic transport properties of our molecules. In brief, as mentioned above, in EM two electrodes are separated only by few nm gap; such separation is generated by the application of consecutive current ramps that damage the material and consequently two electrodes are formed. They are on the top of the third electrode but separated by layers of an isolating material to avoid current leaks. A chip can contain hundreds of such three-

terminal electrodes. The technique has serious limitations toward statistic used, but can be used with electrodes of different nature, as for example graphene of few-layers graphene.[9–11]

Molecular electronic devices based on graphene

The essential components which govern the charge transport on a single-molecule level are the anchoring groups of the molecule under study, the properties of the molecular backbone and the electrodes.

Related to the electrodes, most of the measured systems are based on metal electrodes. Within these metals, gold electrodes are highly used due to the high conductivity, noble character and possibility to create strong covalent bond with thiol groups that they present. However, at room temperature, they exhibit high atomic mobility being unstable[12] and therefore the use of such material in devices is mostly limited to low temperatures. Among other reasons, this has given rise to the search of alternative materials that can function as electrodes in a nano-device. Carbon-based materials (e.g: graphene[9–11], nanotubes[13,14]) are displaying special interest as a solution for stability at high temperatures and reproducibility. The presence of covalent bond-structure provides the system with high stability at high temperatures.[15] Moreover, their good conductivity, low cost and high compatibility with organic systems (by interacting via π-π stacking due to the presence of sp^2-carbon atoms) make the latest excellent candidates for their use as electrodes.[16,17] Motivated by this advantage, this section focuses on the fabrication of three-terminal molecular transistor based on graphene electrodes (representation Figure 2.2, a).

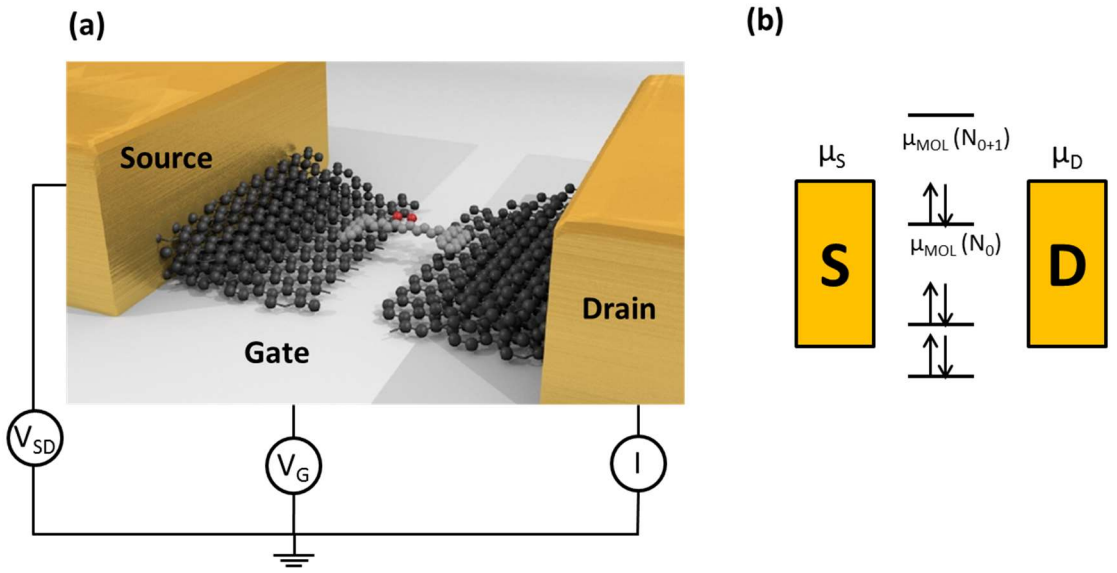

Figure 2.2: (a) Representation of CCMoid molecular transistor based on electrodes graphene layer. (b) Representation of the energy of electrodes bands and molecular states.

Figure 2.2 (a) shows a representation of a CCMoid molecule between two graphene electrodes (source and drain) in a silicon substrate which acts as a gate electrode. The three electrodes are separated by and insulator (layer made of SiO_2) that protects the three-terminal device from current leaks (the gate couples only electrostatically to the molecule). The molecule is attached to the two graphene electrodes by π-π stacking interactions through the anthracene groups contained in both sides of the structures.

Once the molecule is attached, there is a re-organization of the molecular energy, where some its states may be close in energy to the Fermi level of the electrodes, giving rise to the possibility of having electronic transport (electrochemical potential $\mu_{MOL}(N)$, in the Figure 3.1b). In this process, the molecular orbital are not only changing in energy but also broadening, due to hybridization causes by the interaction of the molecule with the electrodes[3,4]**.** This interaction relates to the parameter Γ, called electrode-molecule coupling, which depends on the overlap of the wave functions of the molecule and those of the electrodes.

In general molecules do not present strong coupling with the electrodes and the transport is not lead by tunneling mechanism but by a Coulombic one. Figure 2.3 shows the typical Coulomb blockade representation also called “diamond diagram” a schematic representation of the typical measurement transport for a single molecule system (Γ is small).

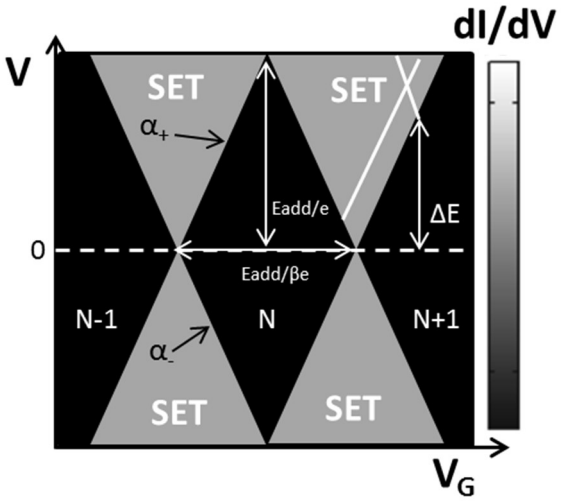

Figure 2.3: Coulomb blockade representation. The black areas correspond to regions where the transport is blocked. In the grey areas the blocked is lifted by resonance tunnelling (SET regime). β is the gate coupling parameter. In addition, white lines correspond to resonant tunnelling though excited states in the SET regime.

As can be seen in the Figure 2.3, two different regions depending on the conductivity can be differentiated. Slanted lines separate regions of high conductance (Single-Electron tunneling (SET) regime, grey regions) from region of zero conductance (black regions).

The conductance values will be given by the position of the molecular levels with respect to the Fermi level of the electrodes. For the example, when the energy of a molecular level (usually HOMO ($\mu_{MOL}(N_o)$ or LUMO ($\mu_{MOL}(N_{o+1})$ is located between the bias windows of the source and drain electrodes (the energy range between the chemical potential of the source and the drain electrode), electron transport should, in principle, be measured (grey region).

In contrast, when no molecular level is present in the bias windows (molecular orbitals are far away from the Fermi level of the electrodes) a resistance to the flow of current is presented and the transport is blocked (black region) (Figure 2.4, a and c). In these cases, by the application of bias voltage (V_{bias}) across the junction (that modifies the chemical potential of the electrodes source and drain, Figure 2.4 a-b) or applying a gate voltage (V_{gate}) (that modifies the energy of the molecular orbitals allowing different states of charge to be accessible, Figure 2.4 c-d) is possible to align the orbitals/Fermi level allowing the current flow again. Within these states, the conduction can also take place through excited states (vibrational or electronic origin). The observation of the Coulomb diamonds corroborates the molecular origin of the electronic transport and the existence of these excitations strength of the coupling.[18]

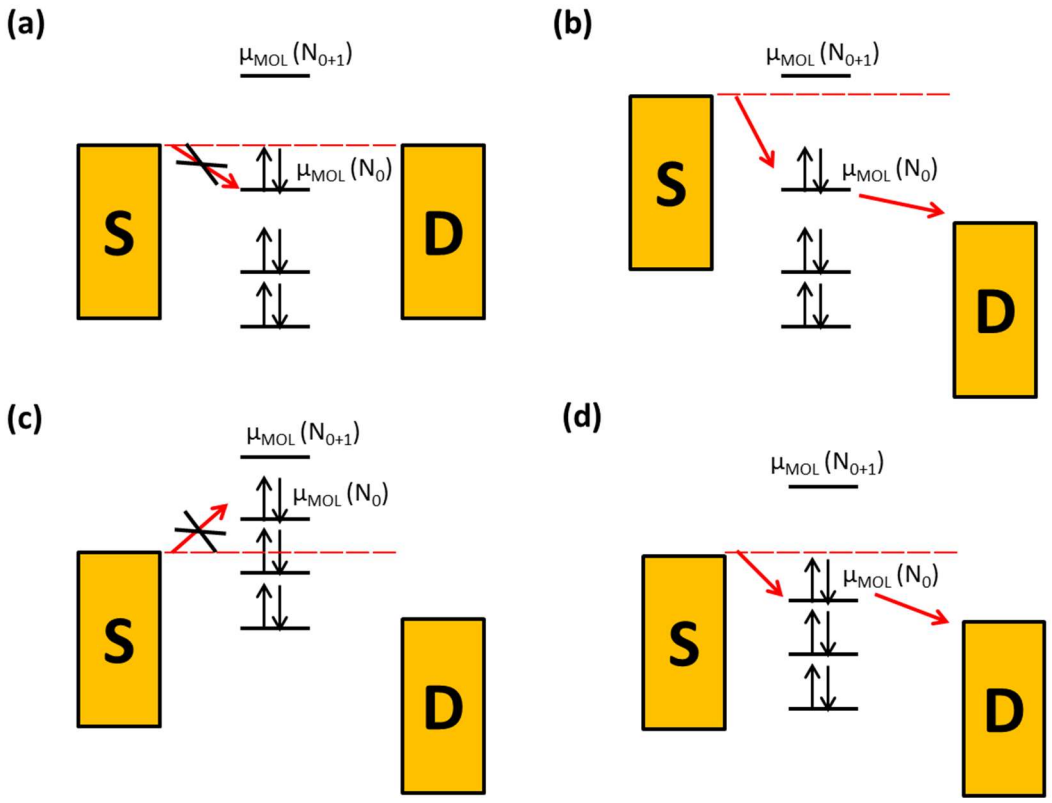

Figure 2.4: Representation of molecular orbitals and electrodes energy bands. (1) electron transport blockade, (2) the application of V_{bias} modify the energy bands of the electrodes allowing the electron transport, (3) electron transport blockade, (4) the application of V_{gate} modify the of molecular orbital allowing the electron transport.

Another important parameter is the interaction between the voltage gate (Si based electrode here) and the molecule, since both are separated by an insulator layer (SiO_2 for our experiments). This interaction is quantified by the coupling-gate parameter (β) and should be as large as possible in order to access to as many charge states as possible. Normally, the gate coupling for a silicon device with a SiO_2 thickness of 250 nm shows values of 10^{-3}.[19]

However, the total level shift induced by the gate is limited, that means that no all the molecules are suitable to be used as components for single-molecular transistors. These molecules are typically > 1nm since smaller molecules present a too high level splitting and their charge state cannot be changed with the gate. [20] Apart to the size, there are two additional requirements that molecules may follow: (i) the presence of anchoring groups, usually situated in the sides of the molecule for its anchoring to the electrodes and (ii) conjugated skeletons (usually containing aromatic rings).[3] The former provides robust electronic data (reproducible) and, it could be important to control the number of conformations of the molecule between the electrodes (although this depends as well on the skeleton of the systems). The second, usually disposes the systems in a planar disposition

favoring the electronic transport.[4] Figure 2.5 shows a schematic of a single-molecule junction and Figure 2.6 shows examples of anchoring groups and molecules used as wires in molecular devices.

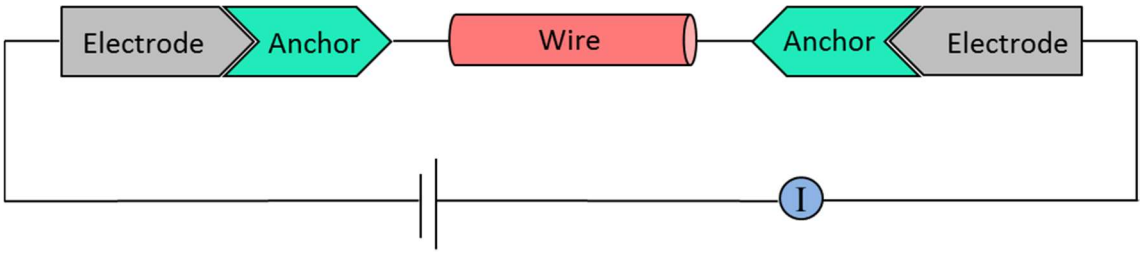

Figure 2.5: A Schematic of a single-molecule junction with electrode, anchor and wire components.

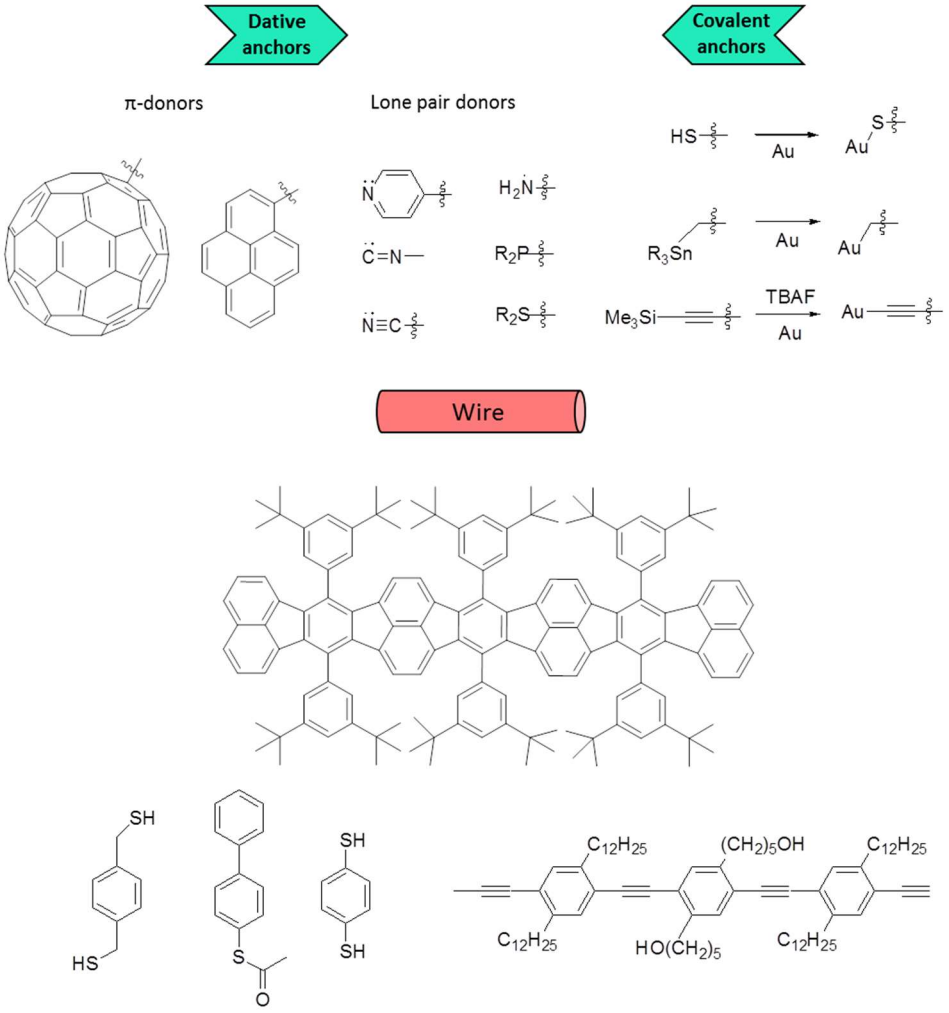

Figure 2.6: Examples of anchoring groups and molecules used as nano-wires in molecular based devices.

Background

The first study of a CCMoid molecule as a component in a molecular transistor device was carried out by our group in collaboration with the group of Professor Herre van der Zant from the Kavli Institute of Nanoscience (TUDelft).[11] In that study, 9Accm (Figure 2.7, a) was used as a nanowire between two electrodes based on few layer graphene (FLG) and a silicon gate electrode (Figure 2.7, c). The formation of the two graphene electrodes was performed by electroburning process, in which the pass of high intensity current provokes the appearance of high temperature, induces by Joule effect, and originates the breaking of the graphene layers. The control of the gap formation with this process is not easy, however gap values between 1-2 nm were obtained (Figure 2.7, b). Then 9Accm was deposited between the electrodes by drop-casting. The interaction of both systems is produced via π-π stacking of the anthracene groups (anchoring groups) of the molecule and the graphene electrodes and, in this case, it takes place mainly in the edges of the graphene layer, since the distance of 9Accm, from its crystal structure (d = 1.71 nm) is similar to the gap. The π-π interaction is limited by the variety of shapes and composition of the edges of the electrodes.[21] Nevertheless, the I-V measurements (current versus voltage graph, Figure 2.7 d) displayed an increase of the intensity current after the molecule was on the nano-devices, in the proposed way in Figure 2.7, c. One of the most relevant points in this work is that the measurement was achieved at room temperature (Figure 2.7, d).

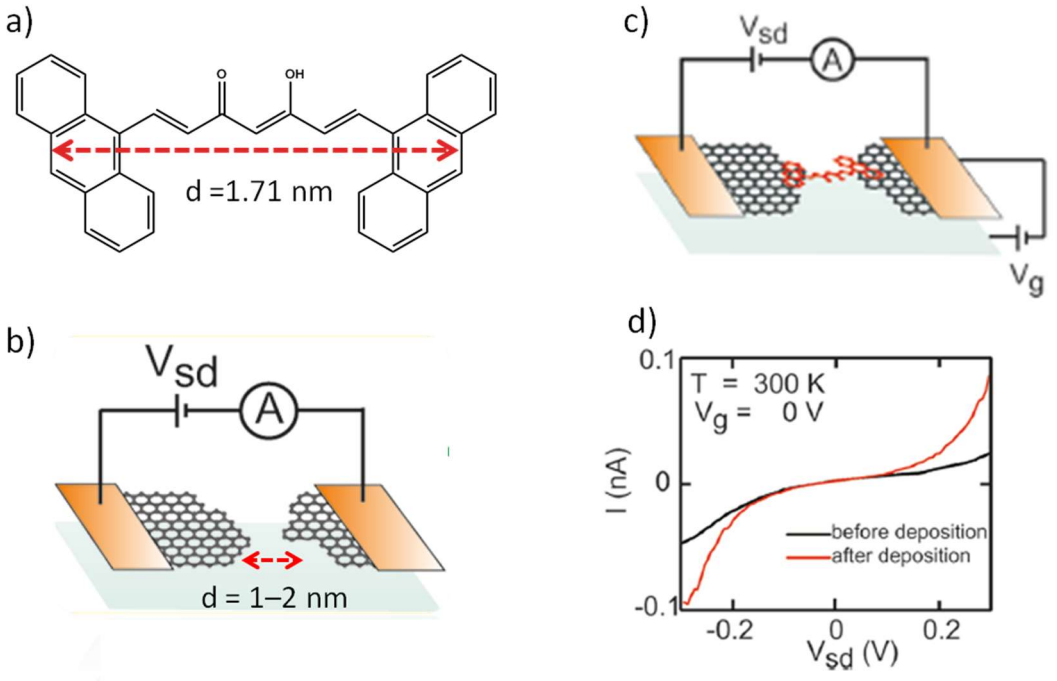

Figure 2.7: (a) Representation of 9Accm (d = 1.71 nm), (b) Scheme of the gap formation after electroburning process, (c) Scheme of the molecule deposited, (d) I-V characteristics before and after 9Accm deposition at T = 300 K.

2.2 Objectives

This section focused on exploring the electron transport properties of a novel CCMoid molecule in a molecular transistor (nano-FET) device related to that explained above. Based in our previous experience, this work describes the improvement of the transport properties with the design and synthesis of a new CCMoid that contains an extended conjugated chain. The extension of the backbone was used to improve the connection between the anchoring groups of the molecule and the graphene electrodes, where now the anthracene groups would sit far away from the graphene edges, expecting this way improvement in the π-π interactions.

2.3 Results and Discussion

2.3.1 Experimental section

Synthesis of 9ALCCMoid

The molecule 9ALCCMoid (Figure 2.8, b) displays a conjugated backbone made of 11 carbon atoms. The system, contains a β-diketone group in the middle of the chain and, as in the previous system 9Accm, two anthracenes groups are present in both sides of the molecule. The final system is a good candidate for been used in molecular electronics, since keeps the anthracene groups that function as anchoring groups responsible of the coupling with the top graphene layer of the two electrodes (π- π stacking). In addition, the conjugated chain would allow the electronic transport providing planarity.

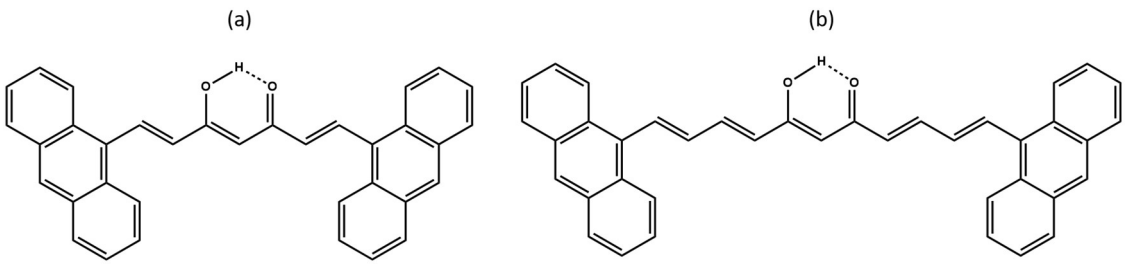

Figure 2.8: Representation of the (a) 9Accm and (b) 9ALCCMoid molecule.

9ALCCMoid was synthesized by modifying Pabon's method[22] (the procedure was described in the Introduction, Figure 2). In this case, the last step, hydrolysis, was not required and the system was achieved in high yield (87 %) after washing with H_2O, MeOH and Et_2O, in that order. Single crystals were obtaining by slow evaporation in THF.

The conjugated chain of the molecule could give rises to the presence of different stereoisomers (E/Z). The presence of the stereoisomers can be studied by different techniques, for example: Circular Dichroism (CD) or proton nuclear magnetic resonance (^{1}H NMR), this thesis concentrates in the latest. This way, in the case of the initial aldehyde reagent, 3-(9-anthryl)acrolein (Figure 2.9), was possible to determine the mixture of both stereoisomers by ^{1}H NMR (Annex 2.1). The ^{1}H NMR spectra show additional proton shifts and the expected ones appear split.

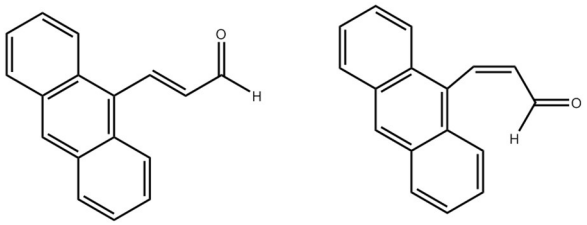

(E) (Z)

Figure 2.9: Representation of the molecular structure of E-3-(9-anthryl)acrolein (left) and Z-3-(9-anthryl)acrolein (right)

Previous works, regarding this subject show different methodologies to isolate isomers or to convert one to the other; in general, we can use thermal methods (heating the solution) or photochemical methods (exposing the solution under sun/UV light with the presence of a catalytic amount of an extern agent, for example iodine).[23]

However, in the case of the 9ALCCMoid, despite of using a mixture of the aldehyde stereoisomers, the ^{1}H NMR spectra only shows the presence of one stereoisomer due to the reduce number of signals. (Figure 2.10)

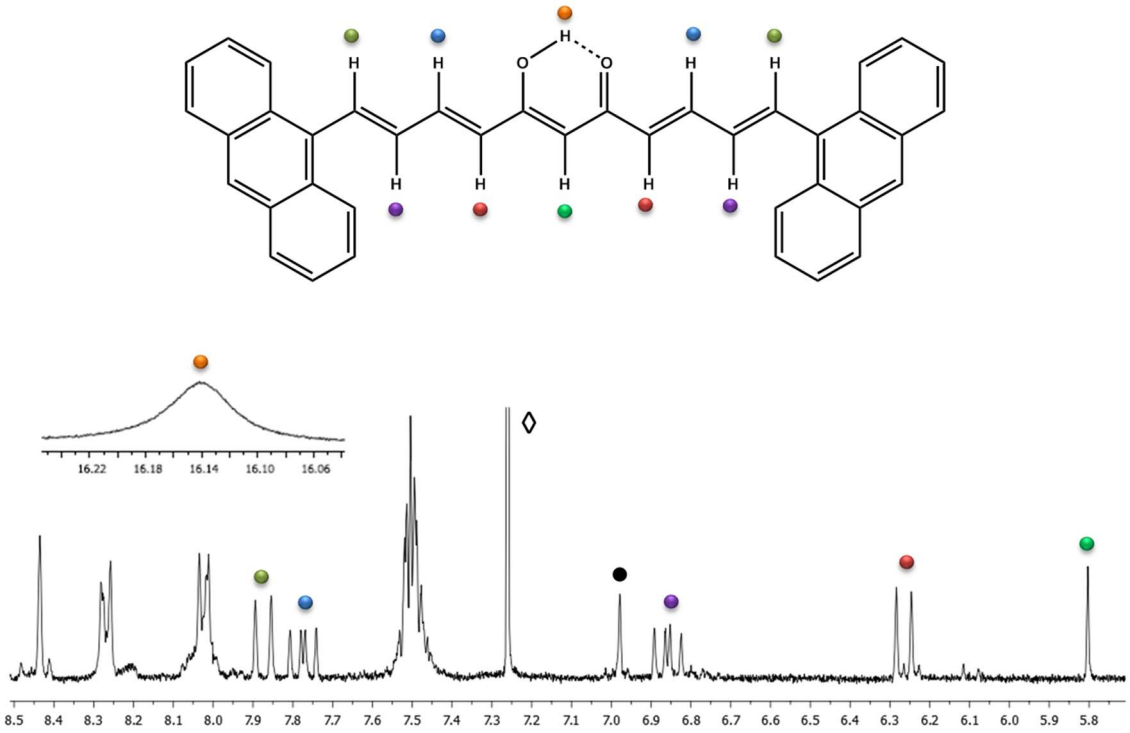

Figure 2.10: ^{1}H NMR spectrum of 9ALCCMoid in $CDCl_3$ (◊ $CDCl_3$, • BHT from the THF)

Related to the β-diketone group, the spectrum displayed a broad signal at 16 ppm corresponding to the enol group (orange spot) and a singlet signal at 5.8 ppm which corresponds to the methane proton (green spot) in the center of the β-diketone group. Both signals indicated the stabilization of the enol form in the molecule.

With regards to the conjugated chain, the assignment of the proton was performed by comparison with predictive models. The coupling constant of their signals (J ≈ 15 Hz) confirm the presence of the E isomer (corroborate later for the crystal structure). This fact is common since the E isomer dominates thermodynamically over the mixture of E/Z or Z-isomers. Particularly, the E-isomers is also the most convenient for our studies since presents the highest length keeping conjugation.

To study the possibility of interconversion between the two isomers, studies in solution by ^{1}H NMR and UV-Visible (Annex 2.2) at different times were performed, but no variation of their spectra was observed. The Mass Spectrometry is shown in the Annex 2.3.

Crystal structure of 9ALCCMoid

The crystal structure of the 9ALCCMoid (Figure 2.11) required the use of synchrotron source due to the small size of the crystals. General crystallographic data of this system is presented in Annex 2.4.

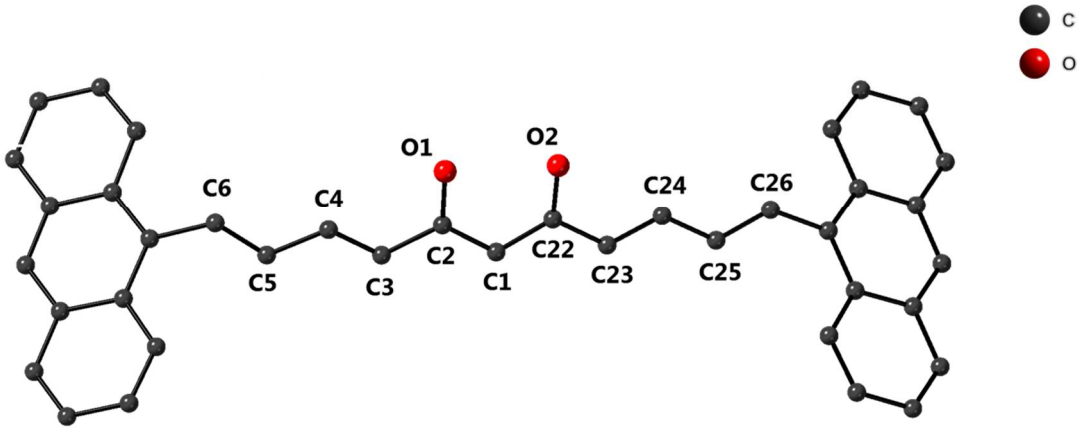

Figure 2.11: Representation of the molecular structure of 9ALCCMoid where the atoms of O (red), C (gray). H atoms have been omitted

9ALCCMoid crystallizes in a P2(1)/n space group with one molecule in the unit cell. The crystal structure shows a gentle bending of the conjugated chain (Annex 3.5). Related to the anthracene arms, both are in the same plane but tilted respects to the conjugated chain showing a torsion angle of 50.5 ˚ (Annex 3.6). Related to the distances, as no symmetry is observed in the structure, different distances were observed in the β-diketone. In this case, two different C-O distances 1.300 Å and 1.291 Å corresponding to C2-O1 and C22-O2 respectively were found. As in others CCMoids, the conjugated chain shows two types of C-C distances. These distances are alternating between C-C (1.433-1.470 Å) (C2-C3, C4-C5, C6-C7, C22-C23, C24-C25 and C26-C27) and C=C (1.334-1.399 Å) (C1-C2, C3-C4, C1-C22, C23-C24 and C25-C26). Some of these distances are summarizes in the Annex 2.5.

The length of the molecule is 2.15 nm and therefore is significantly longer, compared with 9Accm (1.71 nm)[24], and optimal toward deposition of the system in the three terminal devices after performing the electroburning process, which generates gaps ranging from 1-2 nm.[11,15] Therefore, this length should facilitate the coupling of the molecule to the graphene electrodes via π-π stacking since the interaction between anchoring groups and electrodes would take places farther from the edges. The distances comparison of the two structures 9Accm and 9ALCCMoid is shown in Annex 2.6.

Nanofabrication

To get more insight in the fabrication of the final nano-device, a briefly description of the methodology used to achieve it will be presented below, although details regarding this matter exceed the purpose of the thesis. The parts discussed are the result of a short stay in the group of Professor Herre van der Zant at the Delft University of Technology (TUDelft).

Some of the process during the nanofabrication was carried out in the clean room to avoid any kind of contamination. The nanofabrication process can be divided in five different steps: (i) substrate construction (Figure 2.12 (1)), (ii) gap generation (Figure 2.12, (2)), (iii) characterization of the empty gap (I-V studies), (iv) molecule deposition (Figure 2.12, (3)) and (v) devices characterization (I-V studies).

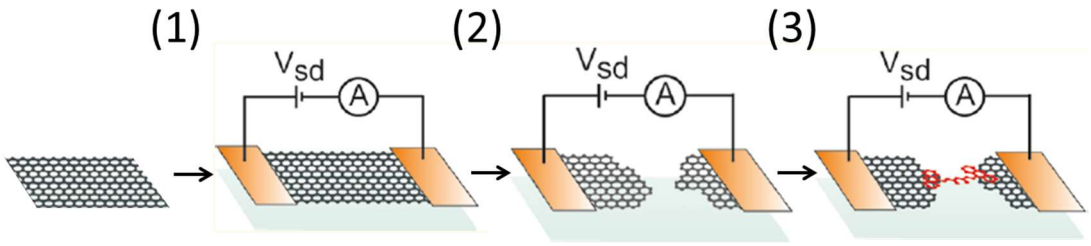

Figure 2. 12: Representation of different steps for the construction of the nanodevices: (1) substrate construction, (2) gap generation by electroburning and (3) molecule deposition.

(i) Substrate construction

The construction of the nano-devices was carried out by the use of nanolithography. A silicon wafer coated with 285 nm of SiO_2 was required as well. This silicon substrate is used as a gate electrode where the SiO_2 acts as an insulator. Then, few-layer graphene flakes (FLG) obtained by mechanical exfoliation of nature graphite, were deposited onto the silicon wafer. Depending of the speed during the exfoliation, graphene layers with different thickness were obtained. By the use of an optical microscope it's possible to distinguish, in a qualitative way, the different thickness. In our experiment, graphene layer, which exhibit violet color were selected. This feature corresponded to an approximate thickness of 10 nm (10-15 layers of graphene).[25,26] The thickness of the few layers graphene flakes are important because the existence of only few layers could give rise to the gating of the source and drain electrodes (when the gate electrode it is coupled with source and drain), and a large number of layer within the flake would difficult the electroburning process. A scheme of the graphene layer deposited on the silicon is shown in Annex 2.7. Finally, metal gold connections were

evaporated in two opposite sides of the selected flake providing the micro-contacts to measure conductance.

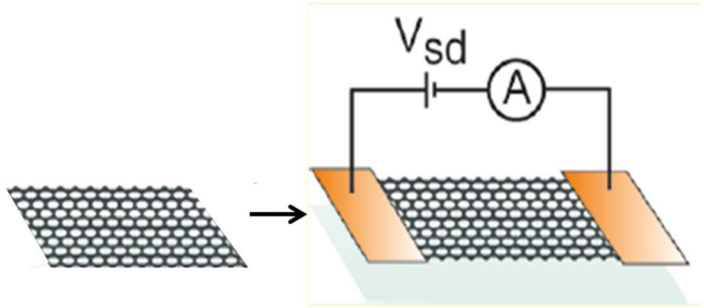

Figure 2.13: Representation of substrate construction

(ii) Gap generation

The gap generation was performed using controlled electroburning technique at room temperature and the presence of air. In this process, high bias voltages were applied between the gold connectors introducing current through the graphene flake. This graphene flake was heat up by Joule's effect where a number of carbon atoms interact then with oxygen; this reaction is triggered by the high temperatures accomplished. This gives rise to the break of the graphene layer in a controlled way (somewhere in the middle of the two gold connectors). The control of the breaking was achieved by recording in a continuously manner the current while a voltage ramp is applied (I-V). In this process, there is a point where the conductance (G = I/V) drops 10 %, then the voltage is swept to zero. Immediately, a new voltage ramp starts again from 0 V. The process was repeated until the gap is generated, having two electrodes made of few-layer graphene separated by a nano-gap.[9–11,27] The evolution of the electroburning process is carried out by I-V measurements (Figure 2.14, left). With every cycle, the intensity achieved is lower due to breaking of the graphene layers. The electroburning is finished when the intensity current it is zero. Conductance measurements were also performed (Figure 2.14, right) observing the same behavior.

The high temperatures caused by the electroburning process give rise to the appearance of functional groups of different nature (carboxylic acids, ketone, etc) located just at the edge of the electrodes where the breaking is performed.[28,29] These groups can decrease the π-π interactions between the molecule and electrodes resulting in a decrease of the conductance values. In the case of 9ALCCMoid, the extensive backbone should bring the anchoring groups farther from the edges, facilitating the coupling of the molecule to the aromatic structure of the graphene.

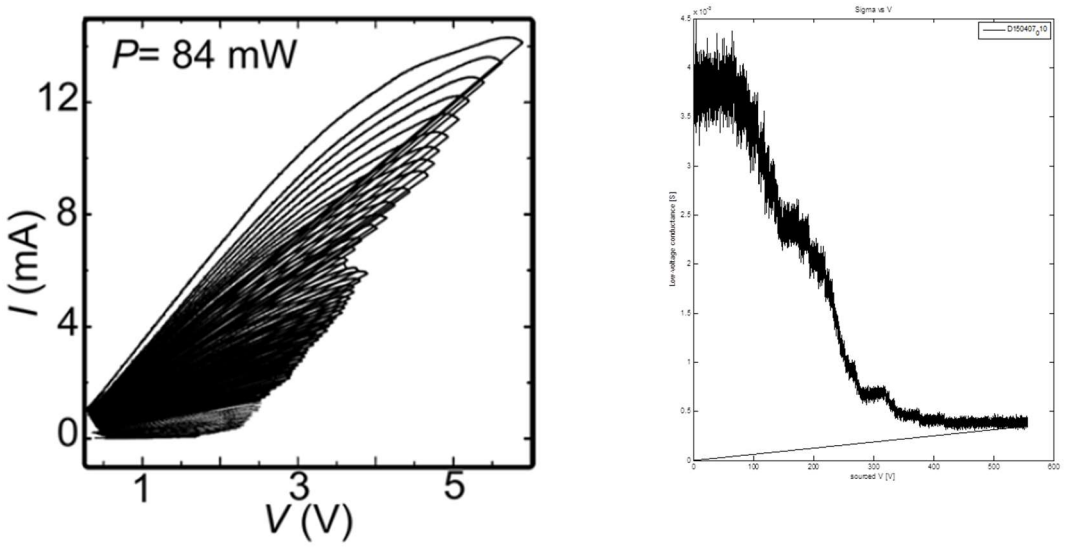

Figure 2.14: (left) Evolution of the I-V characteristics during the electroburning of a device. (right) Evolution of the conductance (G) versus applied voltage.

Finally, to corroborate the proper generation of the gap, measurements of resistance are done. Before the electroburning process, the resistances at low bias of the graphene layer are in order of 200 Ω to 500 Ω. After electroburning, the open gate displays a resistance in the range of 500 MΩ to 10 GΩ.[11]

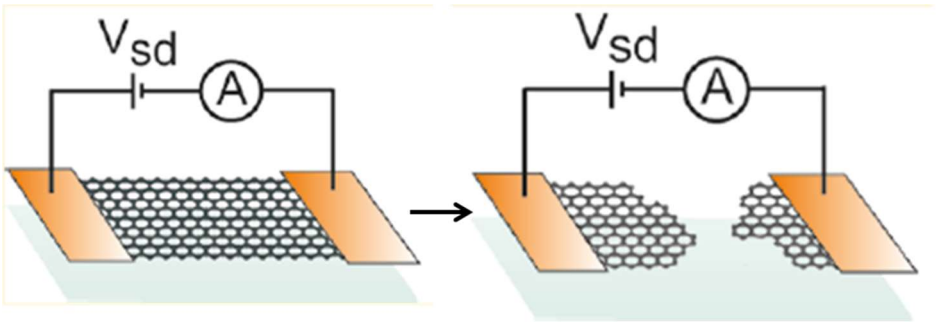

Figure 2.15: Representation of Electroburning process

(iii) Characterization of the empty gap

The characterization of the empty gap is performed by measurements of (I vs V_{bias}) and (I vs V_{gate}) at room temperature and at liquid helium temperature (4.3 K) under vacuum. Comparing

to the Vbias, huge values of V_{gate} (-40 to 40 V) are needed since the electrode gate is covered with a thick insulator layer of SiO_2.[11]

(iv) 9ALCCMoid deposition

The deposition of 9ALCCMoid was performed after the electroburning process to preserve the integrity of the molecular system. This process was carried out by dropcasting method using CH_2Cl_2. Few drops of a solution of the CCMoid 0.1 mM were added and the system was left for 30 min. This time was required for the molecule to reorganize between the electrodes. Then, a vacuum was applied for 30 min to remove the solvent.

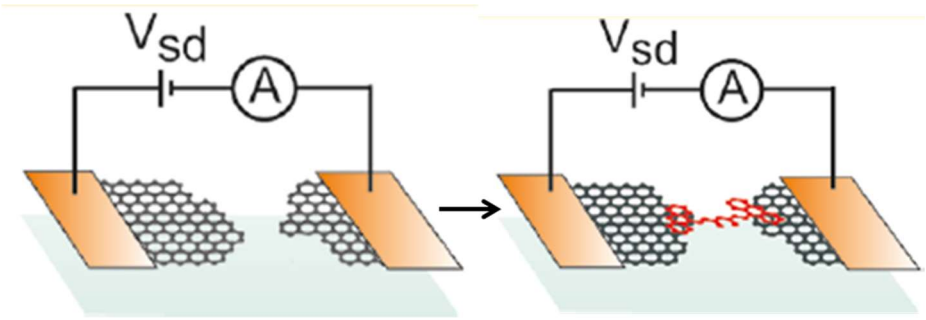

Figure 2.16: Representation of molecular deposition

(v) Devices characterization

The characterization of the devices was carried out under the same conditions than the empty gap, I vs V_{bias}, and, I vs V_{gate}, respectively. Firstly, the characterization was performed at room temperature, and only the systems which present high current measurements were used for the studies at low temperatures (current values of molecules are in order of nanoampere (nA), and if there is no molecule the current this will be of the order of picoampere, pA).

More information could be obtained from a conductance map at 10 K (2D) measurements. To carried out the measurement, the value of the V_{gate} was fixed and the current was measured scanning the V_{bias} (-40 V < V < 40 V). Then the value of V_{gate} was modified and the scanning was repeated.

2.3.2 Characterization

As it was mentioned above, the devices are characterized by I-V measurements.

(i) Empty gap

The characterization of the empty gap is crucial. This step allows us to ensure that the electroburning process has been carried out correctly. This characterization was performed at low temperatures, because at room temperature, small graphene quantum dots located in the gap could mimic the behavior of the target molecule.[30] Therefore, this fact could be discarded performing measurements at low temperatures, where the molecule will present different behavior exhibiting current intensity (I) dependence with the voltage gate (V_{gate}).

Firstly, measurements of I-V_{bias} are recorded and, depending on how the electroburning process was performed, three different I-V_{bias} could be obtained (Figure 2.17).

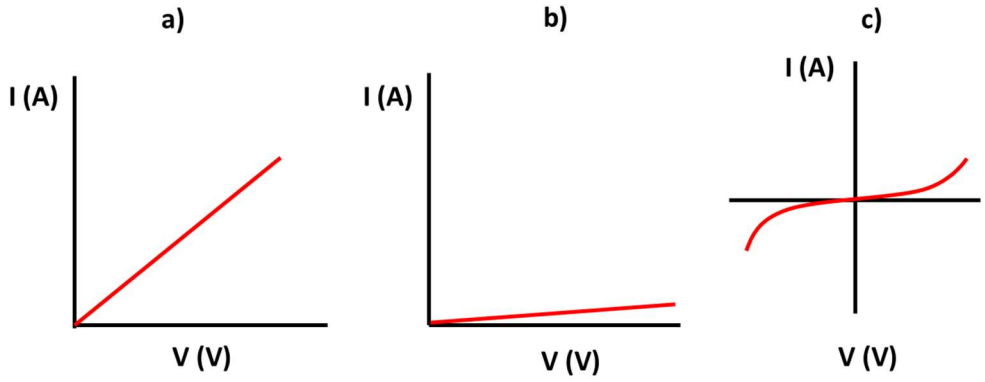

Figure 2.17: Representation of I-V for: (a) system which follow Ohm Law (not open gap, (b) system which present a big gap and (c) system which present tunneling process (small gap).

The first example corresponds to a system which follows the Ohm's Law, being R the slope (V = RI). The R values are then high indicating that they are still some graphene layers without breaking between the electrodes.

The second example shows a very low value of the intensity current. This is inversely proportional to the distances between the electrodes. In the case of Figure 2.17 (b), this measurement would indicate that the distance between the electrodes is large (d > 2 nm).

The third example shows a symmetric current intensity. The intensity current is proportional to the voltage and does not follow Ohm's Law. This sinusoidal form of the I-V graph comes from

tunneling processes only possible when the distances between the electrodes are small, 1-2 nm, after electroburning. This process is not dependent of the temperature, hence it must be present at low and room temperatures.

Figure 2.18 (left) shows the current-voltage (I vs V_{bias}) trace of an open gap at liquid helium temperature before the molecular deposition. As it can be seen, the current intensity presents a S-shape exponential dependence with the applied bias voltage, V_{bias}, as it has been shown in the previous example. This shape is a fingerprinting of the tunnel current between the electrodes.

The size of the gap between the electrodes can be obtained from fitting the solid line (Figure 2.18, left, red line) using Simmon's model.[31] Doing so, a value of d = 1.9 nm ± 0.3 nm was obtained. This distance corresponds to the small region between the electrodes (electroburning process give rise to non-homogeneous gaps).[11]

Moreover, measurements of current-gate voltage (I vs V_{gate}) were carried out (Figure 2.18, right). As the graph shows, there is no gate-dependent transport since there is no molecule between the graphene-based electrodes. Only an increase of the current at the beginning is observed corresponding to the capacitive due to the high junction resistance.

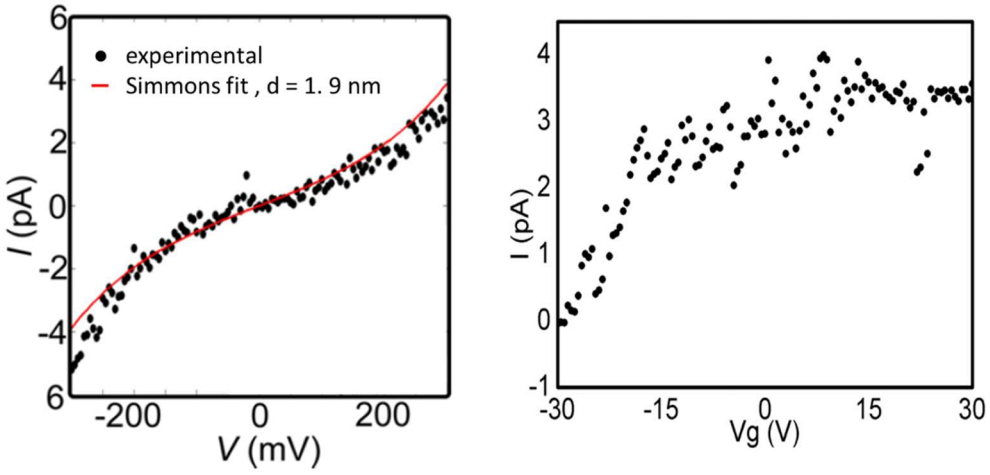

Figure 2.18: (left) Current-bias voltage trace of an open gap at liquid helium temperature before molecular deposition. (right) Current-gate voltage trace of an open gap.

(ii) Final I-V curves after 9ALCCMoid deposition and discussion of the results

In this work, the charge transport measurements were performed at liquid helium temperature and in vacuum following the same conditions applied for the empty gap

characterization. Figure 2.19 (left) shows the current-voltage (I vs V_{bias}) at V_{gate} = 0 after the deposition molecule (red line) and the comparison with the open gap (blue line).

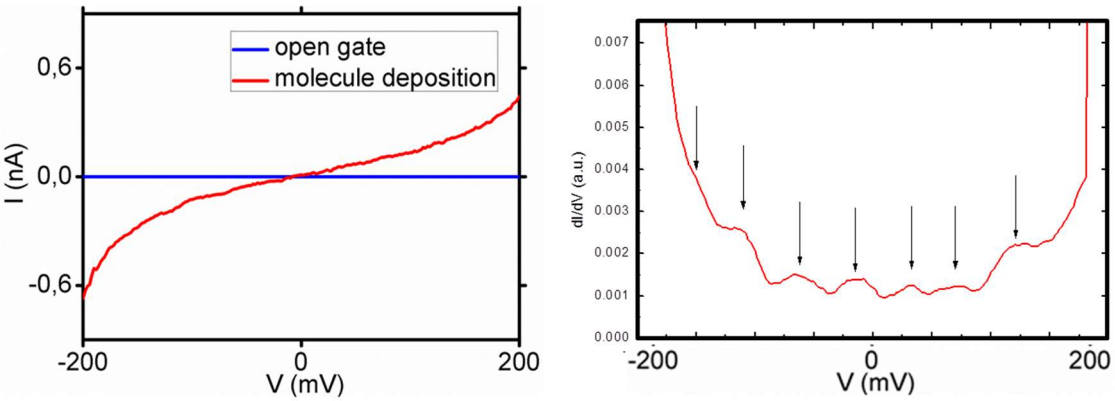

Figure 2.19: (left) I-V characteristics of the devices before and after molecule deposition at T = 4 K and V_{gate} = 0 (right) dI/dV traces measured after molecule deposition.

As it can be observed, there was an increase of the current intensity around 2 orders of magnitude after molecule deposition since the current could flowed through the molecule. When the V_{bias} is zero, no current intensity was observed due to the absence of resonance between the molecular orbitals of the molecule and conductance bands of the electrodes (Figure 2.4, a). Then, when the $V_{bias} \neq 0$, the energy of the conductance band of the electrodes were modified producing resonance with the molecular orbitals and therefore, intensity current was observed (Figure 2.4, b).

Comparing to previous work (performed with 9Accm), the new values obtained were similar.[11] This fact indicates that the extension of the new molecule, 9ALCCMoid, does not reduce the value of the current intensity. Therefore, the increase of the length is not a limiting factor which could be related to an improvement of the attachments (π-π interactions) between the electrodes and anchoring groups (anthracene groups in both molecules). Our studies also show that both molecules display a similar effective transport pathway.

The conductance values were obtained from the derivative of I-V_{bias} graphic (dI/dV) (Figure 2.19, right). In this case it was possible to see several current steps spaced with a constant distance of approximately 50 meV that corresponded to vibrational states (as it will be discussed later with the assistance of theoretical calculations).

In addition, the presence of the molecule was corroborated by measurements of current-gate voltage (I vs V_{gate}) with V_{bias} = 200 mV (Figure 2.20), where a clear gate-dependent transport was observed showing peaks which are fingerprints for resonant transport through a molecule coupled to electrodes.[11]

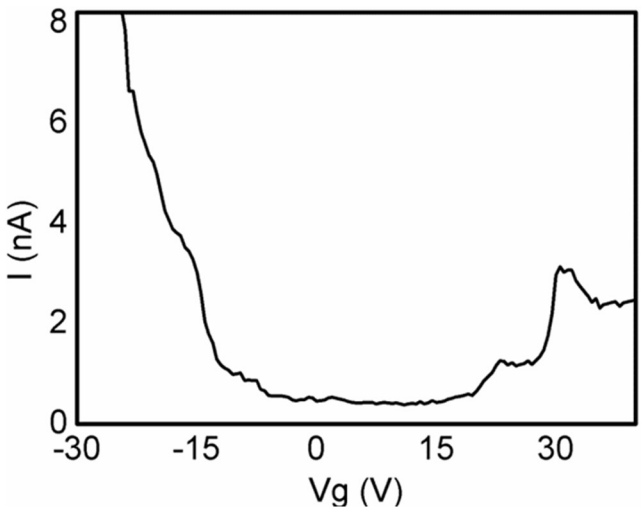

Figure 2.20: Current-gate voltage traces after molecular deposition.

The measurements show two high-current peaks at 23 and 31 V, in that order, that in the case of the empty gap system (Figure 2.18, right) did not appear. At this voltage potential, the molecular orbitals are disposed in resonance with the conductance band of electrodes (Figure 2.4, d). At lower potentials (15 to -15 V), the energy of the molecular orbitals was modified and no intensity current was observed (Figure 2.4, c). Then, additional resonance appeared below –20 V.

In order to perform a full characterization, conductance maps or "Coulomb diamond" diagrams were performed, in which I-V were taken between V_{bias} = ± 200 mV and V_{gate} = ± 40 V. This measurement allows the study of the single molecule origin of the conductance values. An example is shown in Figure 2.21 where the I (nA) color plot measured as a function of V_{bias} and V_{gate}.

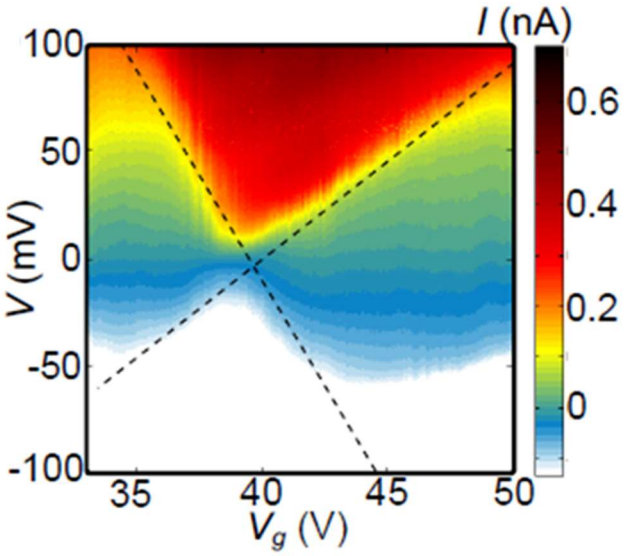

Figure 2.21: Current color plot measure of 9ALCCMoid as a function of V_{bias} and V_{gate} for positive V_{gate}.

Figure 2.21 shows the presence of two different diamonds. Within each diamond, depending on the conductivity value, two different regions can be differentiated: The red-yellow color region corresponds to high-current regions, so-called SET (Single electron tunneling) where the current passes through the molecular orbitals. In this region the intensity current is of the order of nanoampere. In contrast, the blue-white color region which corresponds to no current region, so-called Coulomb blockade regime and the current intensity is picoampere.[11]

The conductance values of the measurements were performed applying the derivative. Figure 2.22 (left), shows the dI/dV color plot numerically derived from the intensity current (I) measurements around the SET region.

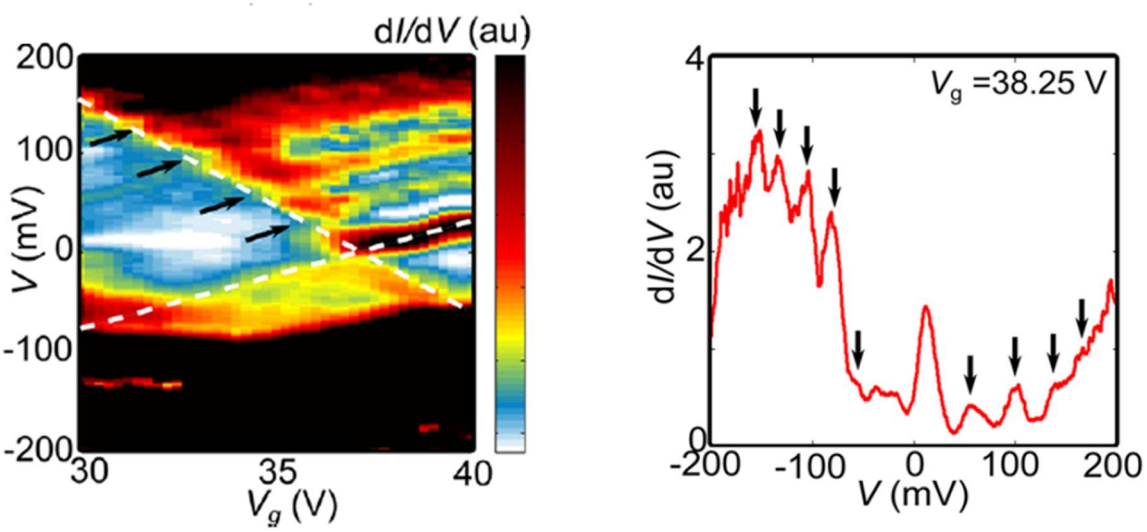

Figure 2.22: (left) dI/dV color plot derived from the measurements of Figure 2.21. (right) dI/dV trace measured at V_{gate} = 38.25 V. In both cases SET excitations are marked with black arrows.

From the positive and negative slops of the Coulomb diamond, it is possible to determine the parameter (β), which corresponds to the coupling between the gate electrode and the molecule.

This value can be estimated by using a capacitive model of a three-terminal transistor (Annex 2.8), providing a value of β = 0.006. This value is similar to others silicon devices with an SiO_2 thickness of 250 nm (that shows values about 10^{-3})**.**[19]

Within the diamond Coulomb representation, the presence of inelastic co-tunneling excitation in the Coulomb blockade regime (white-blue) was observed.[20] (Annex 2.9, not visible in the contrast of Figure 2.22). This transport process had no dependence with the V_{gate} since had a quantum origin and, as the Annex 2.10 shows, the conductive lines are straight. This transport process only is present when there is an intermediate coupling of the molecule with the electrodes, resulting in the hybridization of the molecule states and the electrodes bands. This fact, produces the broadening of quantized levels of the molecule (the temperature is also affected and for that reason the experiments are performed at liquid helium temperature). Therefore, the magnitude of the molecule-electrode coupling, which is quantified by the parameter (Γ), can be estimated as the broadening induces in the SET excitations. Thus, the value is estimated from the full width at half-maximum (FWHM) of the conductance peaks corresponding to the Coulomb diamond edge (Annex 2.10), obtaining a value of Γ = 10 meV.

This value is comparable with the coupling obtained between thiol groups and gold electrodes, indicating that in our case, the Γ intermediate value can be achieve with π-π stacked with the anthracene group of the molecule on few layer graphene (FLG) electrodes is remarkably strong.

On the other hand, this intermediate coupling (Γ) give rise to the presence of another transport. In this case, conductive lines corresponding to excitations states were observed (Figure 2.22, left). These lines (indicated with black arrows) were running parallel to the edges of the coulomb diamond and located at 46(±6), 79(±6), 115(±10), and 150(±10) mV at positive bias. This energy was obtained from the crossing of the lines with the opposite diamond edge. Below 25 mV, was not possible to determine the presence of lines due to the broadening of the Coulomb edge induce by the fact that Γ hinders their resolution.

More information was obtained of a trace dI/dV measured at V_{gate} = 38.25 V (Figure 2.22, right). Again, the excitations conductance peaks were signaled by black arrows. As can be seen in the Figure 2.22 (right), now the negative bias excitation became visible.

Considering the three possible origins of the presence of excitons conductance peaks: (i) magnetic, (ii) electronic or (iii) vibrational, the latter is the most probable origin due to an intermediate electron-phonon coupling. Magnetic states are discarded due to the 9ALCCMoid is a nonmagnetic molecule.[32] To elucidate the origin of such lines theoretical calculations were performed.

2.3.3 Theoretical calculations

To complement the experimental observations and corroborate the vibrational origin of the excitations conductance peaks, theoretical calculations through density functional theory (DFT) were performed. This study has been done thanks to the collaboration with Prof. Eliseo Ruiz from the University of Barcelona.

To carry out these calculations, a model structure was created from a single layer of graphene by deleting a ribbon of four carbon atoms and adding hydrogen atoms to saturate the carbon dangling bonds (mimic the gap between the electrodes). In this graphene layer, the 9ALCCMoid molecule was placed on top with one anthracene group located close to each graphene electrode. The optimized structure is shown in Figure 2.23 (left).

The transmission of the current through the molecule, as a function of the energy is represented in the Figure 2.23 (right). Related to the energy between the HOMO-LUMO, the gap is approximately 2 eV. In general, in the nonmagnetic molecules, the first excited electronic levels are expected to appear close to the energy of the gap. Therefore, in this case the energy is two orders of magnitude higher than the energy observed excitations. This fact indicates that the origin of the excited lines is not expected to be due to electronic excitations as it could be also thought.

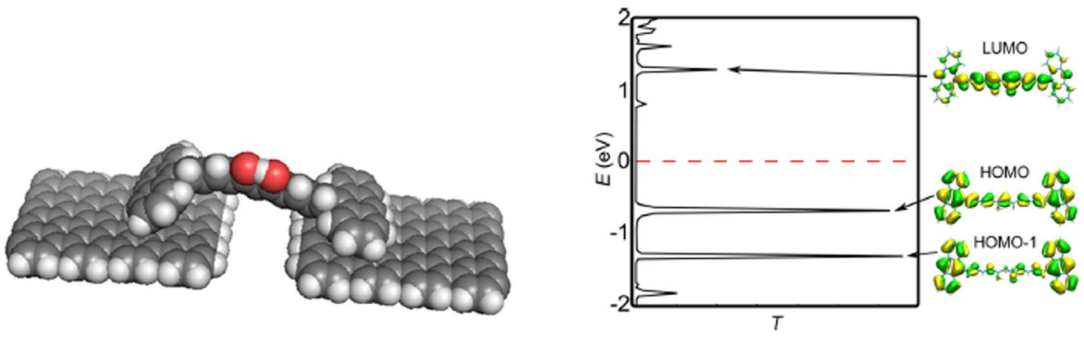

Figure 2.23: (left) Optimized geometry of the 9ALCCMoid molecule on top of graphene electrodes. (right) Transmission spectrum of the 9ALCCMoid and corresponding iso-surfaces for the HOMO, HOMO-1 and LUMO orbitals.

On the other hand, as we can see in the Figure 2.23 (right), the respective transmission peaks are associated with the energy iso-surface of the HOMO, HOMO-1 and LUMO. The lower transition corresponds to the LUMO, which is delocalized over the backbone of the molecule and the β-diketone group. In contrast, the HOMO and HOMO-1 are strongly present in the anthracene anchoring groups favoring the current flow through the molecule exhibiting in both cases higher transmission values, since are located closer to the Fermi level.

The calculated transmission pathway for the ALCCMoid on graphene electrodes is shown in the Figure 2.24. As can be seen, it is assumed that the electrons are injected from the left electrode and then, the transmission fades through the molecule when it reaches the right sides of the electrode. The calculations suggested that the electron tunnel through the molecule take places *via* the anthracene groups but also strongly via the backbone closer to the gap.

An explanation of this fact, could be explained due to the orbital LUMO, which is the most active for the electronic transport, is mainly centered in the backbone and barely present energy in the anthracene groups as it was explained before. This fact could explain also why similar currents were obtained for the 9ALCCMoid and the 9Accm. In both cases the transport path was essentially determined by the distance between the graphene source and drain electrodes.

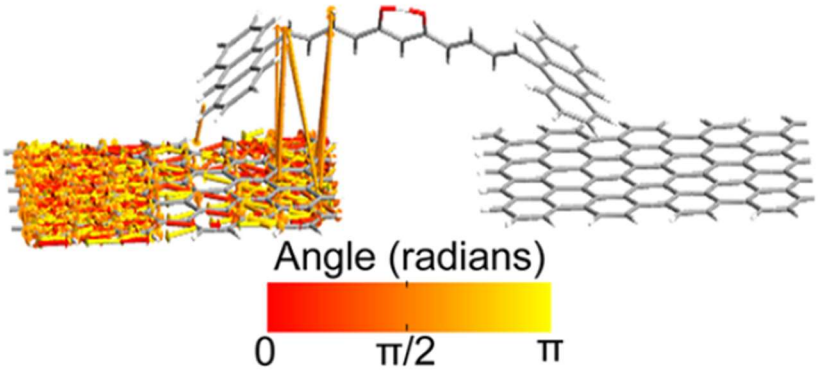

Figure 2.24: Transmission pathway of the 9ALCCMoid on graphene electrodes. The color scale is the direction of the transport in radians: 0 is for rightward transport, π is for leftward transport; and π/2 is transport perpendicular to the graphene plane.

Therefore, to corroborate the vibrational origin of the excitations observed, the calculations of the vibrational modes for the neutral, anions and cation CCMoid molecule without electrodes

were performed. Moreover, for each calculated vibrational mode, the electron-phonon coupling λ parameter was determined (this parameter indicates the coupling of the electron with the normal vibrational modes of the molecule). Figure 2.25 (left) represents the electron-phonon coupling λ of the different vibrational modes of the neutral CCMoid.

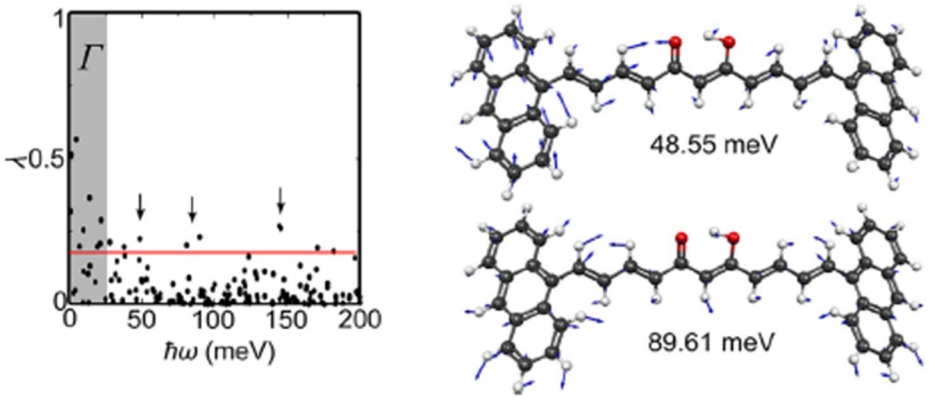

Figure 2.25: (left) Electron-phonon coupling λ of the vibrational modes of the molecules. The arrows mark the intermediate λ vibrations that match in energy with the experimental observations. The shaded area is the approximate broadening induced by the Γ on the Coulomb edge. (right) Two representations of vibrational modes with intermediate λ and energies of 48.55 and 89.61 meV.

As it can be seen, vibrational modes with energies around 50, 90 and 145 meV (indicated with black arrows) shown an intermediate λ (the most coupled and therefore the most expected to be observed experimentally). These energies, at intermediate λ, approximately match with the experimental energies of the SET lines observed in the Figure 2.22 (left) with an intermediate coupling (Γ) (Table 2.1). Therefore, the excitations observed can be attributed to vibrational modes of the molecule. In the Figure 2.25 (right) are represented two representative modes with energies of 48.55 and 89.61 meV. As it shown, the main contributions to the modes are torsions of the C-H bonds located in the anthracene anchoring groups.

Excitation	Experimental, E (meV)	Theory, E (meV)
1	150	145
2	115	X
3	79	89.6
4	46	48.5

Table 2.1: Energy of the SET excitations for 9ALCCMoid molecule and Energy of the Calculated Excitations with Intermediate Franck-Condon coupling.

2.4 Conclusions

In this section, a new CCMoid molecule (9ALCCMoid) was synthesized to be used as nanowire in graphene-electrode molecular transistors devices. This new ligand presented a different structure compare to the common CCMoids, since it was increased the number of carbon of the conjugated skeleton, going from 7 to 11 carbon atoms. The main objective of this new design was focused on achieving better interactions between the molecule and few-layer graphene electrodes. This improvement would be given because the new molecule will fit better between the gap generated by the electromigration process in few layer graphene (FLG) nano-devices. Therefore, an improvement of the conductance properties was explored by comparing with previous work performed using 9Accm (which contains conjugated chain of 7 carbon atoms).

The synthesis of the molecule was carried out following Pabon's method. Apart from the conjugated chain of 11 carbons, the 9ALCCMoid contains anthracene groups located in both sides of the chain. These anthracenes groups could act as anchoring groups with the graphene electrodes via π-π stacking. The possible presence of different stereoisomers due to the presence of the conjugated chain was studied by ^{1}H NMR and UV-Visible experiments. In both cases, consistent spectra in time were obtained, thus ensuring its stability in solution.

The gap generation was carried out by electroburning, in which high voltage values were applied through the graphene layer giving rise to the break process in a controlled way. The open gap systems were characterized at liquid helium temperature measuring the intensity current dependence with the V_{gate} and V_{bias}. In the case of V_{gate}, no intensity current dependence was obtained since no molecule was present. In contrast, V_{bias} showed a S-shape exponential dependence commonly of the tunnel current. By the fit of the I-V_{bias} measure, a distance of 1.9 nm between the electrodes was obtained.

The deposition of the molecule was performed by dropcasting using CH_2Cl_2 as a solvent. The characterization showed an increase of the intensity current of two orders of magnitude and dependence with the V_{gate}. The conductance maps showed the Coulomb Diamond where a high-current SET and coulomb blockage regions were differentiated. This measurement showed an intermediate coupling to the electrodes (Γ = 10 meV) originated for the π-π stacked molecules on few layer graphene electrodes, although theoretical calculations suggested that the molecular backbone can take an active part as a direct transport pathway to the electrodes. Moreover, the presence of intermediate coupling electrodes resulted in the

appearance of co-tunneling regimen in the coulomb blockage region and high-energy lines excitations in the SET region running parallel to the Coulomb edges. The origin of the excitations lines was attributed to vibrational states of the molecule due to intermediate electron-phonon couplings. This fact was then corroborated by DFT calculations. These vibrational modes were associated with torsions of the C-H bonds located in the anchoring groups.

2.5 Experimental Part

Materials: All the reagents used in the work were used as they were received from the commercial company, without further purification.

Synthesis of 9ALCCMoid (1)

The synthesis of 9ALCCMoid was carried out following the Pabon's method. Acetylacetonate (0.83 g, 8.30 mmol was added in a bottom flask with boron oxide (0.44 g, 6.25 mmol) and AcOEt (10 mL). The mixture was heated at 40 ˚C for 30 min. Then, in a separated flask a solution of 3-(9-anthryl)acrolein (4.1 g, 17.65 mmol) and tributyl borate (8.12 g, 35.30 mmol) in AcOEt (20 mL) was prepared and added to the previous. The mixture was stirred at 40 ˚C for 3 h. After cooling down, an excess of n-butylamine (0.44 mL, 4.45 mmol) in AcOEt (10 mL) was added dropwise. The final reaction was stirred at room temperature for 2 days. After that, a red solid precipitate appeared. The solid was filtered and washed with H_2O, MeOH and Et_2O to remove impurities. The yield was 87 %. Crystals of 9ALCCCMoid were achieved by slow evaporation using THF.

IR KBr pellet (ν/cm^{-1}): 3424br, 3068s, 3041s, 3028s, 1603vs, 1506s, 1440s, 1287s, 1121vs, 1000vs, 958 vs, 884vs, 842s, 782s, 728vs, 545s. Elemental analysis calculated for $C_{39}H_{28}O_2 \cdot 0.5H_2O$ (537.21 g·mol^{-1}): C 87.11; H 5.44. Found: C 87.01; H 5.37. ^{1}H-NMR (300 MHz, $CDCl_3$): δ 8.43 (s, 2H), 8.27 (m, 4H), 8.02 (m, 4H), 7.87 (d, 2H), 7.76 (dd, 2H), 7.50 (m, 8H), 6.85 (dd, 2H), 6.26 (d, 2H), 5.81 (s, 1H). MALDI$^+$ (m/z): 527.2 [M-H]$^+$.

Nanofabrication

Nano-device construction

In a first step, a silicon wafer coated with 285 nm of silicon oxide was cleaned by soaking this substrate into a nitric solution for 2 minutes and washed later with acetone. Then, few drops

of photoresist PMMA (Polymethyl methacrylate) were added using spin-coating and the substrate was left for 10 minutes in the oven at 180 ˚C for 10 minutes. After, by electro-beam lithography the circuit was drawn and immediately after, the processing of the substrate was performed by the use of MIBK (Methyl isobutyl ketone) in isopropanol which removes the extra resin. After that, evaporation of gold on the surface was performed, followed by the immersion of the whole system in cold acetone and dichloromethane.

Next, MLG (Multi-layer Graphene) were deposited by mechanical exfoliation onto the SiO_2 and flakes with thickness of approximately 10 nm were chosen by their color contrast under an optical microscope. Then, the process of adding the photoresist PMMA was repeated, and gold pads were deposited on the top of the selected flakes by evaporating gold with electro-beam lithography. Finally, the device was deposited on a carrier and the connections with the circuit were done using Al wire.

Gap generation

The gap between the FLG (Few layer graphene) flakes was carried out by electroburning in open air at room temperature. The initial device resistances values at low bias were between 200 Ω and 500 Ω. A voltage bias was applied to the graphite flake while the current (I) was continuously recorded. The variation in the conductance was monitored and as soon as conductance drops 10 % within the last 200 mV, the voltage was swept to zero. The gap was considered open when the conductance was around 10^{-5} mA, and the resistance in the range of 500 MΩ to 10 GΩ.

Characterization of the empty gap

The characterization of the empty gap was performed at room temperature and at liquid helium temperature (4.3 K) under vacuum. Electrical measurements (I vs V_{bias}) in a range of $-0.4 < V_{bias} < 0.4$ and (I vs V_{gate}) in a range of $-30 < V_{gate} < 30$ with $V_{bias} = 0.3$ V were performed.

Molecular deposition

9ALCCMoid was deposited at room temperature by drop-casting, having a 0.1 mM concentration of the CCMoid in CH_2Cl_2. Then, the system was left for 30 min and after that the vacuum was applied for another 30 min to remove the solvent.

Device characterization

The characterization of the devices was carried out under the same conditions than the empty gap. Only ≈ 0.1 % of the devices (meaning 2 from a total of 23 nanodevices) showed an increase of the current after molecule deposition.

2.6 References

[1] H. NALWA, in *Silicon-Based Mater. Devices*, Elsevier, **2001**, pp. xiii–xiv.

[2] D. Mijatovic, J. C. T. Eijkel, A. van den Berg, *Lab Chip* **2005**, *5*, 492.

[3] D. Xiang, X. Wang, C. Jia, T. Lee, X. Guo, *Chem. Rev.* **2016**, *116*, 4318–4440.

[4] H. Song, M. A. Reed, T. Lee, *Adv. Mater.* **2011**, *23*, 1583–1608.

[5] A. Aviram, M. A. Ratner, *Chem. Phys. Lett.* **1974**, *29*, 277–283.

[6] B. W. Heinrich, L. Braun, J. I. Pascual, K. J. Franke, *Nano Lett.* **2015**, *15*, 4024–4028.

[7] B. Xu, *Science (80-.).* **2003**, *301*, 1221–1223.

[8] M. A. Reed, C. Zhou, C. J. Muller, T. P. Burgin, J. M. Tour, *Science (80-.).* **1997**, *278*, 252–254.

[9] K. Ullmann, P. B. Coto, S. Leitherer, A. Molina-Ontoria, N. Martín, M. Thoss, H. B. Weber, *Nano Lett.* **2015**, *15*, 3512–3518.

[10] J. A. Mol, C. S. Lau, W. J. M. Lewis, H. Sadeghi, C. Roche, A. Cnossen, J. H. Warner, C. J. Lambert, H. L. Anderson, G. A. D. Briggs, *Nanoscale* **2015**, *7*, 13181–13185.

[11] F. Prins, A. Barreiro, J. W. Ruitenberg, J. S. Seldenthuis, N. Aliaga-Alcalde, L. M. K. Vandersypen, H. S. J. Van Der Zant, *Nano Lett.* **2011**, *11*, 4607–4611.

[12] F. Prins, T. Hayashi, B. J. A. de Vos van Steenwijk, B. Gao, E. A. Osorio, K. Muraki, H. S. J. van der Zant, *Appl. Phys. Lett.* **2009**, *94*, 123108.

[13] C. W. Marquardt, S. Grunder, A. Błaszczyk, S. Dehm, F. Hennrich, H. V. Löhneysen, M. Mayor, R. Krupke, *Nat. Nanotechnol.* **2010**, *5*, 863–867.

[14] X. Guo, J. P. Small, J. E. Klare, Y. Wang, M. S. Purewal, I. W. Tam, B. H. Hong, R. Caldwell, L. Huang, S. O'Brien, et al., *Science (80-.).* **2006**, *311*, 356–359.

[15] E. Burzurí, F. Prins, H. S. J. van der Zant, *Graphene* **2012**, *01*, 26–29.

[16] J. A. Mol, C. S. Lau, W. J. M. Lewis, H. Sadeghi, C. Roche, A. Cnossen, J. H. Warner, C. J. Lambert, H. L. Anderson, G. A. D. Briggs, *Nanoscale* **2015**, *7*, 13181–13185.

[17] V. M. García-Suárez, R. Ferradás, D. Carrascal, J. Ferrer, *Phys. Rev. B - Condens. Matter Mater. Phys.* **2013**, *87*, 1–6.

[18] H. Park, J. Park, A. K. L. Lim, E. H. Anderson, A. P. Alivisatos, P. L. McEuen, *Nature* **2000**, *407*, 57–60.

[19] E. A. Osorio, Quantum Transport through Single Molecules, University of Delft, **2009**.

[20] M. L. Perrin, E. Burzurí, H. S. J. Van Der Zant, *Chem. Soc. Rev* **2015**, *44*, 835–1030.

[21] D. Carrascal, V. M. García-Suárez, J. Ferrer, *Phys. Rev. B - Condens. Matter Mater. Phys.* **2012**, *85*, 1–11.

[22] H. J. Pabon, *Recl. Trav. Chim. Pays-Bas* **1964**, *83*, 379.

[23] S. S. Hepperle, Q. Li, A. L. L. East, *J. Phys. Chem. A* **2005**, *109*, 10975–10981.

[24] N. Aliaga-Alcalde, P. Marqués-Gallego, M. Kraaijkamp, C. Herranz-Lancho, H. Den Dulk, H. Görner, O. Roubeau, S. J. Teat, T. Weyhermüller, J. Reedijk, *Inorg. Chem.* **2010**, *49*, 9655–9663.

[25] A. Castellanos-Gomez, R. H. M. Smit, N. Agraït, G. Rubio-Bollinger, *Carbon N. Y.* **2012**, *50*, 932–938.

[26] P. Qi, A. Javey, M. Rolandi, Q. Wang, E. Yenilmez, H. Dai, *J. Am. Chem. Soc.* **2004**, *126*, 11774–11775.

[27] S. G. Sarwat, P. Gehring, G. Rodriguez Hernandez, J. H. Warner, G. A. D. Briggs, J. A. Mol, H. Bhaskaran, *Nano Lett.* **2017**, *17*, 3688–3693.

[28] L. Shen, M. Zeng, S. Yang, C. Zhang, **2010**, 11481–11486.

[29] J. H. Warner, M. H. Rümmeli, L. Ge, T. Gemming, B. Montanari, N. M. Harrison, B. Büchner, G. A. D. Briggs, *Nat. Nanotechnol.* **2009**, *4*, 500–504.

[30] A. Barreiro, H. S. J. Van Der Zant, L. M. K. Vandersypen, *Nano Lett.* **2012**, *12*, 6096–6100.

[31] J. G. Simmons, *J. Appl. Phys.* **1963**, *34*, 1793–1803.

[32] S. Wagner, F. Kisslinger, S. Ballmann, F. Schramm, R. Chandrasekar, T. Bodenstein, O. Fuhr, D. Secker, K. Fink, M. Ruben, et al., *Nat. Nanotechnol.* **2013**, *8*, 575–579.

SECTION III:

MOLECULAR SENSORS

Immobilization of fluorescent Curcuminoids on functionalized SiO_2

3.1 Introduction

Self-assembly surface organization

Currently, the design of molecular based materials for electronic applications has raised a great deal of expectation within the scientific community.[1] Molecular scaled devices would lead to the exponential improvement on the storage density; however, it is mandatory to preserve order and control on the position of molecules.[2] For this reason, one particularly interesting goal in nanoscience focuses on the development of protocols for the fabrication of ordered surfaces based on these nanostructures. The proper characterization of the molecules on surfaces is crucial since on surfaces they may present a different environment from that found in the solid state or solution, and therefore, molecules on surfaces could display different energy, electronic states, reactivity and structures.

To carry out the fabrication of these nanostructures, two different strategies can be followed[3]: (i) top down method, creating shape structures from bulk materials, based on miniaturization (systematic division of the bulk to achieve nanoscale systems) and (ii) bottom up approach, which builds up highly ordered micro- and nano-structures using elementary components through chemical processes. This section describes the methodology used toward the formation of patterns on surfaces based on CCMoids through the latest approach.

Self-assembled Monolayers (SAMs)

Self-assembled monolayers are considered versatile nanostructures since they provide a convenient, flexible and simple way to produce ordered surfaces with specific functionalities that can be used for a wide range of applications.

In general, the stability, packing and orientation of these SAMs will depend on the interaction between the substrate and the adsorbate and the intermolecular interactions between the adsorbates. Depending on the nature of the substrate and the adsorbate, the molecules can be organized in different ways by (i) covalent attachments (ii) electrostatic interactions, (iii) hydrogen bonding, (iv) hydrophobic interactions or (v) van der Waals forces.[4]

In the case of the first example, most of the surfaces present a lack of chemically active functional groups being not possible the direct attachment of molecules by covalent interaction, therefore a previous activation/functionalization process of the surfaces is required in order to create new reactive sites. In the case of a functionalization procedure, the structure of the molecules involved

(Figure 3.1): (i) an anchoring group that has a specific affinity for the substrate, (ii) an aliphatic chain that produces the monolayer organization due to the presence of Van der Waals forces (non-covalent interactions) between the chains and (iii) a terminal group. These three parts, characterize the SAMs, defining their physico-chemical properties and furthermore, their reactive properties on surfaces.

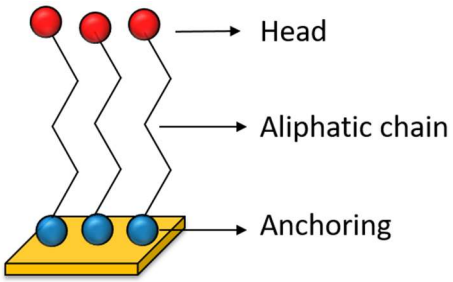

Figure 3.1: General scheme of a SAM

As it was mentioned before, the main objective in this section was the immobilization of CCMoid on surfaces. To carry out this purpose, the functionalization of SiO_2 (substrate used for all the experiments described here), with two types of SAMs, was performed.

This first functionalization focuses on the formation of two different SAMS varying their specific terminal groups in each case. The presence of the latest would allow selective reactions with functional groups from the CCMoids giving rise to the CCMoid immobilization. Thus, the first SAM carried out contained an amide group (which reacted selectively with acidic groups from the CCMoid). The second SAM contained an azide group (which reacted selectively with an alkyne group from the CCMoid by click chemistry.

Once the initial functionalizations were carried out, a second step consisting in the immobilization of the CCMoid by cleavage with the SAMs, was performed, respectively. This step was carried out by the use of a technique known as Microcontact Printing (μ-CP), which is described in detail below.

Microcontact Printing (μ-CP)

The Microcontact Printing (μ-CP) is a soft lithography technique.[5–9] It is a powerful method for the preparation of micropatterned on homogeneous self-assembled monolayers (SAMs).[9] Initially, this technique was proposed by Kumar and Whitesides[10] in 1993 for the purpose of immobilizing alkanethiols on gold surfaces. However, due to its versatile features (experimental simplicity,

reproducibility, low cost, etc) was quickly established in others fields with different applications in physics[11] , chemistry[12] and biology[13].

The concept of this technique is very simple[5,9] (Figure 3.2): an elastomeric stamp, generally the polydimethylsiloxane (PDMS), is fabricated by casting the pre-polymer of PDMS on a master (usually a SiO_2 wafer) whose surface has been previously patterned with a specific relief using photolithography. Then, the PDMS stamp is wetted with an ink solution (in our case containing the acid or alkyne CCMoid) to transfer the molecules by putting into direct contact with functionalized surfaces. This fact gives rises to the formation of a monolayer on the surface by replicating the pattern of the stamp on the substrate.

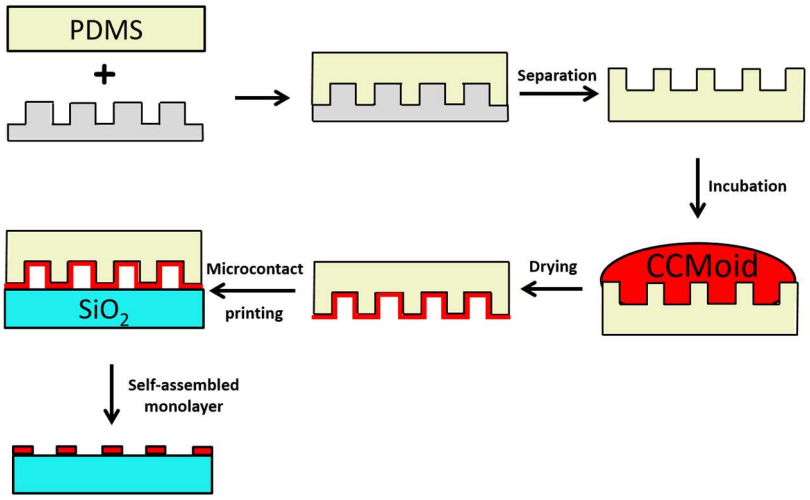

Figure 3.2: General steps in a Microcontact printing process.

Even though the concept of the μ-CP is very simple; there are many parameters which can affect to the performance, making at times very hard to get reproducible protocols. Thus, this work has also focused on finding a protocol that ensures optimal conditions to obtain reproducible results. These studies are explained in more detail below.

Hence, by means of this technique the immobilization of two CCMoids that contain specific functional groups (acid/alkyne) was carried out. These groups, as was mentioned before, would react selectively with the surface (acid and amide; alkyne and azide, respectively) giving rise to the formation of covalent bonds in both cases (Figure 3.3).

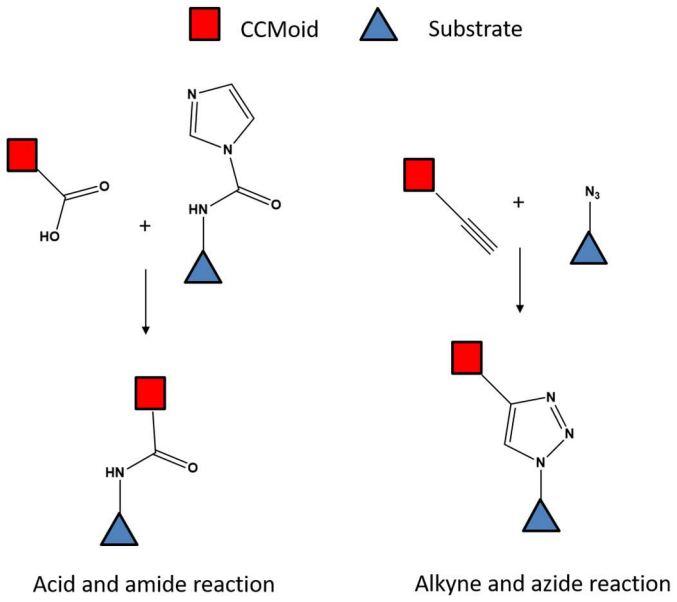

Figure 3.3: General schemes of the covalent anchoring reactions between the CCMoid (contained in the PDMS stamp) and the functionalized substrates

In both cases, these immobilized CCMoids contained a chromophore group (pyrene) situated at both lateral positions (hence, arms of the CCMoids). This fact allows the characterization of the systems by optical fluorescence microscope, among additional techniques.

Fluorescence is extremely sensible to the environment (solvents, pH, temperature, coordination metals, etc). This fact, together with the metal coordination ability of the CCMoids through their β-diketone group, opened up the opportunity of studying these systems as chemical sensors.

Therefore, a detailed study of the influence caused by the coordination to a semimetal (in our case boron) in the properties of these systems was also performed.

3.2 Objectives

This section focuses on the immobilization of CCMoids on functionalized surfaces for their applications as chemical sensors. To carry out this study, two new fluorescent CCMoids, with different functional groups in their central positions (acidic and alkyne moieties), have been synthetized. The immobilization of these CCMoids has been performed by means of μ-CP technique on previously functionalized SiO_2 surfaces (containing amide and azide endings groups). The characterization of the SAMs formation was carried out by using contact angle technique and fluorescence optical microscopy. Moreover, a comparative study of the fluorescence properties of

both systems was performed in solution, in the solid state and on surfaces. Finally, the affinity of CCMoids for boron and the formation of a boron-CCMoid compounds were explored taking advantage of the fluorescence properties of the final systems.

3.3 Results and Discussion

3.3.1 Experimental section

Synthesis of Pyr-acidCCMoid

Pyr-acidCCMoid (Figure 3.4) displays a β-diketone group in the center of a conjugated backbone made of 7 carbon atoms with two pyrene groups located in both sides of the molecule. These groups, together with the conjugated chain, will provide fluorescence properties to the molecule. In the middle of the conjugated chain there is also an alkane chain that ends in a carboxylic group. The presence of this carboxylic group allows the immobilization of the molecule reacting with the amide groups situated on the functionalized surface.

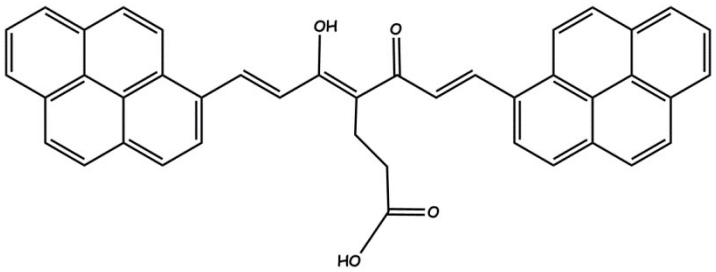

Figure 3.4: Representation of Pyr-acidCCMoid

The molecule was synthesized following Pabon's method[14], (explained in the general introduction), using 4-acetyl-5-oxohexanoic acid as a reagent instead of the common acetylacetonate (acac). The 4-acetyl-5-oxohexanoic acid was obtained from the hydrolysis of an ester group of the commercial reagent Methyl 4-acetyl-5-oxohexanoate (Figure 3.5).

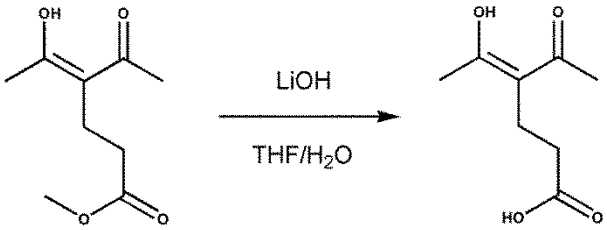

Figure 3.5: Reaction scheme of the hydrolysis of the ester group.

The hydrolysis of the ester group from the acac derivative was carried out in basic media using LiOH in THF/H_2O at room temperature overnight. The reaction was followed by TLC. When the signal corresponding to the ester product disappeared, the reaction was stopped by the addition of small amounts of H_2SO_4. It's important not to exceed the reaction time since the exposition to prolonged times in basic media leads to the degradation of the β-diketone (the molecule breaks in the central position). Then, THF was removed to facilitate the extraction of the product since it is miscible with the water. Once it was removed, the organic molecule was extracted using CH_2Cl_2 and brine. Finally, the organic extractions were dried with Na_2SO_4 and concentrated with a rotatory evaporator obtaining a yellow oil in a 49 % yield.

The next step consists in the formation of the CCMoid and, as it was mentioned before, the CCMoid synthesis was carried out following Pabon's method. In this case was necessary the use of an excess of B_2O_3 to form the boron intermediate compound because boron could also coordinate to the carboxylic acid. Finally, after washing with H_2O, MeOH and Et_2O the corresponding curcuminoid was obtained in an 80 % yield.

The ^1H NMR spectrum of the molecule was measured in DMSO (Figure 3.6). The assignment of all the aromatic signals was not possible due to the presence of a large numbers of signals. This fact relates to the loss of symmetry (by the presence of the "leg") and the presence of pyrene groups.

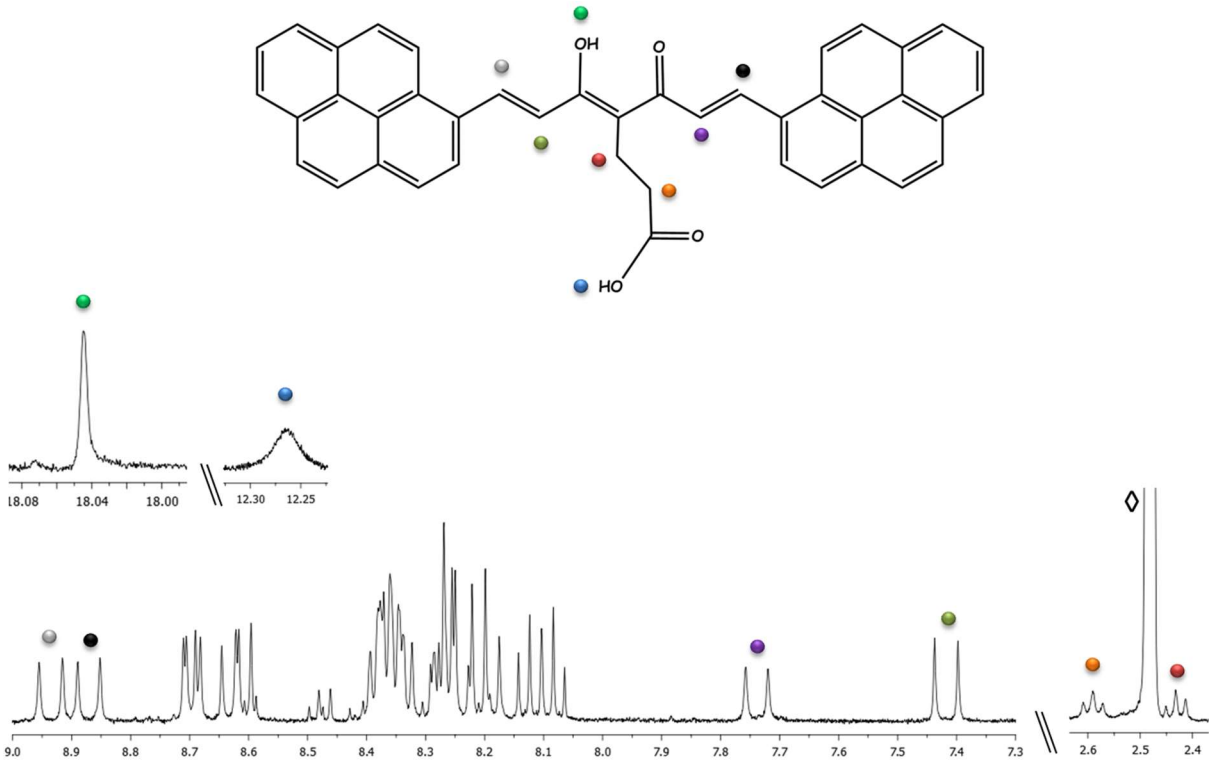

Figure 3.6: ^{1}H NMR spectrum of Pyr-acidCCMoid in DMSO. ◊ DMS*O*

Nevertheless, at low fields it was possible to differentiate a broad band at 12.2 ppm corresponding to the proton from the carboxylic group (blue spot) and a singlet at 18.0 ppm, corresponding to the proton from the enol group (green spot). In this case, the singlet around 6 ppm, which corresponds to the methane proton of the enol form was not observed since the position is functionalized. In relation to the signals of the conjugated chain, four different signals were observed due to the loss of the symmetry. Their assignment was performed by comparison with predictive models. The coupling constant of their signals (J ≈ 15 Hz) confirm the presence of the E isomer. On the other hand, at high fields two triplets were observed corresponding to the carbon leg.

The solid was also characterized by Mass Spectrometry which is shown in the Annex 3.1.

Synthesis of Pyr-alkyneCCMoid

As in the previous system, Pyr-alkyneCCMoid (Figure 3.7), contains a β-diketone group in the middle of the conjugated backbone and two pyrene groups on the sides. In this case, the "leg" position is functionalized with an alkyne attached through a carbon atom. This group allows the reaction with azide groups as it will be seen later.

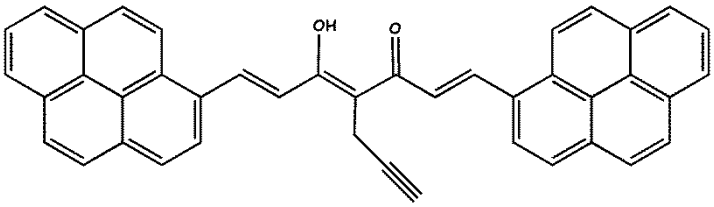

Figure 3.7: Representation of Pyr-alkyneCCMoid

For the synthesis of the Pyr-alkyneCCMoid, first of all it was necessary to synthetized the 3-(prop-2-ynyl)pentane-2,4-dione. This compound was obtained from the reaction between the acetylacetonate (acac) and propargyl bromide. (Figure 3.8) **(REF12).**[15]

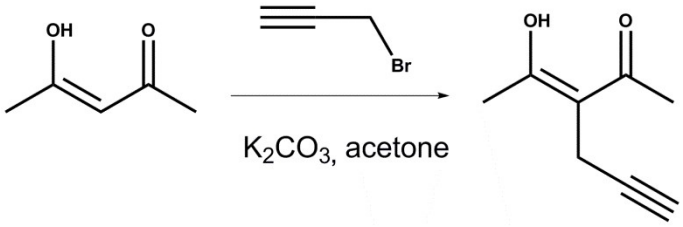

Figure 3.8: Reaction scheme of the synthesis of 3-(prop-2-ynyl)pentane-2,4-dione.

Initially, the acetylacetonate was deprotonated using a salt of K_2CO_3 in acetone under N_2 and the solution becomes yellow. Then, a solution of propargyl bromide was added and the mixture was stirred overnight. The mixture was filtered and the solution evaporated using a rotatory evaporator. Small amounts of a colorless crude were achieved and their purification was performed using a preparative plate instead of a chromatography column. The corresponding fraction give rises to yellow crystals in a 13 % yield.

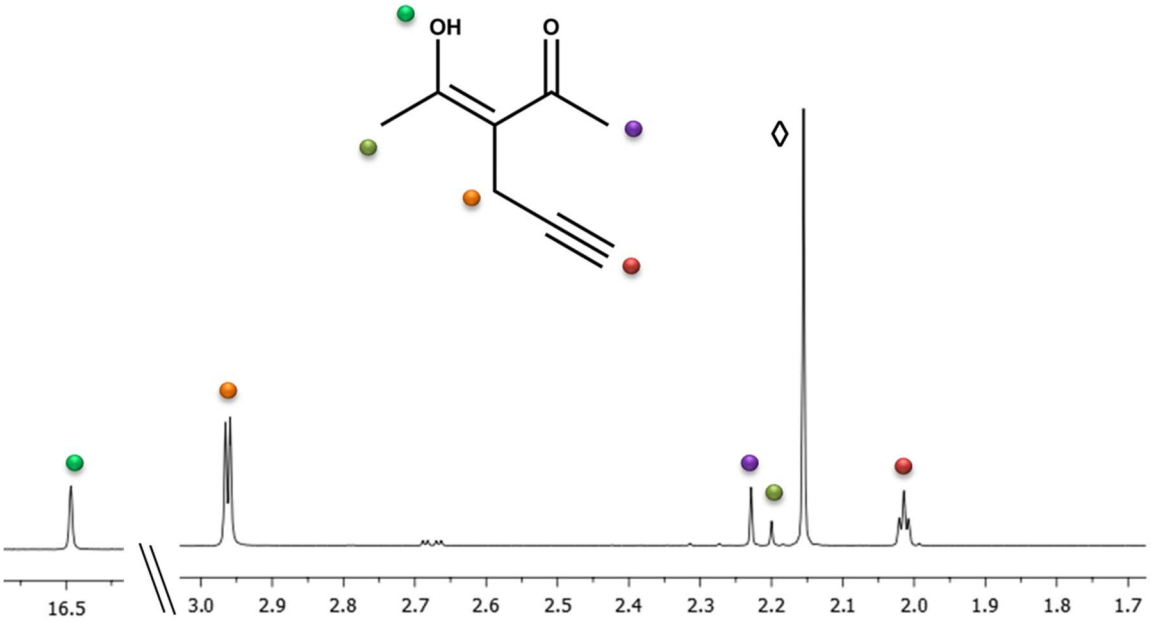

Figure 3.9: ^{1}H NMR spectrum of 3-(prop-2-ynyl)pentane-2,4-dione in $CDCl_3$. ◊ acetone

To achieve the Pyr-alkyneCCMoid the same procedure described before was carried out having a yield of 64 %.

The ^{1}H NMR spectrum of the molecule was measured in $CDCl_3$ (Figure 3.10). As it can be seen, the number of signals is lower compared to the previous systems indicating the presence of symmetry despite having the central part functionalized. In this case, the conjugated chain shows only two signals with coupling constant of 15 Hz.

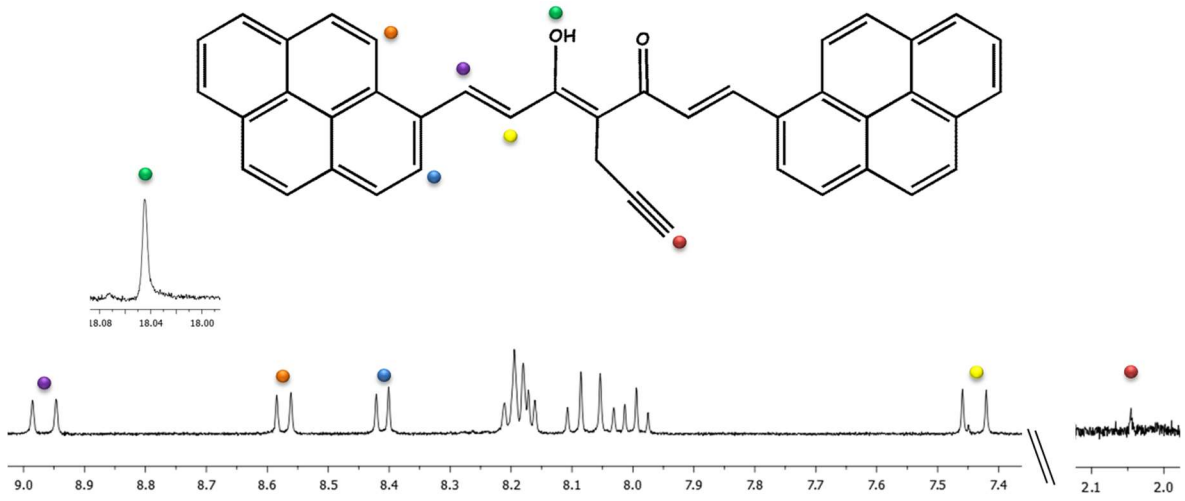

Figure 3.10: ^{1}H NMR spectrum of Pyr-alkyneCCMoid in $CDCl_3$.

The solid was also characterized by Mass Spectrometry which is shown in the Annex 3.1.

Synthesis of Boron-CCMoid

The coordination of the boron compound in solution was carried out by modifying the method described in the literature[16,17] using boron trifluoride diethyl etherate ($BF_3 \cdot Et_2O$) in CH_2Cl_2 in a microwave (MW) reactor during 5 min at 60 ˚C.

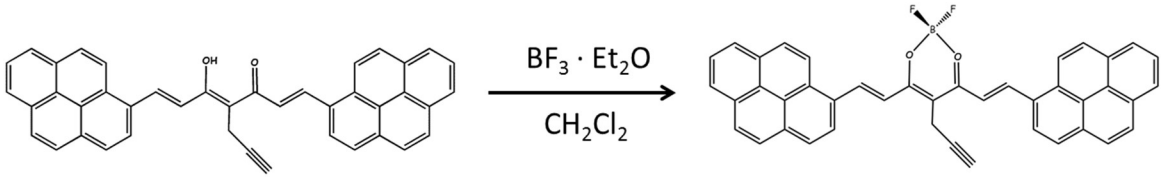

Figure 3.11: Scheme of the boron formation.

3.3.2 Characterization in solution and the solid state

UV-Vis Absorption and Fluorescence Studies

Pyr-acid-CCMoid and Pyr-alkyneCCMoid

The electronic spectra in CH_2Cl_2 solution of Pyr-acidCCMoid and Pyr-alkyneCCMoid with a concentration of 10^{-5} M are shown in Figure 3.12. Both systems presented three vibrational bands typical in systems that contain pyrene groups[18] corresponding to π-π* (274 nm), n- π* (343 and 396) transitions. Then, in both cases a broad band was observed at 479 and 473 nm for the acid and alkyne compound respectively. This band, as we have seen in previous sections is common for all the CCMoids related to the central skeleton.

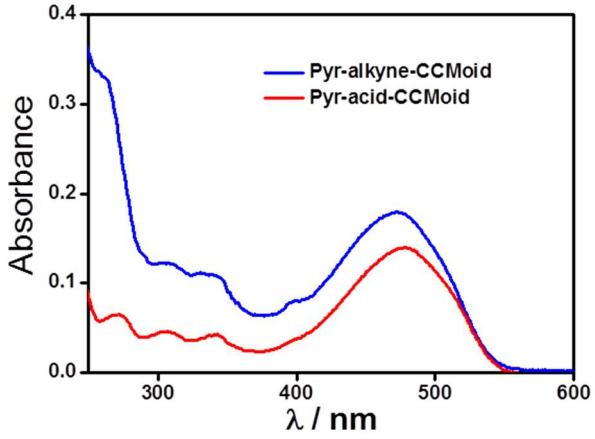

Figure 3.12: UV-Vis spectra of Pyr-acidCCMoid (red) and Pyr-alkyneCCMoid (blue) in CH_2Cl_2 with a concentration of 10^{-5} M.

Regarding the fluorescence emission studies, they were performed in solution (Figure 3.13, left) and the solid state (Figure 3.13, right). In relation to the solution studies, they were carried out in CH_2Cl_2 solution at 10^{-5} M exciting at 485 nm. In both cases, broad bands at 576 and at 578 nm were observed, corresponding to the Pyr-acid-CCMoid and Pyr-alkyne-CCMoid respectively. The emission corresponding to the Pyr-alkyne-CCMoid in the solid state show a broad band shifted at 690 nm. This shift was due to the fluorescent response of the molecule together with the intermolecular interactions among the neighbors.

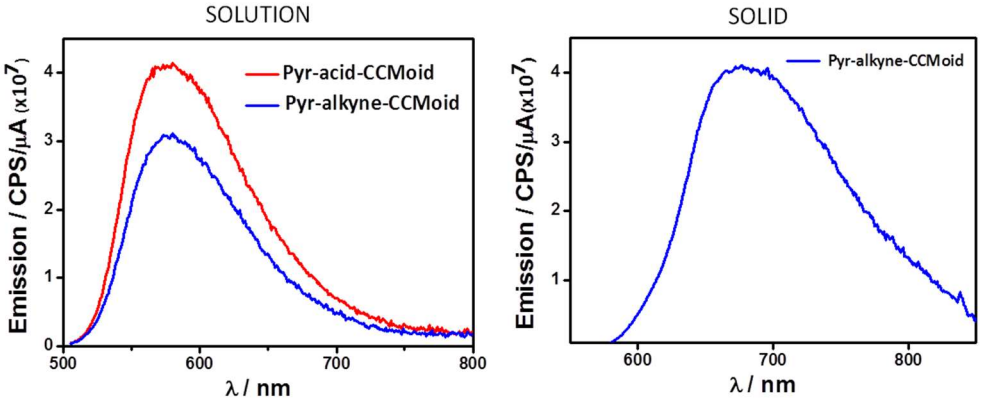

Figure 3.13: (left) Fluorescence spectra of Pyr-acidCCMoid (red) and Pyr-alkyneCCMoid (blue) in CH_2Cl_2 with a concentration of 10^{-5} M. (right) Fluorescence spectra of Pyr-alkyneCCMoid in solid state.

Boron-CCMoid

UV-Vis absorption and Fluorescence emission measurements were repeated in solution for the compound BF_2-Pyr-alkyneCCMoid. Figure 3.14 (left) shows the UV-Vis absorption spectra of the

boron-CCMoid compared to the non-coordinated (free CCMoid). As it can be seen, the boron compound presents a broad band at 553 nm displaying a red shift of 80 nm compared to the free CCMoid. In relation to the emission studies (Figure 3.14, right), the boron compound followed the same behavior displaying a red broad band shift at 680 nm. This red shift emission is commonly in systems that present the BF_2 group.[16,19,20]

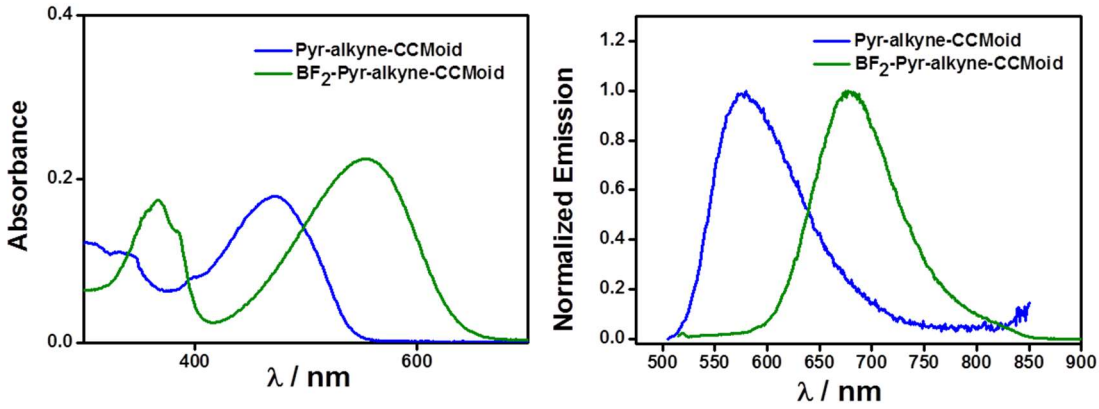

Figure 3.14: (left) UV-Vis spectra of Pyr-alkyneCCMoid (blue) and BF_2-Pyr-alkyneCCMoid (green) in CH_2Cl_2. (right) Comparison fluorescence normalized emission of Pyr-alkyneCCMoid (blue) and BF_2-Pyr-alkyneCCMoid (green).

3.3.3 Immobilization on functionalized surfaces

For the immobilization of the CCMoid on surfaces, three different steps were followed:

(i) Glass surface functionalization with SAMs of IM SAM (IM = imidazole SAM) and N_3 SAM (N_3 = azide SAM).

(ii) Formation of PDMS stamps and incubation with the corresponding CCMoid.

(iii) Microcontact printing process.

The immobilizations of CCMoids on surfaces were carried out by means of microcontact printing (μ-CP). For this purpose, the glass surfaces were functionalized forming SAMs with two different functional groups (IM SAM and N_3 SAM, respectively). On the other hand, formation of the stamps with PDMS and later incubation with a solution of the corresponding CCMoid (Pyr-acidCCMoid and Pyr-alkyneCCMoid) were carried out with a last step where the wetted stamps are left in contact with the previous functionalized surface.

3.3.3.1 SAMs formation

As it was mentioned, two SAMs with different functional group were performed. On one hand the formation of imidazole SAM (IM SAM)[21] to immobilize the CCMoid which contains the carboxylic group (Pyr-acidCCMoid) and on the other, the formation of azide SAM (N_3 SAM)[22–24] to immobilize the CCMoid with alkyne group (Pyr-alkyneCCMoid).

Formation of imidazole SAMs (IM SAM)

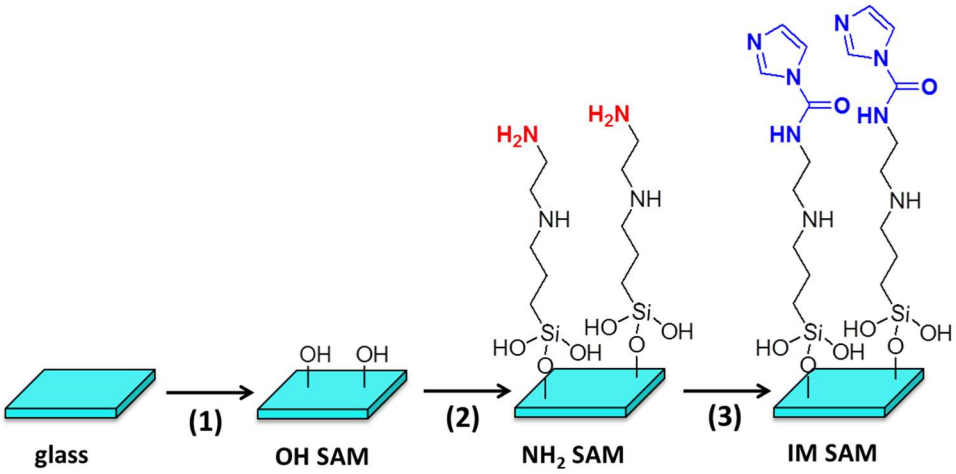

Figure 3.15: Scheme of the functionalization of the substrate (1) Piranha activation, (2) NH_2 SAM formation and (3) IM SAM formation.

In a first step, silicon oxide (SiO_2) or glass substrates were activated by immersing them in a piranha solution H_2SO_4:H_2O_2 (3:1). This way, apart from removing impurities that could contain the surface, the surface activates providing a freshly hydroxyl layer ready to react. Then, the surfaces were incubated overnight in vapors of N-([3-(trimethoxysilyl)propylethylendiamine (TPEDA) (NH_2 SAM). In a further step, the amino SAMs were converted into imidazole SAMs (IM SAM) by reacting them with N,N-carbonyldiimidazole (CDI) in THF at room temperature under N_2 atmosphere. Different reaction times were studied in this case (ranging between 2 and 24 hours). The best results were obtained after the incubation of the surfaces overnight as later was shown the characterization by fluorescence microscopy. In this step is crucial to maintain anhydrous atmosphere since the CDI decomposes instantaneously with the contact water.[25]

Formation of azide SAMs (N_3 SAM)

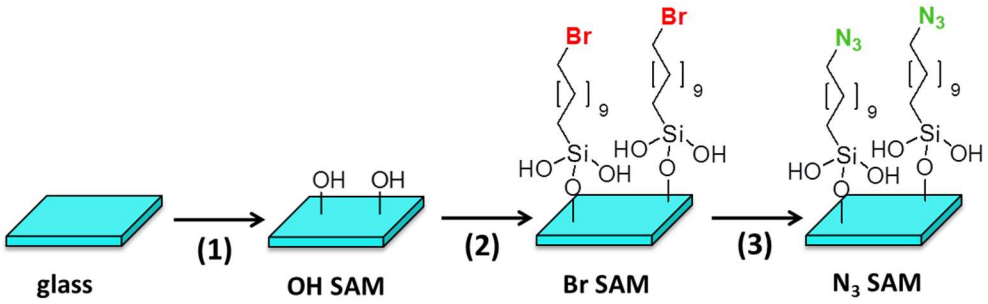

Figure 3.16: Schematic of the substrate functionalization. (1) Piranha activation, (2) Br SAM formation and (3) N_3 SAM formation.

As in the previous case, the surfaces were activated by immersing them in solution of piranha. Then, they were incubated with 11-bromoundecyltrichlorosilane in dry toluene, at room temperature under N_2 atmosphere. Alkyl halide are good candidates for the preparation of SAMs, since they can be subsequently modified into a variety of terminal functional group by S_N2 displacement reactions. Thus, the Br-SAM was converted into the N_3-SAM by incubation of the former with sodium azide (NaN_3) in DMF at 65 ˚C. In this case, despite being good nucleophilics it took two days for the reaction to complete. This group is well-known in click chemistry presenting great stability toward H_2O, O_2 and the majority of organic synthetic conditions.[26]

3.3.3.2 Preparation of the stamp: PDMS

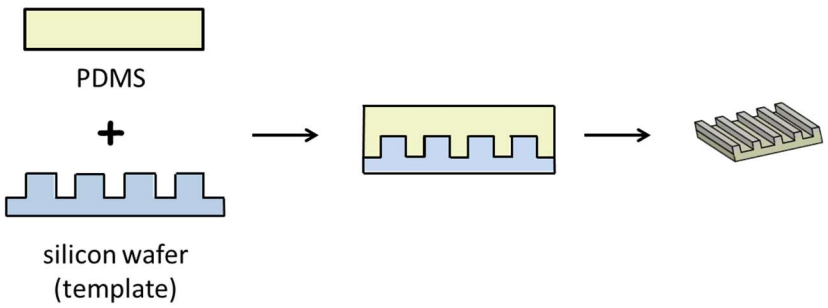

Figure 3.17: Scheme for the formation of PDMS stamps.

The stamp that we used to transfer the design of the master to the substrate is made of a polymer elastomer, in our case poly(dimethylsiloxane) (PDMS), which is a silicon-based crosslinked organic polymer, containing the $–Si(CH_3)_2$-O- structural unit.[5,27]

The preparation of the stamp, as it shown in the Figure 3.18, was carried out by the mixture of the elastomer and the curing agent (crosslinker) in a ratio of 10:1, respectively. Then, the mixture was spread over the silicon wafer (that acts as a template) and degassed in a vacuum desiccator for two hours. When all the bubbles of the air were removed, the mixture was left on the oven at 60 ˚C for 16 hours to cure the polymer. Then, the PDMS was peeled off from the wafer and cut in pieces with the different corresponding patterns.

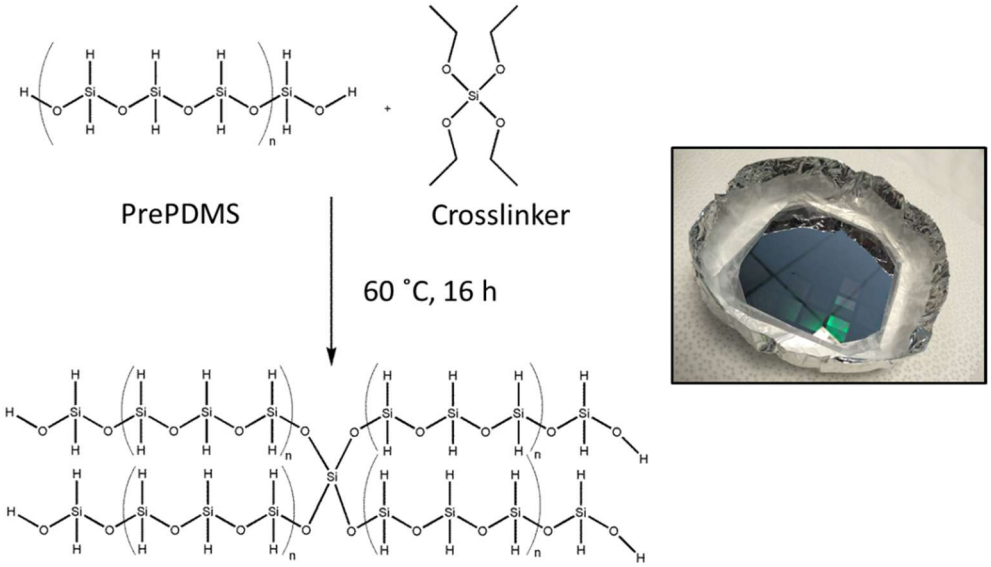

Figure 3.18: Formation of PDMS from precursors (left). Image of PDMS after curing process (right).

After cured, the PDMS presents a hydrophobic surface and polar ink solution would be repelled from it. Therefore, an oxidation treatment of the stamp using a UV/O_3 lamp was performed during 30 min in order to obtain hydrophilic surfaces which would work for polar ink solutions.

3.3.3.3 Microcontact printing (μ-CP)

In order to immobilize the CCMoids on surfaces, microcontact printing, μ-CP, was used to obtain surface patterns with the fluorescent CCMoids. Depending on the functional groups attached to the legs of the CCMoids and the substrates, different methodologies were used.

Patterning of Pyr-acidCCMoid SAMs by microcontact printing

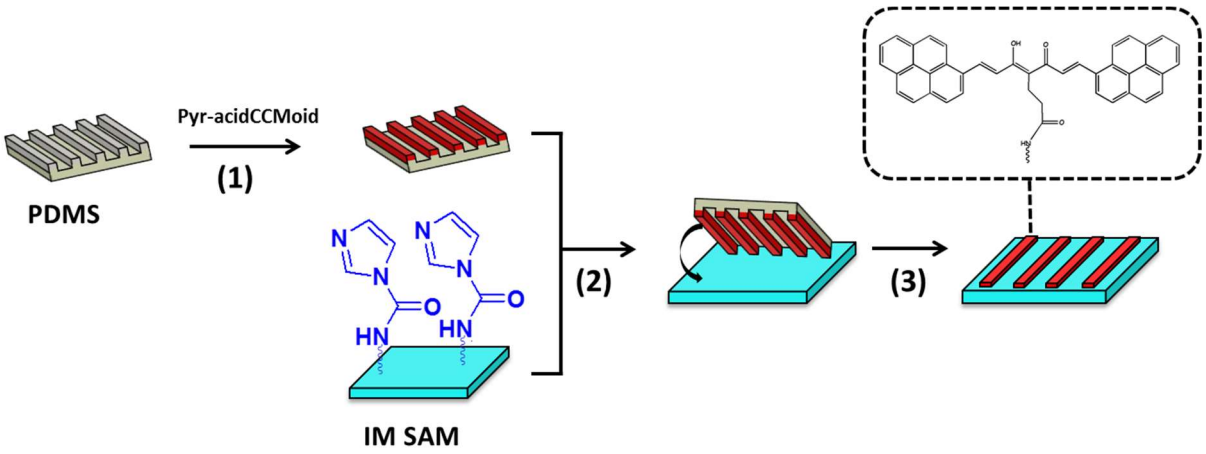

Figure 3.19: Scheme of the microcontact printing process. (1) stamp incubation with a Pyr-acidCCMoid solution, (2) stamp in contact with the surface and (3) the peeling off the stamp.

Firstly, the PDMS stamp was inked with a solution of Pyr-acidCCMoid in DMF. This solvent was chosen because the CCMoid was soluble and also because it does not damage PDMS **(REF21)**.[28] Different solution concentrations and inking times were applied ranging from 0.5 – 6 mM of concentration and from 3 – 60 min (inking time), being the best conditions 4 mM of pyr-acidCCMoid and 60 min of inking time. Then, the stamps were dried with N_2 flow and brought in contact with the IM SAM applying pressure by using a weight of 40 g and covering the system to avoid the contact with light. The force was used to facilitate the interaction between the stamp and the glass substrate. As in the previous case, different printing times were studied, ranging from 15 min to overnight, being the last one the best. Finally, the PDMS stamps were removed and the substrates were rinsed and sonicated in DMF for 10 seconds after printing.

Patterning of Pyr-alkyneCCMoid SAMs by microcontact printing

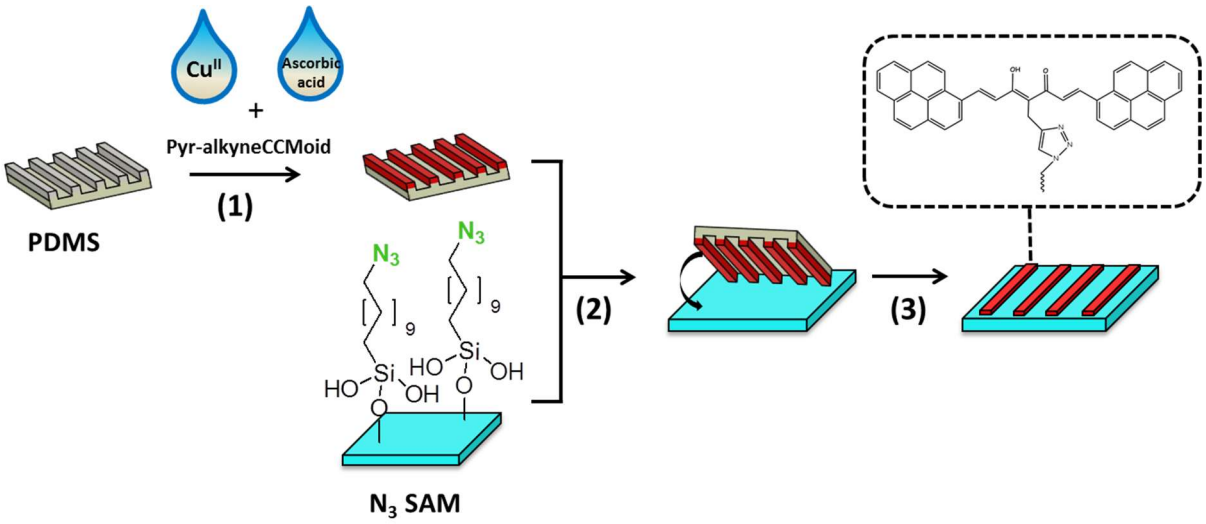

Figure 3.20: Scheme of the microcontact printing process. (1) PDMS stamp containing ink a solution of Pyr-alkyneCCMoid and drops of Cu(II) and ascorbic acid, (2) stamp in contact with the surface and (3) peel off the stamp.

The methodology and conditions used in this case was similar to the previous one, with the difference that now, apart from few drops of the corresponding Pyr-alkyneCCMoid, the stamps were incubated with few drops of a solution of sodium ascorbate and a copper (II) salt. This is necessary for the cycloaddition reaction of azide and alkyne groups. The formation of the 1,4-disubstituted 1,2,3-triazole is catalyzed by the presence of Cu(I) **(REF22)**.[29] In this case, this Cu(I) was prepared in situ by reduction of Cu(II) salt ($CuSO_4 \cdot 5H_2O$) and sodium ascorbate.

3.3.3.4 Boron-CCMoid formation

The boron compound formation was carried out by immersing the functionalize surfaces in a solution of boron trifluoride diethyl etherate ($BF_3{\cdot}Et_2O$) in CH_2Cl_2. In this reaction, the BF_2 group coordinates to the β-diketone part leading to the formation of HF in the media. HF can attack and damage the glass surface. To avoid this fact, the surfaces were only immersed for short periods of time (5-10 seconds) and were washed quickly with an excess of CH_2Cl_2.

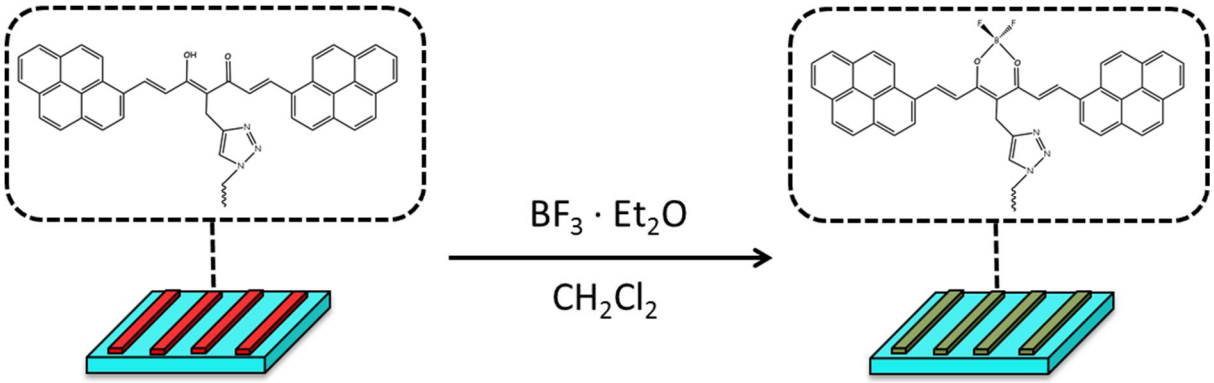

Figure 3.21: General scheme for the formation of boron compounds on surfaces.

3.3.4 Characterization on surface

The different functionalization steps were characterized by contact angle technique. After the CCMoid immobilization, the surfaces were characterized using fluorescence microscopy.

Contact angle

Contact angle technique provides information about the hydrophobic character of the substrate by the measurement of the angle obtained when a drop of Milli-Q water is deposited on the substrate. This way, systems that present polar functional groups interact more with the water drop giving rise to small values of the contact angle. In contrast, systems with apolar functional groups lead to the repulsion of the water yielding to large contact angle values.

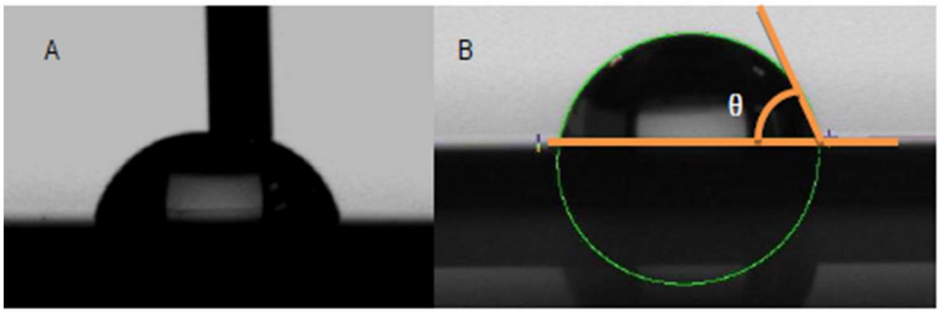

Figure 3.22: (A) Image of the deposition of a water drop on a SAM surface. (B) Representation of the measurement of the contact angle

Figure 3.23 shows the contact angle values corresponding to each step in the immobilization of Pyr-acidCCMoid (a) and Pyr-alkyneCCMoid (b), respectively.

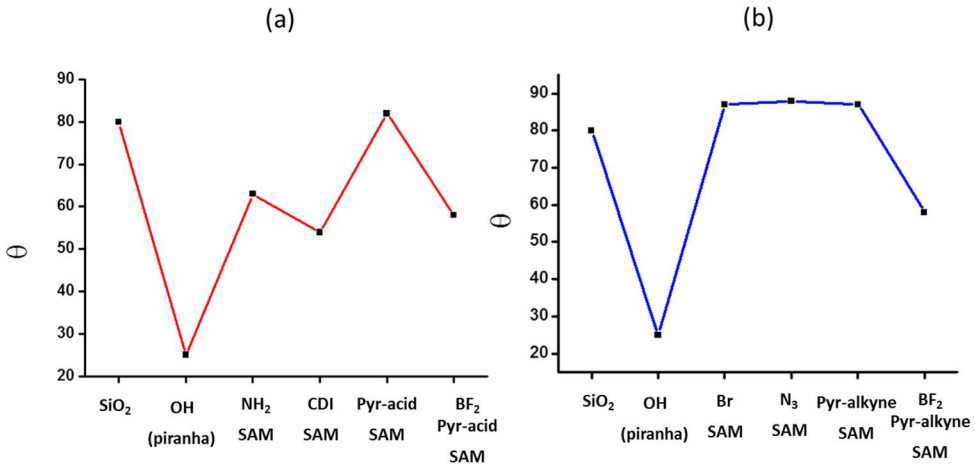

Figure 3.23: Representation of the contact angle versus the functionalization steps for Pyr-acidCCMoid (a) and Pyr-alkyneCCMoid (b).

In both cases, initially the glass substrate shows an angle of 80 ˚. When the substrate is activated with piranha, the value of the contact angle decreases until 25 ˚, due to the presence of the polar hydroxyl groups. With regards to the SAM formation, in the first case the functionalization with TPEDA and CDI modified the contact angle providing values of 63 ˚ and 54 ˚, respectively. Both values are similar to those found in the literature (60 ˚ and 57 ˚) for NH_2 and IM SAM, in that order.[21] On the other hand, the functionalization with Br and N_3 gave rise to values around 83 ˚.[21] After the microprinting with the corresponding CCMoid, in both cases the contact angle show similar high values of 86 ˚, probably due to the presence of the aromatic pyrene groups. Finally, the formation of the boron compounds provided lower values due to the change on the polarity (BF_2 group).

On the other hand, dynamic contact angle measurements were performed in the case of the immobilization of Pyr-acidCCMoid (Figure 3.24). These measurements provided information about the compactness of the formed self-assembly monolayers.[30] Water contact angle measurements show a small hysteresis (8 ˚) between the advancing and receding contact angles for the NH_2 SAM suggesting that the SAM was well packed.[21] In the case of IM SAM, the hysteresis was relatively large (20 ˚) possibly due to imperfections on the surface. In the cases of the immobilization of the CCMoid and the boron compounds, they show hysteresis of (15 ˚) and (16 ˚) respectively, indicating good packing for both systems.

SAMs	θ_a(˚)	θ_r(˚)
NH_2 SAM	63 ± 2	55 ± 2
IM SAM	54 ± 2	34 ± 2
Pyr-acidCCMoid	86 ± 2	71 ± 2
BF_2-Pyr-acidCCMoid	54 ± 2	38 ± 2

Table 3. 1: Advancing θ_a(˚) and receding θ_r(˚) water contact angles.

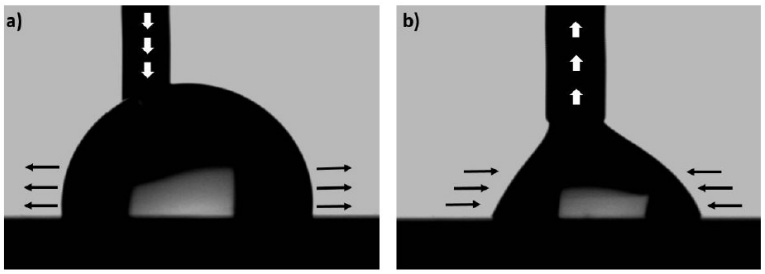

Figure 3.24: Representation of dynamic contact angle. (a) Advancing and (b) receding.

Fluorescence emission

Due to the fluorescence properties derived from the CCMoids, studies using an (i) optical fluorescence microscope and a (ii) confocal fluorescence microscope were carried out in order to visualize the patterns obtained by the use of microcontact printing technique.

From the analysis of the images it has been possible the optimization of previous conditions. These studies have allowed us to assess the relevance of some aspects such as: (i) incubation time of the SAM formation (especially in CDI), (ii) CCMoid concentration, since dilute solutions resulted in not complete immobilization processes and therefore low fluorescence emissions; however, high concentrated solutions could give rise to the formation of aggregations; (iii) the weights used on the stamp; they are very important, since determine how uniform the distribution of the pressure is in the SAMs, where heavy weights would result in the deformation of the stamps; (iv) printing time; this has a great influence on the fluorescence of the systems; (v) the cleaning and sonication processes of the surfaces; in order to eliminate physisorbed material.

Apart from these variables mentioned above, the temperature and the humidity are also crucial, especially the latest. Reproducibility problems were caused mainly by high humidity conditions (> 30 %).

(a) Optic Fluorescence microscopy

Different studies provided us optimal conditions to reproduce successfully our goals. In the case of the IM SAM formation, the conditions consisted on the incubation of the activated surfaces with vapors of TPEDA overnight and then incubation of the resulting ones with solutions of CDI for 24 hours (Annex 3.2). In the case of the N_3 SAMs, the first step consisted on the incubation with 11-bromoundecyltrichlorosilane for 45 min and then incubation with solutions of NaN_3 for two days at 60 ˚C.

In the case of the µ-CP, the conditions were the same for both systems with the exception of the concentration of the CCMoids (being 2 mM for Pyr-acid-CCMoid and 1 mM for Pyr-alkyne-CCMoid, because the alkyne compound presents lower solubility than the former). In both cases, the inking time with the corresponding CCMoid was one hour with the stamp and the printing times were 24 hours. Also, in both cases, a weight of 40 g was used.

Following these conditions, Pyr-acid-CCMoid (A) and Pyr-alkyne-CCMoid (B) were added by microcontact printing on IM and N_3 SAMs, respectively. Figure 3.26 shows 50 µm lines separated by 100 µm accomplished with the Pyr-acid-CCMoid (A) and also 10 µm lines separated by 20 µm for the case of the Pyr-alkyne-CCMoid.

As it can be seen, fluorescence patterns were clearly visible with fluorescence microscopy using a blue filter ($450 < \lambda_{exc} < 480$ nm). The intensity of the pattern printed in both cases was similar indicating the successful covalent immobilization of both CCMoids on the IM SAM and N_3 SAM respectively.

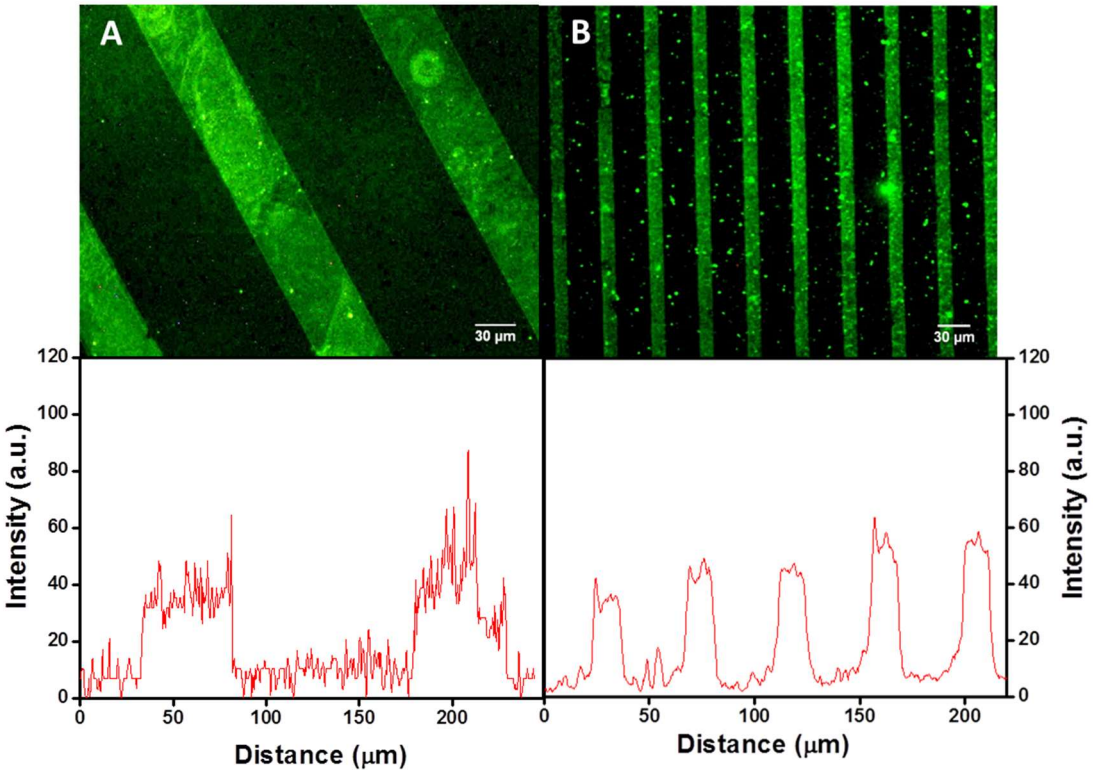

Figure 3.26: Fluorescence microscopy images of Pyr-acidCCMoid (a) and Pyr-alkyneCCMoid (b).

(b) Confocal Fluorescence microscopy

A more detailed study can be performed by the use of confocal fluorescence microscopy. Part of this study relates to the investigation of the stability of the molecules when are irradiated with specific wavelengths. The molecules are degraded by the light showing photobleaching processes at different times depending on the wavelengths used.[31]

Figure 3.27 and 3.28 show the intensity of the fluorescence versus time when the Pyr-acid-CCMoid and Pyr-alkyne-CCMoid are excited with a wavelength of 405 nm. In both cases, there is a huge decrease of the fluorescence emission due to photobleaching processes; after 150 seconds, there are almost no emissions for the two systems.

This fact has influenced negatively on the characterization of the surfaces by optical fluorescence microscopy since long exposure times gave rise to a decrease of the fluorescence emissions.

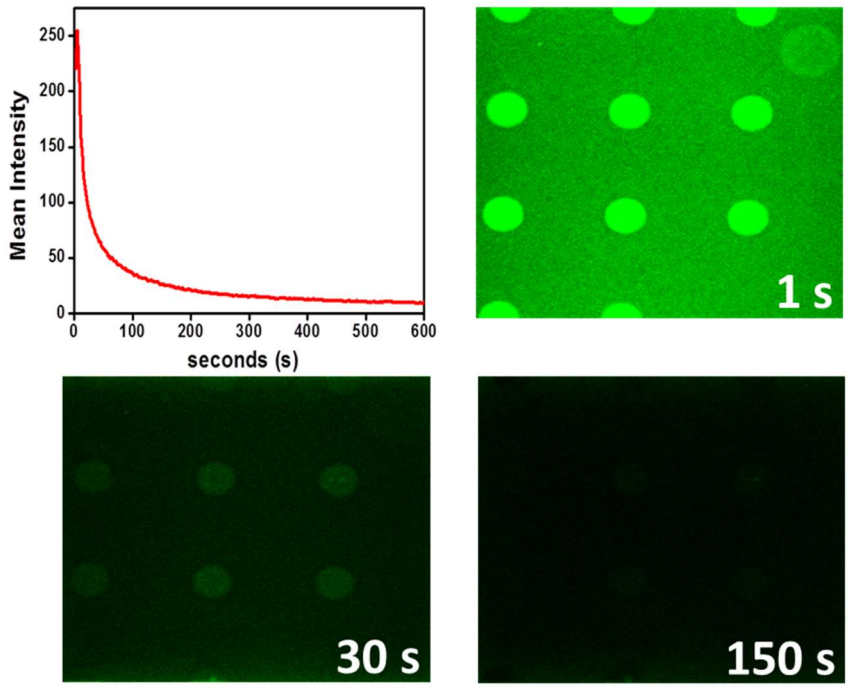

Figure 3.27: Representation of Fluorescence intensity versus time of Pyr-acidCCMoid. Confocal microscope images at different exposition times.

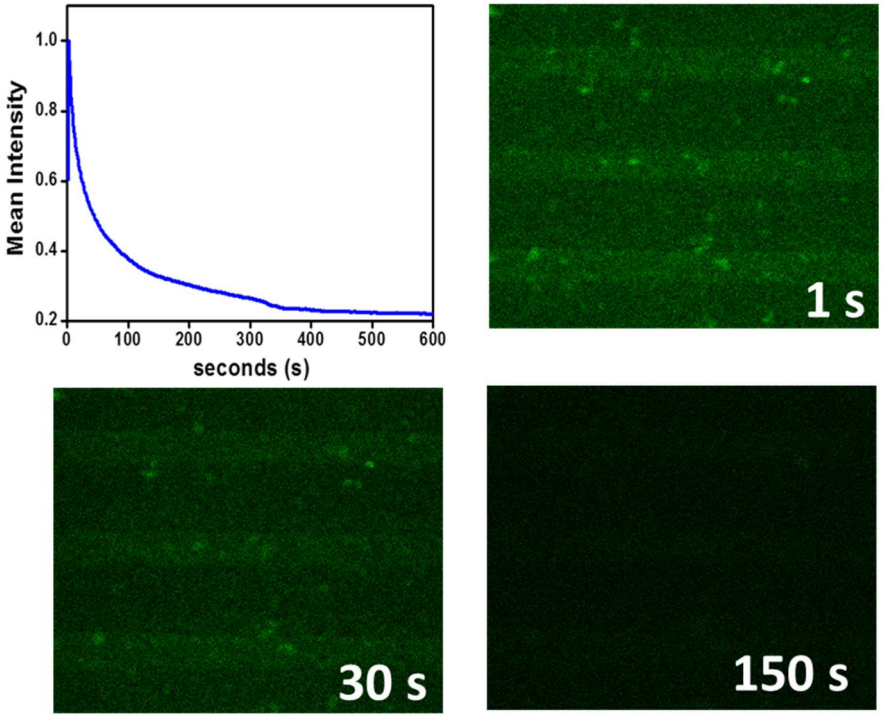

Figure 3.28: Representation of Fluorescence intensity versus time of Pyr-alkyneCCMoid. Confocal microscope images at different exposition times.

Even though the existence of bleaching processes, it was possible to obtain the fluorescence emission spectra of both systems on their respective surfaces (Figure 3.29). Both systems showed the same behavior displaying broad band emissions at 480 and 500 nm, indicating that their different attachments to their surfaces, did not influence in great manner their emissions.

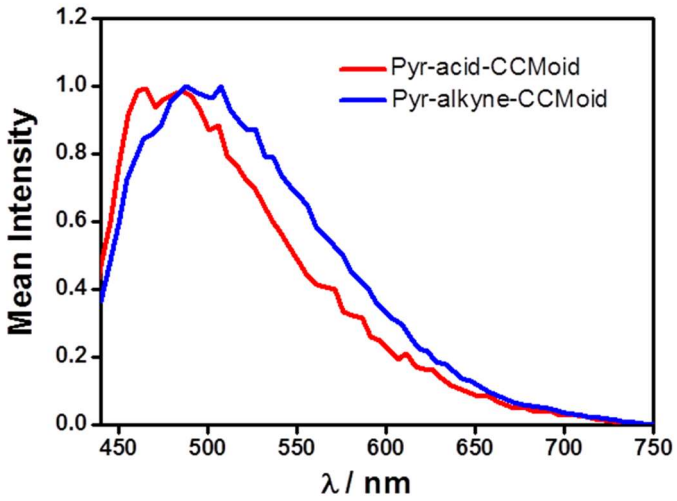

Figure 3.29: Fluorescence spectra of Pyr-acidCCMoid (red) and Pyr-alkyneCCMoid (blue) in surface.

In this way, it was possible to perform the comparison of the emissions, for each compound, in the solid state, in solution and on surfaces (Figure 3.30). As can be seen, there is a strong shift of their emission depending on their state (solid at 700 nm; solution at 600 nm and surface at 480 nm). This emission differences are related to the presence of intermolecular interactions. These interactions are favored in the solid state, which displays the highest shifted emissions. On the contrary, on surfaces, as SAMs, the interactions seem to be less favored.

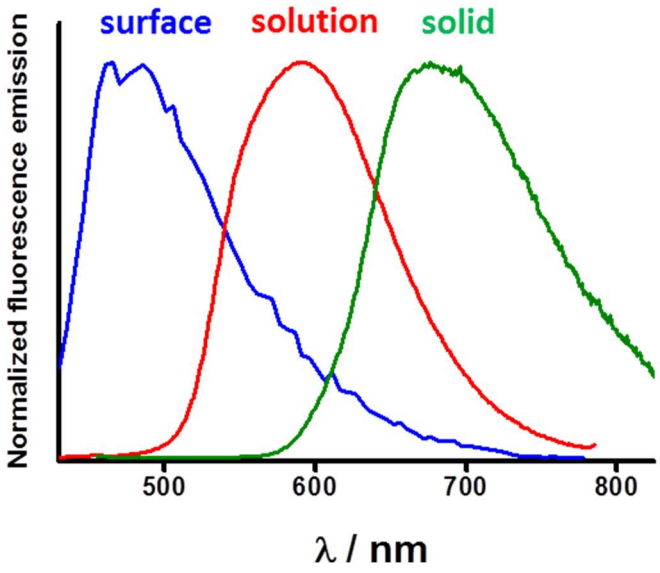

Figure 3.30: Comparison of fluorescence spectra of Pyr-alkyneCCMoid on surface (blue), solution (red) and solid (green).

Boron-CCMoid formation

Studies performed in solution showed how the absorption and emission spectra corresponding to the boron compound displayed a shift towards red regions comparing to the free CCMoid (Figure 3.31).

In the Figure 3.31 and 3.32 are shown the μ-CP pattern corresponding to the Pyr-acid-CCMoid (A) and Pyr-alkyne-CCMoid (C) respectively when are irradiated with a blue light using a "blue filter" ($450 < \lambda_{exc} < 480$ nm). In contrast, after the boron incubation, the boron compound displayed a practically zero emission in this range of wavelengths. However, when these systems were irradiated with a "green filter" ($510 < \lambda_{exc} < 550$ nm), the surfaces show now the μ-CP pattern as they are depicted in the Figures 3.31 and 3.32 corresponding to the BF_2-Pyr-Acid-CCMoid (B) and BF_2-Pyr-Alkyne-CCMoid (D) systems. The main different between these four systems was that the CCMoids emit in the green region ($\lambda_{em} > 515$ nm) meanwhile the BF_2-CCMoids emitted in the red region ($\lambda_{em} > 590$ nm). This behavior is in accordance with that observed in solution and both systems can be used as sensors for boron.

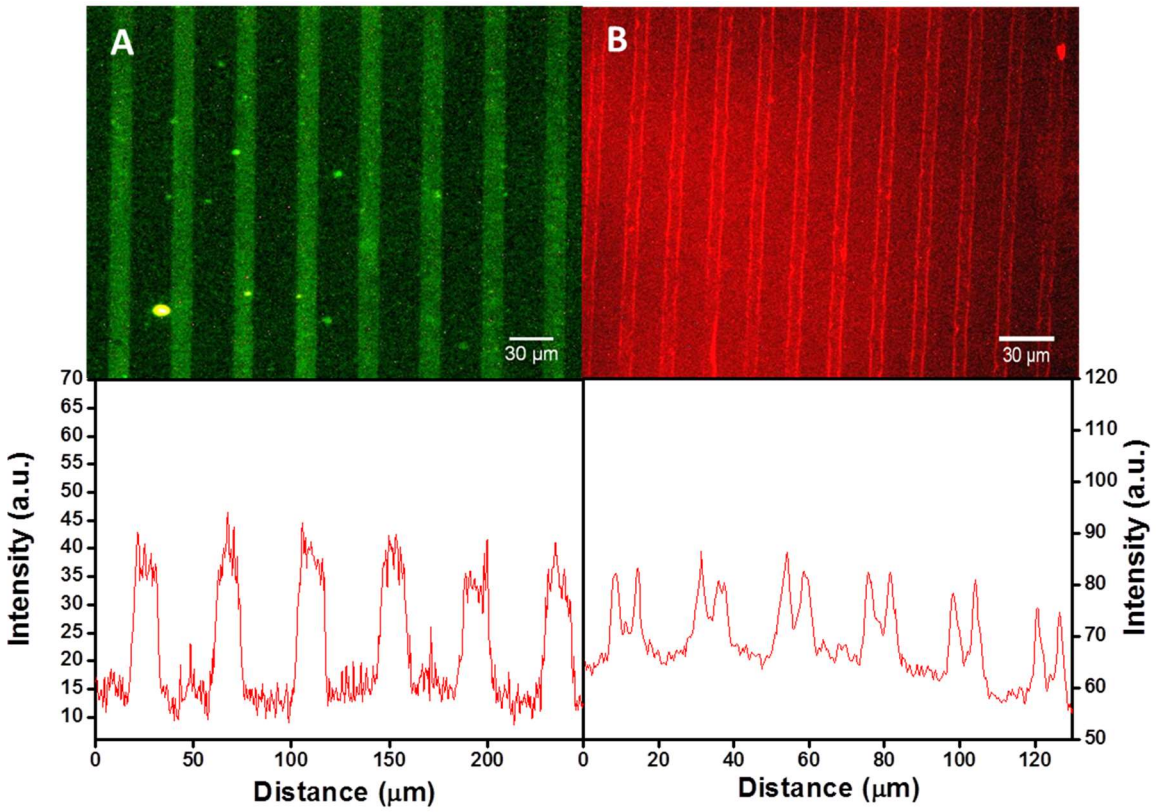

Figure 3.31: Fluorescence microscopy images of (a) Pyr-acidCCMoid and (b) BF_2-PyracidCCMoid.

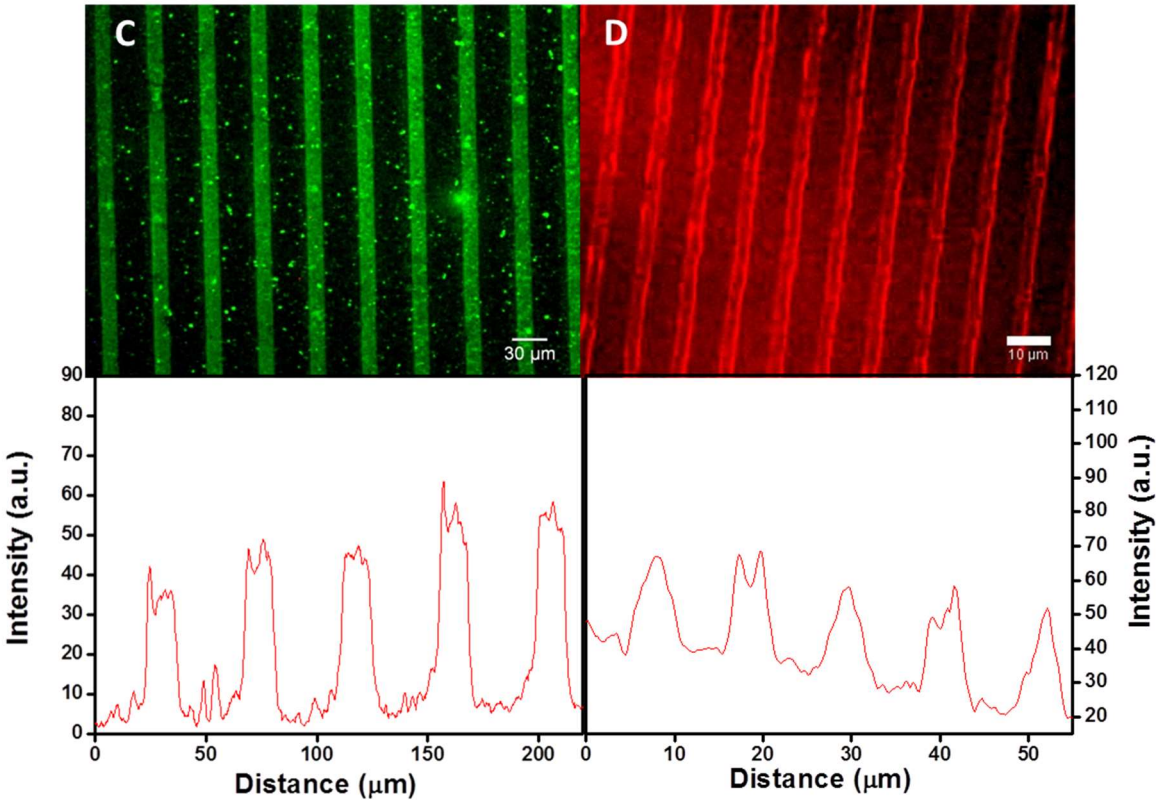

Figure 3.32: Fluorescence microscopy images of (a) Pyr-alkyneCCMoid and (b) BF_2-PyralkyneCCMoid

X-ray photoelectron spectroscopy (XPS)

Further evidence of the functionalization with the boron compounds was given by XPS characterization. Figure 3.33 shows the XPS spectra that encloses the regions of C1s, N1s, B1s and F1s for a glass surface (blank), Pyr-acidCCMoid and BF_2-Pyr-acidCCMoid, in that order. A huge band in the case of C1s and N1s were observed due to the nature of the CCMoid. Specifically, in the case of C1s, different bands were observed due to the different nature of carbon atoms in the molecule. On the other hand, the B1s spectra show intense bands for all the cases related to the impurities of boron on the silicon oxide. However, in the case of BF_2-Pyr-acidCCMoid, an extra peak was observed around 195 eV that may correspond to the BF_2 group. This signal was expected to be small since corresponds only to the molecules that react in the corresponding SAMs. In the case of F1s spectra, a part from a low band in all the cases, BF_2-Pyr-acidCCMoids show an additional intense band at 687 eV that corresponds to the BF_2 groups.

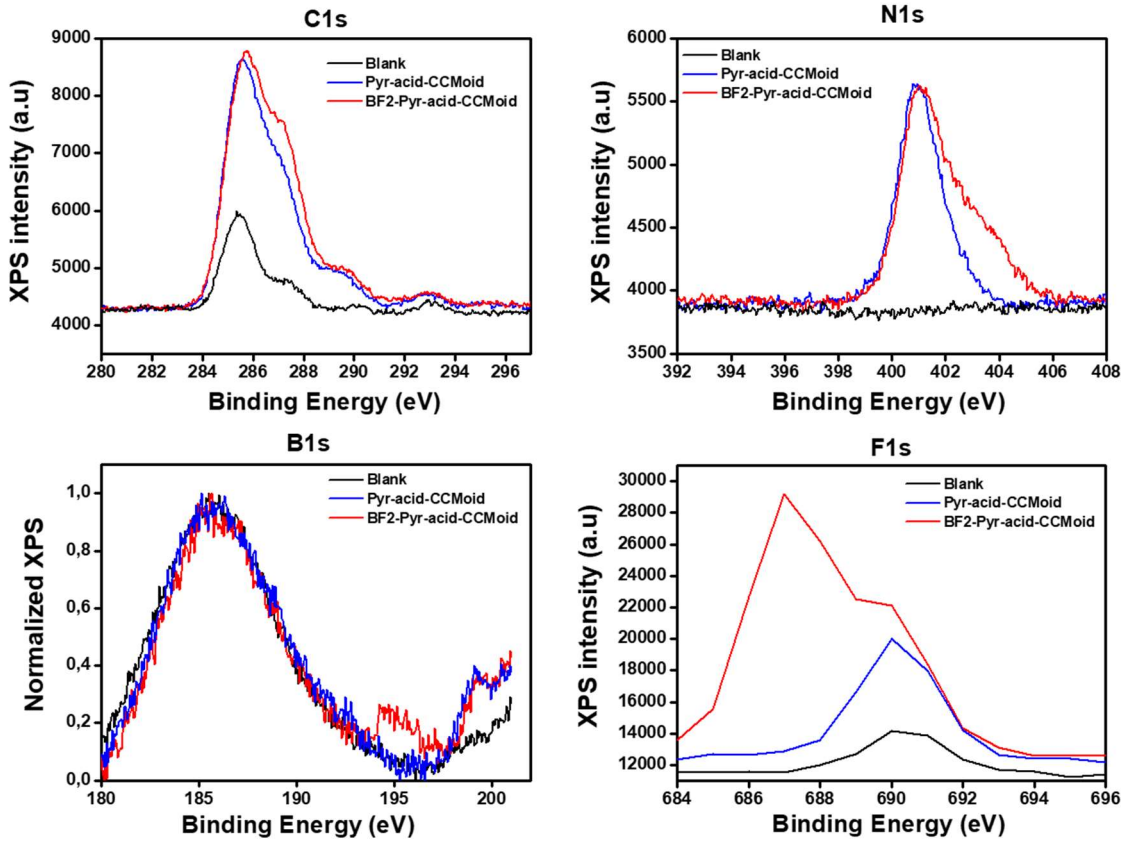

Figure 3.33: X-ray photoelectron spectra of C_{1s}, N_{1s}, B_{1s} and F_{1s} for BF_2-Pyr-acidCCMoid (red), Pyr-acidCCMoid (blue) and Blank (SiO_2 surface) (black).

3.4 Conclusions

In this section, the immobilization of fluorescent CCMoids on SiO_2 surfaces has been performed by the use of microcontact printing technique (μ-CP).

To perform these studies, two new fluorescence CCMoids (Pyr-acidCCMoid and Pyr-alkyneCCMoid) containing both pyrene groups in their lateral positions and different functional groups in the lower parts, the so-called legs (alkyne and acid) were synthetized.

In order to immobilize these CCMoids, the formation of two SAMs with imidazole groups (IM SAM) and azide groups (N_3 SAM) were carried out. The formation of such SAMs depended on several parameters, so obtaining a protocol that gave reproducible results was one of the challenges in this work.

In the case of the IM SAM formation, difficulties regarding reproducible results related to the formation of reactive species (amine and imidazole). Our studies demonstrated that the degradation of the systems was directly related to the conditions of the experiments; thus, the control of the temperature, light exposition and, mainly the humidity gave rise to reproducible results. Moreover, in the case of CDI, different incubation times were performed being overnight the best results. All the different steps were characterized by contact angle providing positive results according to the hydrophobicity nature of each system.

Then, the immobilization of the CCMoids were carried out by microcontact printing technique. This process was also affected by several parameters and studies at different concentrations, printing times and different weights were performed to establish the proper protocols. The best results were obtained using high concentrations of CCMoids (1-2 mM) with significantly weight and long printing times. On the other hand, in the case of pyr-alkyneCCMoid the use of Cu(I), which acts as a catalyst was necessary.

The created patterns were characterized by the use of optical fluorescence microscopy due to the fluorescent nature of the pyrene groups. Furthermore, these surfaces were characterized by the use of confocal fluorescence microscopy. This technique allowed the study of the surfaces stability when they are irradiated. In both cases, a decrease of the fluorescence emission was observed due to photobleaching processes. In addition, fluorescence emission spectra on surface were obtained. This fact made possible the comparison of the fluorescence emission between the different states: solid, solution and surface. In this study, a strong emission depending on the intermolecular interaction was observed, being the solid state the one presenting the highest shift to lower energies.

Finally, the studies corresponding to the use of these systems as sensors for boron showed that, in the presence of the $BF_3{\cdot}Et_2O$, both in solution and on surface, boron compounds were formed showing a shift of the fluorescence emission toward near IR. In the case of the surface, XPS measurements confirmed the formation of the boron-CCMoids.

3.5 Work in progress

One of the most difficult questions to answer using μ-CP is the evaluation of the amount of immobilized material. Experiments to analyze this factor would be required. In principle, the total amount of immobilized CCMoids would correspond to the SAM formation, however this would be a simplistic argument; one may evaluate the bulkiness of the molecules and their possible organization among each other together with the possibility of obtaining multilayers, factors directly related to the conditions of the performance (e.g: concentration, solvents, *etc.*). In the case of the multilayers they are associated with the physisortion of the material which would be removed by sonication.

On the other hand, one of the most useful techniques to determine the height of the immobilized CCMoids is ellipsometry. This technique is based on an optical analysis of the surface, studying variations in the polarization of the light once this "strikes" a material. The variation of the polarization will depend on several factors, such as the refraction index and the height of the material, among others. Studies using ellipsometry will be performed in all future surfaces to analyze in detail their characteristics.

The work in progress related to this section also includes the characterization on surfaces of others CCMoids with different chromophore groups accomplished during the period of my thesis where additional CCMoids containing anthracene and fluorene groups have been synthesized. As before, these molecules present functional groups in the middle of their structures (acid or alkyne groups) to be attached on surfaces.

So far, four new systems have been achieved (Figure 3.34) and the goal now will be to perform a comparative study of the emissions on the solid state, in solution and on surfaces among the three chromophore groups (pyrene, fluorene and anthracene). These studies are in progress since it has been not possible to obtain yet the proper conditions to have good immobilization of some the systems on the functionalized surfaces.

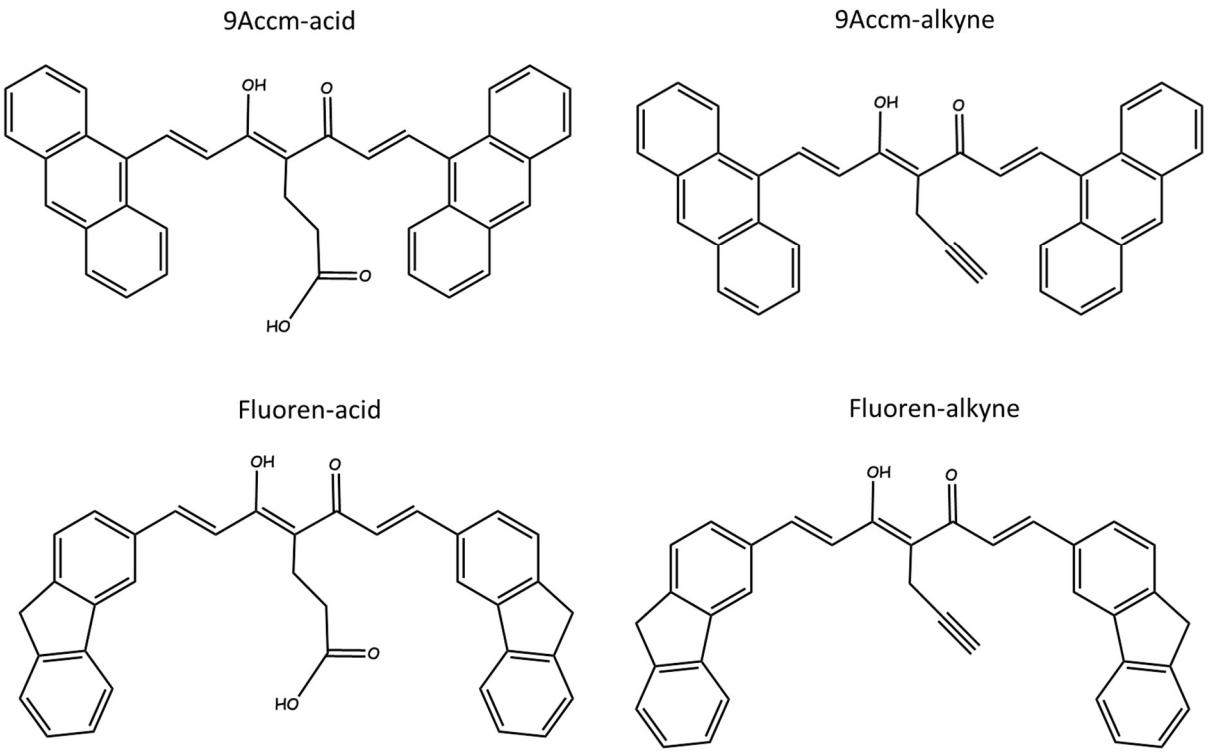

Figure 3.34: Representation of 9Accm-acid, 9Accm-alkyne, Fluoren-acid and Fluoren-alkyne.

3.6 Experimental part

Materials: All the reagents used in the work were used as they were received from the commercial company, without further purification.

Synthesis of Pyr-acidCCMoid

The synthesis of pyr-acidCCMoid requires the preparation of the 4-acetyl-5-oxohexanoic acid.

4-acetyl-5-oxohexanoic acid

Methyl 4-acetyl-5-oxohexanoate (465.5 mg, 2.50 mmol) and LiOH (104.9 mg, 4.37 mmol) were added in a round flask and dissolved in 5 mL of THF and 5 mL of H_2O. The mixture was monitored by TLC and stirred at room temperature overnight. Afterwards, the mixture was acidified with H_2SO_4 (5 %) until pH = 3. Then, THF was removed by rotatory evaporation and the organic product was extracted with CH_2Cl_2, brine and dried with Na_2SO_4. Finally, CH_2Cl_2 was removed by rotatory evaporation obtaining a yellow oil a 49 % yield.

^{1}H-RMN (300 MHz $CDCl_3$, window from 16 to 0 ppm): δ 16.72 (s, 1H), 11.34 (s, 1H), 2.54 (t, 2H), 2.46 (t, 2H), 2.14 (s, 3H), 2.01 (s, 3H). ESI^--MS ($CHCl_3$): m/z 171.06 $[M-H]^-$

Pyr-acidCCMoid

The synthesis of pyr-acidCCMoid was carried out following the Pabon's method. 4-acetyl-5-oxohexanoic acid (265.6 mg, 1.54 mmol) was added in a bottom flask with an excess of boron oxide (120 mg, 1.72 mmol) in 3 mL of AcOEt. The mixture was heated at 40 ˚C for two hours until a white paste was formed. Then, in a separated flask, a solution of 1-pyrenecarboxaldehyde (709.27 mg, 3.08 mmol) and tributyl borate (1.417 g, 6.15 mmol) in AcOEt (4 mL) was prepared and added to the previous solution. The mixture was stirred at 40 ˚C for two hours. After cooling down, an excess of n-butylamine (82.3 µL, 0.83 mmol) in 2 mL of AcOEt was added dropwise. Initially, the solution displayed an orange color which changes to red over the time. The mixture was stirred overnight. After that, a brown-green solid-oil was formed. Then, the mixture was hydrolysed with 5 mL of HCl/H_2O (1:9) and heated at 60 ˚C for five hours approximately until a red color was observed and a precipitated came out. The mixture was filtered and washed with H_2O, MeOH and Et_2O to remove impurities. The yield was 80 %.

IR KBr pellet (ν/cm^{-1}): 3033m, 1907w, 1726s, 1608s, 1408s, 1316m, 1245s, 948m, 840vs, 705s, 521w.

^{1}H-RMN (300 MHz DMSO, window from 20 to 0 ppm): δ 18.0 (s, 1H), 12.2 (s, 1H), 8.95 (dd, 2H), 8.70 (dd, 2H), 8.63 (m, 3H), 8.38 (m, 6H), 8.28 (m, 6H), 8.12 (dt, 2H), 7.76 (d, 1H), 7.44 (d, 1H), 2.60 (t, 2H), 2.45 (t, 2H). $MALDI^-$-MS (DMSO): m/z 595.2 $[M-H]^-$.

Synthesis of Pyr-alkyneCCMoid

For the synthesis of the Pyr-alkyneCCMoid, required the synthesis of 3-(prop-2-ynyl)pentane-2,4-dione in a first step.

3-(prop-2-ynyl)pentane-2,4-dione

In a purged (N_2) schlenk flask, acetylacetonate (2.68 g, 26.8 mmol) and potassium carbonate (4.44 g, 32.12 mmol) was dissolved in acetone (30 mL). The mixture was heated at 45 ˚C and stirred for one hour with a low flux of nitrogen. Then, a solution of propargyl bromide (2.98 mL, 26.75 mmol) was added and the temperature was cooling down to room temperature. The mixture, which presents a yellow color, was stirred overnight. After that, a color changes to brown was observed. The mixture

was filtered and washed with acetone. The solvent was removed by rotatory evaporator and a brown oil was obtained. The resulting residue was purified by a preparative foil using AcOEt/hexane (1:2) as an eluent (R_f = 0.7). The product was extracted with CH_2Cl_2 from the silica and the solvent was removed by rotatory evaporation obtaining yellow crystals with a yield of 13 %.

^{1}H-RMN (300 MHz $CDCl_3$, window from 16 to 0 ppm): (enol form) δ 16.50 (s, 1H), 3.04 (d, 2H), 2.22 (s, 3H), 2.15 (s, 3H), 2.05 (t, 1H); (keto form) δ 3.85 (t, 1H), 2.70 (dd, 2H), 2.05 (t, 1H). ESI$^+$-MS (formic acid): m/z 139.07 $[M+H]^+$.

Pyr-alkyneCCMoid

The synthesis of pyr-alkyneCCMoid was carried out following the same procedure than for the synthesis of Pyr-acidCCMoid, with the difference that in this case 3-(prop-2-ynyl)pentane-2,4-dione (220.2 mg, 1.59 mmol) was used. After the hydrolysis, a red-violet solid was obtained. The mixture was filtered and washed with H_2O, MeOH and Et_2O to remove impurities. The yield was 64 %.

IR KBr pellet (v/cm^{-1}): 1598s, 1534vs, 1395m, 1275m, 1152s, 1055m, 981s, 829m, 765m, 732s, 640w, 576w.

^{1}H-RMN (300 MHz $CDCl_3$, window from 16 to 0 ppm): δ 8.95 (d, 2H), 8.56 (d, 2H), 8.42 (d, 2H), 8.17 (m, 5H), 8.07 (dd, 3H), 8.00 (t, 2H), 7.44 (d, 2H), 3.33 (d, 2H), 2.05 (t, 1H). ESI$^-$-MS (NH_3): m/z 561.18 $[M-H]^-$

<u>Surface immobilization of CCMoids</u>

For the surface immobilization of the CCMoids different steps were followed: (i) glass surface activation (ii) glass surface functionalization (CDI or azide groups) (iii) stamp incubation with CCMoids and (iv) microcontact printing (μ-CP).

Activation of glass surface

Glass or silicon oxide surfaces were cleaned and activated by immersing them in a solution of piranha, H_2SO_4:H_2O_2 (3:1), for 45 min. Afterwards, the slides were rinsed thoughtfully with ultrapure water and dried under N_2 stream flow.

SAMs preparation

- **Preparation of CDI SAMs for acid-CCMoids**

Glass substrates were functionalized with an amino-terminal group using vapors of N-([3-(trimethoxysilyl)propylethylendiamine (TPEDA) (0.1 mL) in a dome overnight, with a continued

pumped for two min to create a fully vapor phase TPEDA atmosphere. Later on, the surfaces were rinsed with ethanol and CH_2Cl_2 sequentially to eliminate the unreacted physiosorbed amino groups; finally they were dried with N_2. Then, a saturated solution of 1,1-carbonyldiimidazole (CDI) in 40 mL of dry THF was prepared where the substrates were immersed and incubated under nitrogen atmosphere for four hours. After that, the substrates were rinsed with dry THF and dried under a N_2 flow. µ-CP was immediately performed due to the high reactivity of the functional groups on surfaces.

- **Preparation of azide SAMs for alkyne-CCMoids**

Glass substrates were functionalized with a bromide-terminal group by the immersion of the substrates in a 2 mM solution of 11-bromoundecyltrichlorosilane (42 µL) in dry toluene (40 mL) for 45 min under nitrogen atmosphere. Then, the substrates were rinsed with toluene and CH_2Cl_2 and dried under a N_2 flow. After that, a saturated solution of NaN_3 in 60 mL of DMF was prepared and the substrate were immersed and incubated at 65 ˚C for two days under N_2 atmosphere. Then, substrates were rinsed with absolute ethanol and mili-Q water and dried under a N_2 flow; µ-CP was performed immediately after.

Preparation of PDMS

PDMS stamps were obtaining from mixing 70 g of polydimethylsiloxane and 7 g of the curing agent (the commercially available two-component siloxane polymer Sylgard 184, from Dow Corning). The mixture was stirred manually and spreading it on patterned silicon wafers. Then, it was degassed by the application of vacuum in a desiccator for approximately two hours. After that, the mixture was cured on the oven at 60 ˚C for 16 hours. Cured PDMS was diced following the distribution of the interested patterns and the stamps were activated by a treatment of UV/O_3 for 30 min. Finally, the stamps were washed with Milli-Q water and dried under N_2.

Stamp incubation

-Stamp incubation for acid-CCMoid

The stamps were incubated in a solution of 2 mM (6 mg, 0.010 mmol) of acid-CCMoid in 5 mL of DMF for t_{ink} = 1 hour. Then, the stamps were dried with N_2.

-Stamp incubation for alkyne-CCMoid

On a PDMS stamp, few drops of a solution of 1 mM alkyne-CCMoid (3 mg, 0.005 mmol) in 5 mL of DMF. In addition, 5 mM of sodium ascorbate in 5 mL of DMF and 5 mM of copper (II) sulphate

pentahydrate in 5 mL DMF were added. Then, the stamps were incubated for t_{ink} = 1 hour and finally were dried under N_2

Microcontact Printing (μ-CP)

To perform the microcontact printing (μ-CP), the stamp was putted in contact with the functionalized glass surface. To improve the contact between them, a weight of 40 g was located above the stamp and leaved for $t_{printing}$ = overnight avoiding exposition to light. Then, the stamp was removed and the surface was washed with DMF, sonicated for 10 seconds and dried with N_2.

Formation of boron-CCMoid

Final functionalized glass surfaces (containing CCMoids) were immersed in a solution of 1 mM (8 μL, 0.02 mmol) in 30 mL of CH_2Cl_2 for 30 seconds. Afterwards, they were washed with CH_2Cl_2, sonicated for 20 seconds, rinsed with more CH_2Cl_2 and dried under N_2.

3.7 References

[1] C. Joachim, J. K. Gimzewski, A. Aviram, *Nature* **2000**, *408*, 541–548.

[2] D. Xiang, X. Wang, C. Jia, T. Lee, X. Guo, *Chem. Rev.* **2016**, *116*, 4318–4440.

[3] D. Mijatovic, J. C. T. Eijkel, A. van den Berg, *Lab Chip* **2005**, *5*, 492.

[4] a Ulman, *Chem. Rev.* **1996**, *96*, 1533–1554.

[5] A. Perl, D. N. Reinhoudt, J. Huskens, *Adv. Mater.* **2009**, *21*, 2257–2268.

[6] C. Wendeln, B. J. Ravoo, *Langmuir* **2012**, *28*, 5527–5538.

[7] T. Kaufmann, B. J. Ravoo, *Polym. Chem.* **2010**, *1*, 371.

[8] L. Wilbur James, A. Kumar, H. A. Biebuyck, E. Kim, G. M. Whitesides, *Nanotechnology* **1996**, *7*, 452–457.

[9] Y. Xia, G. M. Whitesides, *Encycl. Mater. Sci. Technol.* **2001**, 8309–8314.

[10] A. Kumar, G. M. Whitesides, *Appl. Phys. Lett.* **1993**, *63*, 2002–2004.

[11] X. Yo, N. V, D. Qin, J. Tien, *Langmuir* **1998**, *6*, 363–371.

[12] D. I. Rozkiewicz, D. Jańczewski, W. Verboom, B. J. Ravoo, D. N. Reinhoudt, *Angew. Chemie - Int. Ed.* **2006**, *45*, 5292–5296.

[13] G. Csucs, R. Michel, J. W. Lussi, M. Textor, G. Danuser, *Biomaterials* **2003**, *24*, 1713–1720.

[14] H. J. Pabon, *Recl. Trav. Chim. Pays-Bas* **1964**, *83*, 379.

[15] J. A. Lenhart, X. Ling, R. Gandhi, T. L. Guo, P. M. Gerk, D. H. Brunzell, S. Zhang, *J. Med. Chem.* **2010**, *53*, 6198–6209.

[16] K. Kamada, T. Namikawa, S. Senatore, C. Matthews, P. F. Lenne, O. Maury, C. Andraud, M. Ponce-Vargas, B. Le Guennic, D. Jacquemin, et al., *Chem. - A Eur. J.* **2016**, *22*, 5219–5232.

[17] A. Felouat, A. D'Aléo, F. Fages, *J. Org. Chem.* **2013**, *78*, 4446–4455.

[18] Z. H. Khan, B. N. Khanna, *J. Chem. Phys.* **1973**, *3015*, 3015–3019.

[19] C. Ran, X. Xu, S. B. Raymond, B. J. Ferrara, K. Neal, B. J. Bacskai, Z. Medarova, A. Moore, **2009**, *131*, 15257–15261.

[20] M. Rivoal, E. Zaborova, G. Canard, A. D'Aléo, F. Fages, *New J. Chem.* **2016**, *40*, 1297–1305.

[21] S.-H. Hsu, D. N. Reinhoudt, J. Huskens, A. H. Velders, *J. Mater. Chem.* **2008**, *18*, 4959.

[22] A. González-Campo, S. H. Hsu, L. Puig, J. Huskens, D. N. Reinhoudt, A. H. Velders, *J. Am. Chem. Soc.* **2010**, *132*, 11434–11436.

[23] F. A. Scaramuzzo, A. González-Campo, C.-C. Wu, A. H. Velders, V. Subramaniam, G. Doddi, P. Mencarelli, M. Barteri, P. Jonkheijm, J. Huskens, *Chem. Commun.* **2010**, *46*, 4193.

[24] C. Nicosia, J. Cabanas-Danés, P. Jonkheijm, J. Huskens, *ChemBioChem* **2012**, *13*, 778–782.

[25] R. Paul, G. W. Anderson, *J. Am. Chem. Soc.* **1960**, *82*, 4596–4600.

[26] C. O. Kappe, E. Van der Eycken, *Chem. Soc. Rev.* **2010**, *39*, 1280–1290.

[27] H. Schmid, B. Michel, *Macromolecules* **2000**, *33*, 3042–3049.

[28] Lee, Park, Whitesides, *Anal. Chem. Dc-* **2003**, *75*, 6544–6554.

[29] A. Chem, I. Ed, *Angew. Chem. Int. Ed.* **2002**, *41*, 2596–2599.

[30] L. Basabe-Desmonts, J. Beld, R. S. Zimmerman, J. Hernando, P. Mela, M. F. García Parajó, N. F. Van Hulst, A. Van Den Berg, D. N. Reinhoudt, M. Crego-Calama, *J. Am. Chem. Soc.* **2004**, *126*, 7293–7299.

[31] L. Song, E. J. Hennink, I. T. Young, H. J. Tanke, *Biophys. J.* **1995**, *68*, 2588–2600.

SECTION IV:

MOLECULAR HOST-GUEST CHEMISTRY

Host-guest molecular systems based on Curcuminoids

4.1 Chapter I: CCMoids as Guest Molecules

4.1.1 Introduction

Supramolecular chemistry

Supramolecular chemistry has been defined as the chemistry that goes beyond the covalent bond and individual molecules.[1,2] The field has primarily found its inspiration in biological molecules such as proteins or lipids. During the last years, numerous developments have been accomplished regarding topics as: interfaces (mostly from a physical point of view, from basic knowledge to applications, non-covalent interactions (for example toward drug design) and solid state engineering (with development of new materials and polymers).[3] Supramolecular chemistry has become a multidisciplinary creative tool allowing its use in different fields.[1–3] The forces responsible for the final organization and the holding together of the supramolecular assemblies are weak non-covalent interactions, such as, hydrogen bonding, polar attractions, van der Waals forces, hydrophilic-hydrophobic interaction and charge transfer interaction.[1–3]

From a chemical perspective, one of the most important features of the final systems is the presence of such weak interactions. In this sense, the amount of energy required to form or destroy the supramolecular assemblies is significantly small. This gives rise to the formation of supramolecular dynamic systems, where by the application of external stimuli, such as pH, light, temperature or redox processes, it is possible to control the formation/disassembly and therefore properties can be modulated.[4]

Because of the potential applications, one of the most studied systems on supramolecular chemistry is the redox responsive host-guest systems. In general, such systems are usually been constructed by: (i) a host molecule (some well-known are cyclodextrin[5,6] and cucurbituril[7–9]) and (ii) a guest molecule with a redox active group that as affinity for the guest molecule (ferrocene is one of the most typical).[4–8,10]

Among many guest molecules, ferrocene (Fc) is widely used due to its electrochemical responsiveness and ability to interact with a number of host molecules. Fc presents a redox transformation between the neutral (Fc) and oxidized (Fc^+) state, hence from a diamagnetic state to a paramagnetic one. This switch also implies hydrophobicity (Fc)/hydrophilicity (Fc^+) changes, leading to different redox sensitive self-assembly behaviors.[8]

In the case of the host molecules, cyclodextrin and cucurbituril are some of the most famous, especially known to act as host partners for Fc moieties due to the matching of their cavities regarding size and high hydrophobicity.[11] Cucurbituril, CB[n], is a synthetic natural macrocycle product based on glycoluril units (where “n” can vary from 5 to 14) with a pumpkin-shaped

symmetric structure. It contains hydrophobic inner cavity and two identical electronegative carbonyl portals that allow encapsulation of guest molecules by hydrophobic and ion-dipole interactions.[4] In contrast, cyclodextrin, CD, is a natural macrocycle product based on glucopyranose units (where "n" varies from 6 to 8; β-CD contains 7 units). β-CD systems present asymmetric structures (truncated cones) with hydrophobic cavities. In both cases, CB[n] and β-CD, the release of water in the process of guest binding also contributes to thermodynamically favor the formation of highly stable host-guest systems with the inclusion of compounds in aqueous solution.[12]

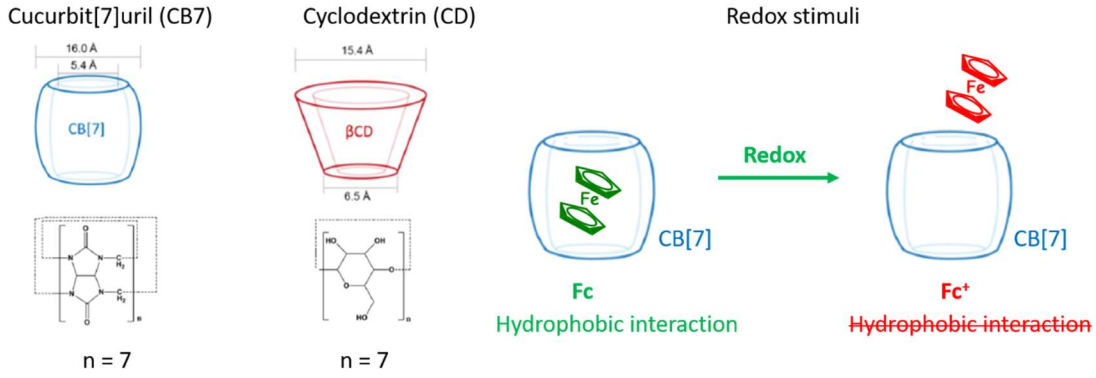

Figure 4.1.1: Cucurbit[7]uril and β-Cyclodextrin molecules. Representation of the redox process in the case of the host-guest system called Fc@CB[7].

Most of the published works related to the systems described above (Figure 4.1.1) has been performed in solution,[7,8,10,11] where only few of them address the same systems on surface .[13–16] The behavior may differ from that found in solution, and therefore it is essential basic studies regarding the latest, for applications as for example chemo- or biosensor systems.[17]

Previous literature on surfaces describes the creation of self-assembly monolayers (SAMs) as the first step, since this is a convenient, flexible and simple way of immobilizing one of the molecules on surfaces. Within these studies, two different approaches have been used to form host-guest systems: (i) SAMs formed by host molecules and later incubation of the functionalized surface with guest molecules or (ii) formation of SAMs using guest molecules and incubation with host molecules.[14]

This section describes the use of the first approach, describing the creation of SAMs with two host molecules: cucurbit[7]uril (CB[7]) and β-cyclodextrine (β-CD) (Figure 4.1.2, right) and the synthesis of two guest CCMoids molecules: FcCCMoid (**1**) and Fc9Accm (**2**) (Figure 4.2, left).

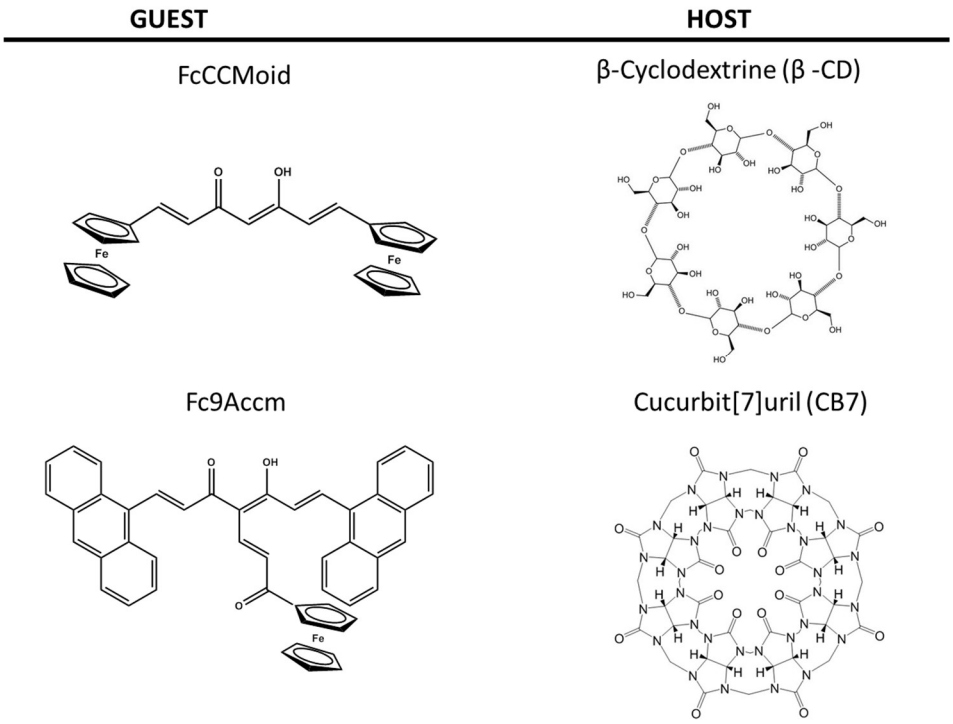

Figure 4.1.2: Representation of (left) guest molecules FcCCMoid (**1**) and Fc9Accm (**2**) (left) and (right) host molecules cucurbit[7]uril (CB[7]) and β-cyclodextrine (β-CD).

The host-SAM formation is a key step, because of the difficulty of arranging the molecules on surfaces. The process of forming the SAMs is governed by the equilibrium between the intermolecular interactions among the molecules and the interface molecule-surface interactions, therefore the election of a suitable substrate that matches with the nature of the guest molecules is crucial.

There, the experiments were carried out using gold substrates with a (111) preferential orientation (Au(111), Figure 4.1.3). Comparing with the other gold faces, this one presents the highest atomic density and is the most stable, being the most suitable for the formation of self-assembled monolayers (SAMs).[18,19]

Different methodologies were used to form the SAMs depending on the applied host molecules (β-CD or CB[7], respectively). In the case of β-CD, an initial functionalization of the molecules with thiol groups was necessary.[14,16] Thiols groups display high affinity for the gold surfaces making possible the generation of well-packed and therefore organized SAMs. In contrast, in the case of CB7, monolayers were achieved by the direct adsorption of such molecules, due to the effective electronic interactions of their carbonyls groups with the gold surfaces.[13] The latest presents advantages *vs.* the β-CD procedure, avoiding intermediate steps and time-consuming.

Once the SAMs containing the host molecules were prepared, they were incubated with a guest molecule FcCCMoid (**1**) and Fc9Accm (**2**) (Figure 4.3,). Both CCMoids contain ferrocene groups as the redox active part. Comparing compounds **1** and **2**, the number of ferrocenes and their arrangement within the molecules are difference. In the case of FcCCMoid (**1**), this system presents two ferrocenes groups which are located on each side of the conjugated chain. In contrast, Fc9Accm (**2**) displays only one ferrocene group in the "leg" of the CCMoid. In the latest, anthracene groups are disposed in each side of the conjugated chain, providing the molecule with fluorescence apart from the electrochemical properties derived from the ferrocene group. Due to the structures of **1** and **2**, it was expected that these systems presented successful dynamic supramolecular host-guest assemblies controlled by redox stimuli.

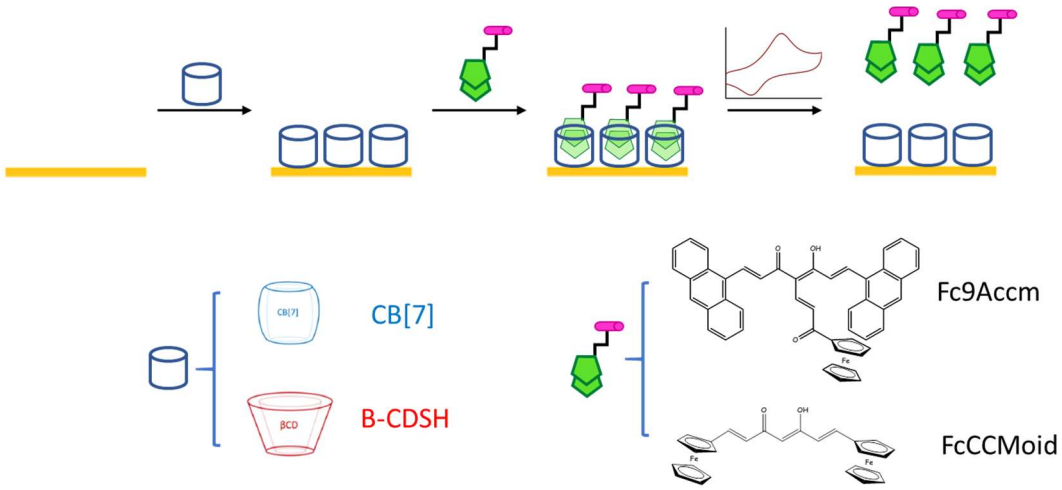

Figure 4.1.3: Schematic representation of the necessary steps to form host-guest systems on surfaces. (i) formation of SAMs of host molecules, (ii) incubation with CCMoid molecules (iii) electrochemistry characterization.

4.1.2 Objectives

The aim in this section is the synthesis and fabrication of supramolecular host-guest systems based on CCMoid ligands and their study in solution and on Au(111) surfaces.

Non-covalent interactions govern the formation of the final supramolecular compounds. These interactions are very sensitive to the nature of the molecules (functional groups, size…) and also the environment (solution, surface…). For this reason, a comparative study in solution and on Au surfaces was carried with the difference host-guest molecules.

Related to the host molecules, the study was carried out using two different types: i) cucurbituril (CB[7]) and ii) β-cyclodextrin (β-CD). Both systems contain hydrophobic cavities that allow the interaction with small hydrophobic guests (Fc); but their nature and sizes are different. This fact allowed us to make also a comparative study between both, studying which one of them presented more affinity for the formation of host-guest compounds.

In relation with the guest molecules, in a first step, the synthesis of two new CCMoids, FcCCMoid (**1**) and Fc9Accm (**2**), was carried out. The presence of different numbers of ferrocenes, as well as their different dispositions, allowed their comparison in the formation of host-guest compounds in solution by the use of UV-Vis absorption and ^{1}H NMR techniques.

As mentioned above, the immobilization of the host molecules was necessary for the preparation of the supramolecular systems on Au surfaces, forming a self-assembled monolayer (SAM). In the case of CB[7], the adsorption on the gold surfaces was performed directly, but in the case of β-CD, a previous functionalization of the molecule with thiol groups was required, to achieve β-CDSH. The correct orientation of the gold surfaces and the formation of the supramolecular self-assembled monolayer (SAM) were confirmed by electrochemical measurements.

The incubation of the two guest CCMoid molecules with the Au (containing the two SAMs with the corresponding host molecules) led to the formation of four different systems: FcCCMoid@SAMCB[7]/Au(111) (**H1G1**), Fc9Accm@SAMCB[7]/Au(111) (**H1G2**), Fc9Accm@SAMb-CDSH/Au(111) (**H2G1**) and FcCCMoid@SAMb-CDSH/Au(111) (**H2G2**). In all of them, electrochemical studies were performed to corroborate the formation of the host-guest compounds. In order to study the dynamism of the host-guest systems stimulated by redox process, a study of the robustness and the reversibility in each system was also performed in order to compared them.

4.1.3 Results and Discussion

4.1.3.1 Experimental section

Synthesis of FcCCMoid

FcCCMoid (Figure 4.1.4) shows a β-diketone group in the middle of the conjugated backbone and two ferrocene groups are located at both sides of the molecule conferring an

organometallic nature to the final CCMoid with electrochemical properties. This feature, as it was mentioned before, is crucial for the development of the desired host-guest behavior.

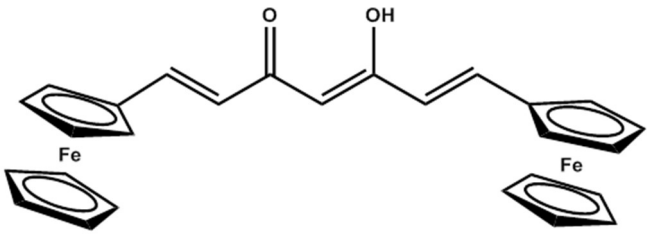

Figure 4.1.4: Representation of the molecular structure of FcCCMoid.

FcCCMoid was synthesized following Pabon's method,[20] (explained in the general introduction). Later, single crystals were obtaining by slow evaporation in $CHCl_3$.

The ^1H NMR spectrum (Figure 4.1.5) of the molecule in solution indicated that the enol form was the only observed displaying two characteristics signals: a broad band at 16.15 ppm (yellow spot) corresponding to the proton from the enol group and a sharp singlet at 5.70 ppm (green spot) assignable to the methane proton of the enol form (integration, here not shown, equal to one H). This is due to the existence of a strong intramolecular hydrogen interaction bond that stabilizes the enol form *vs* the di-keto form. The signals corresponding to the conjugated chain appeared at similar chemical shifts as other CCMoids (7.50 and 6.21 ppm) with coupling constants of 15.6 Hz (E conformation as in Figures 4.4 and 4.5). The two ferrocenes groups were equivalent and show three signals: two of them related to the methane located at the cyclopentadienyl ring bonded to the conjugated chain, and one signal corresponding to the other cyclopentadienyl ring in the Ferrocene sandwich. The solid was also characterized by Mass Spectrometry, shown in Annex 4.1.

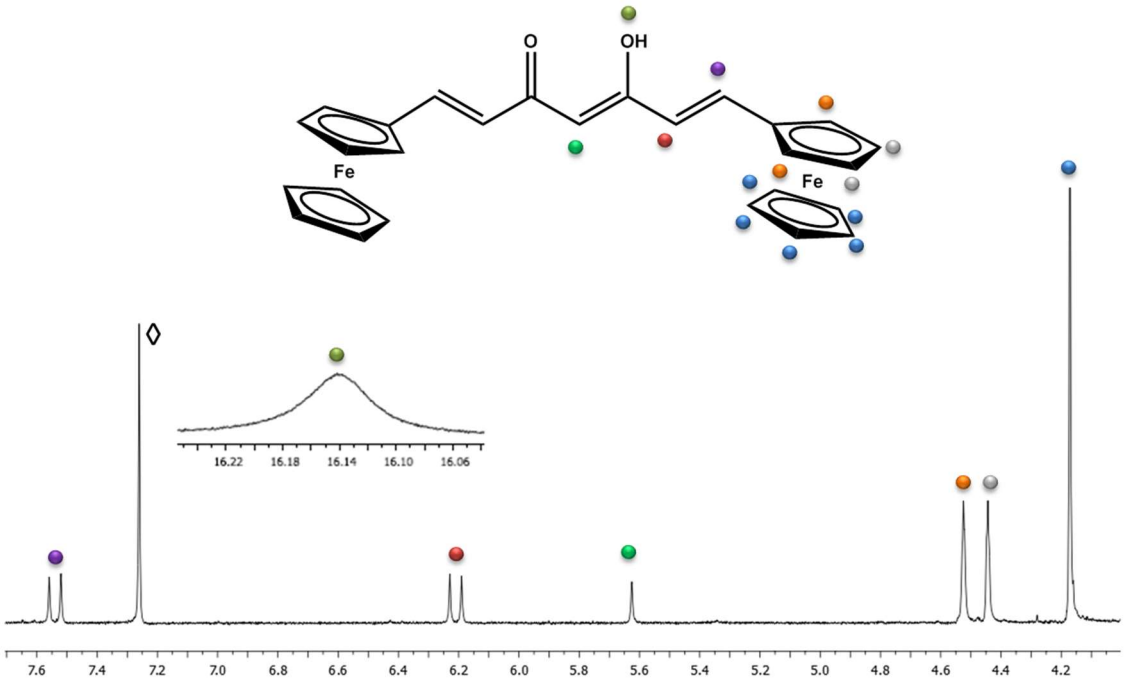

Figure 4.1.5: ^{1}H NMR spectrum of FcCCMoid in $CDCl_3$. ◊ $CDCl_3$.

Synthesis of Fc9Accm

Fc9Accm (Figure 4.1.6), displayed similar features as previous system, where in this case, two anthracene groups were located in each side of the conjugated chain. Moreover, in the middle of the conjugated chain, there was (the so-called leg) with a double bond and a ferrocene group situated at the end of the moiety. In this molecule, the anthracene species provided fluorescence and the ferrocene group electrochemical properties, giving rise to a multifunctional CCMoid system.

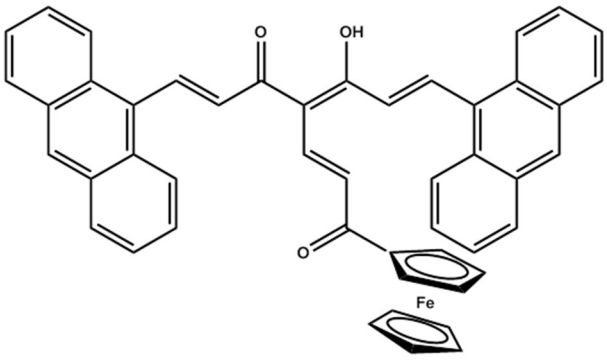

Figure 4.1.6: Representation of the molecular structure of Fc9Accm

The synthesis of the molecule was carried out in two different steps (Figure 4.1.7): (i) synthesis of 9Accm (Pabon's method)[20] and (ii) coordination of the ferrocenyl unit to the central carbon of this CCMoid. This last step was carried out by performing a Michael Addition reaction,[21] that consists in the deprotonation of the enol in the CCMoid, followed by a reaction with the corresponding electrophile. The electrophile ferrocenyl derivative chosen for the study was the ferrocenyl propyone.

The synthesis of ferrocenyl propyone was carried out also in two steps, starting with ferrocenecarboxaldehyde.[22] In a first stage, the latest reacted with ethynylmagnesium bromide (Grignard reaction) to obtain the corresponding propargylic alcohol.[22] Then, the alcohol was oxidized providing the final system, 1-ferrocenylprop-2-yn-1-one. For the second step, different oxidants were used (pyridinium chlorochromate (PCC), cerium ammonium nitrate (CAN) and commercial manganese dioxide) but all of them provided the final product in low yields. Optimal results were accomplished with manganese dioxide (MnO_2) freshly prepared. Finally, the resulting residue was purified by flash chromatography obtaining ferrocenyl propyone as a dark red solid.

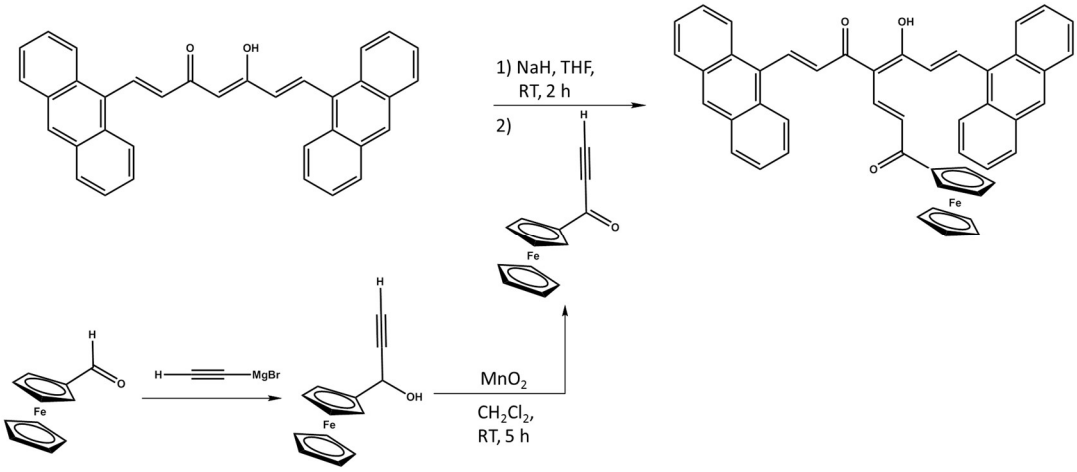

Figure 4.1.7: Synthetic scheme of Fc9Accm

Once all of the reagents were prepared, the synthesis of the ferrocenyl CCMoid was carried out, as mentioned before, by a Michael addition reaction (Figure 4.1.8). 9Accm was deprotoned at room temperature with sodium hydride forming the corresponding carbanion. In this case, a yellow solid precipitated, which may correspond to the salt of the ligand. Then, ferrocenyl propyone was dissolved in dry THF and added dropwise to the previous solution to form the final ferrocenyl CCMoid. The final yield for the latest reaction was 20 %. This is relative low compared with other CCMoid syntheses because the total consumption of the

CCMoid was not possible even after long reaction times, which it was found mainly induced degradation of the starting materials.

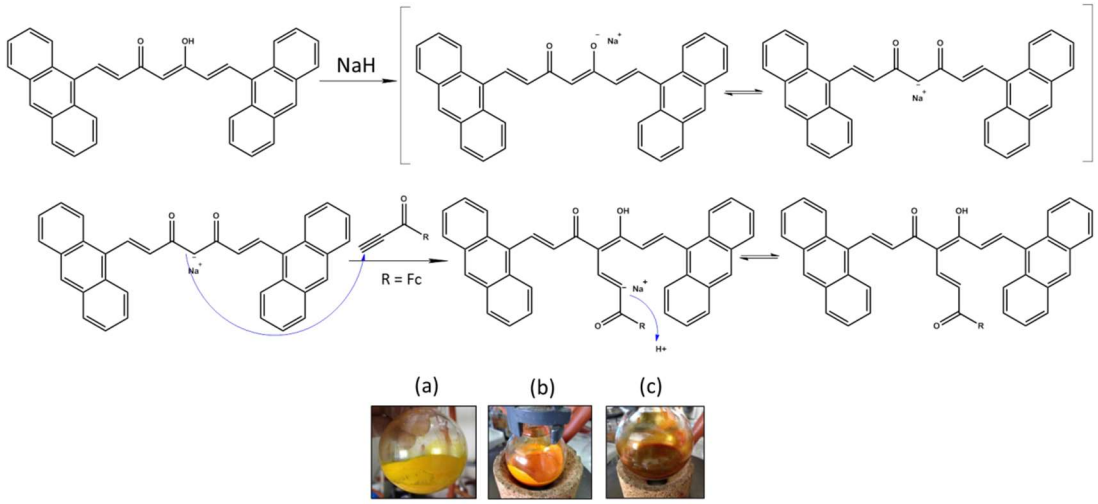

Figure 4.1.8: Possible Michael's reaction mechanism. Picture corresponding to 9Accm deprotonated (a) and (b) and after alkyne addition (c).

The final product was purified using preparative TLC Plates (Figure 4.1.9, number 3).

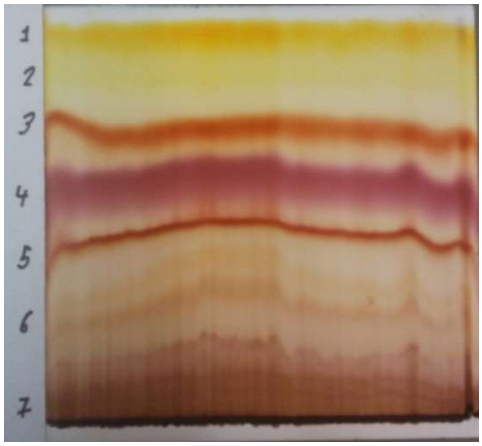

Figure 4.1.9: TLC preparative plate containing Fc9Accm.

The stabilization of the enol form was corroborated in the solid state by X-ray crystallography (Figure 4.1.11) and in solution by ^{1}H NMR (Figure 4.1.10). In solution also, the preservation of the symmetry was evident finding half of the proton shifts from the anthracene groups and the conjugated chain. Comparing with the ^{1}H NMR spectrum of 9Accm, the disappearance of the

signal at 5.85 ppm indicated that the substitution took places at the desired position (Annex 4.2). Two types of signals related to the double bonds were found. The constant couplings of J = 15.7 Hz (8.86 and 7.25 ppm) and J = 15.3 Hz (7.75 and 6.58 ppm) indicated in both case an E conformation (found as well in the crystal structure). The solid was also characterized by Mass Spectrometry which is shown in Annex 4.1.

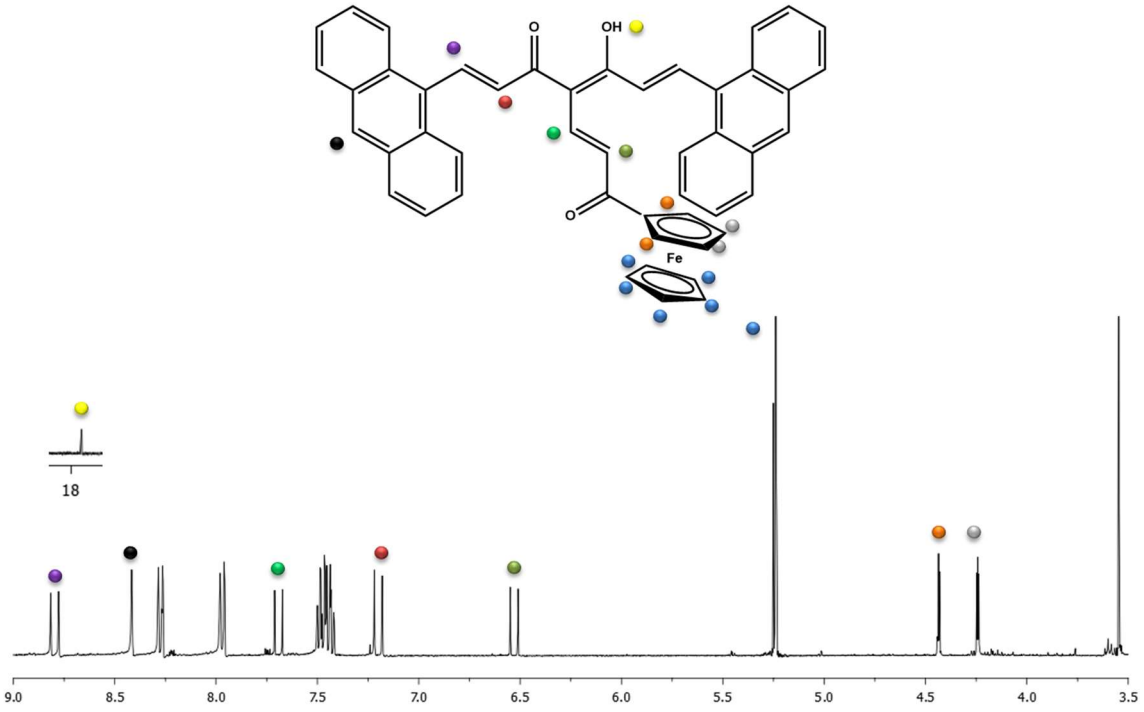

Figure 4.1.10: ^{1}H NMR spectrum of Fc9Accm in THF-d8.

Crystal Structures

The crystal structure of Fc9Accm required the use of a synchrotron source, due to the small size of the crystals; however, the structure of FcCCMoid was obtained by the use of a standard diffractometer. General crystallographic data of the FcCCMoid system is presented in Annex 4.3.

FcCCMoid crystallographic description

FcCCMoid (Figure 4.1.11) crystallizes in a P2/n space group with two molecules in the unit cell.

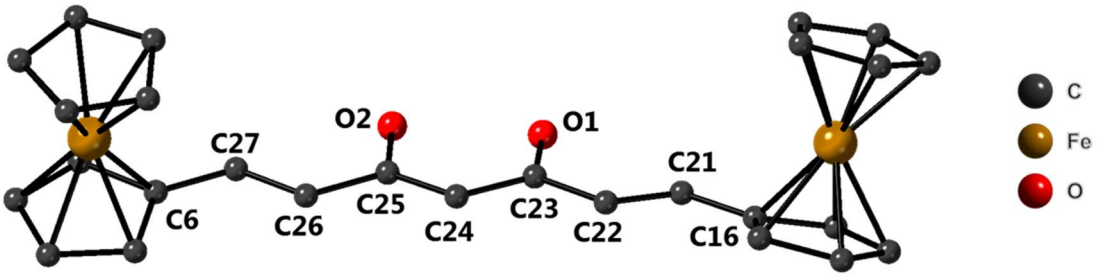

Figure 4.1.11: Representation of FcCCMoid where Fe(green), O(red) and C(grey) atoms are shown. H atoms have been omitted to simplify the structure.

The β-diketone group shows two different distances corresponding to C(23)-O(1) and C(25)-O(2) of 1.285 and 1.320 Å respectively. Similarly, two different distances were also found between C(24)-C(23) and C(24)-C(25) with 1.401 and 1.380 Å, in that order. For that reason, the presence of a tautomeric equilibrium in the crystal was discarded and the enol form is the favored one. These values were similar to those found in the literature for related systems.[23–26] Moreover, the distance between O(1)···H-O(2) is relatively short (2.473 Å, together with an angle of 148.96 °) indicating the presence of an intramolecular hydrogen bond. Related to the conjugated chain, two types of C-C values in an alternated fashion were found corresponding to C-C single bond distances (C(25)-C(26), C(23)-C(22), C(27)-C(6) and C(21)-C(16)) with distance values among 1.426-1.446 Å and C-C double bonds (C(26)-C(27) and C(22)-C(21)) displaying shorter distances (in the range of 1.334-1.319 Å). The chain was completely planar and presented an E conformation, minimizing steric hindrances. Related to the ferrocene group, the C-C distances of the non-substituted ring are between 1.383 and 1.413 Å. In the substitute ring, these values were higher (1.384-1.459 Å). Regarding the disposition of these two moieties, ferrocene rings could present eclipsed and non-eclipsed forms (Figures 4.1.12 right and left, in that order). Such deviations show values between 16.98 ° and 3.19 °.

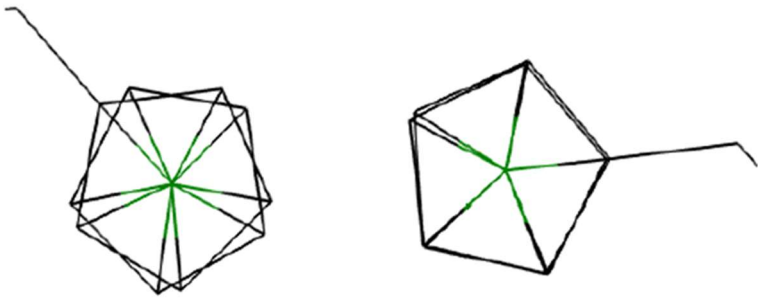

Figure 4.1.12: Disposition eclipsed (right) and non-eclipsed (left) of the ferrocene rings.

The two ferrocenes were located outside of the plane formed by the β-diketone and the conjugated chain, disposed in a perpendicular way. This arrangement was due to the supramolecular packing and the nature of the spacer. Finally, it is important to highlight the existence of Van der Waals intermolecular interactions between the H of the enol and the carbon of the conjugated chain of the neighboring molecules.

Fc9Accm crystallographic description

Fc9Accm (Figure 4.1.13) crystallizes in a P-1 space group with one molecule in the unit cell.

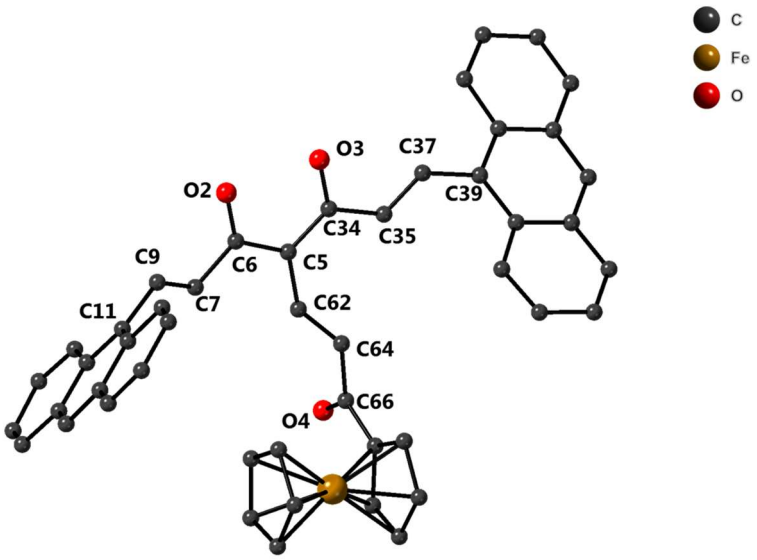

Figure 4.1.13: Representation of Fc9Accm where Fe(green), O(red) and C(grey) atoms are shown. H atoms have been omitted to simplify the structure.

In this case, C-O distances, corresponding to the β-diketone, were similar than in the previous compound, however the C-C distances from the conjugated chain presented higher values (1.439 – 1.397 Å). That may be due to the functionalization of the central position that may lead to a loss of conjugation. Again, the conjugated chain was disposed in the same plane as the β-diketone with a (E) conformation and the C-C distances were similar to other CCMoids[23–26]. The anthracene groups were located on both sides of the conjugated and twisted from each other with an angle of 75.47 ˚. Related to the leg moiety, a conjugated C-C chain with two different C-C values was found. In this sense, C(1)-C(42) and C(43)-C(44) (distances values of 1.486-1.484 Å) and C(42)-C(43) (1.341 Å) corresponded to two single and one double bonds, respectively. The ferrocene group was located outside of the chain plane and both rings were disposed in an eclipsed mode.

4.1.3.2 Study of the host-guest Interactions

Host-guest interaction studies, between the two synthetized host CCMoid molecules (FcCCMoid and Fc9Accm) and the two guest molecules which are the β-cyclodextrine (β-CD) and cucurbit[7]turil (CB[7]) were performed in solution and on surfaces.

4.1.3.2.1 Studies in solution

The host-guest interaction studies carried out in solution were performed using water as a solvent. Water favors the hydrophobic interactions between the host and guest molecules. However, CCMoid molecules are not soluble in water and sonication processes were required to force the possible host-guest interactions. Then, the solutions were stirred overnight giving rise to the formation of host-guest compounds that were named as follows: **FcCCMoid@CB[7]** (**H1G1**)**, Fc9Accm@CB[7]** (**H1G2**)**, FcCCMoid@β-CD** (**H2G1**) and **Fc9Accm@β-CD** (**H2G2**).

The formation of these supramolecular compounds was characterized by UV-Visible absorption and ^{1}H NMR.

UV-Visible Absorption experiments

The UV-Visible absorption measurements were performed in water using quartz cuvettes. Blanks were performed together with control experiments using only the guest molecules (**FcCCMoid** and **Fc9Accm**).

^{1}H NMR studies

^{1}H NMR experiments were performed using deuterated water (D_2O) as a solvent. In all the experiments, the internal standard 3-(Trimethylsilyl)propionic-2,2,3,3-d_4 acid sodium salt (TSP) was used as an internal diamagnetic reference (like normally TMS is used) to analyze with accuracy the shifts of the signals produced by the formation of the host-guest compounds. ^{1}H NMR spectra were collected with a coaxial tube formed by two separated compartments to avoid the possible interaction between the host molecules and the TSP.

The control experiments mentioned above were performed under the same conditions.

4.1.3.2.2 Surface studies

This section was possible thanks to a short stay in the group of Professor José Zagal at the University of Santiago de Chile (USACH).

Host-guest experiments on surfaces were performed using gold substrates. The process to carry out the formation of the supramolecular compounds can be divided in three main steps (Figure 4.1.14):

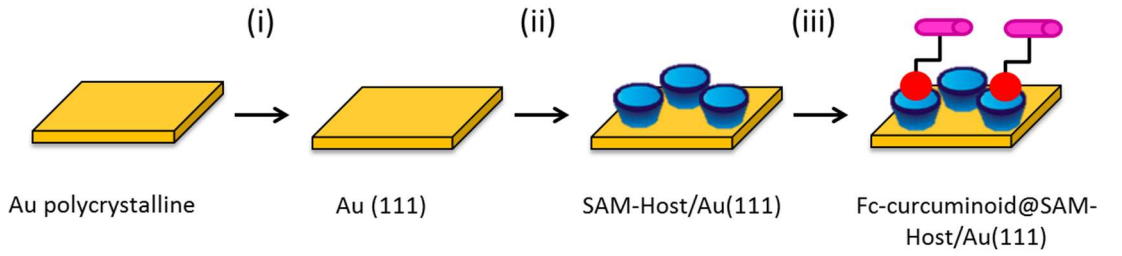

Figure 4.1.14: Representation of different steps to form host-guest on surfaces: (i) annealing process, (ii) host-SAM formation and (iii) incubation with CCMoid.

(i) Annealing of the gold surface to achieve a preferent orientation, **Au(111)**

(ii) Host-SAM formation (**SAM-CB[7]/Au(111)** and **SAM-β-CDSH/Au(111)**) by the incubation of the gold surface with solutions of the different host systems (CB[7] and β-CDSH, respectively).

(iii) Host-guest compounds formation, by incubating gold surfaces with solutions of the two different ferrocene-CCMoid species (FcCCMoid and Fc9Accm) to form **FcCCMoid@SAM-CB[7]/Au(111), Fc9Accm@SAMCB[7]/Au(111), FcCCMoid@SAM-β-CDSH/Au(111)** and **Fc9Accm@SAM-β-CDSH/Au(111).**

In the following sections, the steps required are explained in more detail.

(i) <u>Processing of Au(111) surfaces</u>

One of the most common methods for the fabrication of gold surfaces is the evaporation of metallic gold on glass substrates.[27] This leads to the achievement of surfaces with polycrystalline Au compositions. The sizes of the gold grains are nanometric and not suitable

for the formation of self-assembled monolayer (SAMs). An initial thermal treatment of the surface is needed to increase the size of the grains. This treatment is known as “annealing”, which increases the size of the grains, providing large monoatomic terraces with a preferably crystallographic orientation Au(111) being this one suitable for the formation of SAMs.

Thermal treatments of the gold surfaces were performed with a butane flame at 650 ˚C approximately during 10 min. During the process, the gold plates reach a dark red color. Here, it is important to keep constant the temperature and not to expose the samples to higher values, that could damage the gold plates.

The characterization of the Au(111) surfaces was performed by electrochemistry. In these measurements, the gold surfaces acts as a working electrode. Therefore, it is possible to apply a voltage by connecting it to a potentiostate. Thus, a previous step consisting in the welding of a gold plate is required (Figure 4.1.15, right).

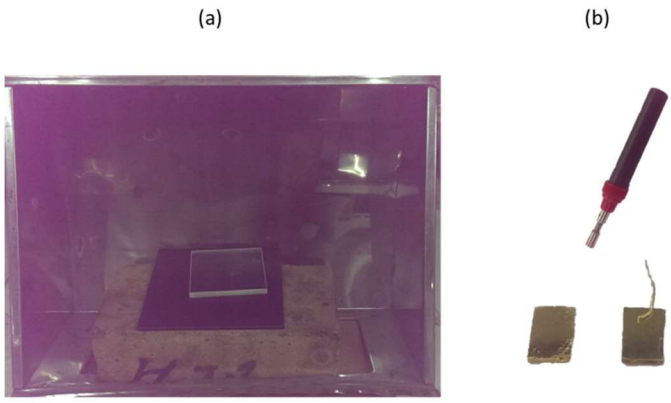

Figure 4.1.15: (a) Place used for the annealing process of the gold plates. (b) gold surfaces: without a wire and with a welded wire.

It is possible to re-use gold surfaces several times. However, it is important to clean properly the surfaces therefore, before the thermal treatment, the surfaces were cleaned by soaking them in a solution of piranha (30 % H_2O_2 + 70 % H_2SO_4) to remove the possibility of having organic materials. The surfaces were immersed for 3 min in the piranha solution and then were washed with copious MilliQ water and dried with N_2. Longer exposition times can damage the substrates.

(ii) <u>Processing of host self-assembly monolayer: SAM-CB[7]/Au(111) and SAM-β-CDSH/Au(111)</u>

The formation of self-assembly monolayer (SAMs) on gold surfaces was performed in solution by self-organization of the CB[7] and β-CDSH groups, respectively. Therefore, after the thermal treatment, the surfaces were leaved to cool down to room temperature and then, were incubated for 24 hours in a 0.01 M solution of the corresponding host. In the case of cucurbit[7]uril (CB[7]), SAMs were performed by spontaneous adsorption of the molecules through the interaction between the carbonyl groups and the gold surfaces. In contrast, in the case of the β-cyclodextrin, a previous functionalization of the β-cyclodextrin with thiol groups (β-CDSH) was used.[14] The presence of thiols group allows the immobilization of the host molecule in the gold substrate due to the high Au-S affinity. The incubation of CB[7] was performed in MilliQ water,[13] but in the case of β-CDSH the use of a mixture of DMSO/H_2O was necessary due to their low solubility in water. Once finished, the gold surfaces were rinsed with MilliQ water and dried with N_2 in order to remove the physiadsorbed molecules.

(iii) Processing of ferrocene derivatives systems: FcCCMoid@SAMCB[7]/Au(111) (H1G1), Fc9Accm@SAMCB[7]/Au(111) (H1G2), FcCCMoid@SAM-β-CDSH/Au(111) (H2G1) and Fc9Accm@SAM-β-CDSH/Au(111) (H2G2)

The formation of host-guest compounds was performed by incubating the gold surfaces with guest solutions. Thus, two functionalized gold surfaces with the host molecules (**SAM-CB[7]/Au(111)** and **SAM-β-CDSH/Au(111)**) were incubated with solutions of the corresponding ferrocene guest (FcCCMoid or Fc9Accm) using a mixture of solvents DMSO/H_2O (1/8). The systems were sonicated for 3 min until reach a fine powder achieving a homogeneous solution color and then were stirred for 24 hours at room temperature. After that time, the gold electrodes were soaked in MilliQ water and dried with N_2, in order to remove the physiadsorbed molecules.

Initially, the experiments were performed incubating the hosts in water solutions. This solvent was chosen because improve the hydrophobic host-guest interaction, but unfortunately, no signals of the host-guest formation were obtained. One of the reasons could be due to the low solubility of the guest molecules (FcCCMoid and Fc9Accm) in water**.** Therefore, in order to solve this, a small amount of dimethyl sulfoxide (DMSO) was added during the incubation process. The DMSO was chosen because the host/guest molecules are soluble in and because its polarity is similar to the water and facilitates hydrophobic interactions. Following this idea, initial experiment using 1 % of DMSO and later 10 % of the same solvent were performed but unsuccessful results were obtained. Finally, the use of 20 % of DMSO provided positive results, with evidences of the host-guest interaction by electrochemistry measurements.

SAM-CB[7]/Au(111) and **SAM-β-CDSH/Au(111)** and the host-guest compounds **FcCCMoid@SAM-CB[7]/Au(111), Fc9Accm@SAM-CB[7]/Au(111), FcCCMoid@SAM-β-CDSH/Au(111)** and **Fc9Accm@SAM-β-CDSH/Au(111)** were characterized by electrochemical measurements, contact angle and XPS.

Surface characterization

Electrochemical experiments

Due to the presence of the ferrocene groups in these CCMoid molecules, the characterization by electrochemistry of the host-guest formation at molecular interfaces could be easily followed.

The electrochemical characterization on surface was performed by the use of cyclic voltammetry (CV), differential pulse voltammetry (DPV) and square wave voltammetry (SWV) techniques. In these experiments, the gold surface acts as a working electrode and the measurements were performed using 0.1 M of Na_2SO_4 as supporting electrolyte, with a scan rate of 50 mV/s and a window of 0-800 mV.

Firstly, the cyclic voltammetry of the **Au(111)** surface was performed using H_2SO_4 as supporting electrolyte. Every oriented face of gold surfaces shows a characteristic voltammogram so this measure allows us to check if the annealing process was done correctly.[19]

Then, electrochemical characterization by CV, DPV and SW of the Host SAMs surfaces **SAM-CB[7]/Au(111)** and **SAM-β-CDSH/Au(111)** were performed. In this case the experiments provide information of the SAM formation. Particularly, in the case of **SAM-β-CDSH** system, electro-desorption experiments using 0.1 M of NaOH were performed.

Finally, the formation of host-guest compounds **FcCCMoid@SAM-CB[7]/Au(111), Fc9Accm@SAMCB[7]/Au(111), FcCCMoid@SAM-β-CDSH/Au(111)** and **Fc9Accm@SAM-β-CDSH/Au(111)** was characterized by CV, DPV and SW. The evidence of formation was given by the appearance of signals corresponding to the ferrocene groups from the CCMoids.

On the other hand, in order to study the influenced of the host molecules, control experiments without the host molecules **FcCCMoid/Au(111) and Fc9Accm/Au(111)** were performed at the same conditions that are mentioned before.

X-ray photoelectron spectroscopy (XPS)

XPS measurements were only performed for the **FcCCMoid@SAMCB[7]/Au(111)**. These experiments were carried out under the same conditions used for the electrochemistry, with the only difference that the incubation with the FcCCMoid were performed using water (without adding 20 % of DMSO).

Contact Angle studies

Contact angle measurements were performed using the same conditions than for the XPS studies.

4.1.3.3 Host-guest experimental results

4.1.3.3.1 Solution Studies

Ultraviolet-visible absorption spectroscopy (UV-Vis)

Characterization of FcCCMoid@CB[7], Fc9Accm@CB[7], FcCCMoid@β-CD and Fc9Accm@β-CD systems in water solution

Figure 4.1.16 shows the UV-Vis absorptoin spectra of the guest and the host-guest compounds corresponding to the system (a) **FcCCMoid@CB[7]**, (b) **FcCCMoid@β-CD**, (c) **Fc9Accm@CB[7]**, and (d) **Fc9Accm@β-CD** in water solution.

In the case of the experiments carried out only with guest molecules (black lines) no signals were observed in the UV-Vis absorption spectra since both ferrocene CCMoid were not soluble in water.

In contrary, with the addition of the corresponding host molecule, several bands start to appear indicating the formation of the host-guest molecule. The nature of these bands can be related with the CCMoid systems. In all cases, a band between 500-600 nm is presented corresponding to the conjugated chain.[26] Furthermore, another band at 400 nm corresponding to the ferrocene group were also observed, being lower in the case of Fc9Accm since there was only one ferrocene group. In this system appeared another signal at 270 nm corresponding to the anthracenes groups.[28]

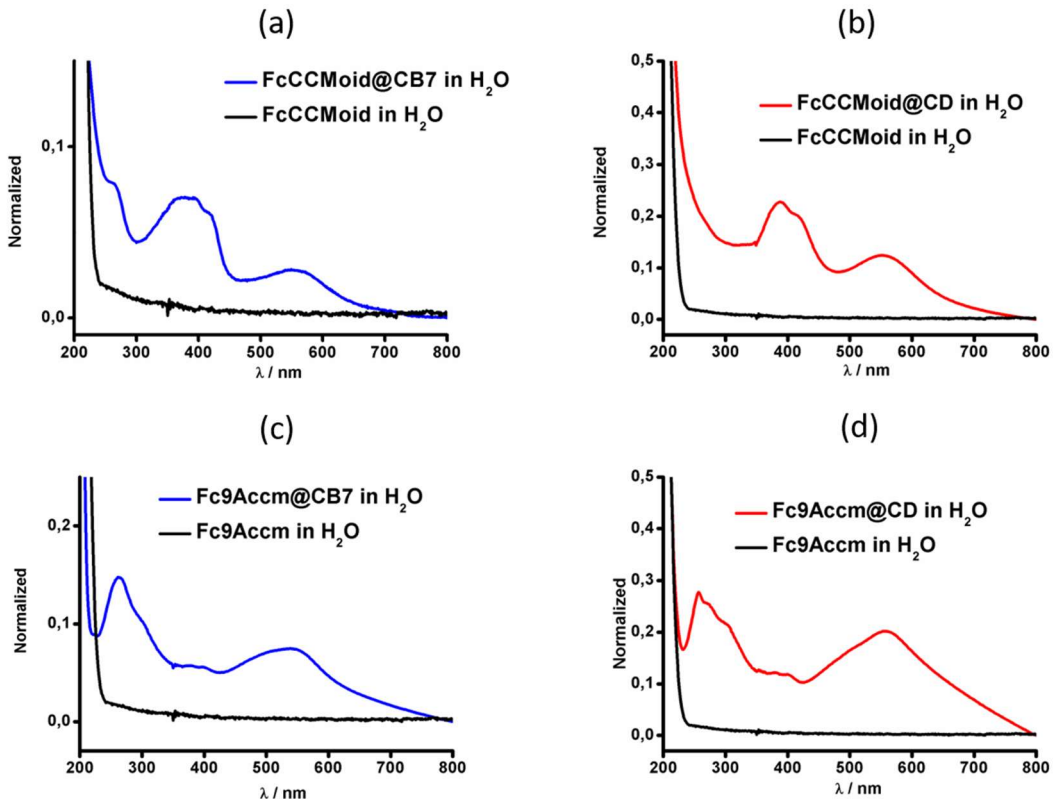

Figure 4.1.16: UV-Visible spectra of FcCCMoid and (a) FcCCMoid@CB7 (b) FcCCMoid@CD in H_2O. UV-Vis spectra of Fc9Accm and (c) Fc9Accm@CB7 (d) Fc9Accm@CD in H_2O.

^{1}H NMR

^{1}H NMR experiments were also carried out, however non conclusive results culd be extracted from our studies mainly due to: (i) the low solubility of the guest molecules in D_2O comparing with the host molecules and (ii) the aromatic nature of both systems (guest and host) that gave rise to overlaps of several signals making extremely difficult their analysis.

Our study was carried out performing the host and guest spectra in a first stage separately and later together. In the latest, the signals observed were mostly related to the host system. However, the appearance of new signals may have a CCMoid origin; at this point further studies have to be performed to confirm the latest statement (Annex 4.4).

4.1.3.3.2 Surface Studies

Electrochemical studies

Characterization of Au(111) in 0.1 M H_2SO_4 in water

The electrochemical characterization of gold surfaces after the annealing process was carried out by cyclic voltammetry (CV). As mentioned before, this technique assists in the corroboration of the gold surface orientation. Every crystallography gold orientation shows a specific voltammogram (fingerprinting) being able to distinguish between the difference orientations Au(111), Au(110) and Au(100) respectively.[29]

The voltammogram corresponding to the gold working electrode with preference orientation (111) in 0.1 M H_2SO_4 is shown in Figure 4.1.17.

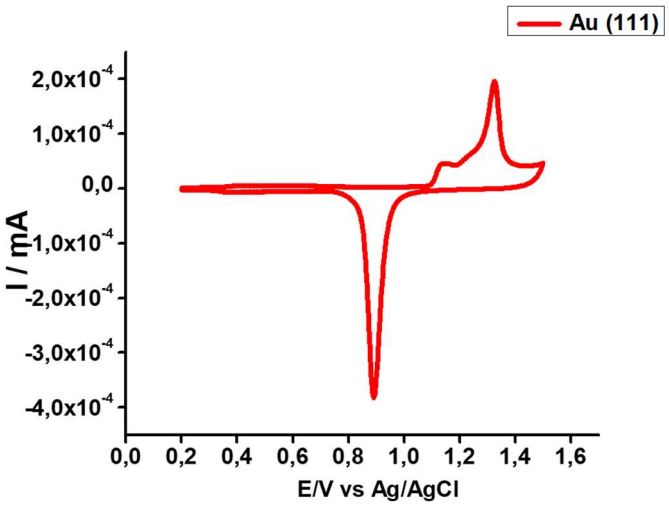

Figure 4.1.17: CV measurement of Au(111) in 0.1 M H_2SO_4

The voltammogram obtained agree with those reported in the literature for Au(111).[29] The voltammogram show an oxidation peak corresponding to the gold oxide formation and the subsequent reduction following the redox equation (1):

$$Au\ (111) + H_2O \rightarrow AuO + 2H^+ + 2e^- \qquad (1)$$

By the integration of the reduction peak it is possible to calculate the real area of the electrode using Equation (2). The calculations were carried out considering that 1 cm^2 of Au(111)

surfaces present a charge of 444 µC for a process of two electrons using the equations as it follows.[30]

$$A_r = \frac{Q_f}{444\ \mu C x cm^2} \quad (2)$$

where, A_r = real area of the electrodes; Q_f is the integrated charge of the entire reduction peak

$$Q_f = \frac{Integrate\ Area}{V_{scans}\ (V)} = \frac{2.25x10^{-5}}{0.05} = 4{,}5x10^{-4}\ C \quad (3)$$

$$4{,}5x10^{-4}\ C\ x \frac{1cm^2}{444x10^{-6}\ C} = 1{,}01\ cm^2$$

Characterization of the host-SAMs: SAM-CB[7]/Au(111) and SAM-β-CDSH/Au(111).

The two different SAMs-Host (i) SAM-CB[7]/Au(111) and (ii) SAM-β-CDSH/Au(111) were characterized by cyclic voltammetry (CV), differential pulse voltammetry (DPV) and squarewave voltammetry (SW).

SAM CB[7]/Au(111) and SAM-β-CDSH/Au(111) 0.1M Na_2SO_4 in water

The cyclic voltammetry of SAM-CB7/Au(111) and SAM-βCDSH/Au(111) compared with those for the non-functionalized and functionalized Au(111) are shown in Figure 4.1.18.

In the case of Au(111) surface (black lines) only one signal, corresponding to the oxidation and reduction process (≈ 0.38 V) of the gold, was observed. However, in the functionalized surfaces, no signal from the gold surfaces was observed in the measured windows (0 - 0.8 V). The loss is due to the passivation of the surface due to the functionalization, emphasizing the fact that is was successfully performed.

The capacitive current (which is the different of the intensity between oxidation and reduction processes) is normally use to analyze the order of the surfaces. In the case of Au(111), it can be seen that this value at low voltage is rather small, indicating a high ordered surfaces (because of the oriented face; this value was higher before the annealing process). Regarding to the functionalized surfaces, both systems show similar behavior; in the two cases higher values that the Au(111) substrate were found, indicating lower order of the surfaces.

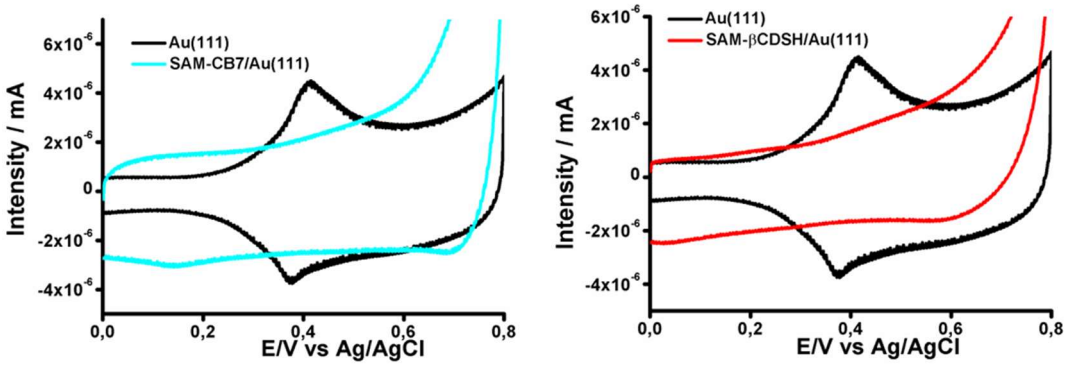

Figure 4.1.18: CV measurement of (a) SAM-CB[7]/Au(111) (b) SAM-β.CDSH/Au(111) and Au(111) in 0.1 M Na_2SO_4.

The differential pulse voltammetry (DPV) and squarewave voltammetry (SW) experiments of both systems are shown in the Figures 4.1.19 and 4.1.20, respectively. As it can be seen, similar redox processes were obtained if one compares the cyclic voltammetry graphs, however, these peaks presented better resolution than those found in the CV experiments and could be identified clearly, due to the better sensibility of both techniques.

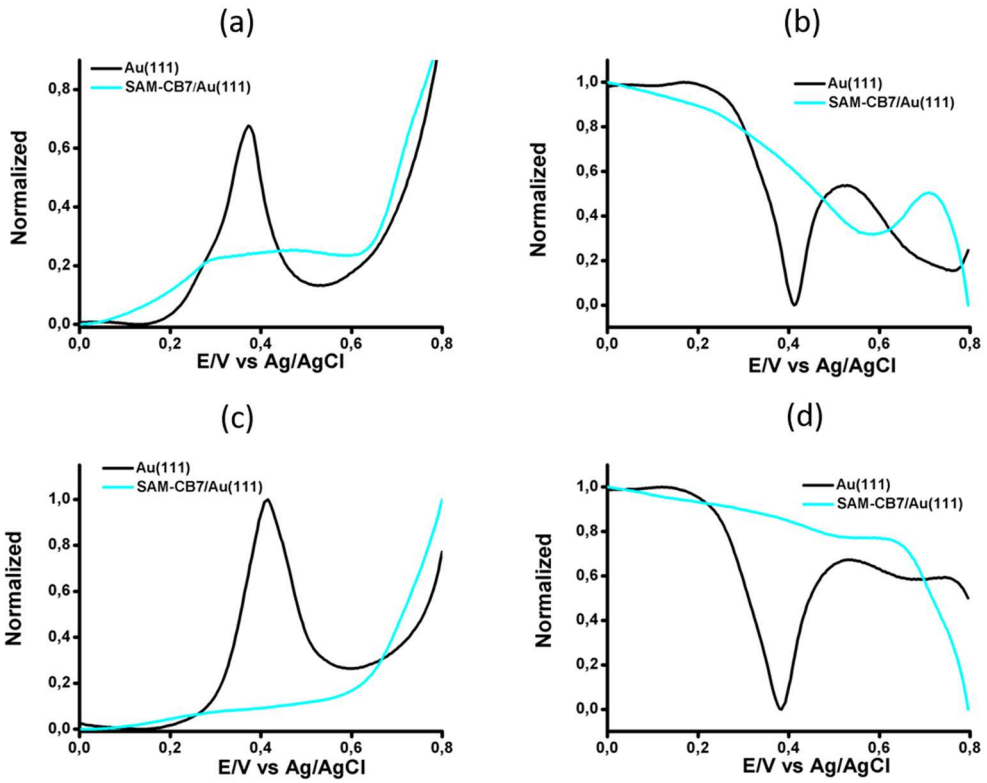

Figure 4.1.19: DPV measurements of SAM-CB[7]/Au(111) (a) oxidation and (b) reduction processes and SAM-β-CDSH/Au(111) (c) oxidation and (d) reduction processes compared with Au(111) in 0.1 M Na_2SO_4.

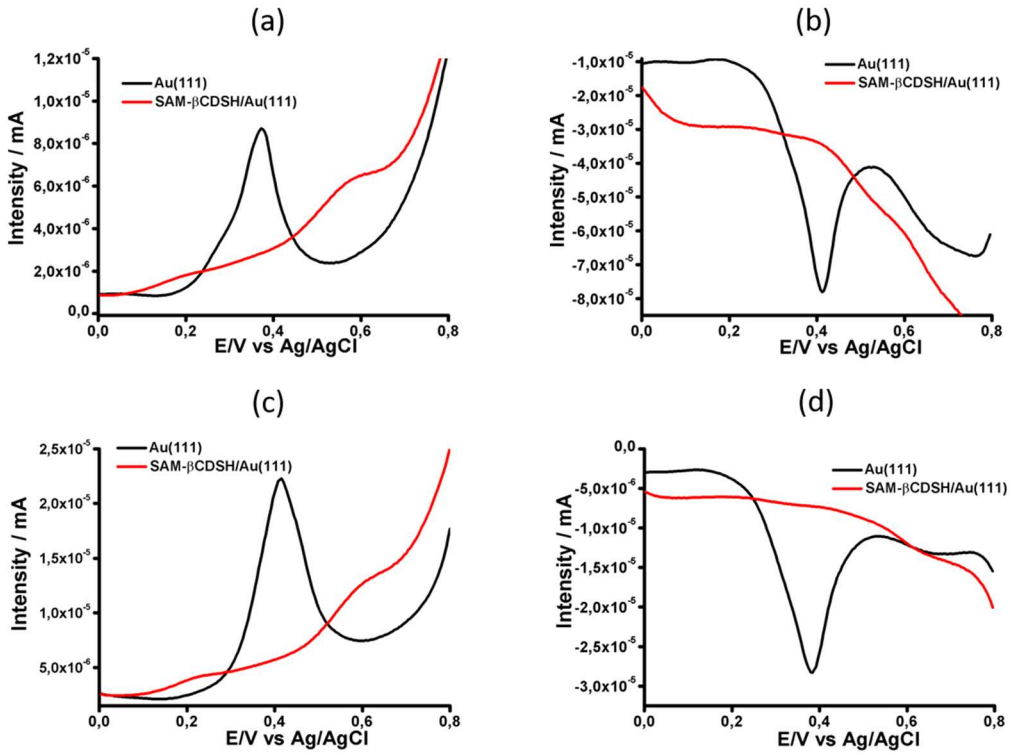

Figure 4.1.20: SW measurements of SAM-CB[7]/Au(111) (a) oxidation and (b) reduction processes and SAM-β-CDSH/Au(111) (c) oxidation and (d) reduction processes compared with Au(111) in 0.1 M Na_2SO_4.

Electro-desorption of the SAM-β-CDSH/Au(111) 0.1 M NaOH

Electro-desorption studies are based on the application of voltage cycles with the aim of oxidizing/reducing the SAM on a given surface to cause the desorption of the molecules that form such SAM. These experiments are very useful because allows us to confirm the SAM-Host formation and helps quantifying the surface density coverage (Γ) of the host molecules on the surface.

In our case, these studies were also performed for the SAM-β-CDSH/Au(111) due to their thiol nature. In this case, it was possible to study their reductive electro desorption by the application of negative voltages.[31]

Figure 4.1.21 (left) illustrates the voltamperommetric response for the reductive electro-desorption process of the β-CDSH SAMs from the Au(111) surfaces with the application of cycle voltage between (0 and -1.6 V). The single desorption wave observed at -0.8 V suggested that the SAMs for this molecule were rather homogeneous. Moreover, the narrow desorption peak indicated the existence of good assembled closed-packed β-CDSH on the Au(111) surfaces. The reductive desorption process could be explained with equation 4, where the product obtained corresponds to thiolate groups that diffuse away from the surface.

$$Au\ (111) - SR + e^- \rightarrow RS^- + Au(111) \qquad (4)$$

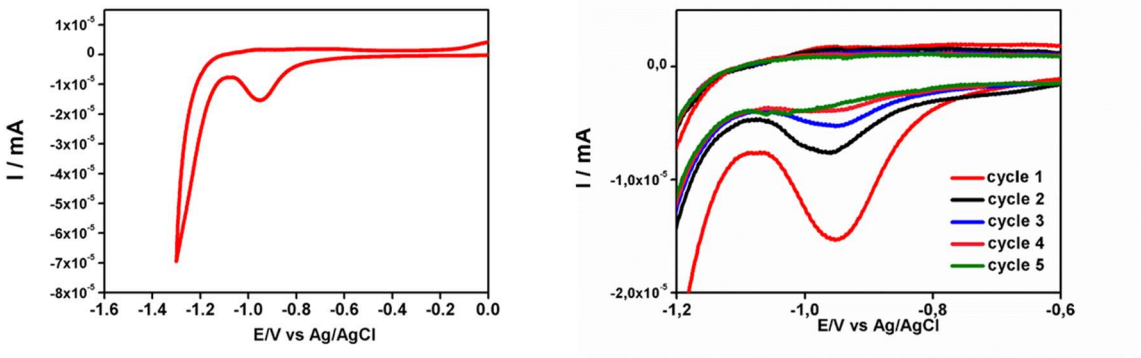

Figure 4.1.21: Electro-desorption of SAM-β-CDSH/Au(111) (a) first cycle, (b) different cycles in 0.1M NaOH.

The electrical charge and surface density associated with the monolayer of β-CDSH showed values of 31.2 μC/cm^2 (Equation 5) and 3.2·10^{-10} mol/cm^2 (Equation 6), respectively. The calculation were carried out by the integration of the reduction peak of the electro desorption curves.

$$Q_f = \frac{Area\ (cm^2)}{Vscans\ (Volt)} = \frac{1.56x10^{-6}}{0.05} = 3{,}12x10^{-5}\ C \qquad (5)$$

$$\Gamma = \frac{Q}{n\ x\ F\ x\ A_r} = \frac{3{,}12x10^{-5}}{1\ x\ 96500\ x\ 1{,}01} = 3{,}2x10^{-10}\ mol/cm^2 \qquad (6)$$

Here, "A_r" is the electrode area (calculated before); "Q" is the integrated charge of the entire anodic wave (from Fc to Fc$^+$); "n" is the number of electrons involved in the redox reaction and "F" is the Faraday constant and number of electrons.

In both cases, the values achieved were similar to related SAM systems published in the literature,[15,32] therefore the presence of multilayers were discarded.

As the desorption is a reversible process,[31,33] further measurements applying different number of redox cycles were performed to corroborate the molecular desorption (Figure 4.1.21, right). Figure 4.1.22 shows the decrease of the intensity of the signals versus the number of performed cycles. After the fifth cycle (green line), there was no signal observed, indicating that most of the molecules in the SAM were removed (desorbed).

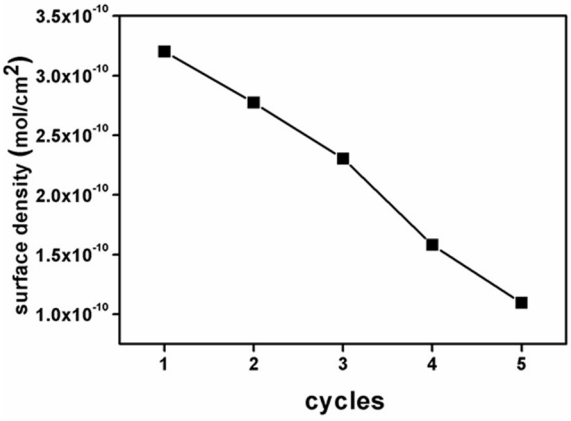

Figure 4.1.22: Representation of surface density vs nº cycles

Characterization of the ferrocene derivatives systems:

The electrochemical characterization of these systems concentrated mainly on the detection of the signal related to the ferrocene groups, which would indicate the formation of the desired host-guest systems. Moreover, studies of the robustness, to study how stable were the host-guest compounds, were also performed. Apart from the characterization of the systems, control experiments (hence, incubation the guest with a gold surface without the presence of the SAM-Host, **FcCCMoid/Au(111)** and **Fc9Accm/Au(111)** were achieved. In this case, only experiments using CB[7] as host molecules were performed due to the lack of time.

Electrochemical characterization of FcCCMoid@SAM-CB[7]/Au(111) and Fc9Accm@SAM-CB[7]/Au(111) in 0.1 M Na_2SO_4

The cyclic voltammetry of the **FcCCMoid@SAM-CB[7]/Au(111)** and **Fc9Accm@SAM-CB[7]/Au(111)** compared with the **SAM-CB[7]/Au(111)** surface (previous to the incubation of the CCMoids) is shown in Figure 4.1.23 (left). As it can be seen, the systems incubated with the guest derivatives ferrocene solutions presented a redox signal between (0.34-0.15 V) corresponding to the ferrocene groups, that indicated the existence of host-guest interactions.[8] In the case of the FcCCMoid, due to the present of two ferrocene groups in its structure, two different signals were expected. In principle, only one of them should be expected to be inside the host due to the steric hindrances. This fact may be related to the asymmetric wave observed for the system. On the other hand, controls experiments with both CCMoids with non-functionalized surfaces (without the host CB[7] were achieved to exclude the possibility of having physiadsorbed molecular material on the substrates; however no

signal was obtained (Annex 4.3), reinforcing the idea that the redox signals explained above have as origin the host-guest SAMs.

Regarding the current capacitive, the three systems presented different values which indicate changes in the electrical surface associated to the successive modifications. In both cases the found energies were lower than the initial situation (without incubation), indicating the creation of more order on the new surfaces.

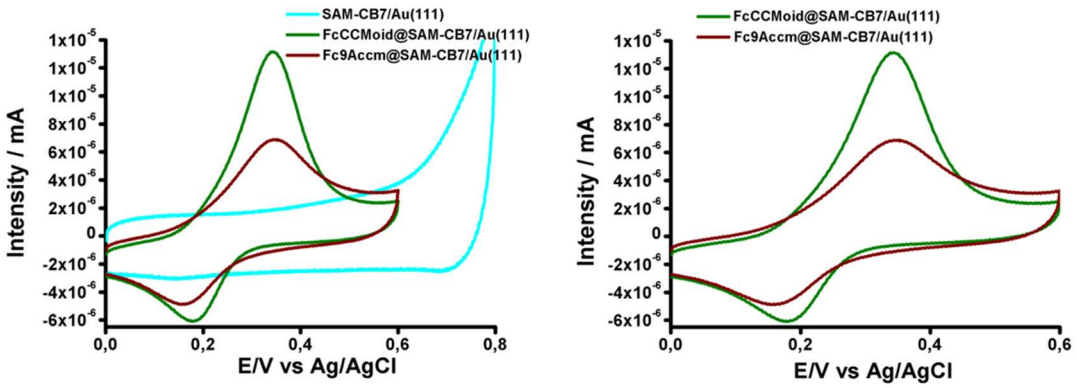

Figure 4.1.23: CV measurements of FcCCMoid@SAM-CB[7]/Au(111), Fc9Accm@SAM-CB[7]/Au(111) and SAM-CB[7]/Au(111)

The experiments performed by DPV and SW showed defined voltammograms (Figure 4.1.24) that corroborated the facts observed in the CV experiments.

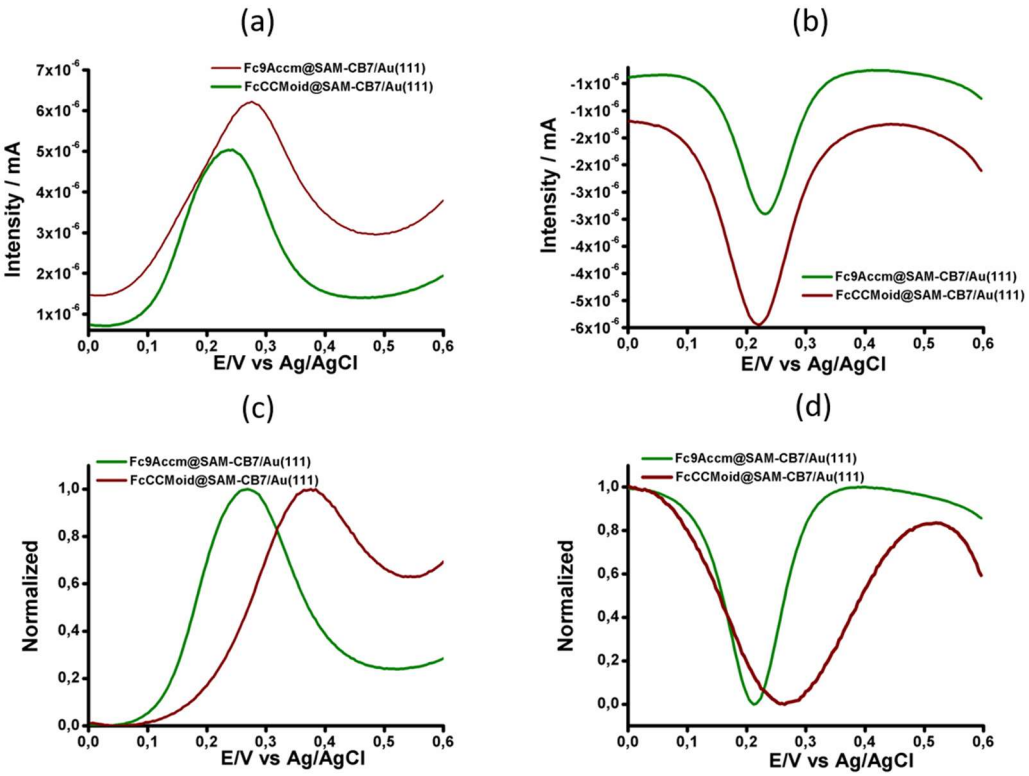

Figure 4.1.24: DPV measurements of FcCCMoid@SAM-CB[7]/Au(111), Fc9Accm@SAM-CB[7]/Au(111) (a) oxidation and (b) reduction processes and SW measurements (a) oxidation and (b) reduction processes.

From these voltammogram, the redox values corresponding to the ferrocene redox signals are shown in the Table 4.1.1

	CV_{oxid} (V)	CV_{red} (V)	DPV_{oxid} (V)	DPV_{red} (V)	SW_{oxid} (V)	SW_{red} (V)
FcCCMoid@SAM-CB[7]/Au(111)	0.34	0.18	0.23	0.23	0.26	0.21
Fc9Accm@SAM-CB[7]/Au(111)	0.34	0.15	0.27	0.21	0.37	0.26

Table 4.1.1: CV, DPV and SW oxidation and reduction processes.

The reversibility of the redox process was studied, therefore the following parameters of the cyclic voltammograms were analyzed: relationship between anodic and cathodic intensities (i_{ap}/i_{cp}) and differential potencial (AEp). An electrochemical process can be considered reversible when the relation between the intensity is equal to 1 and the potential difference it

is small (close to 0.06 V in water solutions). Next Table 4.1.2 shows the parameters for the redox processes of both systems:

	i_{ap}	i_{cp}	i_{ap}/i_{cp}	E_{ap}	E_{cp}	AEp	$E^{o'}$
FcCCMoid	$1.31x10^{-5}$	$-6.06x10^{-6}$	-2.16	0.34	0.18	0.16	0.26
Fc9Accm	$6.91x10^{-6}$	$-4.81x10^{-6}$	-1.43	0.35	0.15	0.20	0.25

Table 4.1.2: Values of intensity anodic peak (i_{ap}), intensity catodic peaks (i_{cp}), relationship between the intensity (i_{ap}/i_{cp}), potential anodic peaks (E_{ap}), potential catodic peaks (E_{cp}), differential potential (AEp), standard potential ($E^{o'}$).

As the table shows, both systems presented non-reversible redox processes where the parameters were farther from ideal reversible systems. However, the system Fc9Accm presented values closer to the reversibility than the system FcCCMoid, that could be related to the effect of the extra Fc group in the latest, missed in the case of Fc9Accm, where the redox waves (hence, oxidation and reductions) were of similar intensity.

Finally, studies of robustness of the systems were carried out. In this case, the goal was to study how stable were the host-guest interactions performing several redox cycles. The cyclic voltammograms of **FcCCMoid@SAM-CB[7]/Au(111)** and **Fc9Accm@SAM-CB[7]/Au(111)**, after several cycles and the relation of the intensity when several cycles were applied and the relation of the intensity with the number of cycles are shown in Figures 4.1.25 (a) and (b).

The voltammograms show redox signals corresponding to the Fe(II)/Fe(III) pair. As expected, those signals decreased in intensity as electrochemical cycles were performed. The reason is that the oxidized molecule contains Fe(III) and becomes more polar (charged); the hydrophobic interactions with the guest disappear and the molecule moves out from the cavity of the host. This fact originates a decrease of the intensity of the ferrocene signal as it is shown in Figure 4.1.25 (c). In both cases, the intensity decreased abruptly after the first cycles. But, comparing both systems (Figure 4.1.25, d), Fc9Accm was more robust because it takes longer (more cycles) for the complete removal of the ferrocene groups from the hosts.

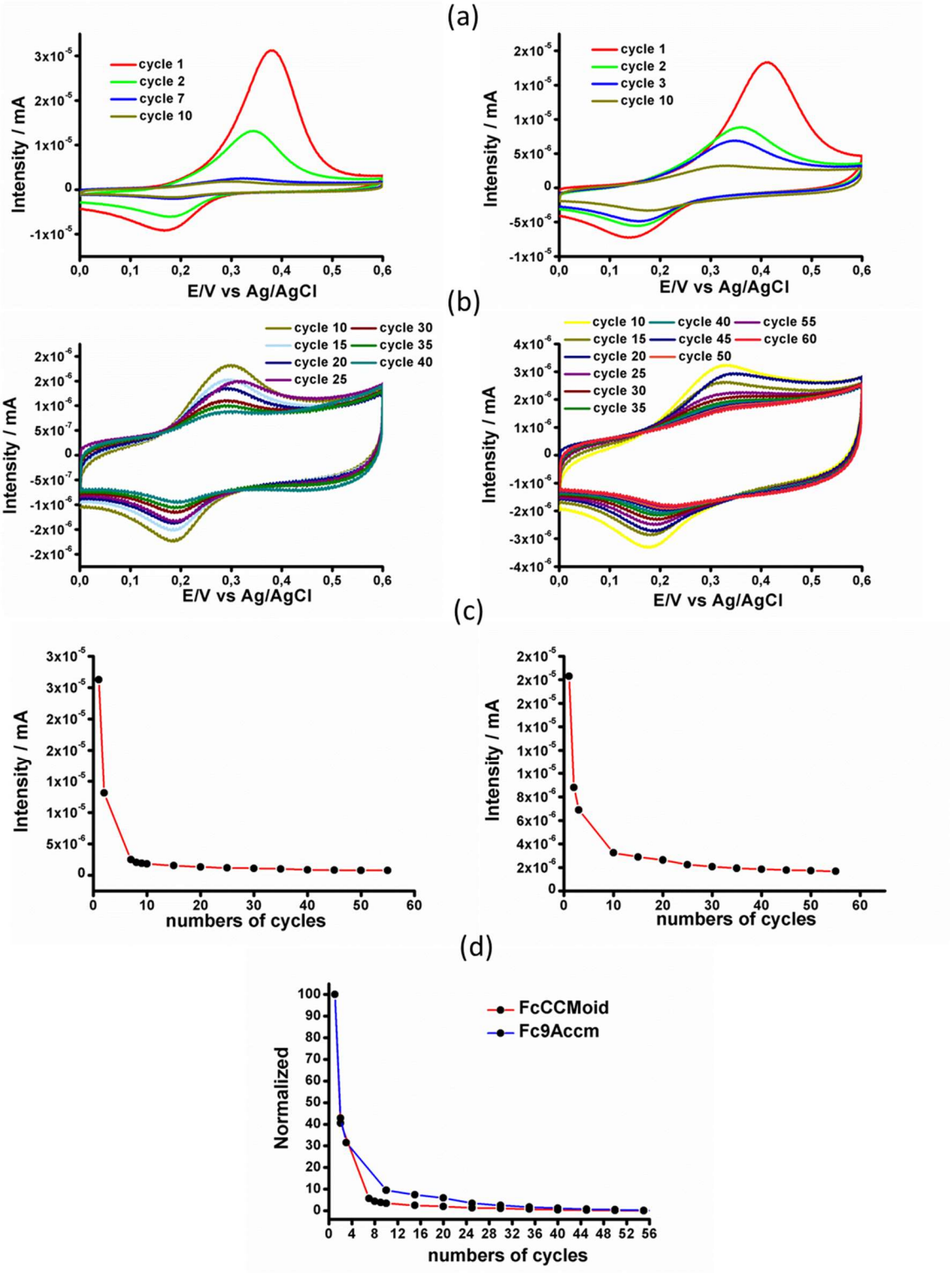

Figure 4.1.25: Studies of robustness (left) FcCCMoid@SAM-CB[7]/Au(111) (right) Fc9Accm@SAM-CB[7]/Au(111) of (a) CV measurements cycles 1-0, (b) CV measurements cycles 10-60, (c) representation of intensity of redox peak vs numbers of cycles and (d) comparative representation of (c).

The robustness of the systems was also followed by DPV and SW (Figure 4.1.26), where in both it was clearly observed the decrease of the intensity after the application of several cycles.

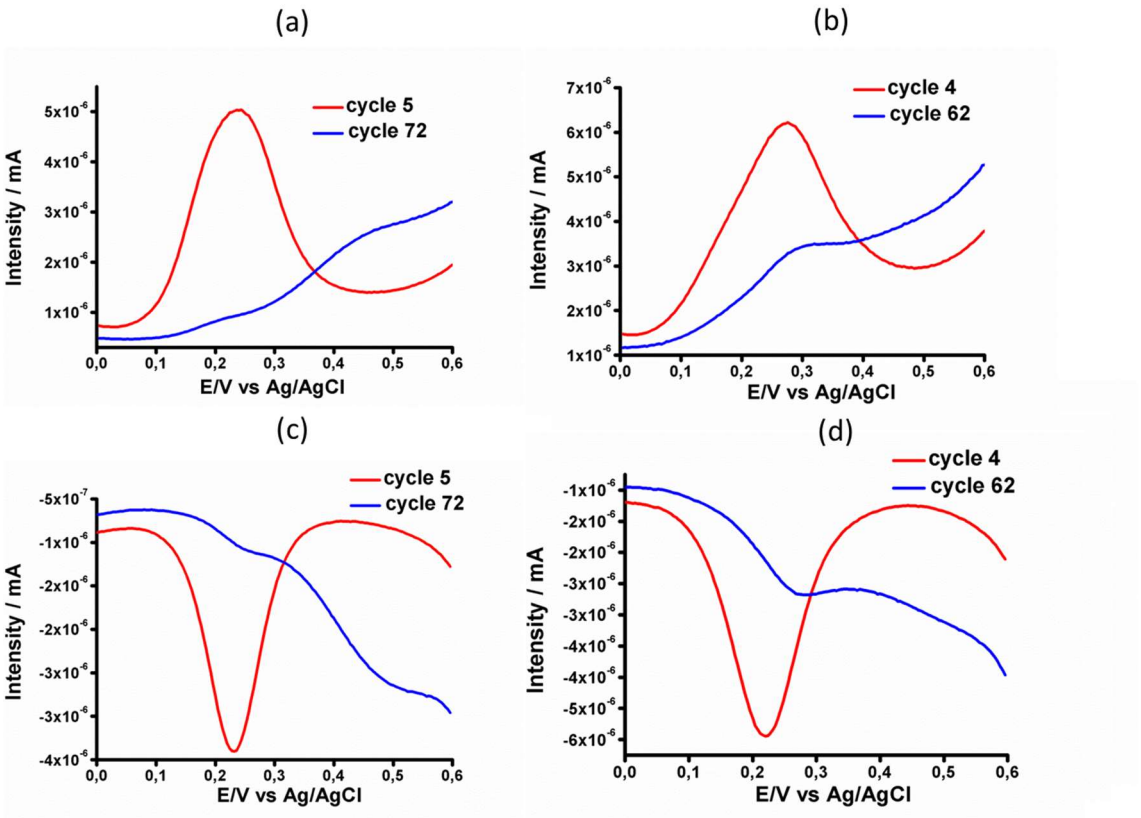

Figure 4.1.26: DPV measurements with different numbers of cycles for FcCCMoid@SAM-CB7/Au(111) (a) oxidation (c) reduction processes and for Fc9Accm@SAM-CB7/Au(111) (b) oxidation (d) reduction processes.

X-ray photoelectron spectroscopy (XPS)

Further evidence of the host-guest formation on surfaces was given by XPS experiments. Figure 4.1.27 shows the XPS spectra corresponding to the region of Fe2p for an Au (111), **SAMCB[7]/Au(111)** and **FcCCMoid@SAMCB[7]/Au(111)**, in that order. In the latest there was a small band around 710 eV. This signal was expected to be small since correspond only to the FcCCMoid molecules that are encapsulated in the corresponding CB[7] SAM.

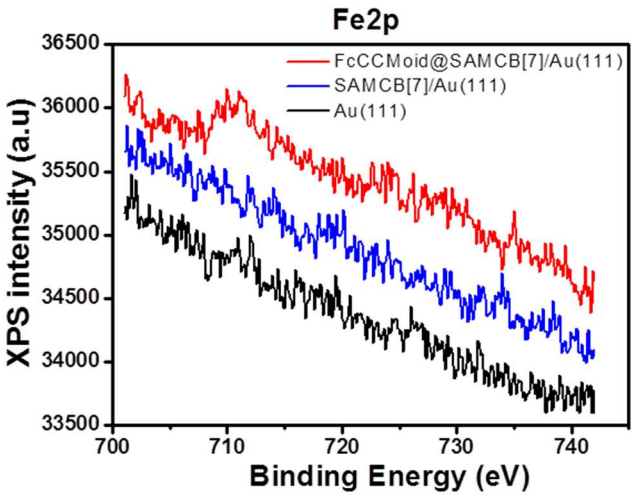

Figure 4.1.27: X-ray photoelectron spectra of Fe_{2p} for FcCCMoid@SAMCB[7]/Au(111) (red), SAMCB[7]/Au(111) (blue) and Au(111) (black).

Contact angle

The contact angle values corresponding of each step are shown in the Table 4.1.3. Au surfaces show angles of approximately 50 ˚. Regarding the SAMs formation, in both cases the values decreased to 37 ˚, for the SAMβ-CDSH, and to 30 ˚ for the SAMCB[7]). The latest was lower, compared to the β-CD, because the presence in the CB[7] structure of carbonyl polar groups. Finally, the incubation with the CCMoids (FcCCMoid and Fc9Accm) provided higher values due to their aromatic nature giving rise to similar values around 77-79 ˚ in both cases.

Surface	θ_a(˚)
Au(111)	50 ± 2
SAMCB[7]/Au(111)	30 ± 2
SAMb-CDSH/Au(111)	37 ± 2
Fc9Accm@SAMCB[7]/Au(111)	77 ± 2
FcCCMoid@SAMb-CDSH/Au(111)	79 ± 2

Table 4.1.3: Contact angle values

4.1.4 Conclusions

In this chapter, we studied the formation of host-guest systems based on CCMoids molecules in solution and on gold surfaces. To carry out this study, two new CCMoids, FcCCMoid and Fc9Accm, were synthesized. These two compounds acted as guest molecules due to the presence of ferrocene groups in both systems. On the other hand, cucurbit[7]uril (CB[7]) and functionalized β-cyclodextrine (β-CD) were used as host systems capable of encapsulating ferrocene groups via hydrophobic interactions.

Regarding to the studies in solution, they were carried out using water as a solvent because it improves the hydrophobic interactions. The host-guest compounds were characterized by UV-Visible and ^{1}H NMR. In relation with UV-Vis experiments the CCMoids were not soluble in water therefore no signals were observed. However, the presence of host molecules in the solutions gave rise to the appearance of signals of CCMoid nature due to the formation of the host-guest compounds (FcCCMoid@CB[7], Fc9Accm@CB[7], FcCCMoid@β-CD and Fc9Accm@β-CD). The ^{1}H NMR spectra showed extra peaks that may correspond to the CCMoids. However, future experiments should be necessary to confirm the nature of such signals.

In relation to the surface studies, the formation of Host-SAMs on gold surfaces and the incubation with the corresponding CCMoid were accomplished. To perform such studies different steps were carried out and details have been provided.

Initially, annealing processes of the polycrystalline gold surfaces were required to obtain preferred Au(111) orientations. The characterization was carried out by the use of cyclic voltammetry technique.

The SAM-CB[7] formation was carried out by the incubation of the CB[7] species in aqueous solution, those interacts with gold surfaceby means of electrostatic interactions due to the carbonyl groups from the molecules. In the case of β-CDSH, it was necessary to perform a previous functionalization of the molecule with thiols groups, that interact coordinative bonds with the gold surface. All the systems were characterized by electrochemical techniques: CV, DPV and SW. In the case of SAM-β-CDSH, reductive electro-desorption experiments were carried out. From this study, the “covering” of the gold surfaces with the formed SAM was analyzed and agreed with others systems reported in the literature.

Finally, the surfaces were incubated with the solution of the CCMoids using DMSO/H_2O obtaining FcCCMoid@SAM-CB[7], Fc9Accm@SAM-CB[7], FcCCMoid@SAM-βCDSH and Fc9Accm@SAM-β-CDSH. These systems were characterized again by CV, DPV and SW, in which redox processes corresponding to the ferrocene groups were observed indicating the formation of host-guest compounds. Control experiments were carried out without the presence of host molecules to discard physisorption processes.

4.2 Chapter II: CCMoid cages

4.2.1 Introduction

In the initial part of this section, host-guest studies focus in the idea of using the CCMoid molecules as guest molecules. Now, a new study related to the subject was initiated but in this case CCMoids were used as host molecules.

To achieve the new molecular host systems, a metallo-CCMoid supramolecular approach was followed. The metallo-CCMoid supramolecular structure assembly (molecular cages based on CCMoids, CCMoidcage) here bases on the coordination of metallic centers with ligands to create cavities that can encapsulate through supramolecular interactions a number of guest molecules. This subject emerged as an important area of research in the last decades.[34–36] The cavities of these 3D architectures have been exploited due to the wide range of properties that the host could exhibited as for as molecular recognition[34,37], drug delivery[38–40] , catalysis[41] and, as biological[42] and chemical sensors[43].

The different design strategies in the formation of these molecular cages have allowed the achievement of cages which different sizes and nature.[44] One of the most common methods employed consists on the self-assembly of metal cations and symmetrical pyridyl-based ligands, which have led to a large variety of molecular cages with predictable coordination. Within these systems, a particularly attractive feature of molecular cages is the self-assembly of $[M_2L_4]^n$ cages (M = metal, L = ligand) (Figure 4.27),[39,40,45] in which the properties of the cages are achieved by modifying and/or functionalizing the proposed ligands. Properties as fluorescence[46], solubility[47] or functionalization to favor host-guest interactions can be induced by varying the structures of the ligands.

Inspired by the previous knowledge on metallosupramolecular structures[39,45], we wanted to explore this type of chemistry synthesizing a molecular cage $[M_2L_4](X)_4$ (where X = counterion) based on CCMoid ligands coordinated to dia/para-magnetic metallic centers that could contain a cavity capable of hosting different molecules. The main idea was to play with different guest molecules that could modify the magnetic behavior of the cage and also could connect both metals magnetically.[48,49] Figure 4.2.1 shows the general scheme of a $[M_2L_4]^n$ cage.

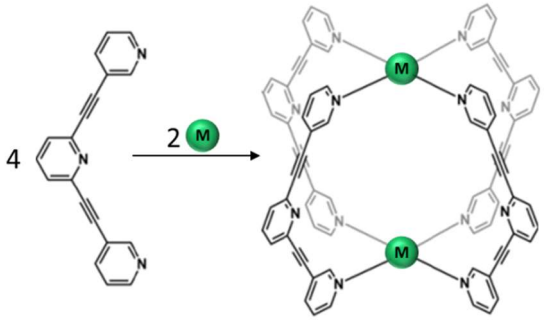

Figure 4.2.1: Scheme of M_2L_4 structure

4.2.2 Objectives

In this case, we concentrated in the synthesis of a novel molecular cage where the CCMoid molecules acted as a host, in a similar way as Figure 4.2.1 depicts.

Hence, this part of the section focuses on the design and synthesis of a new CCMoid ligand (CCMoidcage). The ligand presents the common parts of CCMoids together with alkyne and pyridyl groups situated in the arms of the molecule (Figure 4.2.2) providing rigidity and coordination capability at the same time. Then, coordination reactions were carried out with different metallic salts toward the creation of the molecular cage. All this initial work was part of a project performed in a short stay (two months) in the group of Professor Euan K. Brechin at the University of Edinburgh.

4.2.3 Results and Discussion

3.1 Experimental section

Synthesis of CCMoidcage

The ligand, CCMoidcage (Figure 4.2.2), displays a conjugated backbone made of seven carbon atoms that contain a β-diketone group in the middle and an aryl groups attached to an ending pyridine rings in both sides of the aromatic arms.

On one side, the functionalization of the aryl groups in the *para* positions allows the extension of the final molecule; the presence of the alkyne groups provides certain rigidity. On the other side, the nitrogen of the pyridine groups situated in *meta* positions allows the possibility of coordination to different metallic centers and overall the system would be large enough to create a molecular cage via coordination to the already metallic centers.

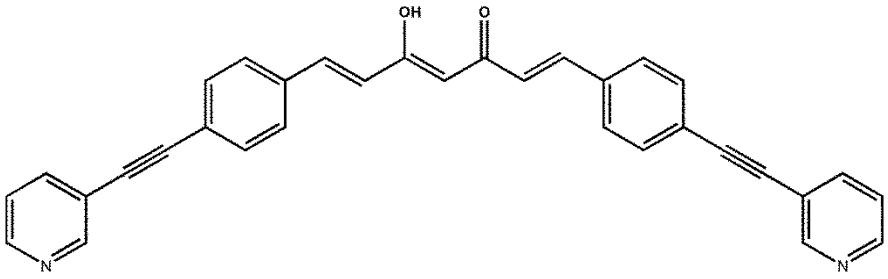

Figure 4.2.2: Representation of CCMoidcage.

The ligand CCMoidcage was synthesized using the Sonogashira Coupling.[50] In the reaction, an aryl halide reacts with a terminal alkyne using palladium (II) and copper (I) as catalysts. In our case, an intermediate CCMoid with iodine aryl groups in the arms of the molecule (IodineCCMoid), reacted with 3-ethynylpyridine, in presents of CuI and $Pd(PPh_3)_2Cl_2$. The presence of an amine base, NEt_3 in our case, was needed being used, in addition, as the solvent of the reaction. The reaction was stirred for four days at 90 ˚C in anhydrous and anaerobic conditions (Figure 4.2.3). The resulting crude was purified by flash chromatography using a gradient elution column.

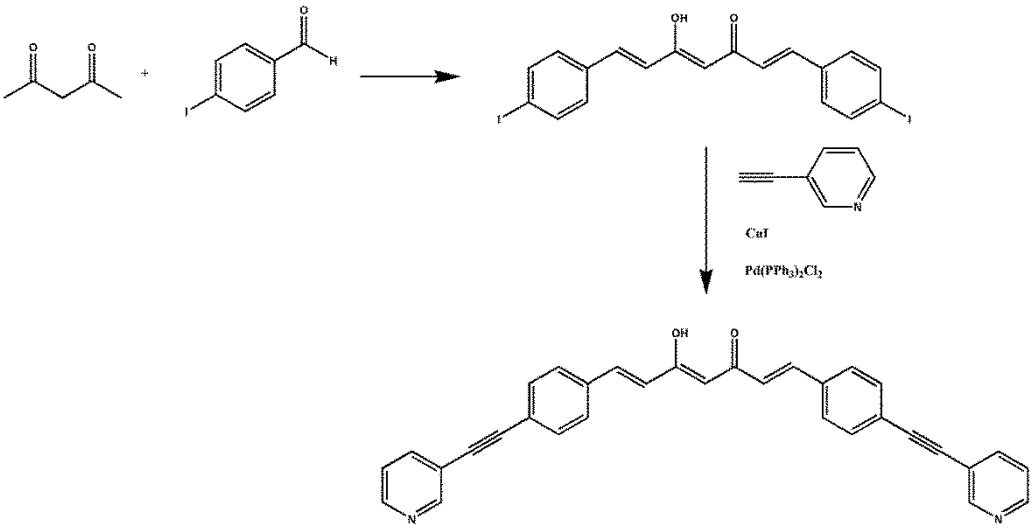

Figure 4.2.3: General synthetic procedure for CCMoidcage

When only CH_2Cl_2 was used as eluent an initial product was isolated in a 35 % yield (R_f = 0.8; in CH_2Cl_2/acetone 10 %). This corresponded to the molecule functionalized only on one side (Figure 4.2.4). The system was well-characterized by ^1H NMR showing a large number of signals, due to the asymmetric structure. Although very interesting, this product was not useful for the formation of molecular cages because the latest requires two coordination sites.

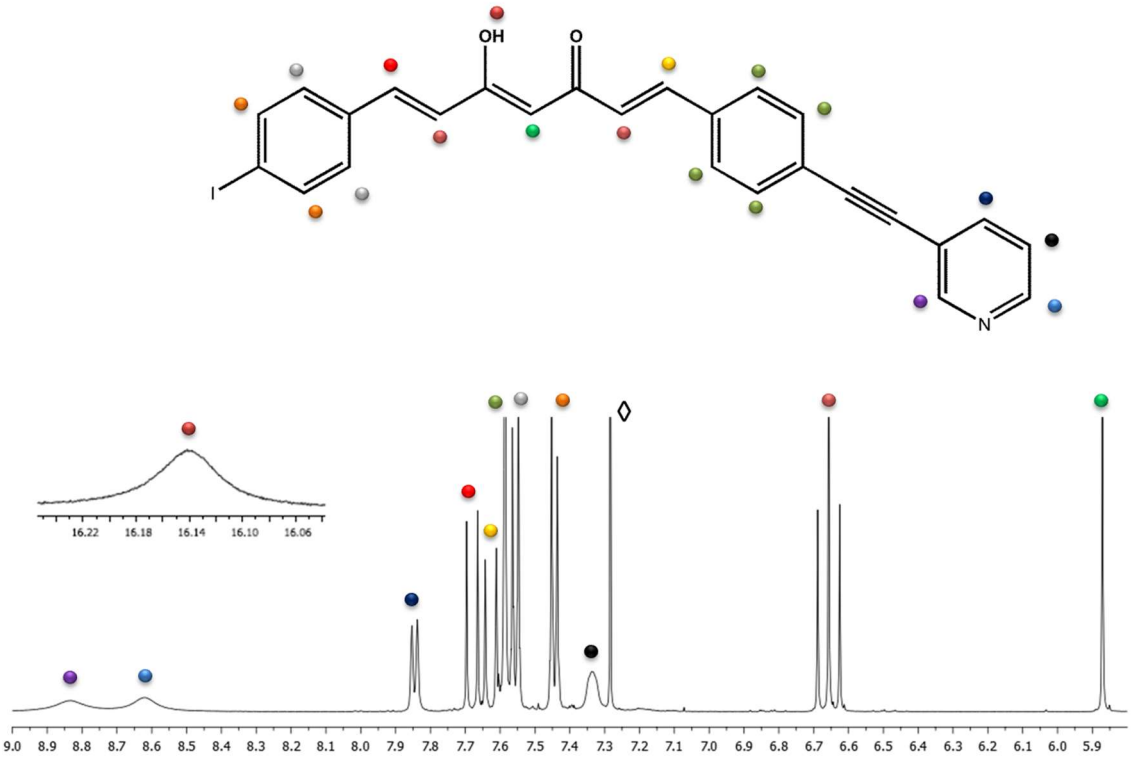

Figure 4.2.4: ^1H NMR spectrum in $CDCl_3$ of a CCMoid with one functionalized side. ◊ $CDCl_3$

Then, the polarity of the solvent mixture was increased gradually by the addition of acetone (20 % of the total volume). Using this ratio, the desired (symmetric) product was obtained (R_f = 0.5; in CH_2Cl_2/acetone 10 %). The system, described above as **CCMoidcage**, has both sides functionalized and the final yield was 40 %. The study in solution by ^1H NMR (Figure 4.2.5) showed a decrease of the number of signals compared with the asymmetric structure, that matches well with the expected for the system. Related to the β-diketone group, a broad signal at 16 ppm (red spot) was identified, corresponding to the enol group, and a singlet at 5.9 ppm was assigned to the methane proton (green spot) in the center of the same moiety. The constant coupling of the peaks related to the conjugated chain displayed the presence in solution of only one isomer (isomer E, J ≈ 15 Hz). In addition, the peaks corresponding to the pyridyl groups appeared more intense comparing with the asymmetric structure due to the higher number of protons. This NMR analysis provided the necessary information to confirm the formation of the desired molecule.

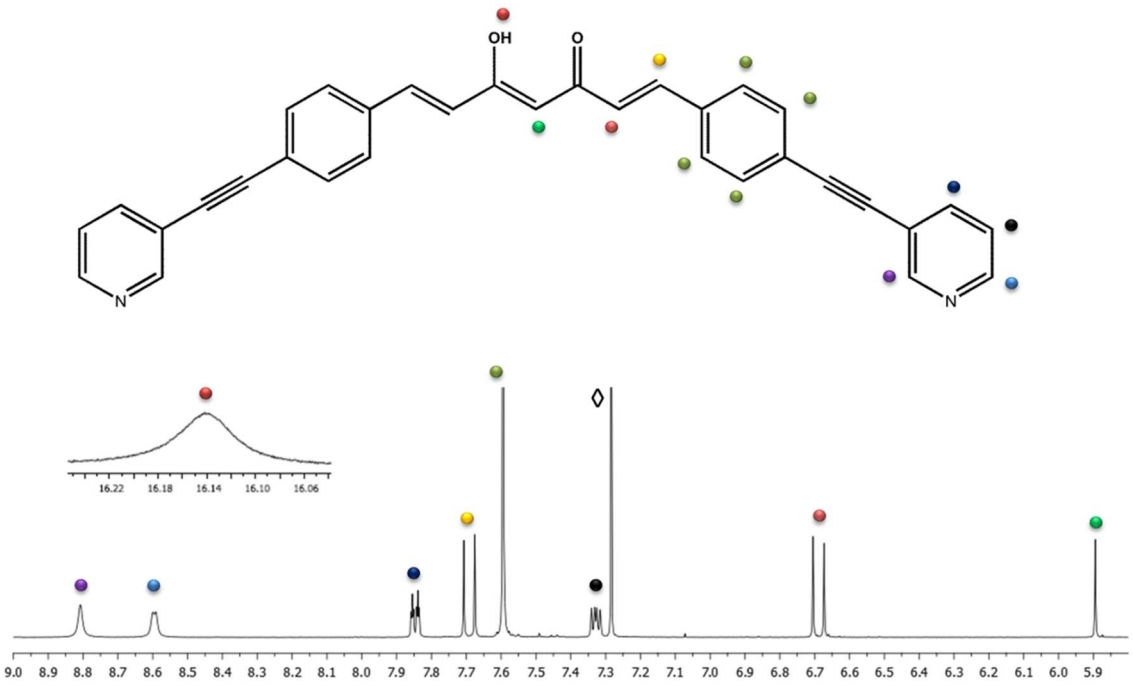

Figure 4.2.5: ^1H NMR spectrum of CCMoidcage in $CDCl_3$. ◊ $CDCl_3$.

Molecular cage formation:

To form the expected cavity that would lead to the formation of the final molecular cages, the coordination with metallic centers through the β-diketone and pyridine groups was attempt.

The ideal structure of our molecular cage would be formed by four ligands coordinated in each side with two metals giving a stoichiometry of $[M_2L_4]^n$ (Figure 4.2.1). However, the ligand contains also a β-diketone where metals will be coordinate giving rise to different systems, probably with stoichiometry of $[M_6L_4]^m$ (Annex 4.5).

For that reason, reactions that fulfill both stoichiometries were performed. However, the coordination reactions could also lead to systems with a mixture of both stoichiometries, making difficult to obtain single crystals suitable for X-ray diffraction analysis. In order to solve this problem, two different methodologies were proposed: (i) the use of metallic centers that could present a preferential coordination toward nitrogen[51] or (ii) the blocking of the β-diketone by the functionalization with a BF_2 group.[52,53]

Focusing in the first point, the nature of the metallic salts (metal center and counterions) plays crucial roles. The initial idea was the use of metal centers with square planar geometries, like palladium (Pd), platinum (Pt) or nickel (Ni), in order to complete their coordination spheres in their equatorial plane with four N from the different pyridine moieties of neighboring CCMoids. In addition, the ligand is neutral, and the final compound would be positive charged, so the choice of suitable counterion was very important. In this case, the idea was to used big counterion like triflate (OTf), tetrafluoroborate (BF_4) or hexafluorophosphate (PF_6) that could help in the crystallization process of the compounds. As most of these desired metallic salts are not commercial, a "metal exchange reaction" with the corresponding counterion silver species was performed.

This way, in the coordination reactions a solution of a metal halide (e.g.: $PdCl_2$) was added dropwise to a silver salt with the corresponding counterion (e.g.: $Ag(PF_6)$) and the mixture was stirred protected from light. Briefly after, the silver halide was precipitated (AgCl) and removed by filtration. Finally, the resulting solution of $Pd(PF_6)_2$ was added dropwise to the CCMoid ligand. Depending on the metal, a color changes was observed meanwhile the addition process was carried out. Then, final mixture was stirred for 30 min. After that time, different methodologies to crystallize the compound were performed: (i) slow evaporation, (ii) liquid-vapor diffusion and (iii) layering liquid-liquid processes.

Among all the different experiments attempted, only one reaction resulting from the mixture of **CCMoidcage** with $[Cu(PF_6)_2]$ using a $[M_6L_4]$ stoichiometry provided a crystalline product. However, the resolution of the crystallographic data showed that the results were not as expected, since with the data showed the achievement of the protonated ligand instead of the formation of a molecular cage. A plausible explanation of this fact could be in the way the metal exchange is performed. $[Cu(PF_6)_2]$ requires a preliminary reaction between $AgPF_6$ and $CuBr_2$ to be performed. In principle, AgCl is precipitated and the desired $[Cu(PF_6)_2]$ remains in

solution; the solid is filtered but some Ag may remain in solution giving rise to an acidic medium that may protonate the ligand hampering the coordination reaction.

The protonate-CCMoidcage (Figure 4.2.6) crystallizes in a P121/c1 space group with one molecule in the unit cell, two molecules of hexafluorophosphate and one molecule of water.

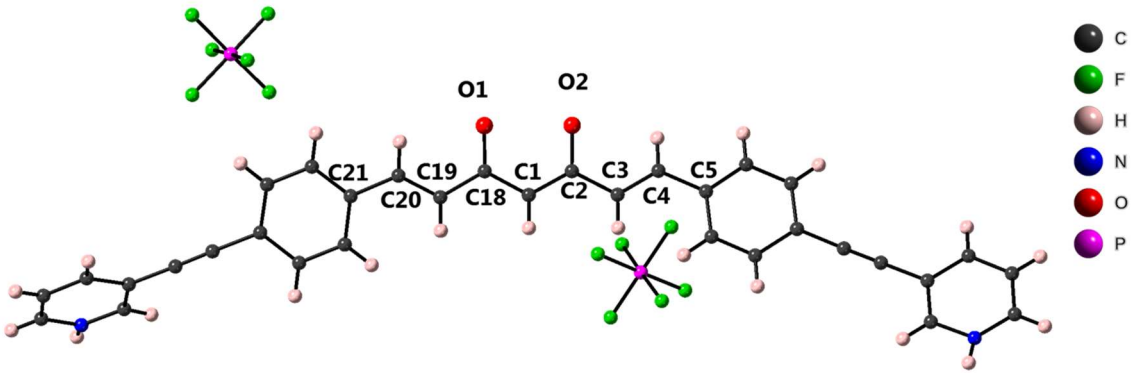

Figure 4.2.6: Representation of protonated-CCMoidcage where O (red), C (grey), N (blue), H (ligh-grey), F(green) and P(pink) atoms are shown.

The β-diketone group shows two different C-O distances: C(2)-O(1) and C(18)-O(2) with 1.315 and 1.294 Å values respectively. The different distances between C(2)-C(1) and C(1)-C(18) at 1.388 and 1.414 Å confirmed the stabilization of the enol form. Related to the conjugated chain, as for other CCMoids, two different distances were found: C(3)-C(4) and C(19)-C(20) with values of 1.330 and 1.329 Å corresponding to the double bond and C(2)-C(3), C(4)-C(5), C(18)-C(19) and C(20)-C(21) (1.444 – 1.487 Å) matching well with what it is expected for single bonds. The chain shows a (E) conformation being totally planar. The aryl groups were disposed in the same plane than the chain, being only one side slightly distorted. Related to the pyridyl groups, one side was located in the same plane as the aryl group, disposing the nitrogen group perpendicular to the conjugated chain. In the other side, the pyridyl group was located out of the plane of the aryl group.

4.2.4 Future work

The achievement of the molecular cage was not possible probably due to the above discussed points and the limited time of the research stage. However, a new modification of the ligand in order to facilitate the formation of the molecular cage should be performed. Initial attempts in this direction were made by the reaction of the ligand with $BF_3{\cdot}O(Et)_2$ coordinating the β-diketone group with a BF_2 moiety. This reaction was carried out using a microwave reactor (MW). As mentioned above, this reaction may allow the blocking of the β-diketone group (Figure 4.2.7) avoiding possible $[M_6L_4]$ and $[M_2L_4]$ mixtures and facilitating the achievement of single crystals.

Future coordination experiments should be carried out with the new system BF_2-CCMoidcage.

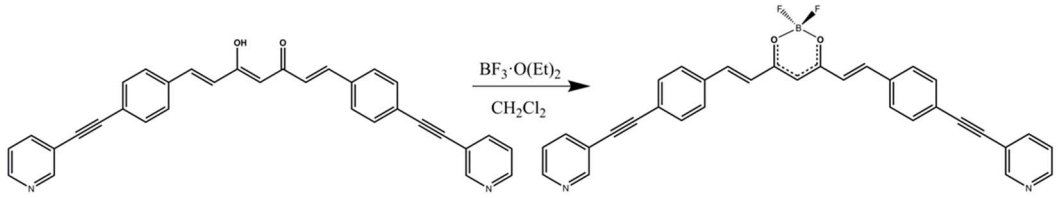

Figure 4.2.7: Schematic reaction of BF_2-CCMoidcage

4.3 Experimental part

Materials: All the reagents used in the work were used as they were received from the commercial company, without further purification.

Chapter I: CCMoids as guest molecules

Synthesis of FcCCMoid

The synthesis of FcCCMoid was carried out following Pabon's method. Acetylacetonate (1g, 9.98 mmol) and boron oxide (0.5 g, 5.14 mmol) were mixed in a bottom flask in AcOEt (10 mL). The reaction mixture was heated at 40 ˚C for 30 min. Then, in a separate flask a solution of ferrocenecarboxaldehyde (4.1 g, 19.15 mmol) and tributyl borate (9.2 g, 39.39 mmol) in AcOEt (10 mL) was prepared and added to the previous solution. The mixture was stirred and gently heated at 40 ˚C for 3 h. After cooling down, an excess of n-butylamine (0.5 mL, 50 mM) in AcOEt (10 mL) was added dropwise. The final reaction was stirred at room temperature for 2 days. After that, a violet-green solid was formed. Then, a solution of 10 % of HCl was added and the mixture heated at 60 ˚C for 2 hours. A color change to light violet was observed and the mixture was filtered and washed with H_2O, MeOH and Et_2O to remove impurities. The yield was 68 %. Crystals of FcCCMoid were achieved by slow evaporation in $CHCl_3$.

IR KBr pellet (v/cm^{-1}): 3087w, 2921w, 1616vs, 1516m, 1455m, 1290m, 1244m, 1143m, 1028m, 964m, 820m, 495m, 478m, 467m. Elemental analysis calculated for FcCCMoid ($Fe_2C_{27}O_2H_{24}$): C, 65.85; H, 4.92 and found: C, 65.42; H, 4.90. ^{1}H-RMN (300 MHz $CDCl_3$, window from 16 to 0 ppm): δ 16.13 (s, 1H), 7.53 (d, 2H), 6.21 (d, 2H), 5.63 (s, 1H), 4.52 (d, 4H), 4.48 (d, 4H), 4.17 (s, 10H). ESI^+-MS ($CHCl_3$): m/z 493.05 $[M+H]^+$, 1007 $[2M+Na]^+$.

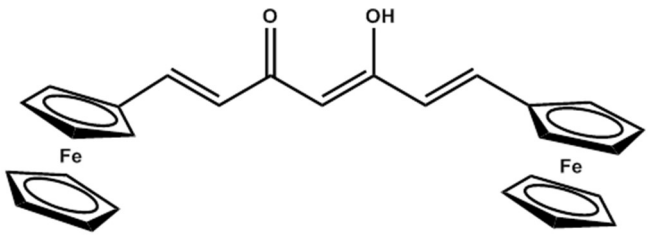

Synthesis of Fc9Accm

For the synthesis of Fc9Accm first it was required the achievement of 1-Ferrocenyl-2-propyn-1-one and 9Accm. The synthesis of 1-Ferrocenyl-2-propyn-1-one was obtained in a two-steps reaction with the use of ferrocenecarboxaldehyde.

1-Ferrocenylprop-2-yn-1-ol: ethynylmagnesium bromide (8.33 mL, 0.45 M in THF, 3.75 mmol) was added to a solution of ferrocenecarboxaldehyde (535.1 mg, 2.50 mmol) in dry THF (5 mL) and the resulting solution was stirred at room temperature for 1 h under N_2. An aqueous saturated solution of NH_4Cl (10 mL) was then added to the latest. Then, 10 mL of CH_2Cl_2 were added and the organic layer was separated with brine. On the other hand, the aqueous layer was extracted with diethyl ether (3x10 mL). The combined organic extracts were dried with Na_2SO_4 and the solvent removed by the use of a rotary evaporator. The resulting brown liquid (2-3 mL) was dissolved in 2 mL of hexane put in a high vacuum line. After a while, a yellow solid was obtained in a yield of 41 %.

^{1}H-RMN (300 MHz $CDCl_3$, window from 16 to 0 ppm): δ 5.15 (m, 1H), 4.34 (m, 2H), 4.23 (s, 5H), 4.21 (m, 2H), 2.61 (s, 1H) and 2.14 (m, 1H). ESI$^+$-MS ($CHCl_3$): m/z 240.02 m/z $[M+H]^+$.

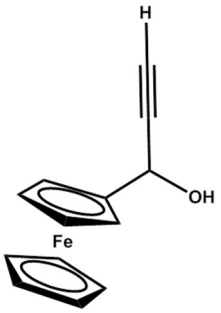

1-Ferrocenyl-2-propyn-1-one: fresh manganese (IV) oxide (2.61 g, 30.0 mmol), was prepared and added to a stirred solution of ferrocenylpropynol (240 mg, 1 mmol) in CH_2Cl_2 (6 mL). The reaction mixture was monitored by TLC and stirred at room temperature for 5 h. Then, the solution was filtered through celite and washed with CH_2Cl_2 until the filtered solvent was colourless. Then, the solvent was removed by rotary evaporation obtaining a dark red oil. The resulting residue was purified by flash chromatography (cyclohexane-diethyl ether 4:1). The oxidized red product (R_f = 0.5) was obtained in a 61 % yield.

^{1}H-RMN (300 MHz $CDCl_3$, window from 16 to 0 ppm): δ 4.95 (d, 2H), 4.63 (d, 2H), 4.28 (s, 5H), 3.25 (s, 1H). ESI$^+$-MS ($CHCl_3$): m/z 239.01 m/z $[M+H]^+$

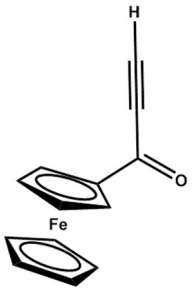

Synthesis of MnO_2: in a three-necked flask, potassium permanganate (26.1 g, 165 mmol) was dissolved in water (160 mL). The mixture was gently heated to facilitate the solubility of the reagent. Simultaneously, a solution of $MnSO_4 \cdot H_2O$ (22.85 g, 135 mmol) in water (40 mL) and a 40 % solution of NaOH (31.8 mL, 0.67 mol) were added to the initial mixture. As a result, MnO_2 was started to precipitate. The mixture was still stirred for 1 h heated in a water bath at 60 ˚C. After cooling down, the mixture was filtered (filter plate nº 4) and washed with extra water until the filtered solvent was colorless. Then, the solid was dried in an oven for 2-3 days. Finally, a dark brown powder solid was obtained in an 81 % yield.

Synthesis of 9Accm: The synthesis of 9Accm was performed following the literature procedure.[24]

Fc9Accm: an anhydrous suspension of NaH 60% (14 mg, 0.35 mmol) in THF (2 mL) was added dropwise to a solution of 9Accm (125 mg, 0.263 mmol) in anhydrous THF (3 mL) at 0 ˚C. Afterwards, the mixture was stirred for 30 min, then warmed to room temperature with continuous stirring that continued for 2 h more, allowing the precipitation of most of the sodium salt of the CCMoid. This came out as a yellow solid. Then, a solution of 1-ferrocenyl-2-propyn-1-one (125 mg, 0.526 mmol) in anhydrous THF (2 mL) was added dropwise, and the reaction mixture monitored by TLC and stirred for 3 h. A dark brown precipitated was then achieved. The mixture was hydrolyzed with H_2SO_4 5 % (10 mL, 9.63 mmol). A color changed was observed for the solution and in the process the solid was re-dissolved. The mixture was extracted with ethyl acetate, $NaHCO_3$ and brine. The organic extract was dried with Na_2SO_4 and the solvent was removed by rotary evaporator, giving a dark red solid. The residue was purified by the use of a preparative foils using CH_2Cl_2 as eluent. Finally a dark red solid was obtained in a 20 % of yield.

^{1}H-RMN (300 MHz THF-d_8, window from 16 to 0 ppm): δ 16.21 (s, 1H), 8.86 (d, 2H), 8.45 (s, 2H), 8.31 (d, 4H), 8.01 (d, 4H), 7.75 (d, 1H), 7.48 (8, 8H), 7.25 (d, 2H,), 6.58 (d, 1H), 5.27 (s, 5H), 4.47 (d, 2H), 4.27 (d, 2H). ESI$^-$-MS ($CHCl_3$): m/z 713.19.05 $[M-H]^-$.

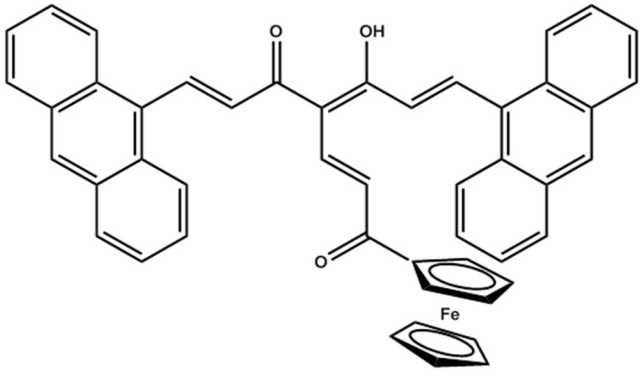

Synthesis of Host's molecules

Cucurbit[7]uril (CB7): This molecule was purchased from STREM chemicals, inc.

β -Cyclodextrin (β -CD): This molecule was purchased from Aldrich

Per-6-thio-β-Cyclodextrin (β-CDSH): The synthesis of this compound was performed by Dra. Marta Riba following a two-step procedure described by Gadelle *et al.* Initially, 552.2 mg (0.48 mmol) of (β-CD) were dried under vacuum for several hours at 80 °C. To that solid, a solution of iodine (2.60 g, 10.24 mmol) in 10 mL of DMF and 2.70 g (10.29 mmol) triphenylphosphine were added in this order. The mixture was stirred under Ar for several hours. Then, the mixture was added to a round-bottom flask containing the β-CD under the same conditions and under argon atmosphere. The solution was then stirred for 15 hours at 80 ˚C under Ar giving as a result per-6-iodo-β-cyclodextrin as a solid that was filtered. To the dried per-6-iodo-β-cyclodextrin, 0.6 g (7.88 mmol) of thiourea were added the mixture was dissolved in 15 mL of DMF under inert conditions and stirred for 19 hours at 70 ˚C under Ar atmosphere. Then, the solvent was removed by the use of a rotary evaporator and an oily solution was obtained. 0.2 g of NaOH in 50 mL of ultrapure water were added and the mixture was stirred under reflux for 1 hour. Then, an aqueous solution of potassium bisulfate was added until a pH of 3-4 was reached. The mixture was cooled down by using an ice bath and the solid was filtered and washed with ultrapure water and dried.

Surface procedure

Annealing process of gold surfaces, Au (111): Small pieces of gold slides (1 x 0.5 cm^2) were cleaned by immersion in a piranha solution (a 3:1 mixture of concentrated H_2SO_4 and H_2O_2 30 %) for 3 min. Later, the cleaned gold slide was rinsed with copious amounts of MilliQ water, and dried under N_2. The annealing process was carried out with a butane flame using a blowtorch for 5 min until a dark red color was observed. Then, a gold wire connection was made and the surfaces were allowed to cold down at room temperature.

Preparation of SAM CB[7]: gold surfaces were incubated overnight in a 0.01 mM solution of cucurbit[7]uril in 10 mL of MilliQ water. Then, the surfaces were rinsed with MilliQ water and dried with N_2.

Preparation of SAM β-CDSH: gold surfaces were incubated overnight in a 0.01 mM solution of β-CDSH in 10 mL of solution (6 mL DMSO and 4 mL MilliQ water). Then, the surfaces were rinsed with MilliQ water and dried with N_2.

Preparation of final SAMs, CCMoid incubation: 4 mM solutions of the corresponding CCMoids (FcCCMoid or Fc9Accm) were prepared having always a final volume of 40 mL (20 % of DMSO: 8 mL of DMSO and 32 mL MilliQ water). Then, the mixtures were sonicated for 2 min until a fine powder was reached and the solutions display homogeneous color. Functionalized gold surfaces were incubated in the corresponding solutions using sealed containers (with special glass holders) that kept the samples vertically tilted. The system was stirred overnight at room temperature inside a box, avoiding light contact. Then, the gold surfaces were immersed in MilliQ water and dried with N_2.

Chapter II: CCMoid cages

Synthesis CCMoidcage:

IodineCCMoid: The synthesis of IodineCCMoid was carried out following the Pabon's method. Acetylacetonate (220.6 mg, 2.20 mmol) was added with boron oxide (109.2 mg, 1.56 mmol) in AcOEt (2 mL). The mixture was heated at 40 ˚C for 30 min until a white paste was formed. Then, a solution of 4-Iodobenzaldehyde (1g, 4.40 mmol), tributyl borate (2.0 g, 8.84 mmol) in AcOEt (3 mL) was added. The mixture was stirred at 40 ˚C for 3 h. Then, after cooling down to room temperature, an excess of n-butylamine (325.2 µl, 3.3 mmol) in AcOEt (3 mL) was added dropwise. The final reaction was stirred at room temperature overnight. Next day, a brown-yellow precipitate solid appeared. Then, a solution HCl 10 % (5 mL) was added and the mixture was heated at 60 ˚C for 2 hours. A color change to light yellow was observed and the mixture was filtered and washed with H_2O, MeOH and Et_2O to remove impurities. The yield was 57 %.

^{1}H-RMN (500 MHz $CDCl_3$, window from 16 to 0 ppm): δ 15.79 (s, 1H), 7.74 (d, J = 8.3 Hz, 4H), 7.59 (d, J = 15.5 Hz, 2H), 7.28 (d, J = 8.5 Hz, 4H), 6.62 (d, J = 15.8 Hz, 2H), 5.82 (s, 1H).

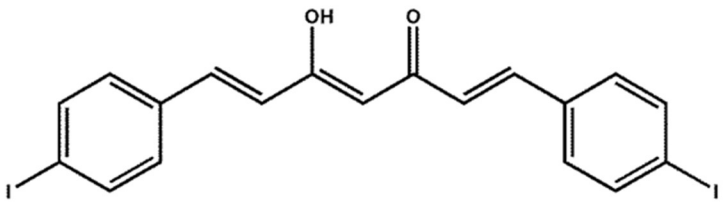

CCMoidcage: 250 mL of NEt_3 was added in a round bottom flask and the system was purged with N_2. Then, the IodineCCMoid (2.0 g, 3.78 mmol) and 3-Ethynylpyridine (1.45 g, 14.40 mmol) were added. The mixture was stirred for 10 min. After, a salt of CuI (138.9 mg, 0.73 mmol) and $Pd(PPh_3)_2Cl_2$ (284.7 mg, 0.41 mmol) were added and the final solution was stirred at 50 ˚C for 1 h under N_2. Then, the temperature was increased until 90 ˚C and the sample was stirred for four days. After that time, the solvent was removed by rotary evaporation and the product was solubilized in CH_2Cl_2 and filtered. The resulting residue was purified by a gradual flash chromatography (CH_2Cl_2, CH_2Cl_2-10 % acetone, CH_2Cl_2– 20 % acetone). The final product was obtained in a yield of 40 %. Apart from this product, a solid with only one functionalized side was possible to be extracted.

CCMoidcage ^{1}H-RMN (500 MHz $CDCl_3$, window from 16 to 0 ppm): δ 15.82 (s, 1 H), 8.78 (s, 2H), 8.57 (d, J = 4.2 Hz, 2H), 7.82 (d, J1 = 7.9 Hz, 2H), 7.68 (d, J = 15.8 Hz, 2H), 7.57 (s, 8H), 7.30 (dd, J1 = 7.7 Hz, J2 = 4.3 Hz, 2H), 6.68 (d, J = 15.8 Hz, 2H), 5.87 (s, 1H). ESI$^-$-MS ($CHCl_3$): m/z 477.32 $[M-H]^-$.

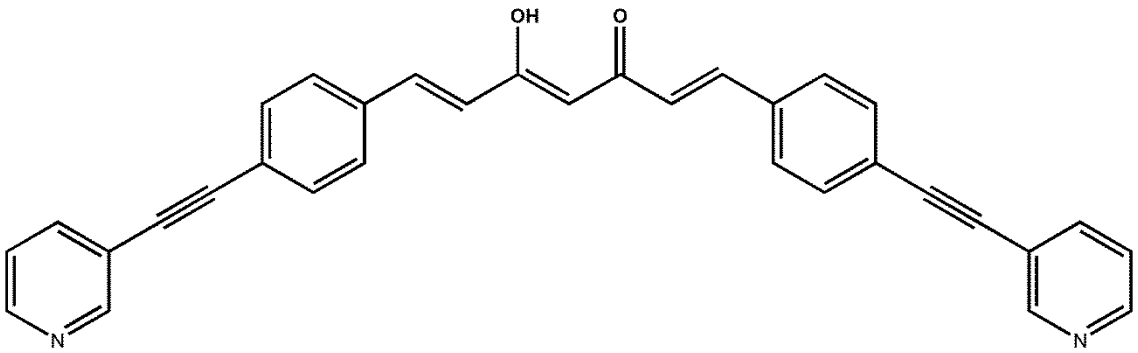

^{1}H-RMN (500 MHz $CDCl_3$, window from 16 to 0 ppm): δ 15.80 (s, 1H), 8.81 (s, 1H), 8.59 (s, 1H), 7.82 (d, J = 7.8 Hz, 1H), 7.66 (d, J = 15.8 Hz, 1H), 7.60 (d, J = 15.8 Hz, 1H), 7.56 (s, 4H), 7.53 (d, J = 8.4 Hz, 2 H), 7.42 (d, J = 8.4 Hz, 2 H), 7.33 (m, 1 H), 6.62 (m, 2 H), 5.85 (s, 1H). ESI$^-$-MS ($CHCl_3$): m/z 454.20 $[M-H]^-$.

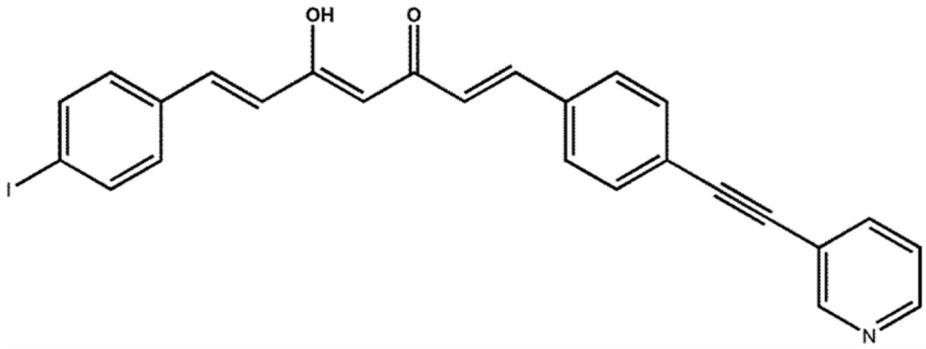

Molecular cage

In a vial, $CuBr_2$ (14 mg, 0.062 mmol) was dissolved in 4 mL of CH_2Cl_2 and 4 mL of acetonitrile obtaining a green solution. Then, $Ag(PF_6)$ (39.62 mg, 0.16 mmol) was added directly and a white solid was precipitated (AgCl) while the solution became blue ($Cu(PF_6)_2$). The mixture was

filtered and a solution of **CCMoidcage** (20 mg, 0.041 mmol) in 5 mL of CH_2Cl_2 was added to the filtered solution. A change of color to brown was observed together with the formation of a yellow precipitate. Finally, the mixture was stirred for 30 min and filtered. The brown solution was crystalized via liquid-vapor diffusion with Et_2O and yellow crystals were obtained after one day.

4.4 References

[1] J.-M. Lehn, *Science (80-.).* **1985**, *227*, 849–856.

[2] J.-M. Lehn, *Supramolecular Chemistry*, Wiley-VCH Verlag GmbH & Co. KGaA, Weinheim, FRG, **1995**.

[3] J. M. Lehn, *Eur. Rev.* **2009**, *17*, 263–280.

[4] A. E. Kaifer, W. Li, S. Yi, *Isr. J. Chem.* **2011**, *51*, 496–505.

[5] L. Zhao, S. Hao, Q. Zhai, H. Guo, B. Xu, H. Fan, *Soft Matter* **2017**, *13*, 3099–3106.

[6] A. Harada, *Acc. Chem. Res.* **2001**, *34*, 456–464.

[7] S. Yi, W. Li, D. Nieto, I. Cuadrado, A. E. Kaifer, *Org. Biomol. Chem.* **2013**, *11*, 287–293.

[8] A. E. Kaifer, *Acc. Chem. Res.* **2014**, *47*, 2160–7.

[9] J. W. Lee, S. Samal, N. Selvapalam, H. Kim, K. Kim, *Acc. Chem. Res.* **2003**, *36*, 621–630.

[10] X. Xia, H. Yu, L. Wang, Z. ul-Abdin, *RSC Adv.* **2016**, *6*, 105296–105316.

[11] W. S. Jeon, K. Moon, S. H. Park, H. Chun, Y. H. Ko, J. Y. Lee, E. S. Lee, S. Samal, N. Selvapalam, M. V. Rekharsky, et al., *J. Am. Chem. Soc.* **2005**, *127*, 12984–12989.

[12] F. Biedermann, V. D. Uzunova, O. A. Scherman, W. M. Nau, A. De Simone, *J. Am. Chem. Soc.* **2012**, *134*, 15318–15323.

[13] Q. An, G. Li, C. Tao, Y. Li, Y. Wu, W. Zhang, *Chem. Commun.* **2008**, 1989.

[14] M. T. Rojas, A. E. Kaifer, R. Königer, J. F. Stoddart, *J. Am. Chem. Soc.* **1995**, *117*, 336–343.

[15] L. Qi, H. Tian, H. Shao, H.-Z. Yu, *J. Phys. Chem. C* **2018**, acs.jpcc.8b01067.

[16] A. González-Campo, S. H. Hsu, L. Puig, J. Huskens, D. N. Reinhoudt, A. H. Velders, *J. Am. Chem. Soc.* **2010**, *132*, 11434–11436.

[17] M. Holzinger, A. Le Goff, S. Cosnier, *New J. Chem.* **2014**, *38*, 5173–5180.

[18] D. B. Amabilino, *Surfaces for Supramolecular Systems*, **2016**.

[19] M. Zehner, D. Gibbs, **1991**, *43*.

[20] H. J. Pabon, *Recl. Trav. Chim. Pays-Bas* **1964**, 379.

[21] A. Arezki, E. Brule, **2009**, 1606–1609.

[22] S. Barriga, C. F. Marcos, *Tetrahedron* **2002**, *58*, 9785–9792.

[23] N. Aliaga-Alcalde, L. Rodríguez, M. Ferbinteanu, P. Höfer, T. Weyhermüller, *Inorg. Chem.* **2012**, *51*, 864–873.

[24] N. Aliaga-Alcalde, P. Marqués-Gallego, M. Kraaijkamp, C. Herranz-Lancho, H. Den Dulk, H. Görner, O. Roubeau, S. J. Teat, T. Weyhermüller, J. Reedijk, *Inorg. Chem.* **2010**, *49*, 9655–9663.

[25] M. Menelaou, F. Ouharrou, L. Rodríguez, O. Roubeau, S. J. Teat, N. Aliaga-Alcalde, *Chem. - A Eur. J.* **2012**, *18*, 11545–11549.

[26] N. Aliaga-Alcalde, L. Rodríguez, *Inorganica Chim. Acta* **2012**, *380*, 187–193.

[27] Z. H. Liu, N. M. D. Brown, A. McKinley, *J. Phys. Condens. Matter* **1997**, *9*, 59–71.

[28] R. N. Jones, *Chem. Rev.* **1947**, *41*, 353–371.

[29] S. Strbac, A. Hamelin, R. R. Adzić, *J. Electroanal. Chem.* **1993**, *362*, 47–53.

[30] F. J. Rodríguez Nieto, G. Andreasen, M. E. Martins, F. Castez, R. C. Salvarezza, A. J. Arvia, *J. Phys. Chem. B* **2003**, *107*, 11452–11466.

[31] J. C. Love, L. A. Estroff, J. K. Kriebel, R. G. Nuzzo, G. M. Whitesides, *Self-Assembled Monolayers of Thiolates on Metals as a Form of Nanotechnology*, **2005**.

[32] I. Ponce, J. F. Silva, R. Oñate, M. C. Rezende, M. A. Paez, J. H. Zagal, J. Pavez, F. Mendizabal, S. Miranda-Rojas, A. Muñoz-Castro, et al., *J. Phys. Chem. C* **2012**, *116*, 15329–15341.

[33] C. B. Gorman, H. A. Biebuyck, G. M. Whitesides, *Langmuir* **1995**, *11*, 2242–2246.

[34] W. Meng, B. Breiner, K. Rissanen, J. D. Thoburn, J. K. Clegg, J. R. Nitschke, *Angew. Chemie - Int. Ed.* **2011**, *50*, 3479–3483.

[35] G. Zhang, M. Mastalerz, *Chem. Soc. Rev.* **2014**, *43*, 1934–1947.

[36] T. K. Ronson, S. Zarra, S. P. Black, J. R. Nitschke, *Chem. Commun.* **2013**, *49*, 2476.

[37] Y. Inokuma, T. Arai, M. Fujita, *Nat. Chem.* **2010**, *2*, 780–783.

[38] I. A. Bhat, R. Jain, M. M. Siddiqui, D. K. Saini, P. S. Mukherjee, *Inorg. Chem.* **2017**, *56*, 5352–5360.

[39] J. E. M. Lewis, E. L. Gavey, S. A. Cameron, J. D. Crowley, *Chem. Sci.* **2012**, *3*, 778–784.

[40] A. Schmidt, V. Molano, M. Hollering, A. Pöthig, A. Casini, F. E. Kühn, *Chem. - A Eur. J.* **2016**, *22*, 2253–2256.

[41] P. F. Kuijpers, M. Otte, M. Dürr, I. Ivanović-Burmazović, J. N. H. Reek, B. De Bruin, *ACS Catal.* **2016**, *6*, 3106–3112.

[42] T. R. Cook, V. Vajpayee, M. H. Lee, P. J. Stang, K. W. Chi, *Acc. Chem. Res.* **2013**, *46*, 2464–2474.

[43] G. Lyu, Q. Chen, F. Jiang, D. Yuan, H. Xue, L. Liang, L. Liu, M. Hong, *Cryst. Growth Des.* **2016**, *16*, 3569–3572.

[44] J. Ferrando-Soria, A. Fernandez, E. Moreno Pineda, S. A. Varey, R. W. Adams, I. J.

Vitorica-Yrezabal, F. Tuna, G. A. Timco, C. A. Muryn, R. E. P. Winpenny, *J. Am. Chem. Soc.* **2015**, *137*, 7644–7647.

[45] Z. Li, N. Kishi, K. Hasegawa, M. Akita, M. Yoshizawa, *Chem. Commun.* **2011**, *47*, 8605.

[46] A. B. S. Elliott, J. E. M. Lewis, H. Van Der Salm, C. J. McAdam, J. D. Crowley, K. C. Gordon, *Inorg. Chem.* **2016**, *55*, 3440–3447.

[47] Y.-H. Li, Y. Zhang, Y.-M. Legrand, A. van der Lee, J.-J. Jiang, C.-X. Chen, C.-Y. Su, M. Barboiu, *Dalt. Trans.* **2017**, *46*, 15204–15207.

[48] Y. Zheng, M. Evangelisti, R. E. P. Winpenny, **2011**, 3692–3695.

[49] D. N. Woodruff, F. Tuna, M. Bodensteiner, R. E. P. Winpenny, R. A. Layfield, *Organometallics* **2013**, *32*, 1224–1229.

[50] A. Elangovan, Y. Wang, T. Ho, **2003**, *5*, 1841–1844.

[51] A. A. Mohamed, *Coord. Chem. Rev.* **2010**, *254*, 1918–1947.

[52] K. Kamada, T. Namikawa, S. Senatore, C. Matthews, P. F. Lenne, O. Maury, C. Andraud, M. Ponce-Vargas, B. Le Guennic, D. Jacquemin, et al., *Chem. - A Eur. J.* **2016**, *22*, 5219–5232.

[53] A. Felouat, A. D'Aléo, F. Fages, *J. Org. Chem.* **2013**, *78*, 4446–4455.

SECTION V:

MOLECULAR DONOR-ACCEPTOR CHEMISTRY

Curcuminoids with donor/acceptor properties

In this section, we carried out the synthesis and photophysical studies of a family of CCMoids with acceptor/donor properties, to explore their use as active components in the fabrication of solution-processed organic solar cells (OSCs) devices (e.g.: bulk heterojunctions organic solar cells, BHJ-OSCs). For this purpose, two CCMoid families were synthesized varying the nature of their terminal groups (donor/acceptor). Moreover, in each family two more different modification on their structure were performed in order to study the influence of each modification on their optical and electronic properties. This way, coordinated boron species were accomplished, by linking BF_2 moieties to the β-diketone group of the new CCMoids, and the addition of a leg, by the use of an acac derivative in the CCMoid syntheses, was also performed.

5.1 Introduction

Overall, the conjugated nature of the CCMoid backbone, together with the presence of aromatic groups in its structure promote excellent optical as well as electronic properties in most of CCMoids.[1]

As a result, some of these features have been already exploited in studies of single molecule conductance as it has been explained in Section II. However, these properties can be used, in a higher scale, for example forming part of OPVs (organic photovoltaics solar cells) or optoelectronic devices. OPVs are devices based on organic molecules capable of producing energy using solar radiation.[2–5] The growing demand of renewable energy sources has caused the rapid development of this field giving rise to the synthesis and use of a large number of semiconductors polymers with donor/acceptor properties and remarkable efficiency values (≈ 14 %).[6–8] Most of these OPVs devices, specially BHJ-OSCs, are fabricated using a conjugated polymer and a fullerene derivative as the active components, being the donor and the acceptor parts, respectively.[5,9] Most of the progress in the field has mainly focused on the design of new donor polymers,[10,11] where fullerene derivatives have been almost exclusively used as electron acceptors due to their excellent electron withdrawing ability and high electron mobility.[9] However, despite their advantages, these systems also display certain limitations such as a relatively low absorption in the visible region, difficult chemical modification and an elevated cost, among others.[12]

This fact has triggered the appearance of alternative systems that present (i) high charge carrier transport, (ii) specific gap energy and (iii) soluble in common organic solvents; and improve fullerene drawbacks.

Among these systems, CCMoids are presented as promising candidates to be used in OPVs.[13,14] On one hand, the presence of the conjugated chain provides absorption bands in the visible region (allowing the harvest of photons from the solar spectrum). Moreover, the versatile ways of

functionalizing these systems give the possibility of tuning their optical and electronic properties. In this regard, the addition of donor/acceptor groups as aromatic terminal groups for the CCMoids as well as coordination to the β-diketone and addition of extra groups (in the leg position of the CCMoid) were explored to study the tuning of the band gap, energy levels and solubility, among other properties.[15]

Hence, in this work the synthesis and study of CCMoids which present donor and acceptor groups were carried out. For that, two different CCMoid families were synthesized; one of them using an acceptor terminal group (1,2,3-benzothiadiazole) and the other using a donor terminal group (fluorene). These functional groups were chosen after carrying out a bibliographic search where it was found that these groups are common moieties used in donor/acceptor compounds.[16–18]

In addition, the new families of compounds were extended by the introduction of an ester group connected at the methine- position of the CCMoid skeleton (giving T-shaped molecules). The position of the ester group could influence the conjugated chain and therefore the electronic properties[19] together with the solubility and supramolecular packing of the final material. The second modification focused on the coordination of a BF_2 group to the β-diketone. Difluoroboron β-diketone compound form an important family of photo- and electroactive molecules commonly used in photovoltaic applications.[14,20–22] In the case of CCMoids, their coordination could give rise to the formation of Donor-Acceptor-Donor (D-A-D) architectures in which A is the central dioxaborine ring and D are the terminal aromatic moiety. These systems show higher molar absorptivity values (ε) than the free analogous (non-coordinated ligand) and shift to higher wavelenghts (near-IR); this behavior is understood as intramolecular charge transfer processes (ICT) in the molecules,[23] being attractive molecules for the creation of photovoltaics devices since they require high and large UV-Vis absorption areas of the solar spectrum.[4,5]

Thus, the main objective was the study of the effects of the three above modifications (aromatic groups, ester functionalization and coordination of BF_2 group) in the transport and optoelectronic properties of the systems. For that, HOMO (the highest energy occupied molecular orbital) and LUMO (the lowest energy unoccupied molecular orbital) studies were necessary, since can be related to the conductive properties.[24]

In our case, the study and estimation of these values was performed by the use of two techniques: UV-Visible and Electrochemistry. The UV-Vis measurements provide information about the transition between electronic levels of the molecule, allowing the determination of the different energy of the frontier molecular orbital (HOMO-LUMO energy gap). On the other side, the electrochemical studies can evaluate the effects of the system by passing current through the molecule (oxidation/reduction) and, thus allow us to know the energy of the HOMO and LUMO, and therefore the gap.

Finally, the results for all the systems under study were evaluated. The analysis of each modification afforded valuable insights regarding the optoelectronic and transport properties and provided ideas for further improvement in the design of novel CCMoids.

5.2 Objectives

This chapter is focused on the synthesis and study of CCMoids with donor/acceptor properties to be used in the fabrication of organic solar cells (OSCs). To carry out this study, eight new CCMoids were synthesized, divided in two families depending on the nature of their terminal group: acceptor (**A**) (1,2,3-benzothiadiazole) and donor (**D**) (fluorene) (Figure 5.1).

As explained above, two extra modifications were performed in each family. On one side, an ester group in the central position (**A3** and **D3**); and on the other, the formation of the boron compound (**A2, A4**) and (**D2, D4**) were analyzed.

Then, to determine the electronic properties and therefore future applications of the CCMoid, a study of their solubility in different solvents was performed together with the analysis of the acceptor/donor properties by UV-Vis absorption spectrometry and electrochemical measurements; the final results were compared with the well-known donor (P3HT) and acceptor ($PC_{61}BM$) systems.

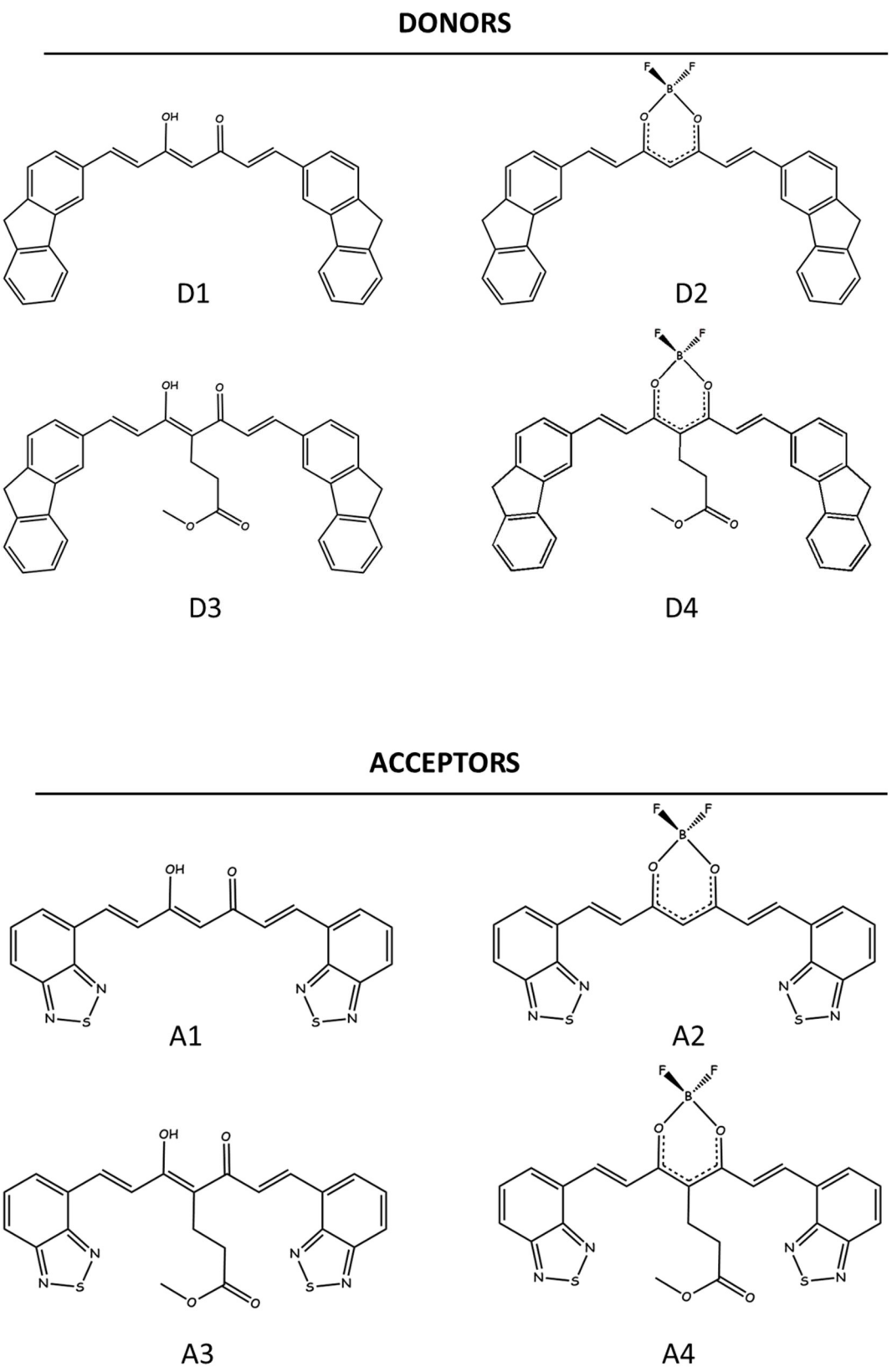

Figure 5.1: Representation of donor CCMoids: D1, D2, D3 and D4 (top) an acceptor CCMoids: A1, A2, A3 and A4 (bottom).

5.3 Results and Discussion

5.3.1 Experimental section

Here, in the search of the systems based on CCMoids, that present acceptor and donor properties, eight new CCMoids have been synthesized. These systems display modifications in their structure that consist on:

(i) Modification of the aromatic side groups: systems that present fluorene groups, classified here as donor molecules (**D1, D2, D3** and **D4**) and CCMoid that contain 1,2,3-benzothiazole groups, acceptor (**A1, A2, A3** and **A4**). The choice of these groups was inspired on several acceptors/donors compounds found in the literature which presented these groups.[16–18,24]

(ii) Addition of an alkyl moiety with an ester terminal group (as a leg) in the methane position **(A3** and **D3)**: this modification increases the solubility of the systems in a variety of organic solvents.

(iii) Coordination of boron: it is well-known that the formation of boron compound modifies the electronic structure of the molecule by affecting the HOMO and LUMO energies.[14,20–22]

Synthesis of A1, A3, D1 and D3

The synthesis of these CCMoids was carried out following Pabon's method[25] (discussed in the introductory section of general remarks). In the case of the **A1** and **D1**, acetylacetonate was used as a reagent; on contrary, for the synthesis of **A3** and **D3** methyl 4-acetyl-5-oxohexanoate was used. In all cases, the reaction carries on by the formation of boron intermediates that breaks under mildly conditions using water without the need of acidic solutions. The yield values of **D1** and **D3** are similar to others CCMoids synthesized (≈ 70 %), however, **A1** and **A3**, displayed values significantly lower. Such results may relate to solubility problems, low reactivity of the corresponding aldehyde or the sum of both.

Synthesis of A2, A4, D2 and D4

The synthesis of BF_2-CCMoids (**A2, A4, D2** and **D4**) required the modification of the method described in the literature[26,27] with the assistance of a microwave reactor. After the reaction, all the products presented a significantly change of color due to the boron coordination. On the other hand,

the new coordination compounds display different solubility properties comparing with the free CCMoids ligands, being the latest insoluble in aprotic polar solvents.

The achievement of the compounds was confirmed by ^{1}H NMR and, in most of the cases, crystallographic data was accomplished by the use of single X-ray diffraction. In relation to the ^{1}H NMR experiments, Figures 5.2 5.3 show the spectra corresponding to **A1**, **A2**, **A3** and **A4**, and **D1**, **D3** and **D4**, respectively (it was not possible to obtain a good spectrum for **D2** due to its low solubility). In the case of compound **A1** and **D1**, both present a singlet around ≈ 6 ppm assigned to the –CH- methine group. This signal did not appear in the spectra of **A3** and **D3** since there are functionalized with an alkyl chain (that display two triplets at ≈ 2.7 and 3.2 ppm, in that order) and terminal ester groups that display singlets at ≈ 3.7 ppm in both cases. The protons related to the conjugated chain appear as two doublets at ≈ 6.8 and 7.8 ppm for compounds **D1** and **D3**. These signals were slightly displaced for **A1** and **A3** (≈ 7.6 and 8.0 ppm). The couplings constants for such protons were around 15 and 16 Hz, indicating a *trans* dispositions in all cases (E conformation, as Figure 5.1 shows). On the other hand, a singlet at ≈ 16 ppm, corresponding to the enol proton, shows the stabilization of the enol form in all the compounds.

As expected, the ^{1}H NMR corresponding to the boron compounds show a displacement of most of the signals, due to the coordination of the BF_2 group. This coordination changes the electronic density, increasing the delocalization of the π-orbitals and giving rise to some shifts to low fields. The most affected protons will correspond to the protons that are the closest to the BF_2 group. In the case of **A2**, the signal related to the methine shows a displacement around (≈ 1 ppm). Apart from the latest, the signals corresponding to the conjugated chain were shifted too and the signal derived from the enol group disappears, corroborating the coordination.

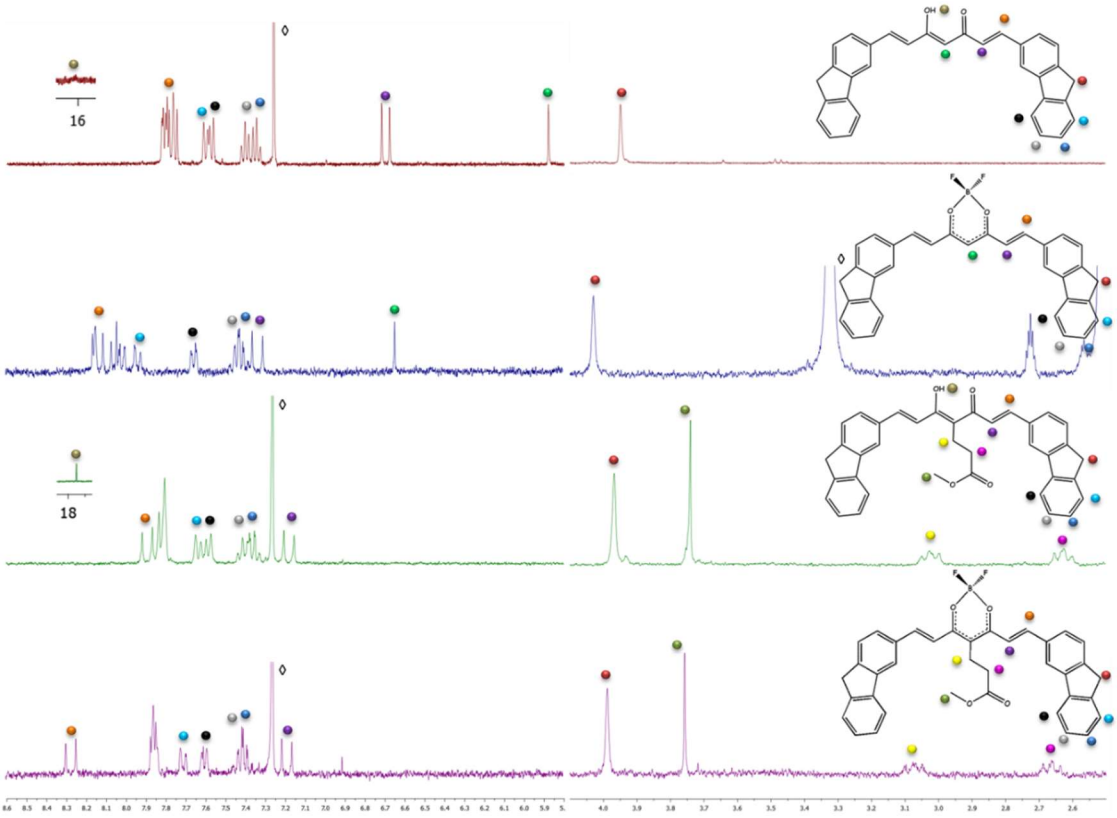

Figure 5.1: ^{1}H NMR spectra of D1 (red), D2 (blue), D3 (green) and D4 (pink) in $CDCl_3$ (D2 in DMSO). ◊ corresponds to the solvent peak.

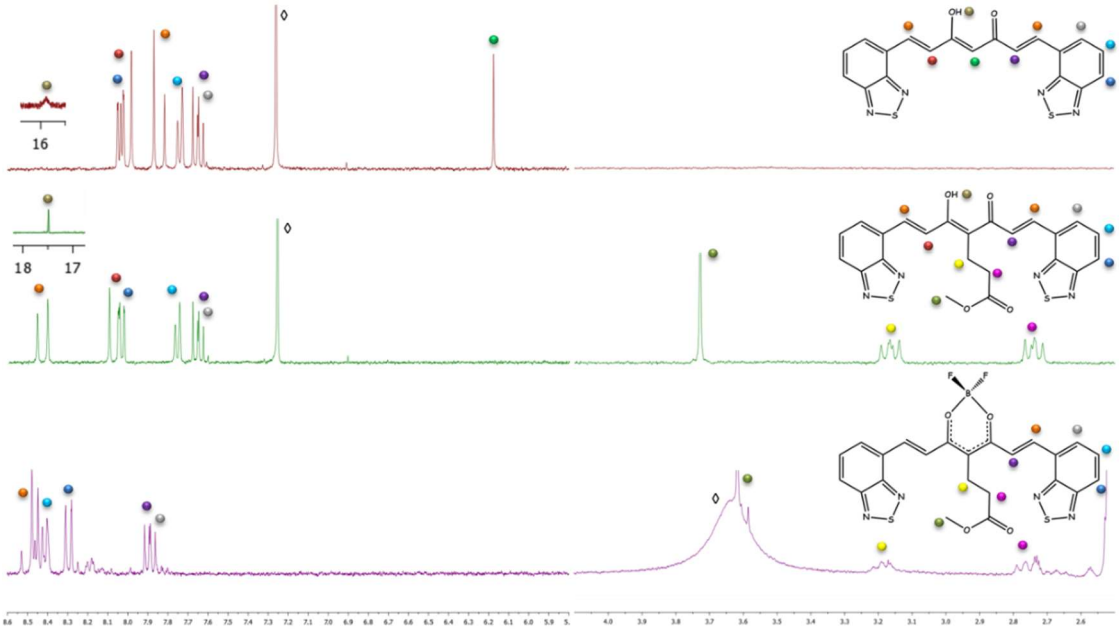

Figure 5.2: ^{1}H NMR spectra of A1 (red), A3 (green) and A4 (pink) in $CDCl_3$ (A4 in DMSO). ◊ corresponds to the solvent peak.

Crystal structures

The analysis of the crystallographic data of **D1**, **D2**, **D3**, **D4**, **A3** and **A4** required the use of synchrotron source due to the small size of the crystals. The crystal data for **A1** and **A2** was not accomplished during the process of this thesis. General crystallographic data for the rest of systems are presented in Annex 5.1.

Compound D1

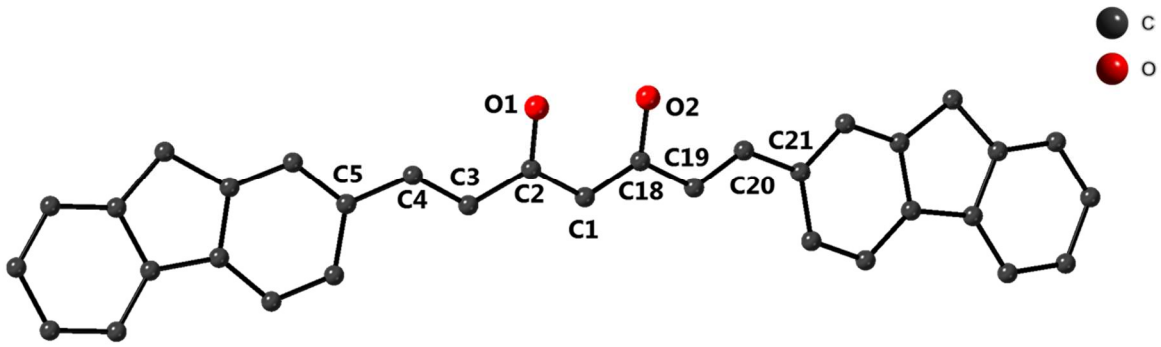

Figure 5.3: Representation of D1 where the atoms of O (red), C (gray) are shown. For clarity hydrogen atoms are omitted.

The crystal structure presents a orthorhombic space group -P 2ac 2ab with eight molecules in the unit cell. The asymmetric unit contains one CCMoid molecule. The structure shows a β-diketone group in the middle of a conjugated chain of seven carbon atoms and fluorene groups in each side of the backbone. The β-diketone group shows two different C-O distances, 1.303 and 1.323 Å corresponding to C2-O1 and C18-O2 respectively, indicating the stabilization of the enol form. Related to the conjugated chain, two types of C-C distances values were found corresponding to C-C single bond (between 1.457 and 1.470 Å) and C-C double bond (1.329 – 1.331 Å). The conjugated chain is slightly bended with a final E conformation in both sides of the β-diketones, minimizing steric hindrances. The fluorene groups are disposed in the same plane. No remarkable intermolecular interactions between the neighboring compounds were found.

Compound D2

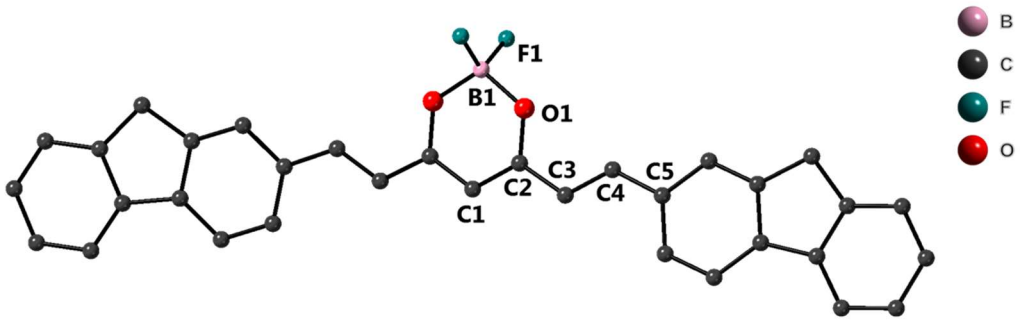

Figure 5.4: Representation of D2 where the atoms of O (red), C (gray), B (pink) and F (yellow) are shown. For clarity hydrogen atoms are omitted.

The crystal structure presents a monoclinic space group C2/c with six molecules in the unit cell. The asymmetric unit contains half molecule of the compound. The structure shows a boron center with a pseudo-tetrahedral geommetry coordinated to two oxygen atoms from the β-diketone group and two fluoride atoms. The two B-O and B-C distances were identical with values of 1.480 and 1.367 Å, respectively. These distances are in agree with similars systems reported in the literature.[14,20–22] The angles shown are expected for a pseudo-tetrahedral geommetry being of 107.84 ˚ (F1-B1-O1). Related to the β-diketone, there is only one C-C and C-O distances (1.388 Å and 1.301 Å, respectively) indicating the delocalition due to the boron coordination. Related to the conjugated chain, there are two different C-C distances, which correspond to C-C single bonds (C2-C3, C4-C5 being 1.444 and 1.450 Å, respectively) and the C-C double bond named C3-C4, with a distance of 1.344 Å. As for D1, the two fluorene groups were disposed in the same plane that included the conjugated chain and β-diketone groups (only the fluorine atoms are located out of the plane). The structure show different intermolecular interactions (Figure 5.6); there are interactions between the carbon atoms from the β-diketone groups of neighboring molecules and, in addition, the boron and oxygen atoms interact with the fluorene rings of the nearby.

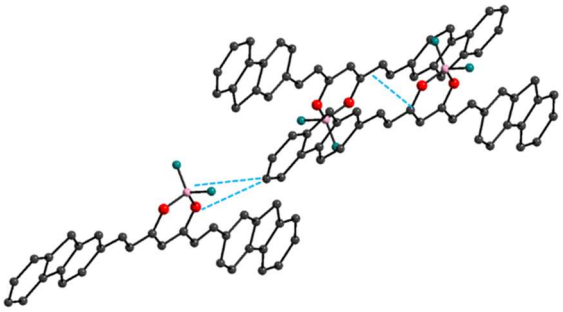

Figure 5.6: Intermolecular interactions (blue lines) of compound D2.

Compound D3

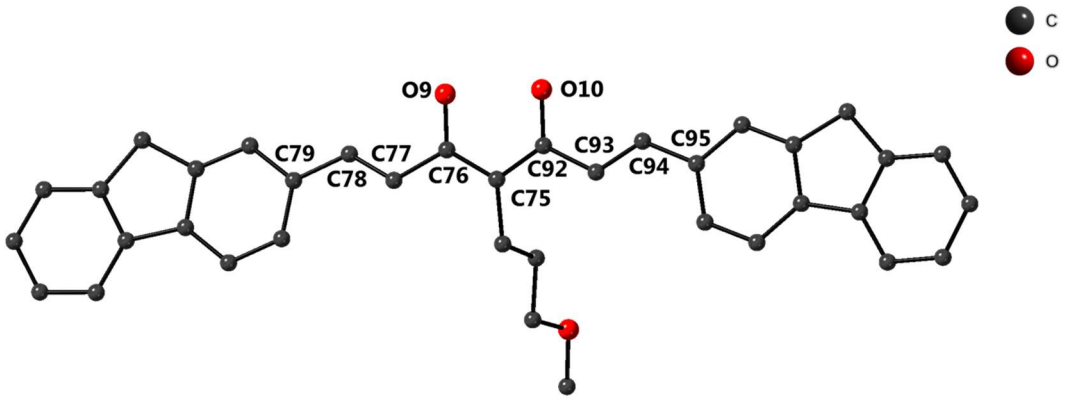

Figure 5.7: Representation of D3 where the atoms of O (red), C (gray) are shown. For clarity hydrogen atoms are omitted.

The crystal structure presents a monoclinic space group $P2_1/n$ with sixteen molecules in the unit cell and the asymmetric unit contains one molecule of CCMoid. The structure is almost identical as the previous described. Again, the β-diketone group shows two C-C and C-O different distances indicating the stabilization of the enol form. The molecule is completely planar, with the conjugated skeleton, β-diketone moiety and fluorene groups contained in the same plane. Now, in the middle of the β-diketone there is an alkyl chain showing a terminal ester group. The C-C distances observed in the alkyl leg are 1.517 and 1.527 Å, corroborating that they are C-C single bonds. The alkyl chain is disposed almost perpendiculary to the plane of the rest of the molecule. In relation to the intermolecular interactions (Figure 5.8), the keto moiety of the ester group shows interactions with the neighboring molecules.

Figure 5.8: Intermolecular interactions (blue lines) of compound D3.

Compound D4

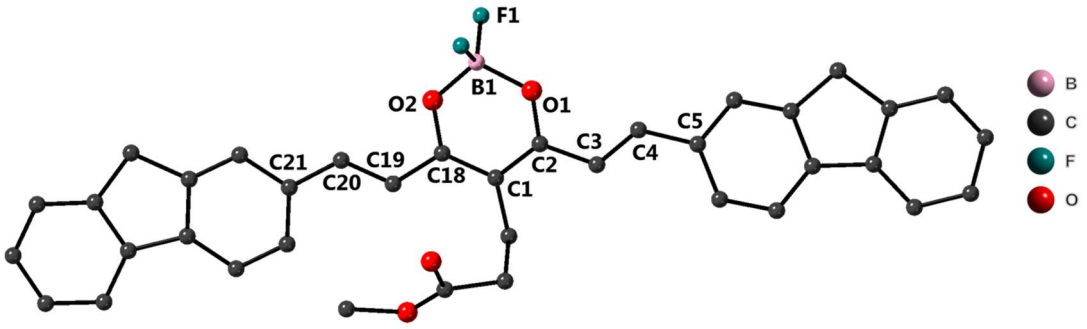

Figure 5.9: Representation of D4 where the atoms of O (red), C (gray), B (pink) and F (yellow) are shown. For clarity hydrogen atoms are omitted.

The crystal structure presents a monoclinic space group C2/c with eight molecules in the unit cell. The asymmetric unit contain one molecule of CCMoid. As in the case of **D2**, the structure shows a boron atom with pseudo-tetrahedral geommetry coordinated to two oxygen and two fluoride atoms. General features are identical to the previous systems. The main difference, resides as for compound **D3** in the existence of, an alkyl chain coordinated through a C atoms to the middle of the β-diketone. The ester from this alkyl chain disposes perpendicular to the conjugated chain. Several intermolecular interactions can be observed (Figure 5.10). The CCMoids organisize superposing their π-conjugated systems, forming dimers separated by a distances of ≈ 3.56 Å. On the other hand, different C-H···F interactions having distances of ≈ 3.54 Å are observed.

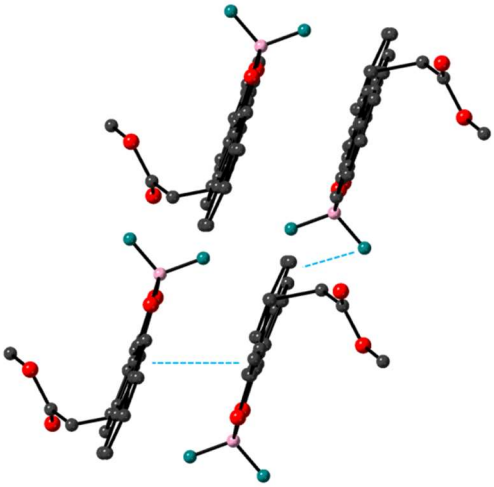

Figure 5.10: Representation of the intermolecular interactions observed for D4.

Compound A3

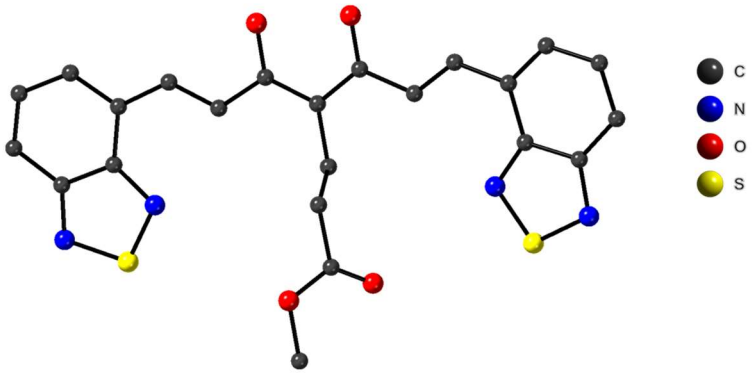

Figure 5.11: Representation of A3 where the atoms of O (red), C (gray), N (blue) and S (yellow) are shown. For clarity hydrogen atoms are omitted.

A3 presents a monoclinic space group $P2_1/n$ with four molecules in the unit cell and the asymmetric unit contains only one CCMoid molecule. General structure corresponds to a CCMoid where a β-diketone group is disposed in the middle of a conjugated chain of seven carbon atoms and 1,2,3-benzothiadiazole groups are on each side of the chain. As in the other free ligands, there are two different C-C and C-O distances in the β-diketone group indicating the stabilization of the enol form. Both 1,2,3-benzothiadiazole groups locate in the same plane together with the conjugated chain and the β-diketone group. As in the previous system, the alkyl chain is located out of this plane. At the intermolecular level, it's possible to observe a variety of interactions. Sulfur groups interact with the nitrogen atoms from neighboring molecules (S2-N4, Van der Waals interactions), as it can be seen in the Figure 5.12, displaying a distances of 3.228 Å. On the other hand, one of the oxygen atoms from the β-diketone and one carbon atom from the benzothidiazole moieties interact with the methyl of the ester group.

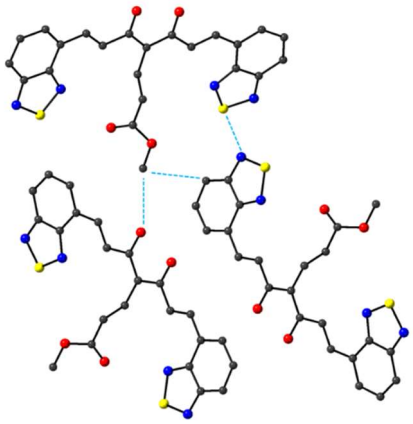

Figure 5.12: Representation of the intermolecular interaction of A3.

5.3.2 Solubility studies

One of the main limitations for the use of compounds in organic solar cells is their low solubility. Thus, solubility studies of all the achieved CCMoids were accomplished. The creation of solar cells requires the use of solutions containing the active molecular materials; there are a variety of techniques such spin coating, screen printing, inkjet printing, among others, that can help in the final deposition of such solutions into a final substrate. In this way, it is important to solubilize the maximum amount possible avoiding the formation of precipitates or aggregates and normally, solvents with high boiling points are used. Concentrations are described in this case as mg per mL, and it is accepted that above 10 mg/mL the compounds display remarkable solubility.[2,3]

Table 5.1 shows the results from the solubility test on different solvents using 1 mg of the CCMoids. This table also displays the literature values for P3HT (donor) and $PC_{61}BM$ (acceptor) for comparative reasons.[28]

Compound	DMF (mL)	DMSO (mL)	THF (mL)	MeOH (mL)	CH_2Cl_2 (mL)	CB (mL)	DB (mL)
D1	0.4	1.0	0.7	Insoluble	1.0	1.0	0.7
D2	0.8	1.0[(a)]	1.0[(a)]	Insoluble	Insoluble	1.0[(a)]	1.0[(a)]
D3	0.2	0.1	0.5	Insoluble	1.0	1.0	1.0
D4	0.2	0.3	0.2	Insoluble	0.5	1.0	1.0
A1	0.2	Insoluble	1.5	Insoluble	1.5	1.3	1.0
A2	1.0[(a)]	1.0[(a)]	1.0[(a)]	Insoluble	1.0[(a)]	-	-
A3	0.1	0.5	0.1	Insoluble	1.0[(a)]	1.0	0.1
A4	0.6	1.0	0.1	Insoluble	1.0[(a)]	Insoluble	Insoluble
P3HT	-	-	0.9	< 10	-	0.06	0.30
$PC_{61}BM$	-	-	0.6	< 10	-	0.02	0.02

(a) By adding 1 mL of solvent the CCMoid is partially soluble

(b) No information was found for the solubility of P3HT and $PC_{61}BM$ in DMF, DMSO and CH_2Cl_2.

Table 5.1: Solubility assays using 1 mg of CCMoid.

From the table above, it can be concluded that the systems containing ester groups **(D3** and **A3)** present improvement of the solubility if one compares them with the those without this group **(D1** and **A1)**. On the other hand, in the majority of the cases, the formation of the boron compound leads to a decrease of the solubility. From all the systems, it is remarkable the solubility of **A3** in DB

(dichlorobenzene), DMF (N,N-Dimethylformamide), THF (Tetrahydrofuran) and CH_2Cl_2. However, it exists an obvious difference with we compare with $PC_{61}BM$ or P3HT, being these two more soluble that our family of systems.

5.3.3 Studies of acceptor/donor properties

In this section we will carry out a study of the photophysical properties of the CCMoids previously synthesized.

Initially, the UV-Vis absorption studies have been carried out in solution. These measures could provide information about the absorption range of the systems (important factor since the goal is to have the highest absorption band in the solar spectrum range). This study includes the value of the molar absorptivity (ε).

In addition, similar studies were carried out in the solid state. In this case the main objective was to simulate the conditions of the solar cell; the solution studies were not taken into account because of the extra solvent effect. The solid state measurements allowed us to determine the energy gap (distances between HOMO-LUMO) as it has been described for previous polymers and small molecules in the literature.[24] These values were also determined by the performance of electrochemical measurements.

The analysis of the results obtained from each technique, and the comparison among all the studied CCMoids allowed us to elucidate the influence of each modification (aromatic groups, presence of the ester groups and formation of boron compound).

Optical Properties:

UV-Visible absorption experiments

These measurements gave us information about: (i) the energetic separation between the HOMO and LUMO energy gaps (E_g^{op}) of the CCMoids, (ii) absorption range of each compounds and (iii) absorptivity molar values of the absorption bands.

UV-Vis in solution

The UV-Vis spectra of **D1** and **D2** (free ligand and BF_2-CCMoid, respectively) and the ones from **D1** and **D3** (free ligand and the latest containing an ester group in the leg position) are shown in the Figure 5.13.

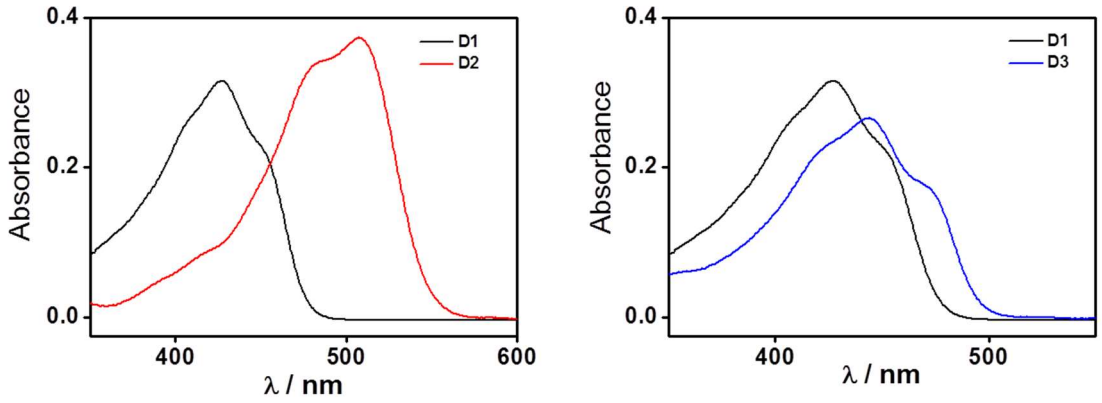

Figure 5.53: (left) UV-Visible spectrum of D1 (black line) and D2 (red line). (right) UV-Vis spectrum of D1 (black line) and D3 (blue line); all at concentration of 10^{-5} M in CH_2Cl_2.

As it happens in all CCMoids materials, and it was already explained in the first sections of the thesis, **D1-D3** present a characteristic broad band between 350-600 nm, that relates to the CCMoid skeleton (conjugated chain and β-diketone moiety) and it is the sum of some π-π* transitions displaying shoulders nearby to a maxima absorption value. Also, in all the cases at higher energies (approximately 290 nm, not shown in Figure 5.13) appear the transitions corresponding to the fluorene groups. At the lowest energy range, **D1** shows a maxima value at 425 nm with shoulders at both sides. In the case of **D2**, a bathochromic shift from the values observed at **D1** is clearly observed, having now the maxima absorption value at 508 nm and an intense should at high energies (485 nm). Such change directly relates to the modification of the central part, by the coordination of the BF_2 group with the β-diketone. This behavior has been observed in other BF_2-compounds[14,20–22] and normally it is accompanied by an increase of the absorptivity molar (ε) as can be shown in the Table 5.2.

On the other hand, the influence in their optical properties of the ester group (**D3** vs **D1**) is less prominent than the one observed for **D2** but still remarkable. As Figure 5.13 shows, **D3** presents a bathochromic shift with respect to **D1** of approximately 20 nm, due to the presence of the electron-withdrawing group (from 453 to 472 nm).

Compound	Abs	λ (nm)	ε (L·mol^{-1}·cm^{-1})
D1	0.23	453	45360
D2	0.38	508	76702
D3	0.18	472	35660
D4	0.37	520	74760

Table 5.2: Values of the maxima absorptivity for compounds D1-D4.

The displacement to lower energies implies a decrease in the HOMO-LUMO gap, therefore, an improvement on the electronic properties of the molecules. However, it is well-reported that CCMoids are solvatochromic materials and such types of transitions can be highly influenced by the nature of the solvents.[29–31] Therefore, to avoid such effects, UV-Visible measurements in solid state were performed.

UV-Vis in the solid state

These measurements were carried out by the use of an integrating sphere obtaining diffuse reflectance spectra. Figure 5.14 shows the diffuse reflectance spectra of compounds **A1, A2, A3, A4, D1, D2, D3** and **D4**. Due to the saturation effects, the samples were diluted with KBr, here used as a matrix, that did not interfere in the final absorbance responses but provided values above 0. This was not corrected but KBr blanks were performed for each sample. The final data, shown in Table 5.3 and 5.4, has been processed as it is described for polymers and small molecules in solar cell studies and conductive polymers studies.[24]

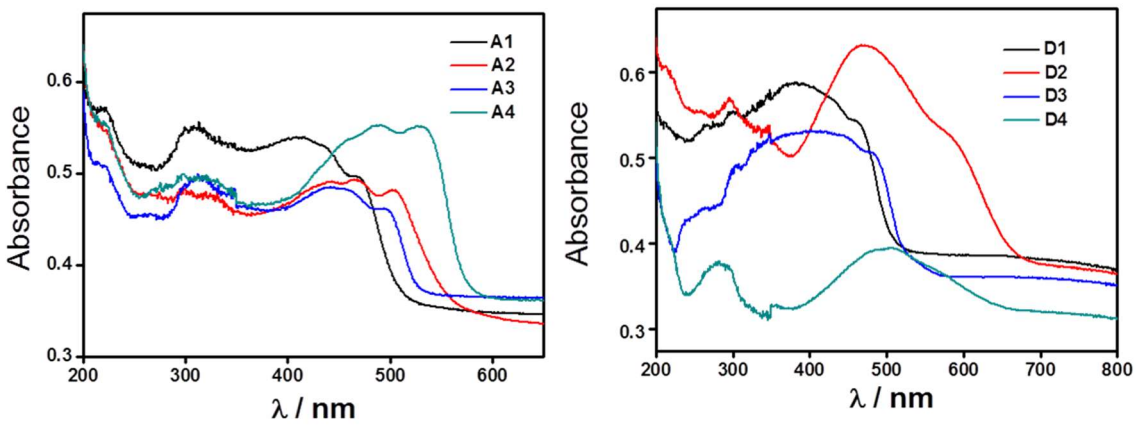

Figure 5.64: (left) UV-Vis absorption spectra of A1, A2, A3 and A4 in the solid state. (right) UV-Vis absorption spectra of D1, D2, D3 and D4 in the solid state. In all cases KBr was used as a matrix and the legend color of each graph relates to the final systems, acceptor or donors, respectively.

Comparing the spectra obtained in the solid state with those in solution (Figure 5.13), it was observed that now the absorbance values appear at higher (less energetic) wavelengths. Comparing the systems, a similar behavior as the one observed in solution is depicted. Figure 5.15 represents the UV-Vis absorption spectra of the donor systems (**D1-D3**). Here, the boron compound, **D3**, shows a shift of 150 nm with respect to **D1**. On the other hand, the influence of the ester group is lower as

before, displaying a shift of 50 nm to the red region. The calculations of the final absorbance values (λ_{onset}) was performed by the use of the onset, as it is shown in Figure 5.16 and explained below.

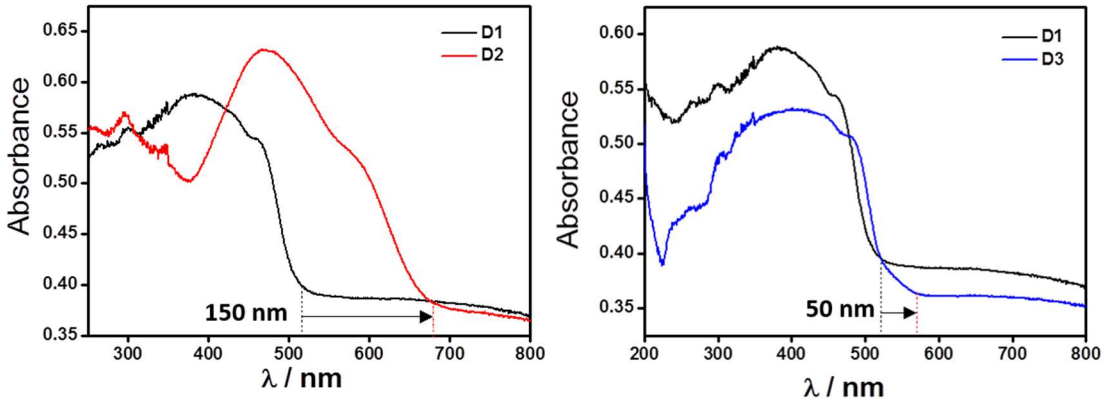

Figure 5.7: (left) UV-Vis spectra in the solid state of D1 (black line) and D2 (red line). (right) UV-Vis spectra in the solid state of D1 (black line) and D3 (blue line).

Table 5.3 shows that, in general, the compounds that present coordination with the BF_2 group (**A2, A4, D2** and **D4**) display shift to the near-infrared region; being able to absorb in an extended region of the total solar absorption spectrum.

Compound	Abs	λmax (nm)	Absorption region (nm)
A1	0.49	467	274-517
A2	0.48	504	403-572
A3	0.55	497	282-527
A4	0.46	527	395-567
D1	0.55	464	244-504
D2	0.53	587	377-653
D3	0.40	486	281-553
D4	0.50	512	383-650

Table 5.3: Absorbance values for compounds A1-A4 and D1-D4 in the solid state.

From these measurements it is possible to calculate the energy separation, hence, the gap between the HOMO and LUMO. These calculations are performed by the analysis of the tail of the absorption curve corresponding to the first transition (the less energetic). Thus, two tangent lines are drawn; one line for the curve and another parallel to the baseline. The crossing point corresponds to the

λ_{onset} (Figure 5.16). Then, by the use of Planck-Einstein equation 1 it is possible to obtain the E_g^{op} value:

$$E_g^{op} = h\upsilon = \frac{hc}{\lambda} = \frac{1240}{\lambda_{onset}} \qquad (1)$$

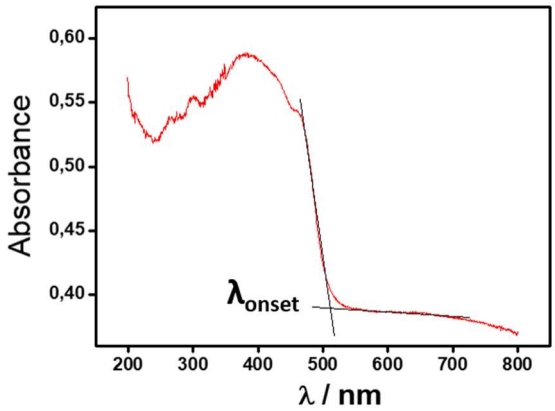

Figure 5.86: UV-Vis spectrum showing the calculation of the λ_{onset} for A2 in the solid state using a matrix of KBr.

The results are shown in Table 5.4, and the spectra in Annex 5.2.

	A1	A2	A3	A4	D1	D2	D3	D4
λ_{onset} / nm	508	662	530	643	509	561	524	572
E_g^{op} / eV	2.43	1.87	2.33	1.92	2.43	2.21	2.36	2.16

Table 5.4: λ_{onset} values and calculated optical gaps for A1-A4 and D1-D4, respectively.

Summarizing the information, boron CCMoids, acceptors and donor (**A2, A4, D2** and **D4**), show the smallest gap values, agreeing well with those found in the UV-Vis spectra in solution. This confirms the idea of the increase of the electronic delocalization by the coordination of BF_2 groups.

On the other hand, as it happens in the case of UV-Vis measurements in solution, the presence of the ester group in the central position has no dramatic influence in the values of the gaps (although in all the cases there is a decrease of the energy gap) being similar to the ones observed for the free CCMoids without an ester leg (for example, **A1** and **A3** displayed values of 2.43 and 2.33, respectively, and **D1** and **D3** of 2.43 and 2.36, in that order). Compering both families, acceptor and donor CCMoids, the energy gap is similar in both, for 1,2,3-benzodiathiazole and fluorene groups.

Electrochemical properties

Cyclic voltammetry (CV) and Differential pulse voltammetry (DPV)

Electrochemical studies were carried out by cyclic voltammetry (CV) and differential pulse voltammetry (DPV) techniques. These measurements allowed the analysis of the redox properties of the CCMoids and the estimation of the HOMO and LUMO energies (as before) providing values for the electrochemical gap E_g^{ec}, that among other things allows the comparison between the donor and acceptor characters of both families, A and D.

The cyclic voltammograms in CH_2Cl_2 corresponding to **A1, A2, A3** and **A4** together with those of **D1, D2, D3** and **D4** are shown in the Figures 5.17 and 5.18, respectively. All of them are calculated with respect of the Fc/Fc^+.

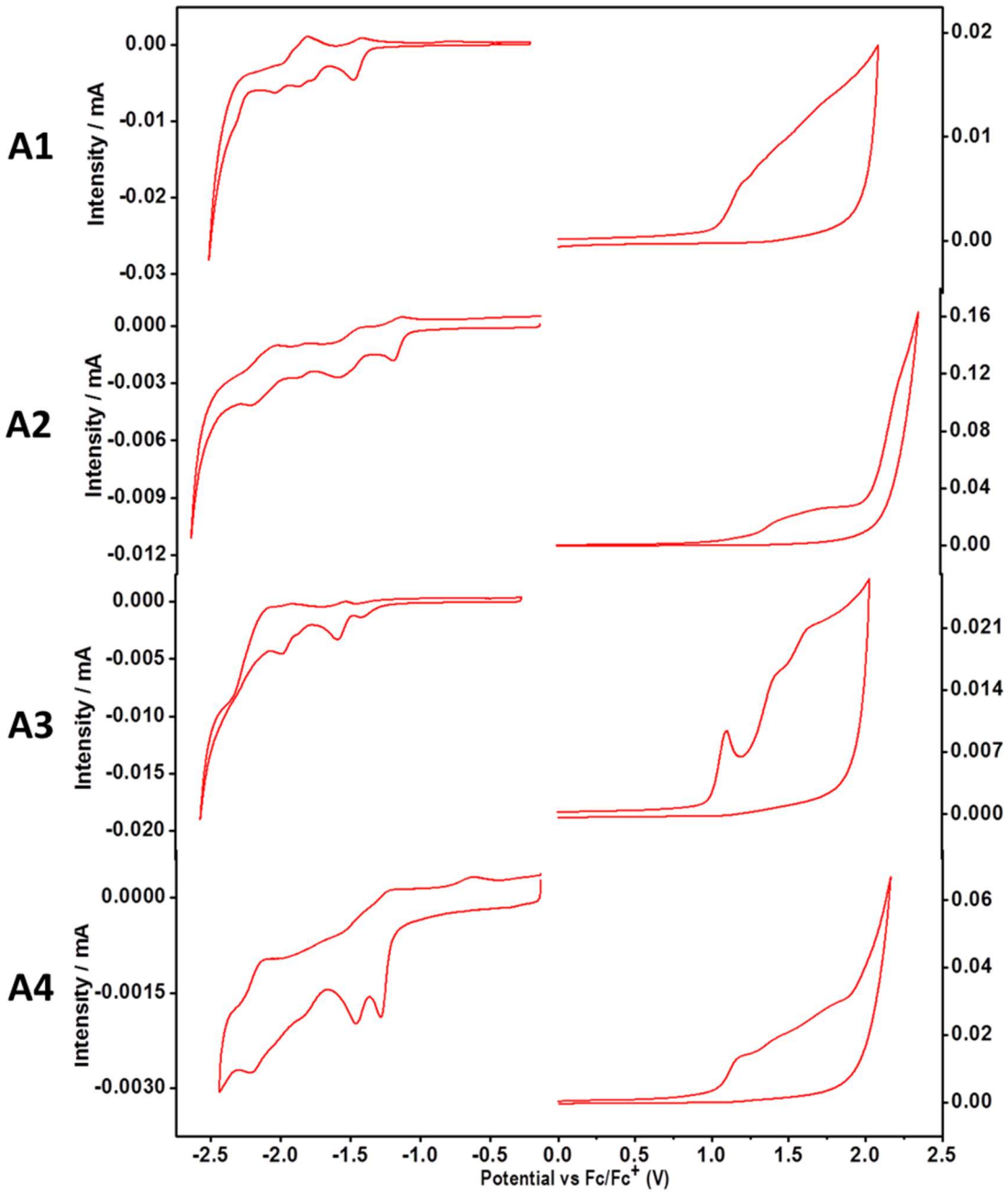

Figure 5.17: Cyclic voltammograms of A1, A2, A3 and A4 vs. Fc/Fc^{+}

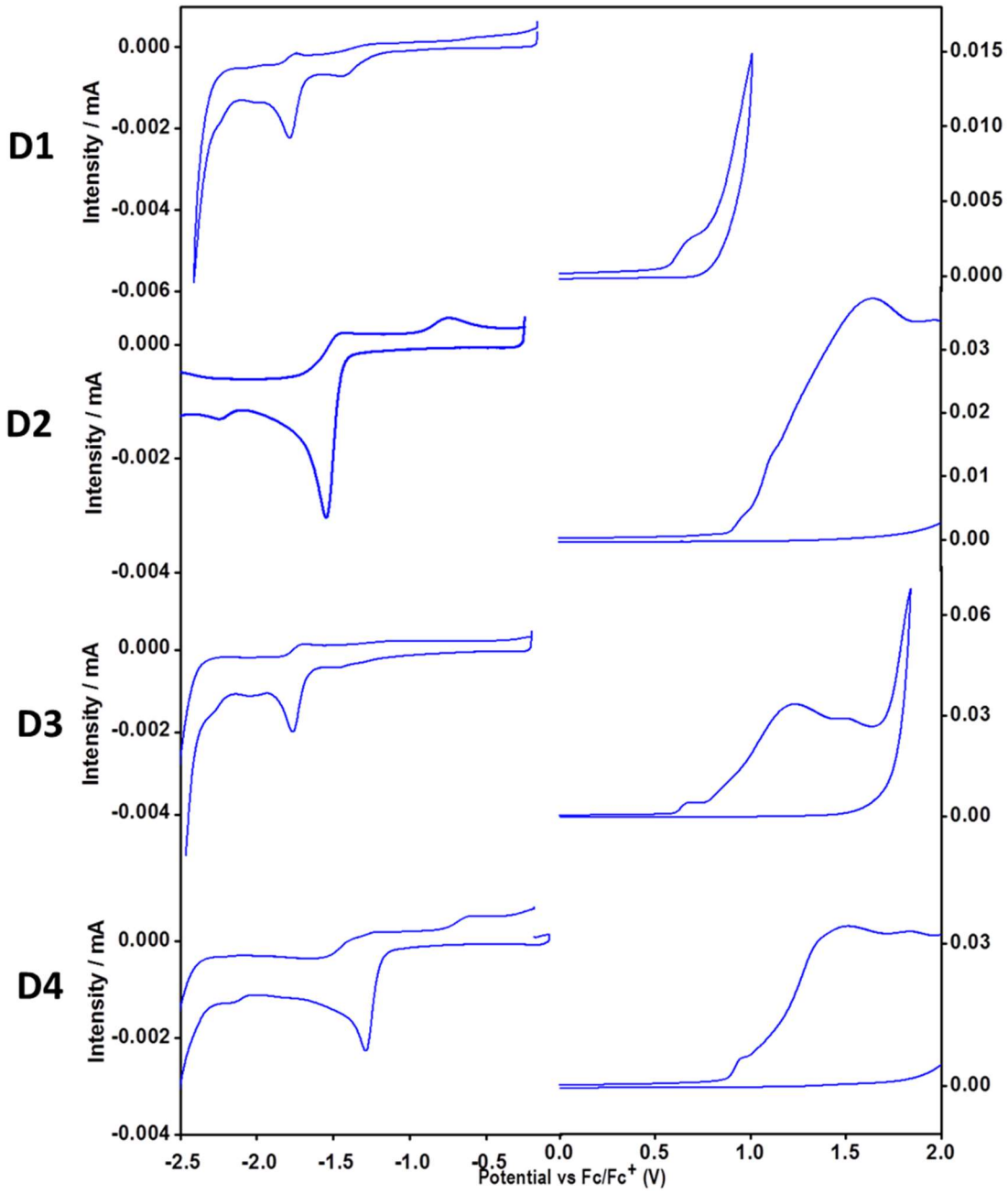

Figure 5.9: Cyclic voltammograms of D1, D2, D3 and D4 vs. Fc/Fc^{+}.

As it can be seen, most of the CCMoids present similar electrochemical features, displaying all irreversible oxidation and reduction processes.[15,32,33] The oxidation part is usually attributed to the terminal aromatic units and, the reduction process is related to the conjugated chain and the β-diketone group. [15,32,33] Thus, modifications performed in the central part of the molecules (as the BF_2 coordination), will have more impact in the reduction process and in contrast, modifications of the aromatic terminal groups will influence more the oxidation part.

The following Table 5.5 summarizes the results obtained from the CV measurements:

	Oxidation			Reduction			
Compound	Ep_a^1 (V)	Ep_a^2 (V)	Ep_a^3 (V)	Ep_c^1 (V)	Ep_c^2 (V)	Ep_c^3 (V)	Ep_c^4 (V)
D1	0.70	-	-	-1.43	-1.78	-	-
D2	0.96	1.64	1.98	-1.24	-1.79	-	-
D3	0.84	1.53	1.89	-1.77	-	-	-
D4	0.94	1.47	1.84	-1.29	-	-	-
A1	1.18	-	-	-1.48	-1.77	-1.86	-2.04
A2	1.33	-	-	-1.23	-1.88	-2.22	-
A3	1.10	1.42	1.62	-1.41	-1.59	-1.99	-
A4	1.16	-	-	-1.29	-1.46	-1.83	-2.19

Table 5.5: Oxidation and reduction peaks obtained by CV

Depending on the chemical substitution at the arms, the number of processes vary. In the case of 1,2,3-benzodiathiazole groups (A), the CV voltammograms shows higher number of reduction peaks compared to the fluorene groups (D). The opposite facts occur in the oxidation region, where now the fluorene groups display more oxidation processes. This fact could be related to the presence of strong electron-withdrawing groups (as the 1,2,3-benzodiathiazole) that may provide anodic shifts giving rise to additional oxidation processes not detected within the electrochemical windows of the distilled CH_2Cl_2. On the other hand, the irreversibility nature of the processes (oxidations and reductions) together with the lack of theoretical calculations that would add information on the final energy diagrams, allow us plausible explanation regarding the origin of the processes.

In addition, DPV measurements were performed since this technique provides high sensibility allowing a better analysis of the redox processes. The determination of the HOMO and LUMO energy has been accomplished using this technique analyzing the first oxidation potential, which corresponds to the ionization potential (IP; removal of one electron from the highest occupied

molecular orbital, HOMO) and reduction potential related to the electronic affinity (EA; addition of one electron to the lowest unoccupied orbital, LUMO).

The calculated values of these energies were performed by calculating the onset using the DPV voltammograms, therefore by tracing two tangent lines as it was shown for the UV-Vis absorption studies in the solid state. The first oxidation potential corresponds to the $(E_{onset})^{oxid}$ and in a similar way, the first reduction potential to the $(E_{onset})^{red}$.

Then, the values are substituted in the equation (2) and (3) to calculate the energy of the HOMO and LUMO vs. the ferrocene molecule in the vacuum conditions. Such procedure allows us to compare our data with other published:

$$E_{HOMO} = -(\left(E_{onset}\right)^{oxid}) + 4.8\ eV \qquad (2)$$

$$E_{LUMO} = -(\left(E_{onset}\right)^{red}) + 4.8\ eV \qquad (3)$$

The value of 4.8 eV corresponds to the potential of the Fc/Fc^+ couple below the vacuum level[34,35] used as a reference. Finally, the energy gap is calculated by:

$$E_g^{ec} = (E_{LUMO}) - (E_{HOMO})\ eV \qquad (4)$$

The DPV voltammograms in CH_2Cl_2 of compounds **A1, A2, A3** and **A4** with **D1, D2, D3** and **D4** are shown in the Figures 5.19 and 5.20, respectively.

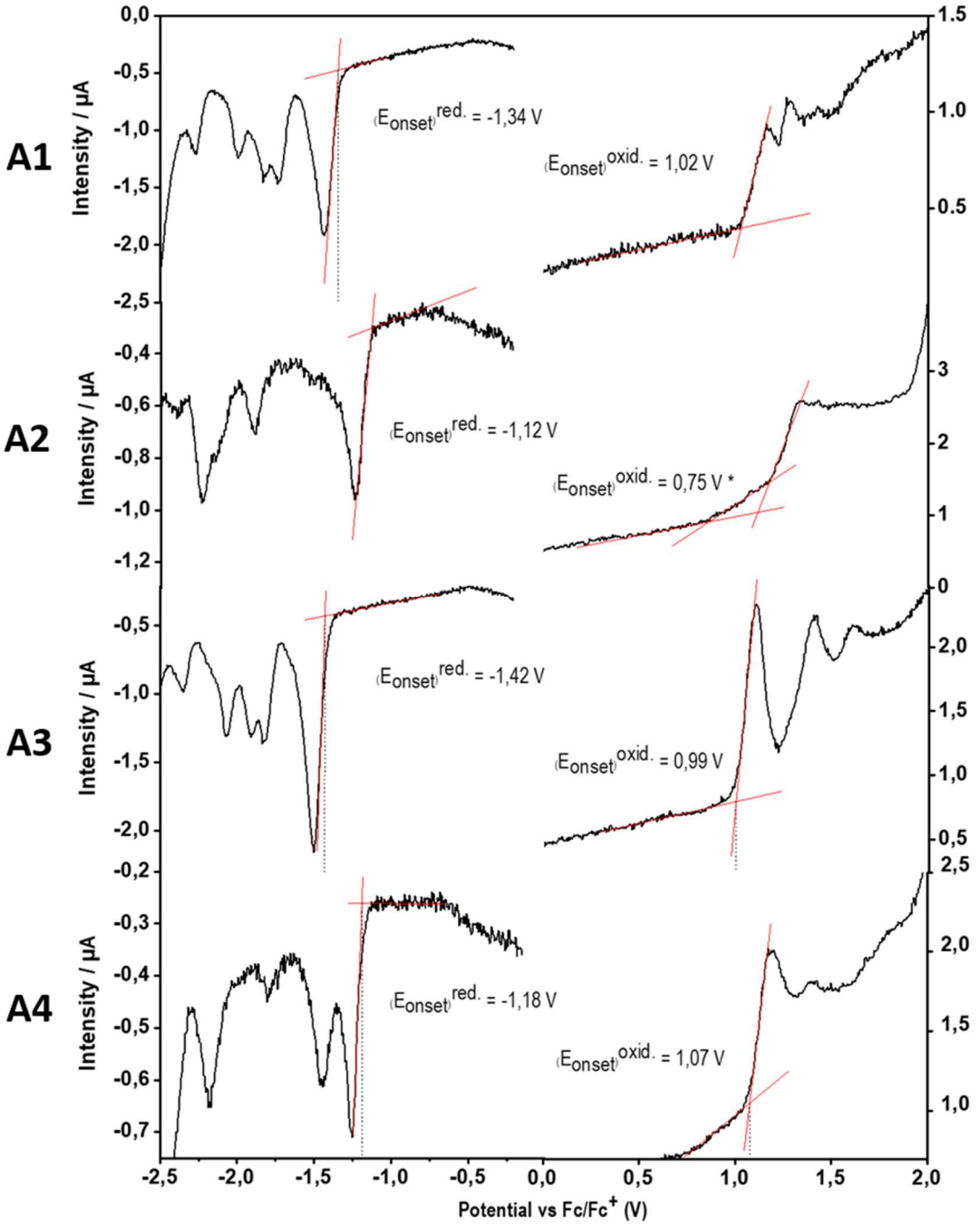

Figure 5.109: Differential Pulse Voltammograms (DPV) of A1, A2, A3 and A4 vs. Fc/Fc^{+}.

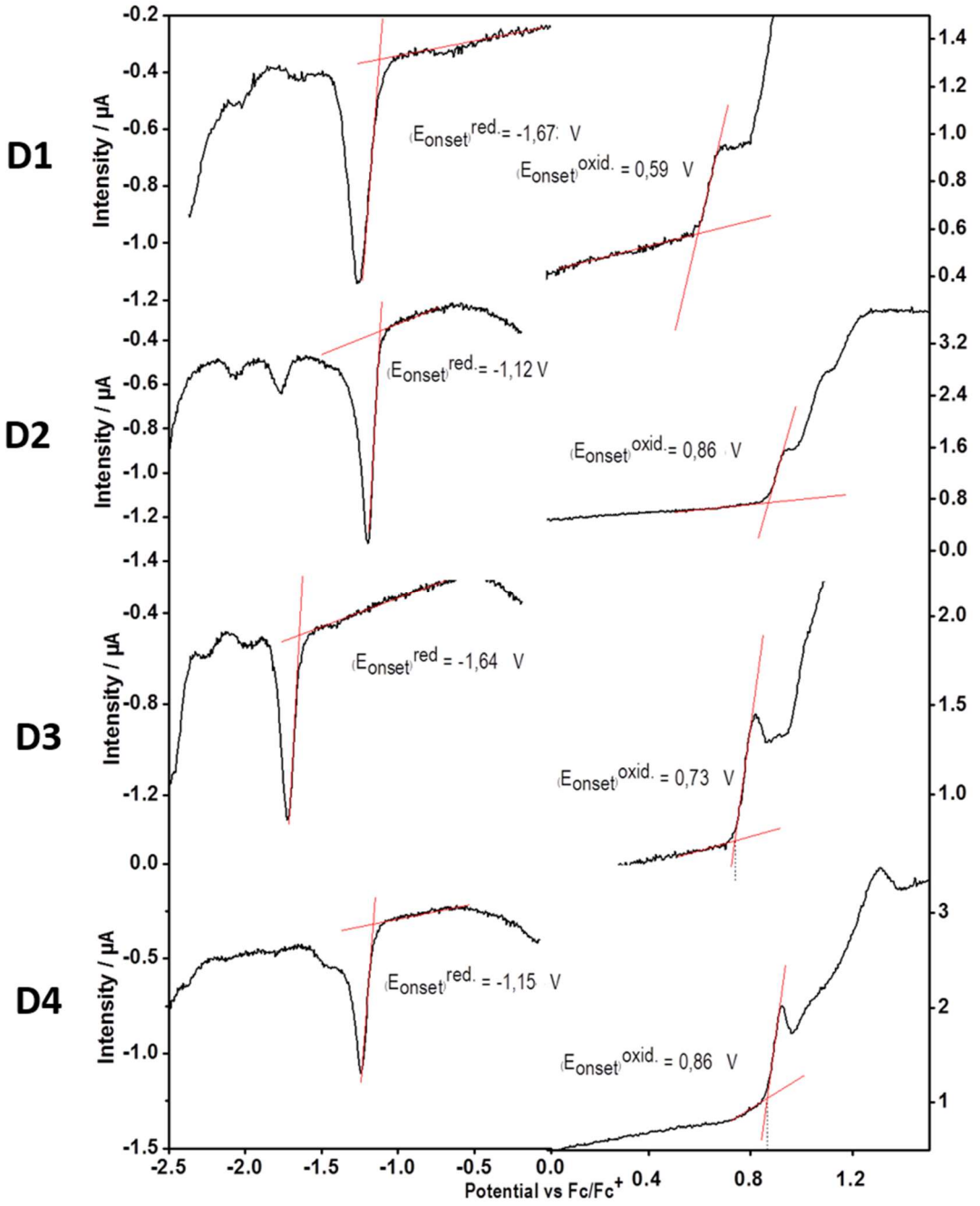

Figure 5.20: Differential Pulse Voltammograms (DPV) of D1, D2, D3 and D4 vs. Fc/Fc^{+}.

Table 5.6 summarizes the results obtained from the DPV measurements for all the CCMoids under study:

Compound	1 st Oxid (V)	1 st Red (V)	E_{HOMO} (eV)	E_{LUMO} (eV)	E_g^{ec}	E_g^{op}
D1	0.59	-1.67	-5.39	-3.13	2.26	2.44
D2	0.87	-1.12	-5.67	-3.68	1.99	1.87
D3	0.74	-1.64	-5.54	-3.16	2.38	2.34
D4	0.87	-1.15	-5.67	-3.65	2.01	1.93
A1	1.02	-1.35	-5.82	-3.45	2.37	2.43
A2	0.75*	-1.13	-5.55*	-3.67	*	1.87
A3	0.99	-1.43	-5.79	-3.37	2.42	2.37
A4	1.08	-1.19	-5.87	-3.61	2.26	2.17

Table 5.6: First oxidation and reduction potentials refereed to Fc/Fc^+. Results of the HOMO and LUMO energy levels and comparison between the electrochemical and optical energy gap are shown.

Among all the samples under study, **A2** was difficult systems to be analyzed and accurate data was not possible. This was due to the existence of two possible oxidation processes, observed by DPV, the first smooth and a second more pronounced. At the moment we do not have further studies that will allow us to discard the first processes, although it is almost negligible, and two possible values can be calculated. UPS experiments should be performed in all the samples to calculate in an accurate way the gap and to assess the sensibility of our methods (UV-Vis absorption in the solid state and DPV).

Regarding the rest of data, analyzing the results obtained it can be observed that the first oxidation voltage values (mostly associated to the aromatic terminal groups) of the compounds containing 1,2,3-benzodiathiazole (A) have the tendency of shifting toward high voltages (≈ 1-1.11 V) (are more difficult to oxidize) compared with the fluorene groups (A) (≈ 0.59-0.87 V), in agreement with the electron-withdrawing capacity of the 1,2,3-benzodiathiazole group.

On the other hand, comparing the first reduction process of the free ligand (e.g.: **D1** = -1.67 V) with its coordinated homologue (with the BF_2 groups), it can be observed that the first reduction processes of the boron compounds show a strong shift toward small voltages (e.g.: **D2** = -1.12 V). The electro-withdrawing capacity of the BF_2 group makes it easier to reduce and therefore, the energy of the LUMO decrease. This reduction process may be also associated with the dioxaborine ring, which helps the stabilization of the radical anion.[36,37]

As it was observed already in the UV-Visible, the presence of the ester group in the *meso* position has a weaker impact on the electrochemical properties of the molecules. Comparing **D1** and **D3** values, it can be seen that both oxidation and reduction signals present similar values.

Finally, comparing the values of the energy gaps obtained from the UV-Vis absorption (E_g^{op}) and the electrochemical (E_g^{ec}) measurements, it can be seen that both display similar values. From these results it can be concluded that the presence of BF_2 group on the compounds has a great influence on the gap values obtained, giving rise to lower values. In contrast, the nature of the terminal group and the functionalization in *meso* position does not play an important role in the electrochemical properties.

Figure 5.21 shows the HOMO-LUMO energy levels of the systems studied by electrochemistry. Also, the same Figure includes two well-known compounds studied with the same techniques and used as acceptor and donor systems: P3HT (donor) and $PC_{61}BM$ (acceptor). This allowed their comparison with the analyzed CCMoid systems concluding that CCMoids are in the range of the values expected for such species and could be good candidates for testing their electronic properties.

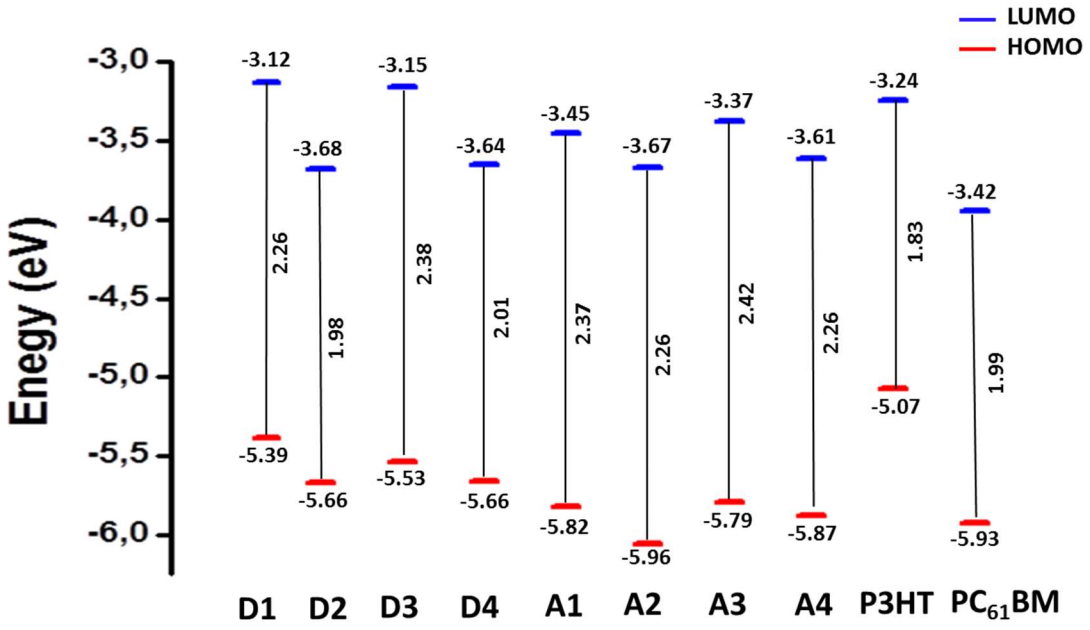

Figure 5.21: Schematic representation of the HOMO and LUMO energetic levels of all the CCMoids and their energy gaps compared with P3HT and $PC_{61}BM$.

From the comparison, it can be observed that **D1** and **D3** display LUMO values similar to those of P3HT (donor), therefore they could act as a donor, meanwhile compounds **D2, D4** and **A4** (that coordinated to boron) present values that agree with acceptor systems, as $PC_{61}BM$.

5.4 Conclusions

In this section, the syntheses of different CCMoids with donor/acceptor properties were carried out. For this purpose, two families of CCMoids were designed using two different aromatic terminal groups: 1,2,3-benzothiadiazole (D) and fluorene (A) groups as a donor/acceptor moieties, respectively. Within each family, two modifications were performed to study the effects on the final optoelectronic properties; the *meso* position of the conjugated chain was functionalized by adding an alkyne chain ended in an ester group and, also the β-diketone groups were coordinated to a BF_2 group.

The synthesis of these compounds, together with the derivatives corresponding to the addition of the ester group was carried out following Pabon's method and, in the case of the BF_2-CCMoids, they were achieved by the use of a microwave reactor (MW). In most of the cases, was possible to obtain crystal structures of the CCMoids by slow evaporation or layering methods.

To study their possible application forming part on the fabrication of the OPVs, different studies were performed:

Firstly, a study of solubility using different organic solvents for all the systems was performed. These experiments determined that DMF and DMSO were promising solvents since they were able of solubilizing large amounts of the CCMoids and both exhibit high boiling points. Furthermore, comparing among the different CCMoids it can be concluded that those presenting ester groups show an increase in their solubility. Among them, **D3** deserves a special mention showing good solubility in DB (dichlorobenzene), being the latest one of the most used solvents in the fabrication of OPVs. However, for the rest of compounds the solubility in this solvent is still far away from the observed for the $PC_{61}BM$ or P3HT.

The optoelectronic properties of these CCMoids were studied by UV-Visible. These studies confirmed the highly conjugated nature of the CCMoids, since they present intense band in the UV-Vis region of π-π* nature. Initially, these studies were carried out in solution for the fluorene family (D). These were considered as preliminary studies since the present of the solvent may influence the absorption spectra. In spite of this, the analysis of the absorption spectra showed that the modification of the ester group gave rises to a bathochromic shift of 20 nm. In relation with the BF_2 compounds, this shift was even more pronounced, showing a shift of 50 nm. This behavior was common in systems containing such group.

The UV-Visible experiments performed in the solid-state by diffuse reflectance a similar tendency. Thus, the presence of the ester groups as well as the variation in the aromatic terminal

donor/acceptor groups not showed significant effects on the optical properties (gap values were similar). On the contrary, the modification performed in the β-diketone group by the coordination with BF_2 groups has a great influence on such properties, showing a large shift on their absorption spectra toward lower energies due to the increase of the electronic delocalization. This fact leads to the stabilization of the LUMO level and therefore, smaller gap values. Moreover, this shift allows covering an extensive area from the near-IR absorption region of the solar spectrum.

In relation to the CV and DPV measurements performed, similar behaviors to previous published CCMoids were observed; obtaining irreversible oxidations (attributed to the terminal aromatic groups) and reductions (attributed to conjugated chain and β-diketone) processes. In relation to the different aromatic groups, a significant influence can be observed, since the present of the acceptor group 1,2,3-benzodiathiazole results in a shift of the first oxidation peak toward more positive potentials (1-1.1 V) in comparison to fluorene group (0.59-0.87 V), and therefore higher gap values were achieved.

On the other hand, the presence of the BF_2 groups has a great influence in the reduction processes, giving rise to a shift of the first reduction signal toward lower voltage values, facilitating the reduction of the CCMoids and therefore decreasing the energy of the LUMO level. On the contrary, the presence of ester groups leads to low influence on their electrochemical properties, but showing more important role in the solubility properties.

Therefore, the obtaining of small gap values can be carried out by the use of electron-donor group in the terminal position, together with the coordination of BF_2 groups. In addition, the presence of ester group can lead to an increase of the solubility of the systems, without varying the optoelectronic properties.

Finally, in relation to the gap values obtained from the UV-Visible and electrochemistry measurements; both techniques show similar values. However, it is important to highlight that their comparison must be carried out only in a qualitative way since the physical processes in each technique are different.

5.5 Work in progress

In this case, to corroborate the experimental results obtained from the HOMO and LUMO values, it would be necessary to perform UPS experiments of the systems and theoretical calculations of these levels.

5.6 Experimental part

Materials: All the reagents used in the work were used as they were received from the commercial company, without further purification.

Synthesis of D1

The synthesis of **D1** was carried out following Pabon's method. Acetylacetonate (259.8 mg, 2.6 mmol) was added in a bottom flask with boron oxide (129.5 mg, 1.9 mmol) in 4 mL of AcOEt. The mixture was heated at 40 ˚C for 2 hours until a white paste was formed. Then, tributylborate (2.4 g, 10.4 mmol) in 2 mL of AcOEt was added to the flask and the mixture was stirred for ten minutes. After that, fluorene-2-carboxaldehyde was added directly to the flask and the mixture was stirred at 50 ˚C for 2 hours. After cooling down, an excess of n-butylamine (0.2 mL, 1.3 mmol) in 1 mL of AcOEt was added dropwise. The mixture was stirring for few days. After that, an orange precipitate was obtained. The mixture was filtered and dried with Et_2O. Then, the solid was added to an Erlenmeyer flask together with 80 mL of H_2O and the mixture was stirred for 8 hours. Finally, a yellow solid was obtained, it was filtered and washed with methanol. The yield was 70 %. Suitable crystals for X-ray diffraction analysis were achieved by slow evaporation in DMF.

IR KBr pellet (ν/cm^{-1}): 3050m, 1907w, 1621s, 1316m, 944m, 733s. ^{1}H-RMN (300 MHz $CDCl_3$, window from 20 to 0 ppm): δ 16.15 (s, 1H), 7.80 (m, 6H), 7.76 (d, J = 15.8 Hz, 2H), 7.60 (d, J = 12.1 Hz, 2H), 7.58 (d, J = 11.8 Hz, 2H), 7.40 (t, J = 7.4 Hz, 2H), 7.35 (t, J = 7.4 Hz, 2H), 6.72 (d, J = 15.8 Hz, 2H), 5.90 (s, 1H), 3.97 (s, 4H). ESI$^+$-MS (CH_2Cl_2): m/z 451.17 $[M+H]^+$.

Synthesis of D2

In a microwave tube, compound **A1** (60 mg, 0.2 mmol), $BF_3 \cdot Et_2O$ (36 µL, 0.2 mmol) and CH_2Cl_2 (4 mL) were added. A color change from yellow to dark red was observed. The mixture was heated by microwave radiation with continuous stirring (600 rpm); the parameters used limited the temperature to 60 ° C, meanwhile microwave energy (15 W) was applied for 5 minutes. After that, a violet precipitated was obtained. The solid was filtered, washed with methanol and dried with Et_2O. The yield was 60 %. Suitable crystals for analysis were achieved by vapor-liquid diffusion (CH_2Cl_2/Et_2O).

IR KBr pellet (ν/cm^{-1}): 3027m, 2360m, 1034m, 731s. Elemental analysis calculated for D2 ($C_{33}H_{23}BF_2O_2 \cdot 1H_2O$): C, 79.22; H, 4.63 and found: C, 76.34; H, 4.84. ^{1}H-RMN (300 MHz DMSO-d_6,

window from 20 to 0 ppm): δ 8.14 (d, J = 15.5 Hz, 2H), 8.06 (s, 2H), 8.02 (d, J = 6.4 Hz, 2H), 7.94 (d, J = 9.1 Hz, 2H), 7.66 (d, J = 6.1 Hz, 2H), 7.43 (t, J = 7.4 Hz, 2H), 7.34 (d, J = 15.7 Hz, 2H), 6.65 (s, 1H), 3.97 (s, 4H). ESI^+-MS (CH_2Cl_2): m/z 499.16 $[M+H]^+$.

Synthesis of D3

D3 was achieved following the same procedure used for **D1**, but using methyl 4-acetyl-5-oxohexanoate (479 mg, 2.6 mmol) instead of acetylacetonate. Finally, an orange precipitate was obtained in a 70 % yield. Suitable crystals were achieved by vapor-liquid diffusion ($CHCl_3/Et_2O$).

IR KBr pellet (v/cm^{-1}): 3049m, 2361m, 1728s, 1603s, 730s. ^{1}H-RMN (300 MHz $CDCl_3$, window from 20 to 0 ppm): δ 17.75 (s, 1H), 7.91 (d, J = 15.4 Hz, 2H), 7.85 (m, 3H), 7.66 (d, J = 8.3 Hz, 2H), 7.61 (d, J = 7.4, 2H), 7.43 (t, J = 7.4 Hz, 2H), 7.37 (t, J = 8.3 Hz, 2H), 7.20 (d, J = 15.4 Hz, 2H), 3.99 (s, 4H), 3.76 (s, 3H), 2.63 (t, J = 2H), 2.23 (t, 2H). ESI^+-MS (CH_2Cl_2): m/z 537.20 $[M+H]^+$.

Synthesis of D4

D4 was synthesized following the methods described for **D2**, but using compound **D3** (60 mg, 0.1 mmol) as a starting material and adding $BF_3 \cdot Et_2O$ (30 µL, 0.1 mmol) and 4 mL of CH_2Cl_2. After the microwave process, a violet precipitate was obtained in a 60 % yield. Suitable crystals were achieved by vapor-liquid diffusion ($CHCl_3/Et_2O$).

IR KBr pellet (v/cm^{-1}): 3052m, 2362m, 1744s, 1020m, 730s. Elemental analysis calculated for D4 ($C_{37}H_{29}BF_2O_4 \cdot 1.7\ H_2O$): C, 75.78; H, 4.98 and found: C, 71.25; H, 4.58. ^{1}H-RMN (300 MHz $CDCl_3$, window from 20 to 0 ppm): δ 8.24 (d, J = 15.1, 2H), 7.88 (m, 3H), 7.73 (d, J = 7.8 Hz, 2H), 7.62 (d, J = 7.4 Hz, 2H), 7.43 (t, J = 8.3 Hz, 2H) 7.42 (t, J = 7.5 Hz, 2H), 7.21 (d, J = 15.2 Hz, 2H), 4.01 (s, 4H), 3.78 (s, 3H), 3.10 (t, 2H), 2.68 (t, 2H). ESI^+-MS (CH_2Cl_2): m/z 585.20 $[M+H]^+$.

Synthesis of A1

A1 was synthesized as **D1**, but using 75.6 mg (1.08 mmol) of B_2O_3, 152.2 mg (1.5 mmol) of acetylacetonate, 1.4 g (6.3 mmol) of tributylborate, 500 mg (3.1 mmol) of 1,2,3-benzothiadiazole-4-carbaldehyde and 78.7 µL (0.8 mmol) of n-butylamine. A dark orange precipitate was obtained as a boron intermediate. Finally, after the hydrolysis, a yellow solid precipitate was obtained in a 20 % yield. Suitable crystals were achieved by slow evaporation in DMF.

IR KBr pellet (ν/cm^{-1}): 3078m, 1624s, 809s. Elemental analysis calculated for A1 ($C_{19}H_{12}N_4O_2S_2$): C, 58.15; H, 3.08; N, 14.28 and found: C, 58.02; H, 2.86; N, 14.16. ^{1}H-RMN (300 MHz $CDCl_3$, window from 20 to 0 ppm): δ 15.79 (s, 1H), 8.07 (d, J = 1 Hz, 1H), 8.05 (d, J = 1 Hz, 1H), 8.03 (d, J = 15.4 Hz, 1H), 7.87 (d, J = 15.8 Hz, 2H), 7.76 (m, 2H), 7.67 (d, J = 15.4 Hz, 1H), 7.66 (d, J = 1.1 Hz, 1H), 6.11 (s, 1H). ESI$^+$-MS (CH_2Cl_2): m/z 391.03 $[M+H]^+$.

Synthesis of A2

A2 was achieved following the same procedure used for compound **D2**, but using 60 mg (0.2 mmol) of compound **A1**, 32 µL (0.2 mmol) of $BF_3 \cdot Et_2O$ and 4 mL of CH_2Cl_2. A color change from yellow to red was observed in the process. After the microwave reaction, a red precipitate was obtained in a 50 % yield. So far, no crystals have been obtained.

IR KBr pellet (ν/cm^{-1}): 3033m, 2363m, 1618s, 1227m, 810s. Elemental analysis calculated for A2 ($C_{19}H_{11}BF_2N_4O_2S_2$): C, 51.84; H, 2.52; N, 12.73 and found: C, 51.6; H, 2.41; N, 12.74. ESI$^+$-MS (CH_2Cl_2): m/z 320.09 $[M+H]^+$.

Synthesis of A3

A3 was achieved by the same procedure used for **A1**, but using 284 mg (1.5 mmol) of methyl 4-acetyl-5-oxohexanoate, instead of acetylacetonate. Finally, an orange precipitate was obtained in a 60 % yield. Suitable crystals were achieved by vapor-liquid diffusion (THF/Et_2O).

IR KBr pellet (ν/cm^{-1}): 3033m, 2364m, 1732s, 1612s, 809s. Elemental analysis calculated for A3 ($C_{23}H_{18}N_4O_4S_2$): C, 57.73; H, 3.79; N, 11.71 and found: C, 57.56; H, 3.82; N, 11.57. ^{1}H-RMN (300 MHz $CDCl_3$, window from 20 to 0 ppm): δ 17.49 (s, 1H), 8.45 (d, J = 15.4 Hz, 4H), 8.10 (d, J = 15.4 Hz, 1H), 8.07 (d, J = 1.4 Hz, 1H), 7.78 (m, 3H), 7.68 (d, J = 15.4 Hz, 1H), 7.67 (d, J = 1.4 Hz, 1H) 3.75 (s, 3H), 3.19 (t, 2H), 2.79 (t, 2H). ESI$^+$-MS (CH_2Cl_2): m/z 477.07 $[M+H]^+$.

Synthesis of A4

A4 was attained using the same method as for **A2**, but using 60 mg (0.1 mmol) of compound **A3**, 32 µL (0.1 mmol) of $BF_3 \cdot Et_2O$ and 4 mL of CH_2Cl_2. A color change from yellow to red was observed. After the microwave process a red precipitate was obtained in a 50 % yield. Suitable crystals were achieved by slow evaporation in DMF.

IR KBr pellet (ν/cm^{-1}): 3036m, 1737s, 1604s, 1024m, 811s. ^{1}H-RMN (300 MHz DMSO-d_6, window from 20 to 0 ppm): δ 8.51(d, J = 15.3 Hz, 2H), 8.46 (m, 2H), 8.30 (d, J = 1.4 Hz, 2H), 7.89 (d, J = 15.4 Hz, 2H), 7.88 (d, J = 1.2 Hz, 2H), 3.59 (s, 3H), 3.18 (t, 2H), 2.74 (t, 2H). ESI^{+}-MS (DMSO): 525.05 $[M+H]^{+}$.

5.7 References

[1] F. Prins, A. Barreiro, J. W. Ruitenberg, J. S. Seldenthuis, N. Aliaga-Alcalde, L. M. K. Vandersypen, H. S. J. Van Der Zant, *Nano Lett.* **2011**, *11*, 4607–4611.

[2] Y. Lin, Y. Li, X. Zhan, *Chem. Soc. Rev.* **2012**, *41*, 4245.

[3] L. Lu, T. Zheng, Q. Wu, A. M. Schneider, D. Zhao, L. Yu, *Chem. Rev.* **2015**, *115*, 12666–12731.

[4] D. Wohrle, D. Meissner, C. Liman, *Adv. Mater.* **1991**, *3*, 36420367.

[5] S. Guenes, H. Neugebauer, N. S. Sariciftci, S. Gunes, *Chem. Rev.* **2007**, *107*, 1324–1338.

[6] W. Zhao, S. Li, H. Yao, S. Zhang, Y. Zhang, B. Yang, J. Hou, *J. Am. Chem. Soc.* **2017**, *139*, 7148–7151.

[7] Y. Cui, H. Yao, B. Gao, Y. Qin, S. Zhang, B. Yang, C. He, B. Xu, J. Hou, *J. Am. Chem. Soc.* **2017**, *139*, 7302–7309.

[8] Z. Xiao, X. Jia, L. Ding, *Sci. Bull.* **2017**, *62*, 1562–1564.

[9] R. Ganesamoorthy, G. Sathiyan, P. Sakthivel, *Sol. Energy Mater. Sol. Cells* **2017**, *161*, 102–148.

[10] Z. Li, K. Jiang, G. Yang, J. Y. L. Lai, T. Ma, J. Zhao, W. Ma, H. Yan, *Nat. Commun.* **2016**, *7*, 1–9.

[11] C. Sun, F. Pan, H. Bin, J. Zhang, L. Xue, B. Qiu, Z. Wei, Z. G. Zhang, Y. Li, *Nat. Commun.* **2018**, *9*, 1–10.

[12] G. Zhang, J. Zhao, P. C. Y. Chow, K. Jiang, J. Zhang, Z. Zhu, J. Zhang, F. Huang, H. Yan, *Chem. Rev.* **2018**, acs.chemrev.7b00535.

[13] F. Archet, D. Yao, S. Chambon, M. Abbas, A. D'Aléo, G. Canard, M. Ponce-Vargas, E. Zaborova, B. Le Guennic, G. Wantz, et al., *ACS Energy Lett.* **2017**, *2*, 1303–1307.

[14] M. Tsuchikawa, A. Takao, T. Funaki, H. Sugihara, K. Ono, *RSC Adv.* **2017**, *7*, 36612–36616.

[15] G. Canard, M. Ponce-Vargas, D. Jacquemin, B. Le Guennic, A. Felouat, M. Rivoal, E. Zaborova, A. D'Aléo, F. Fages, *RSC Adv.* **2017**, *7*, 10132–10142.

[16] M. Grishina, O. Bol'shakov, A. Potemkin, V. Potemkin, *Dye. Pigment.* **2017**, *144*, 80–93.

[17] J. Cameron, M. M. Abed, S. J. Chapman, N. J. Findlay, P. J. Skabara, P. N. Horton, S. J. Coles, *J. Mater. Chem. C* **2018**, *2*, DOI 10.1039/C7TC05075E.

[18] V. N. Viswanathan, A. D. Rao, U. K. Pandey, A. V. Kesavan, P. C. Ramamurthy, *Beilstein J. Org. Chem.* **2017**, *13*, 863–873.

[19] A. Felouat, A. D'Aléo, A. Charaf-Eddin, D. Jacquemin, B. Le Guennic, E. Kim, K. J. Lee, J. H. Woo, J. C. Ribierre, J. W. Wu, et al., *J. Phys. Chem. A* **2015**, *119*, 6283–6295.

[20] G. Bai, C. Yu, C. Cheng, E. Hao, Y. Wei, X. Mu, L. Jiao, *Org. Biomol. Chem.* **2014**, *12*, 1618–1626.

[21] A. Felouat, A. D'Aléo, F. Fages, *J. Org. Chem.* **2013**, *78*, 4446–4455.

[22] A. Chaicham, S. Kulchat, G. Tumcharern, T. Tuntulani, B. Tomapatanaget, *Tetrahedron* **2010**, *66*, 6217–6223.

[23] E. Kim, A. Felouat, E. Zaborova, J.-C. Ribierre, J. W. Wu, S. Senatore, C. Matthews, P.-F. Lenne, C. Baffert, A. Karapetyan, et al., *Org. Biomol. Chem.* **2016**, *14*, 1311–1324.

[24] A. Etcheverry-Berríos, I. Olavarría, M. L. Perrin, R. Díaz-Torres, D. Jullian, I. Ponce, J. H. Zagal, J. Pavez, S. O. Vásquez, H. S. J. van der Zant, et al., *Chem. - A Eur. J.* **2016**, *22*, 12808–12818.

[25] H. J. Pabon, *Recl. Trav. Chim. Pays-Bas* **1964**, 379.

[26] K. Kamada, T. Namikawa, S. Senatore, C. Matthews, P. F. Lenne, O. Maury, C. Andraud, M. Ponce-Vargas, B. Le Guennic, D. Jacquemin, et al., *Chem. - A Eur. J.* **2016**, *22*, 5219–5232.

[27] A. Felouat, A. D'Aléo, F. Fages, *J. Org. Chem.* **2013**, *78*, 4446–4455.

[28] F. MacHui, S. Langner, X. Zhu, S. Abbott, C. J. Brabec, *Sol. Energy Mater. Sol. Cells* **2012**, *100*, 138–146.

[29] C. F. Chignell, P. Bilskj, K. J. Reszka, A. G. Motten, R. H. Sik, T. A. Dahl, *Photochem. Photobiol.* **1994**, *59*, 295–302.

[30] I. Yang, S. M. Jin, J. Kang, V. Ramanathan, H. M. Kim, Y. D. Suh, S. K. Kim, *Bull. Korean Chem. Soc.* **2011**, *32*, 3090–3093.

[31] S. M. Khopde, K. I. Priyadarsini, D. K. Palit, T. Mukherjee, *Photochem. Photobiol.* **2000**, *72*, 625–631.

[32] N. Aliaga-Alcalde, L. Rodríguez, M. Ferbinteanu, P. Höfer, T. Weyhermüller, *Inorg. Chem.* **2012**, *51*, 864–873.

[33] M. Rivoal, E. Zaborova, G. Canard, A. D'Aléo, F. Fages, *New J. Chem.* **2016**, *40*, 1297–1305.

[34] P. I. Djurovich, E. I. Mayo, S. R. Forrest, M. E. Thompson, *Org. Electron. physics, Mater. Appl.* **2009**, *10*, 515–520.

[35] J. Pommerehne, H. Vestweber, W. Guss, R. F. Mahrt, H. Bässler, M. Porsch, J. Daub, *Adv. Mater.* **1995**, *7*, 551–554.

[36] E. Kim, A. Felouat, E. Zaborova, J.-C. Ribierre, J. W. Wu, S. Senatore, C. Matthews, P.-F. Lenne, C. Baffert, A. Karapetyan, et al., *Org. Biomol. Chem.* **2016**, *14*, 1311–1324.

[37] G. Canard, M. Ponce-Vargas, D. Jacquemin, B. Le Guennic, A. Felouat, M. Rivoal, E. Zaborova, A. D'Aléo, F. Fages, *RSC Adv.* **2017**, *7*, 10132–10142.

ANNEX

ANNEX

General Remarks

Annex A.I.1: Pabon's reaction mechanism.

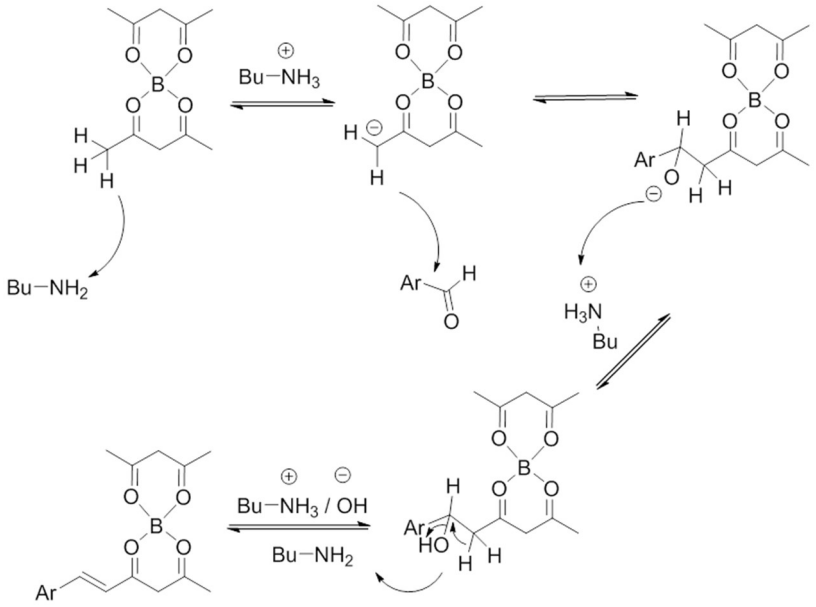

Figure A.I.1: Pabon's reaction mechanism.

Section I: Molecular Magnetism

Annex 1.1: SMM behavior

When an external magnetic field is applied (H≠0), the magnetic moment which is located in the same direction as the external magnetic field, it will stabilize and therefore its level will be populated (levels with Ms = -S stabilize respect to Ms = +S). By removing the external magnetic field (H=0), there is no preference orientation and both states will be degenerates. In this point, the system will tent to relax reaching an equilibrium giving rise to an equal population of its states until reaching M = 0. However, the presence of an energy barrier results in a slow magnetic relaxation.

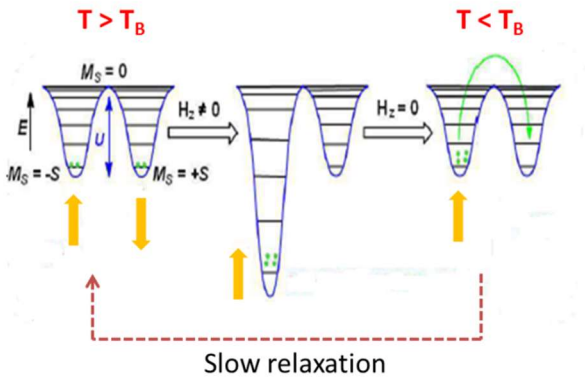

Figure A.1.1: Relaxation of magnetization through active thermally process.

Annex 1.2: Magnetic Relaxation Mechanism

The relaxation of the magnetization can take place by four different processes: three of them are thermally activated classical (i) Direct, (ii) Orbach and (iii) Raman and the other corresponds to a quantum process through the tunnel effect (QTM). (Figure I.3). The equation that governs the relaxation of the magnetic moment for all the molecules with S> ½ is the following, which, as can be seen, presents the four terms corresponding to each mechanism:

$$\tau^{-1} = \tau_{Dir}^{-1} + \tau_{QTM}^{-1} + \tau_{Ram}^{-1} + \tau_{Orb}^{-1}$$

$$\tau^{-1} = AH^4T + \frac{B_1}{1 + B_2H^2} + CT^n + \tau_0^{-1}\, e(-\frac{E_a}{k_BT})$$

Following, each process will be detailed:

(i) Thermal relaxation process (Orbach): is produced through an excited "real" state, due to the interaction with a phonon coming from the vibrations of the network system. This phonon presents enough energy to reach the maximum of the barrier (Ms = 0) and cause its inversion and relaxation by emitting another phonon. This mechanism takes place at high temperatures and follows the Arrhenius law, showing a linear dependence. From this equation the value of the thermal barrier (Ueff) can be calculated.

$$\tau^{-1} = \tau_0^{-1} \exp\left(\frac{-E_a}{kT}\right)$$

(ii) Raman relaxation process: it is similar to the previous one with the difference that in this case the nature of the excited state is virtual. In this process two phonons intervene and generally takes place at intermediate temperatures.

$$\tau^{-1} = CT^n$$

(iii) Direct relaxation process: it takes place directly between the two ground states Ms with different direction. This process is dependent on the magnetic field and takes place at intermediate temperatures.

$$\tau^{-1} = AH^4T$$

(iv) Process through tunnel effect (QTM): This mechanism is carried out due to the mixture of ± MS levels that produces transitions between these resonant levels located on both sides of the barrier, without overcoming the barrier. This mechanism is independent of the temperature, but depends on the applied magnetic field as we will see below:

$$\tau^{-1} = \frac{B_1}{1 + B_2H^2}$$

Annex 1.3: Cole-Cole equations

Cole-Cole Formula

$$\chi''(\chi') = \frac{(\chi_T - \chi_S)}{2\tan\left[\frac{(1+\alpha)\pi}{2}\right]}\left[(\chi' - \chi_S)(\chi_T - \chi') + \frac{(\chi_T - \chi_S)^2}{4tan^2\left[\frac{(1+\alpha)\pi}{\alpha}\right]}\right]^2$$

where, χ_S is the adiabatic susceptibility, χ_T isothermal susceptibility.

Annex 1.4: Mass spectrum of compound 1 and 2.

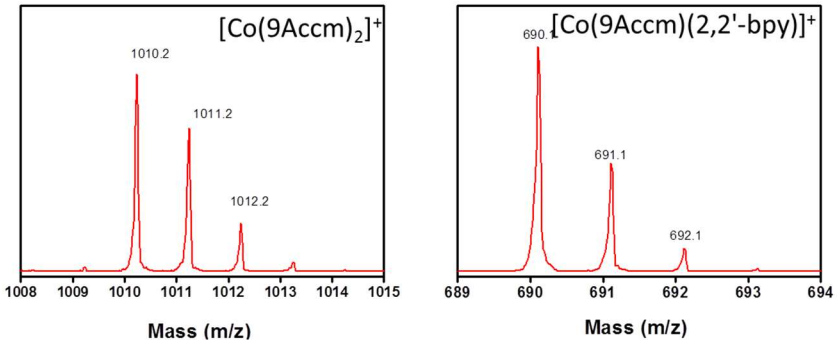

Figure A.1.2: Mass spectra of compound 1 (left) and compound 2 (right).

Annex 1.5: Crystallographic data and refined structure for compounds 1 and 2.

Table A.1.1 Crystallographic data and refined structure for compounds 1 and 2

	Compound (1)	**Compound (2)**
Formula	$C_{80}H_{56}CoN_2O_4$	$C_{80}H_{54}CoN_2O_4,CHCl_3$
M_r	1168.20	1285.55
Crystal system	monoclinic	monoclinic
Space group	P21/c	P21/n
λ (Å)	0.77490	0.77490
a (Å)	11.4437(11)	17.249(3)
b (Å)	8.9623(9)	16.900(3)
c (Å)	29.228(3)	22.440(4)
α (°)	90.00	90.00
β (°)	94.705(2)	108.612(3)
ϒ (°)	90.00	90.00
V (Å^3)	2987.6(5)	6200(2)
T [K]	100(2)	100(2)
Z	2	4
ρ (g/cm^3)	1.229	1.377
Shape and colour	plate yellow	plate orange
Crystal size (mm^3)	0,12x0,05x0,01	0,07x0,04x0,02
Reflections	4277	13457
Parameters	394	820
Restraints	0	0
R_{int}	0.0817	0.1171
R_1 [a]	0.0468	0.0744
wR2 [b]	0.1185	0.1627
S	0.987	0.943

[a] $R_1 = \sum| |F_o| - |F_c| |/\sum|F_o|$, for I>2σ(I). [b] $wR_2 = \{\sum[w(Fo^2 - F_c^2)^2]/\sum[w(F_o^2)^2]\}^{1/2}$, for all data.

Table A.1.2: Selected interatomic distances [Å] and angles for compound 1.

Co1 O1	2.002(2)	**O2 Co1 O2**	180.00(8)
Co1 O1	2.002(2)	**O1 Co1 N1**	90.06(12)
Co1 O2	2.033(2)	**O1 Co1 N1**	89.94(12)
Co1 O2	2.033(2)	**O2 Co1 N1**	88.51(11)
Co1 N1	2.209(4)	**O2 Co1 N1**	91.49(11)
Co1 N1	2.209(4)	**O1 Co1 N1**	89.94(12)
O1 Co1 O1	180.00(11)	**O1 Co1 N1**	90.06(12)
O1 Co1 O2	90.13(9)	**O2 Co1 N1**	91.49(11)
O1 Co1 O2	89.88(9)	**O2 Co1 N1**	88.51(11)
O1 Co1 O2	89.88(9)	**N1 Co1 N1**	180.00(16)
O1 Co1 O2	90.12(9)	**O1 Co1 O2**	90.12(9)

Table A.1.3: Selected interatomic distances [Å] and angles for compound 2.			
Co1 O2	2.012(3)	**O3 Co1 O1**	87.87(10)
Co1 O4	2.065(3)	**O2 Co1 N1**	167.39(12)
Co1 O3	2.069(3)	**O4 Co1 N1**	88.45(12)
Co1 O1	2.071(3)	**O3 Co1 N1**	101.17(12)
Co1 N1	2.109(4)	**O1 Co1 N1**	95.55(12)
Co1 N2	2.115(3)	**O2 Co1 N2**	91.16(12)
O2 Co1 O4	88.95(11)	**O4 Co1 N2**	88.48(11)
O2 Co1 O3	90.97(11)	**O3 Co1 N2**	174.37(11)
O4 Co1 O3	86.35(10)	**O1 Co1 N2**	97.41(11)
O2 Co1 O1	88.22(11)	**N1 Co1 N2**	76.44(14)
O4 Co1 O1	173.52(11)	**O3 Co1 O1**	87.87(10)

Annex 1.6: ^{1}H NMR paramagnetic spectra of compound 3, 4, 5 and 6.

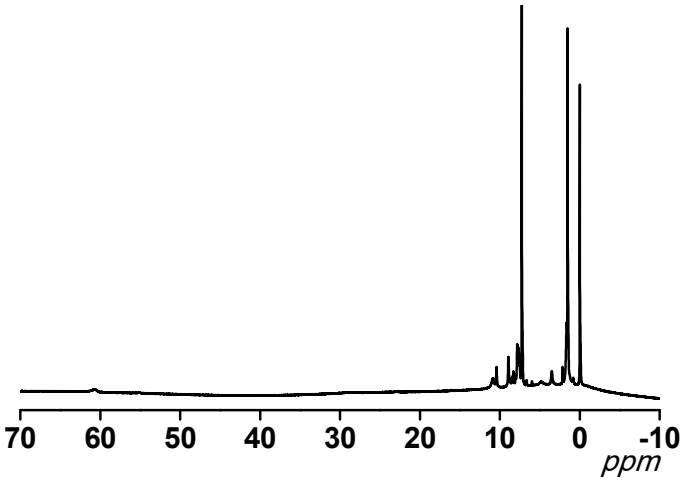

Figure A.1.3: ^{1}H NMR spectrum of compound 3 in $CDCl_3$ between -10-70 ppm.

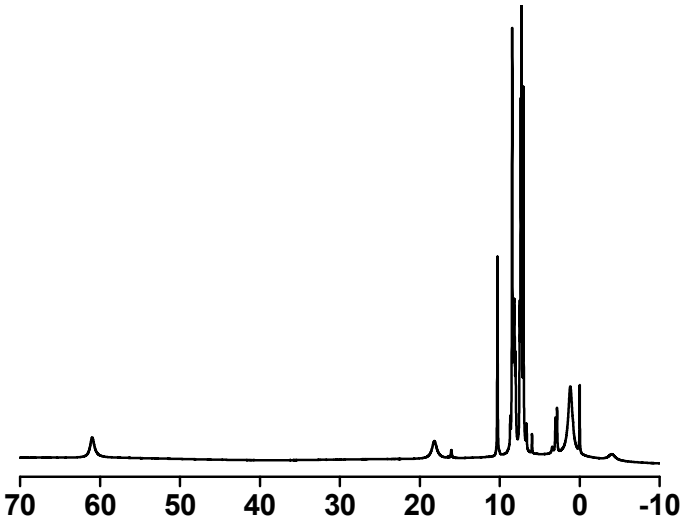

Figure A.1.4: ^{1}H NMR spectrum of compound 4 in $CDCl_3$ between -10-70 ppm.

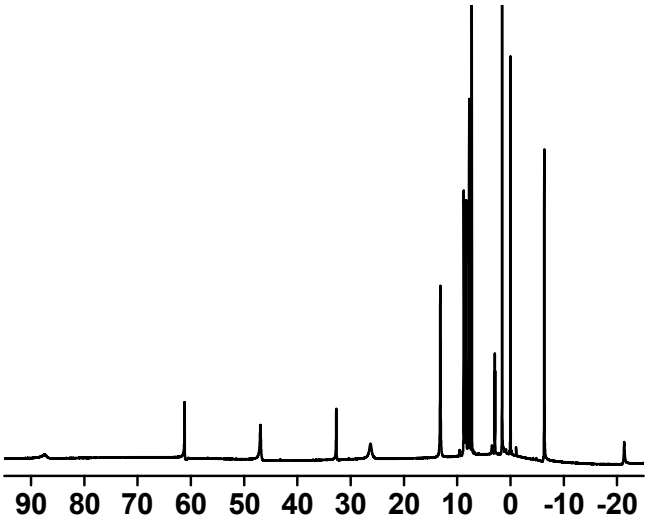

Figure A.1.5: ^{1}H NMR spectrum of compound 5 in $CDCl_3$ between -20-100 ppm.

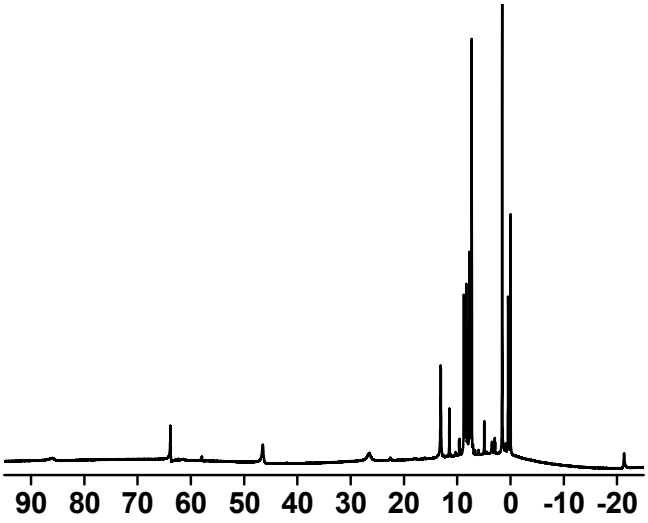

Figure A.1.6: ^{1}H NMR spectra of compound 6 in $CDCl_3$ between -20-100 ppm

Comparison of ^{1}H NMR spectra of the “cis” compounds

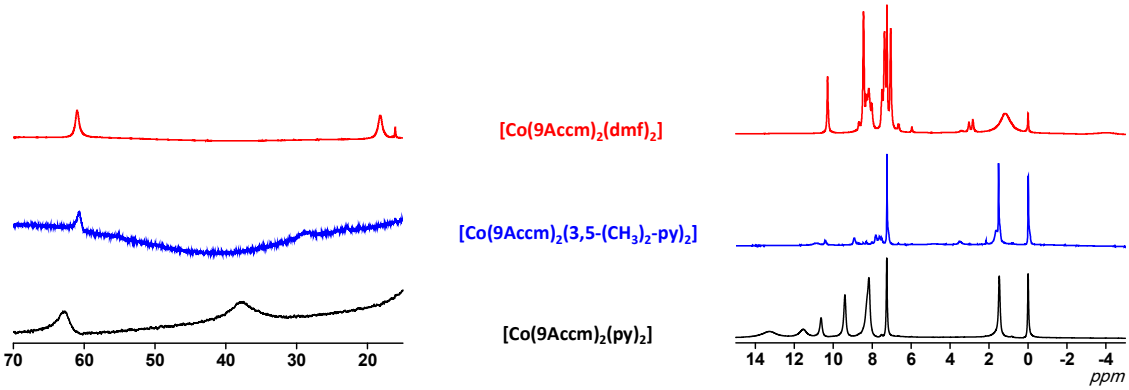

Figure A.1.7: Comparison ^{1}H NMR spectra of trans compounds 1, 3 and 4.

Comparison of ^{1}H NMR spectra of the “trans” compounds

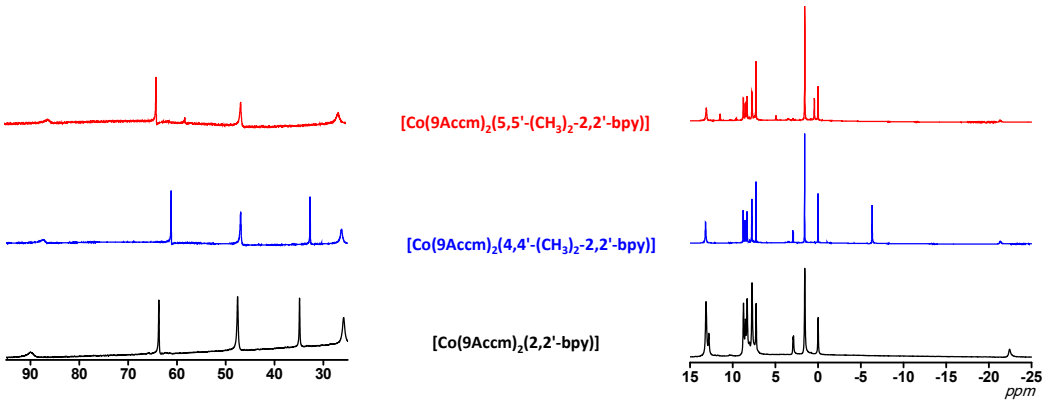

Figure A.1.7: Comparison ^{1}H NMR spectra of cis compounds 2, 5 and 6.

Annex 1.7: ^{1}H NMR paramagnetic shifts

Table A.1.4: RMN ^{1}H chemical shifts of compounds 1, 3 and 4 and similar compounds from the literature.

(1) $Co(9Accm)_2(py)_2$	*(3) $Co(3,5\text{-lutidine})_2(9Accm)_2$*	*(4) $Co(dmf)_2(9Accm)_2$*	*Ref[1]: $Co(acac)_2(py)_2$*	*Ref[2]: $Co(acac)_2$(3-picoline)$_2$*	
63.0	60.6	60.9			***-CH-***
38.0	28.8		58.7	44.7	***ortho-***
		18.2	3.06		**DMF**
13.2				18.9	***meta-***
11.5	10.8		28.5		***para-***
10.6	10.4	10.3			**9Accm**
9.4	8.9				
8.2	8.3	8.5			**9Accm**
7.4	7.6	7.4			**9Accm**
7.2	7.2	7.2			$CDCl_3$
		7.0			
	3.5				**methyl**
		2.8			
1.6	1.6	1.6			H_2O
		-4.0			**DMF**

[1] J. Chinese Chem. Soc, 23, 185-194 (1978)

[2] The Journal of Chemical Physics, 39, 1211 (1963)

Table A.1.5: ^{1}H NMR chemical shifts of compounds 2, 5 and 6 and similar compounds from the literature.

(2) $Co(9Accm)_2(2,2'\text{-bpy})$	*(4) $Co(9Accm)_2(4,4'\text{-}(CH_3)_2\text{-}2,2'\text{-bpy})$*	*(5) $Co(9Accm)_2(5,5'\text{-}(CH_3)_2\text{-}2,2'\text{-bpy})$*	*Ref[1]: $Co(acac)_2(2,2'\text{-bpy})]$*	*Ref[2] $Co(2,2'\text{-bpy})_3Cl_2$*	
89.6	86.3	84.8	74.5	81.0	***ortho-***
63.6	61.3	63.9	62.6	74.5	***meta'-***
47.5	46.9	46.5			**9Accm**
34.9	32.6		24.6	38.5	***meta-***
26.0	26.3	26.5			**9Accm**
13.1	13.1	13.1			**9Accm**
12.8		11.4	4.5	6.08	***para-***
9.5					
8.7	8.7	8.7			**9Accm**
8.5	8.5	8.5			**9Accm**
8.3	8.3	8.3			**9Accm**
7.7	7.7	7.7			**9Accm**
7.2	7.2	7.2			$CDCl_3$
		4.9			**methyl**
2.8	2.8				
1.6	1.6	1.6			H_2O
	-6.3				**methyl**
-22.4	-21.2	-21.2			***-CH-***

[1] J. Chinese Chem. Soc, 23, 185-194 (1978)

[2] Journal of the American Chemical Society, 90:8, April 10, 1968

Annex 1.8: Comparison UV-Vis spectra of complexes 1 and 2 in THF.

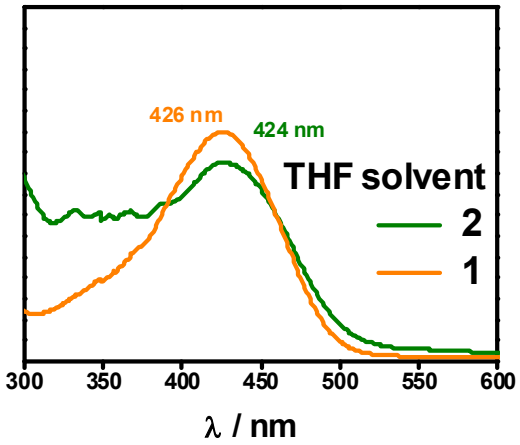

Figure A.1.7: Comparison UV-Vis spectra of complexes 1 and 2 in THF.

Annex 1.9: Comparison emission spectra of compound 1 in THF and CH_2Cl_2.

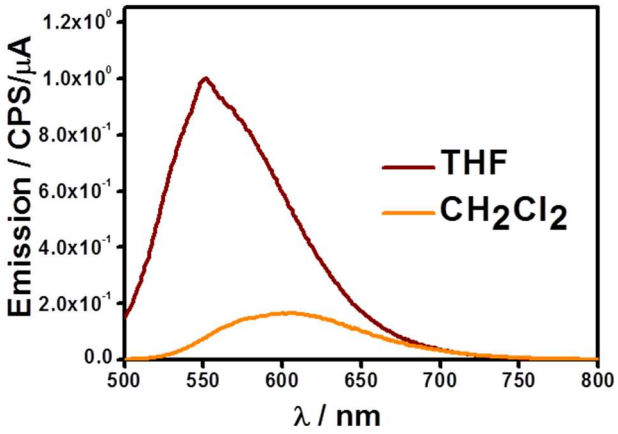

Figure A.1.8: Comparison emission spectra of compound 1 in THF and CH_2Cl_2.

Annex 1.10: Frequency dependence of the χ_{AC}' for compound 1 and 2 under 1500 Oe dc field, respectively.

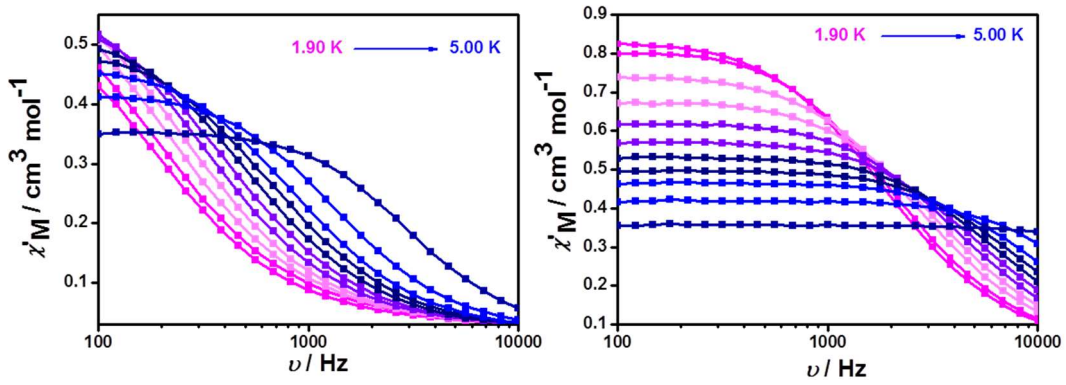

Figure A.1. 9: Frequency dependence of the $\chi_{ac'}$ for compound 1 (left) and compound 2 (right) under 1500 Oe dc field.

Annex 1.11: Value of the fit Cole-Cole obtained for compound 1 and 2

Table A.1.6: Value of τ, Xt, Xs and α obtained for compound 1.

Compound	T	τ	α	Xs	Xt
1	1,9	0,0091	0,18	0,023	0,64
	2	0,0089	0,19	0,023	0,67
	2,25	0,0074	0,18	0,022	0,67
	2,75	0,0060	0,17	0,021	0,65
	3	0,0047	0,15	0,021	0,61
	3,25	0,0037	0,14	0,020	0,57
	3,75	0,0029	0,13	0,020	0,53
	4,2	0,0023	0,12	0,019	0,50
	5	0,0018	0,10	0,020	0,47

Table A.1.7: Value of τ, Xt, Xs and α obtained for compound 2.

Compound	T	τ	α	Xs	Xt
2	1,9	0,83x10-4	0,101	0,048	0,84
	2	0,75x10-4	0,095	0,050	0,81
	2,25	0,58x10-4	0,092	0,052	0,74
	2,75	0,47x10-4	0,084	0,055	0,68
	3	0,38x10-4	0,076	0,057	0,62
	3,25	0,31x10-4	0,066	0,060	0,57
	3,75	0,25x10-4	0,057	0,062	0,53
	4,2	0,20x10-4	0,047	0,065	0,49
	5	0,16x10-4	0,038	0,066	0,46

Annex 1.12: Representation of ln (τ) vs 1/T of the high temperature region and fitted by Arrhenius equation

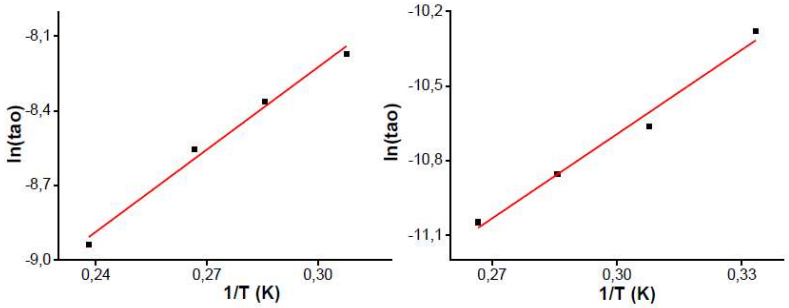

Figure A.1.10: ln(τ) vs 1/T and fit to Arrhenius equation for compound 1 (left) and 2 (right).

Annex 1.13: AFM Images

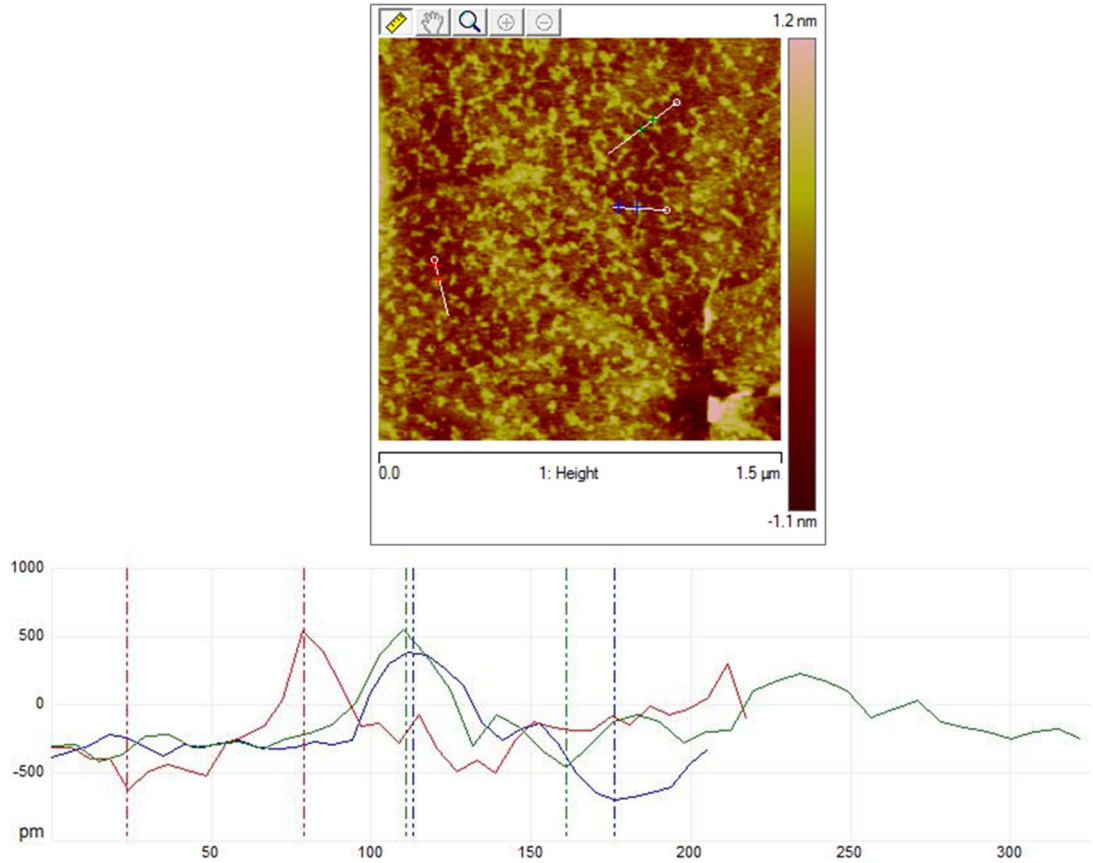

Figure A.1.11: AFM experiments (tapping mode) for compound 1.The measured height values are: Blue (1.1 nm), Red (1.2 nm) and Green (1.0 nm). These values were calculated by the difference between the vertical lines of the same color.

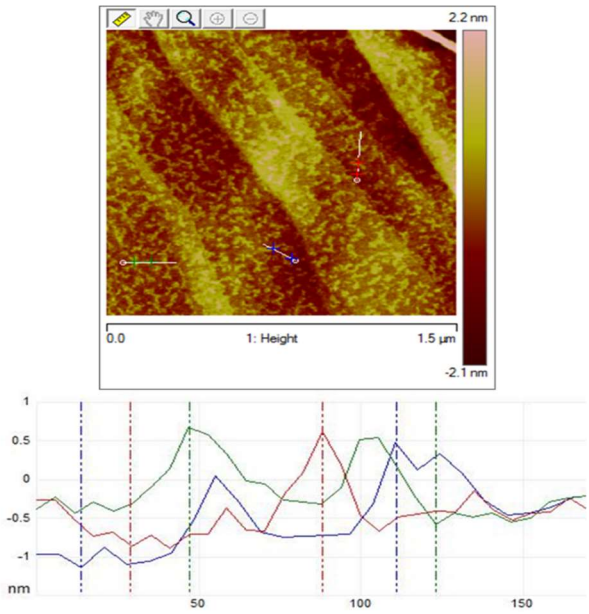

Figure A.1.12: AFM experiments (tapping mode) for compound 2. The measured height values are: Blue (1.6 nm) Red (1.5 nm) and Green (1.2 nm). These values were calculated by the difference between the vertical lines of the same color.

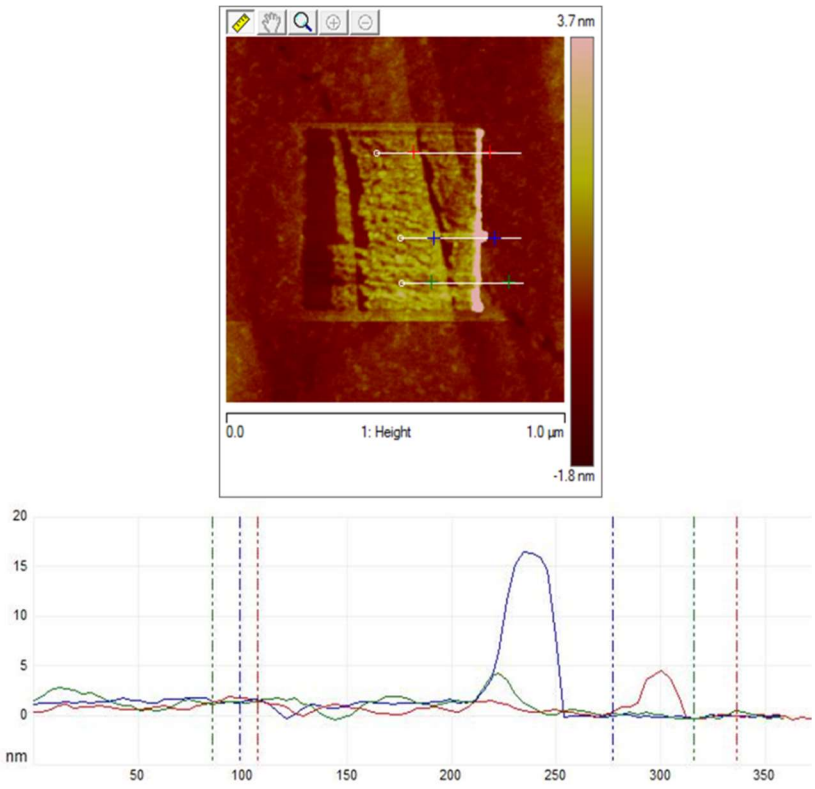

Figure A.1.13: AFM experiments (tapping and contact mode) of compound 2. . The measured height values are: Blue (1.2 nm) Red (1.3 nm) and Green (1.4 nm). These values were calculated by the difference between the vertical lines of the same color.

Annex 1.14: Mass spectra of compound 7, 8, 9, 10 and 11.

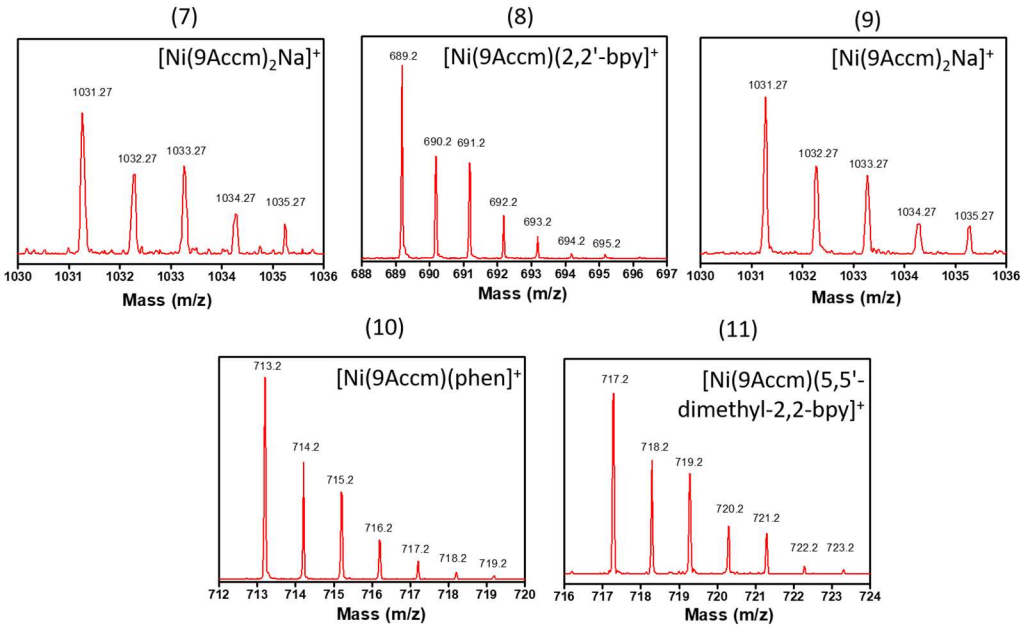

Figure A.1.14: Mass spectra of compound 7, 8, 9, 10 and 11.

Annex 1.15: Crystallographic data and refined structure for compounds 7, 8 and 9.

Table A1.8: Crystallographic data and refined structure for compounds 7, 8 and 9.

	Compound (7)	**Compound (8)**	**Compound (9)**
Formula	$C_{80}H_{56}N_2NiO_4$, 2(C_5 H_5 N)	C_{80} H_{54} N_2 Ni O_4, CH_2Cl_2	$C_{82}H_{60}N_2NiO_4$, 2(CH_2Cl_2)
M_r	1326.18	1250.89	1365.86
Crystal system	Triclinic	Monoclinic	Triclinic
Space group	P-1	P21/n	P -1
λ (Å)	0.71073	1.54178	0.71073
a (Å)	10.3434(6)	17.397(3)	10.4753(7)
b (Å)	11.0419(6)	16.622(3)	10.6803(7)
c (Å)	15.7671(9)	22.603(4)	15.7102(10)
α (°)	72.943(2)	90.00	75.475(3)
β (°)	75.948(2)	109.137(9)	86.586(4)
ϒ (°)	80.426(2)	90.00	75.449(4)
V (Å^3)	1661.24(16)	6175.0(19)	1646.88(19)
T [K]	100(2)	100(2)	101(2)
Z	1	4	1
ρ (g/cm^3)	1.326	1.346	1.380
Shape and colour	orange parallelepiped	yellow prism	orange block
Crystal size (mm^3)	0,29x0,27x0,14	0,11x0,08x0,02	0,19x0,15x0,10
Reflections	53141	69461	27660
Parameters	448	812	431
Restraints	0	0	0
R_{int}	0.0384	0.0984	0.0742
R_1[a]	0.0416	0.0487	0.0720
wR2[b]	0.1096	0.1276	0.2116
S	1.031	0.946	0.1823

Table A.1.9: Selected interatomic distances [Å] and angles for compound 7.

Ni1 O17	2.0093(8)	**O19 Ni1 O19**	180.00(5)
Ni1 O19	2.0382(8)	**O17 Ni1 N41**	90.11(3)
Ni1 O17	2.0094(8)	**O17 Ni1 N41**	89.89(3)
Ni1 O19	2.0382(8)	**O19 Ni1 N41**	91.51(3)
Ni1 N41	2.0872(9)	**O19 Ni1 N41**	88.49(3)
Ni1 N41	2.0872(9)	**O17 Ni1 N41**	89.89(3)
O17 Ni1 O17	180.0	**O17 Ni1 N41**	90.11(3)
O17 Ni1 O19	89.78(3)	**O19 Ni1 N41**	88.49(3)
O17 Ni1 O19	90.22(3)	**O19 Ni1 N41**	91.51(3)
O17 Ni1 O19	90.22(3)	**N41 Ni1 N41**	180.00(16)
O17 Ni1 O19	89.78(3)	**O17 Ni1 O19**	90.12(9)

Table A.1.10: Selected interatomic distances [Å] and angles for compound 8.

Ni1 O57	1.991(2)	**O59 Ni1 O19**	174.87(10)
Ni1 O17	2.039(2)	**O57 Ni1 N81**	90.63(11)
Ni1 O57	2.040(2)	**O17 Ni1 N81**	175.15(10)
Ni1 O17	2.050(2)	**O59 Ni1 N81**	96.82(10)
Ni1 N81	2.061(3)	**O19 Ni1 N81**	87.81(10)
Ni1 N92	2.069(3)	**O17 Ni1 N92**	168.72(11)
O57 Ni1 O17	90.92(9)	**O17 Ni1 N92**	100.33(11)
O57 Ni1 O59	89.58(9)	**O19 Ni1 N92**	90.06(11)
O17 Ni1 O59	87.79(9)	**O19 Ni1 N92**	93.07(10)
O57 Ni1 O19	88.14(9)	**N41 Ni1 N92**	78.23(12)
O17 Ni1 O19	87.65(9)	**O17 Ni1 O19**	90.12(9)

Table A.1.11: Selected interatomic distances [Å] and angles for compound 9.

Ni1 O1	2.0478(19)	**O2A Ni1 N1**	91.36(10)
Ni1 O1	2.0478(19)	**O2A Ni1 N1**	91.36(10)
Ni1 O2A	1.996(2)	**O2A Ni1 N1**	88.64(10)
Ni1 O2A	1.996(2)	**O2A Ni1 N1**	88.64(10)
Ni1 N1	2.107(3)	**O2A Ni1 O1**	90.94(8)
Ni1 N1	2.107(3)	**O2A Ni1 O1**	89.06(8)
O1 Ni1 O1	180.000(1)	**O2A Ni1 O1**	89.06(8)
O1 Ni1 N1	88.02(10)	**O2A Ni1 O1**	90.94(8)
O1 Ni1 N1	91.98(10)	**O17 Ni1 O2A**	180.00(7)
O1 Ni1 N1	91.98(10)		
O1 Ni1 N1	88.02(10)		

Annex 1.16: ^{1}H NMR paramagnetic shifts

Table A.1.12. RMN ^{1}H chemical shifts of compounds 8, 10 and 11 and similar compounds from the literature.

(8) Ni(9Accm)$_2$(2,2'-bpy)	*(10) Ni(9Accm)$_2$(phen)*	*(11) Ni(9Accm)$_2$(5,5'-(CH$_3$)$_2$-2,2'-bpy)*	*Ref^{1}: Ni(acac)$_2$(2,2'-bpy)]*	*Ref Ni(acac)$_2$(phen)*	
-	-	-	-	-	***ortho-***
57,5	-	58	48,6	-	***meta'-***
42,6	40,8	42,3			**9Accm**
39,0	37,3	38,2	31,5	32,6	**9Accm**
38,3	42,9	-			**meta-**
-	22,16	-			**meta'**
13.6	16,1	13,6	5,4	7,25	***para-***
9,0	9,0	9,0			***9Accm***
8,7	8,7	8,7			**9Accm**
8,5	8,5	8,5			**9Accm**
8,3	8,3	8,3			**9Accm**
7,7	7,7	7,7			**9Accm**
7,2	7,2	7,2			$CDCl_3$
-12,4	-12,3	-12,3			***-CH-***

Annex 1.17: ^{1}H NMR paramagnetic spectra of compound 1 and 3 in $CDCl_3$.

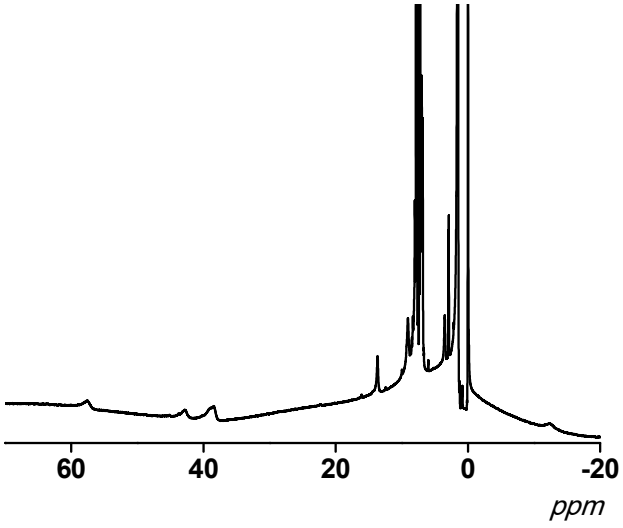

Figure A.1.15: ^{1}H NMR spectra of 7 in $CDCl_3$ between -25 to 60 ppm.

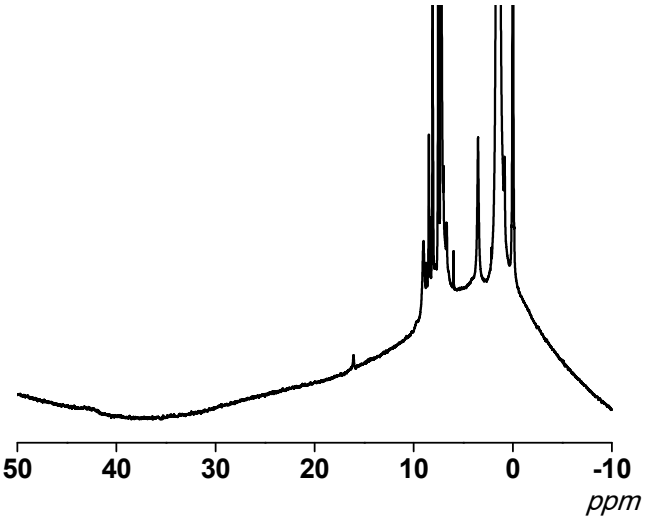

Figure A.1.16: ^{1}H NMR spectra of 9 in $CDCl_3$ between -10 to 50 ppm.

Annex 1.19: Emission spectra of compound 8, 9, 10 and 11 at different concentration 10^{-4} M (red) and 10^{-6} M (blue) in CH_2Cl_2.

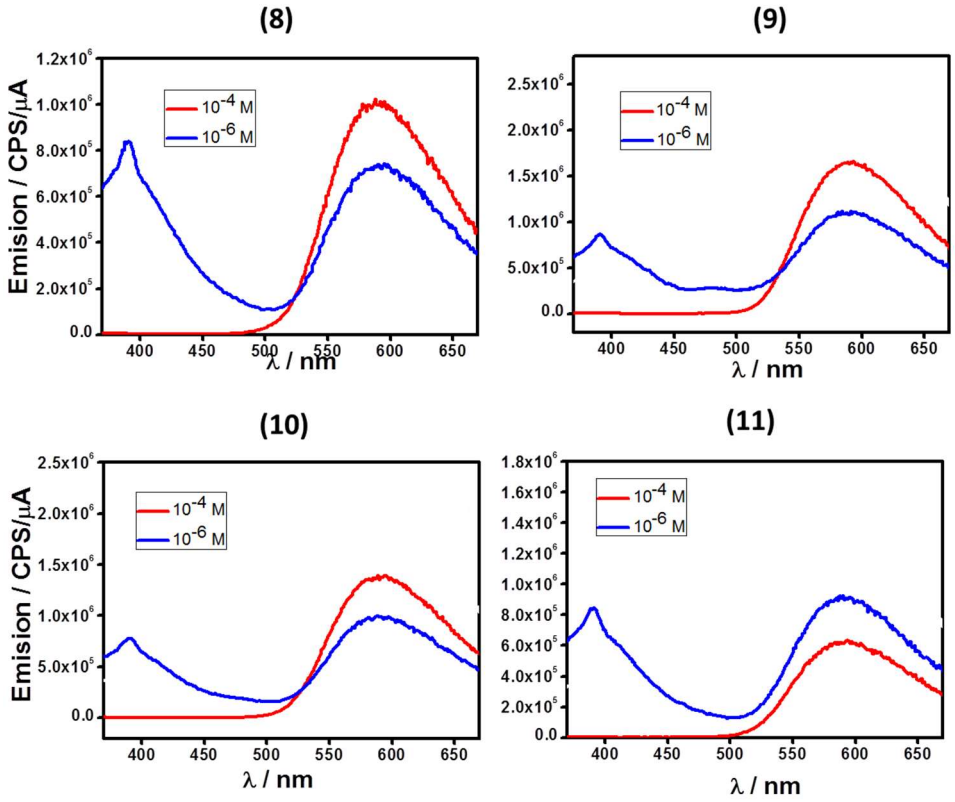

Figure A.1.17: Emission spectra of compound 8, 9, 10 and 11.

Annex 1.20: Mass spectrum of compound 12 and 13.

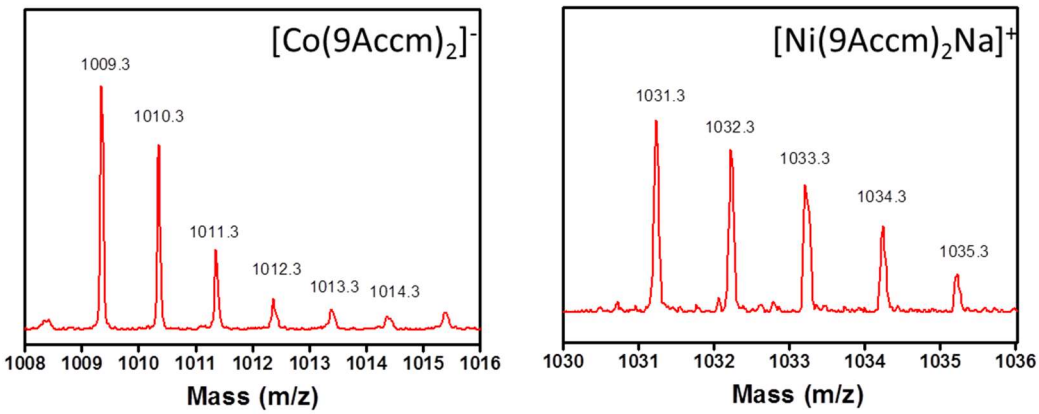

Figure A.1.18: Mass spectra of compound 12 and 13.

Annex 1.21: Crystallographic data and refined structure for compounds 12 and 13.

Table A.1.13: Crystallographic data and refined structure for compounds 12 and 13

	Compound (12)	**Compound (13)**
Formula	$C_{83}H_{57}CoN_3O_5$	$C_{89.60}H_{77.40}NiN_{5.20}O_{7.20}$
M_r	1235.24	1400.86
Crystal system	monoclinic	monoclinic
Space group	C2/c	C2/c
λ (Å)	0.77490	0.71073
a (Å)	24.4070(9)	24.752(4)
b (Å)	11.3374(4)	11.2866(14)
c (Å)	26.9466(11)	26.852(3)
α (°)	90.00	90.00
β (°)	97.873(3)	97.737(14)
ϒ (°)	90.00	90.00
V (Å^3)	7386.2(5)	7433.1(16)
T [K]	100(2)	100(2)
Z	4	4
ρ (g/cm^3)	1.111	1.252
Shape and colour	needle red	block yellow
Crystal size (mm^3)	0.15x0.05x0.01	0.05x0.05x0.05
Reflections	3755	4149
Parameters	477	485
Restraints	253	140
R_{int}	0.0515	0.1758
R_1[a]	0.0640	0.0861
wR2[b]	0.1987	0.2317
S	1.060	0.835

Table A.1.14: Selected interatomic distances [Å] and angles for compound 12 (left) and compound 13 (right).			
Co1 O1	2.030(3)	**Ni1 O2A**	2.001(7)
Co1 O2	2.062(3)	**Ni1 O1**	2.042(7)
Co1 N1	2.137(5)	**Ni1 N2**	2.081(13)
Co1 N2	2.147(5)	**Ni1 N1**	2.131(12)
O1 Co1 O1	176.92(16)	**O2A Ni1 O2A**	176.5(4)
O1 Co1 O2	89.10(13)	**O2A Ni1 O1**	88.4(3)
O1 Co1 O2	90.94(13)	**O2A Ni1 O1**	91.7(3)
O2 Co1 O2	178.58(16)	**O1 Ni1 O1**	179.4(4)
O1 Co1 N1	88.46(8)	**O2A Ni1 N2**	91.8(2)
O2 Co1 N1	90.71(8)	**O1 Ni1 N2**	89.7(2)
O1 Co1 N2	91.54(8)	**O1 Ni1 N1**	90.3(2)
O2 Co1 N2	89.29(8)	**N2 Ni1 N1**	180.0
N1 Co1 N2	180.0		

Annex 1.22: ^{1}H NMR paramagnetic shifts of compound 12 in $CDCl_3$ and compound 13 in C_5D_5N and similar compounds from the literature.

Table A.1.15: RMN ^{1}H chemical shifts of compounds 12 in $CDCl_3$ and compound 2 in C_5D_5N and similar compounds from the literature.

(12) [Co(9Accm)$_2$(4,4'-bpy)]	*(13) [Ni(9Accm)$_2$(py)$_n$(H$_2$O)$_m$]*	*(1) Co(9Accm)$_2$(py)$_2$*	
61.5		63.0	***-CH-***
	45.3		***meta-***
22.2		38.0	***ortho-***
16.1			
10.3		13.2	***meta-***
9.2		11.5	
			para-
	11.1		
8.67	8.7		**9Accm**
8,62	8,5		**9Accm**
8,4			**9Accm**
8,3	8,2	8,2	**9Accm**
8,0	8,0		**9Accm**
7,5	7,5	7,4	**9Accm**
7,3		7,3	$CDCl_3$
7,2	7,2		
6,6			
5,9	4,9		
2,17			
	-11,3		***-CH-***

Annex 1.23: Representation χ_{AC}" vs. ν at different magnetic fields H_{DC} of compound 12

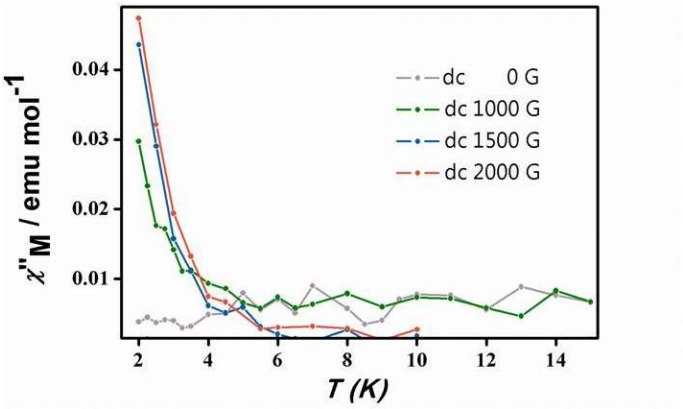

Figure A.1.19: Representation of χ_{AC}'' vs T at different magnetic fields H_{DC} of compound 12.

Annex 1.24: AFM Images

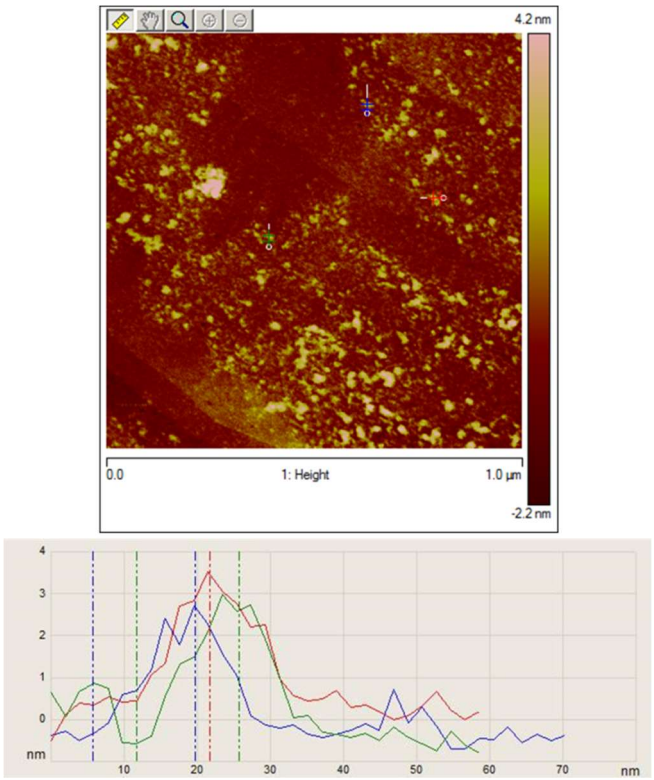

Figure A.1.20: AFM experiment (tapping mode) of compound 12 at 10^{-5} M. The measured height values are: Blue (3.0 nm), Red (3.2 nm) and Green (3.1 nm). These values were calculated by the difference between the vertical lines of the same color.

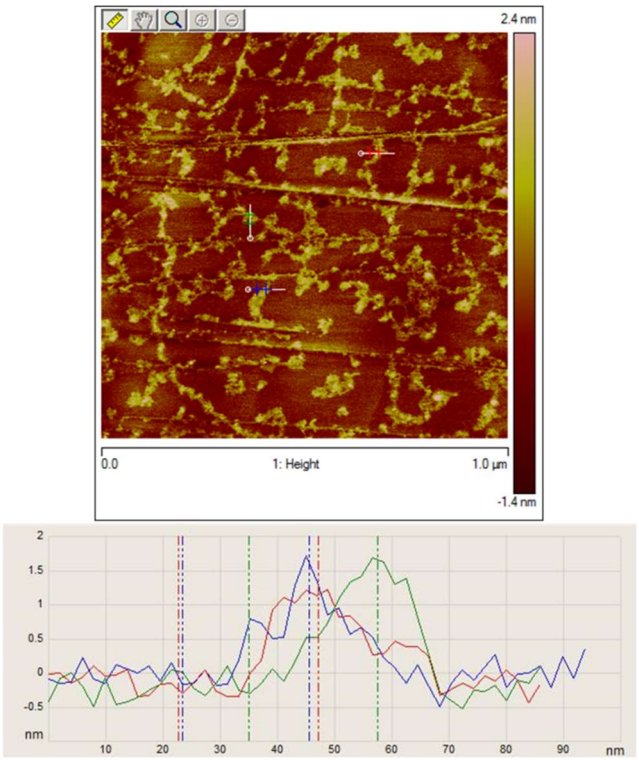

Figure A.1.21: AFM experiment (tapping mode) of compound 12 at 10^{-6} M. The measured height values are: Blue (1.8 nm), Red (1.4 nm) and Green (1.9.1 nm). These values were calculated by the difference between the vertical lines of the same color.

Section II: Molecular Electronics

Annex 2.1: ^{1}H NMR corresponding to the 3-(9-anthryl)acrolein.

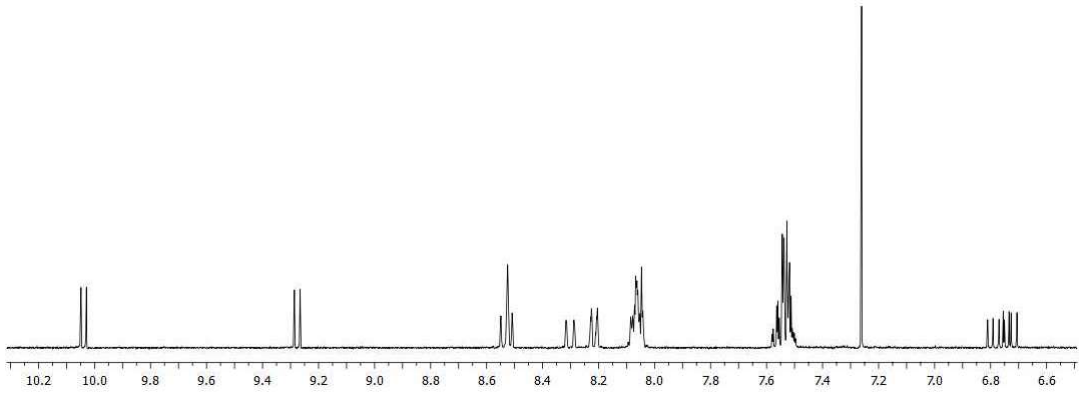

Figure A.2.1: ^{1}H NMR corresponding to the 3-(9-anthryl)acrolein.

Annex 2.1: UV-Visible of 9ALCCMoid in THF at different times.

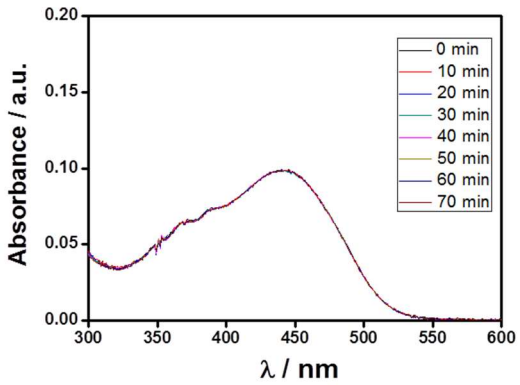

Figure A.2.2: UV-Visible of 9ALCCMoid in THF at different times.

Annex 2.3: Mass spectrum of 9ALCCMoid.

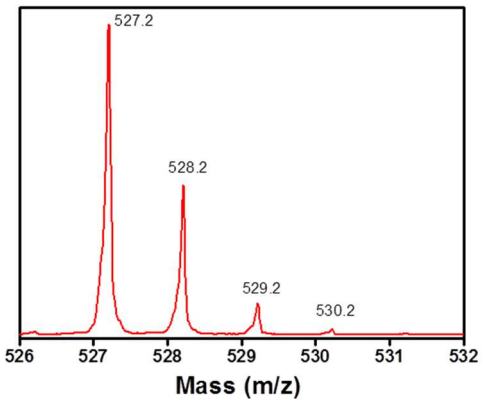

Figure A.2.3: Mass spectrum of 9ALCCMoid.

Annex 2.4: Crystal data and structure refinement for 9ALCCMoid.

Table A.2.1. Crystal data and structure refinement for 9ALCCMoid.

	9ALCCMoid
Formula	$C_{39}H_{28}O_2$
M_r	528.61
Crystal system	monoclinic
Space group	P21/n
λ (Å)	0.77490
a (Å)	15.0392(6)
b (Å)	7.5918(3)
c (Å)	23.3980(9)
α (°)	90.00
β (°)	92.949(3)
ϒ (°)	90.00
V (Å^3)	2667.92(18)
T [K]	100(2)
Z	4
ρ (g/cm^3)	1.316
Shape and colour	needle red
Crystal size (mm^3)	0,12x0,02x0,02
Reflections	3705
Parameters	373
Restraints	0
R_{int}	0.065
R_1 [a]	0.0391
wR2 [b]	0.1003
S	1.025

Annex 2.5: Selected interatomic distances [Å] and angles for 9ALCCMoid.

Table A.2.2: Selected interatomic distances [Å] and angles for 9ALCCMoid.

O1-C2	1.30(2)	**C2-O1-H1**	102.50(10)
O1-H1	1.24(2)	**C22-O2-H1**	101.30(9)
O2-C22	1.29(2)	**C2-C1-C22**	120.57(19)
O2-H1	1.31(2)	**O1-C2-C1**	120.54(18)
C1-C2	1.39(3)	**O1-C2-C3**	117.94(18)
C1-C22	1.39(3)	**C1-C2-C3**	121.48(19)
C2-C3	1.45(3)	**C4-C3-C2**	123.20(19)
C3-C4	1.34(3)	**C3-C4-C5**	125.15(19)
C4-C5	1.43(3)	**C6-C5-C4**	121.88(19)
C6-C7	1.46(3)	**C5-C6-C7**	127.84(19)

Annex 2.6: ORTEP representation of 9ALCCMoid showing the gentle bending of the molecule.

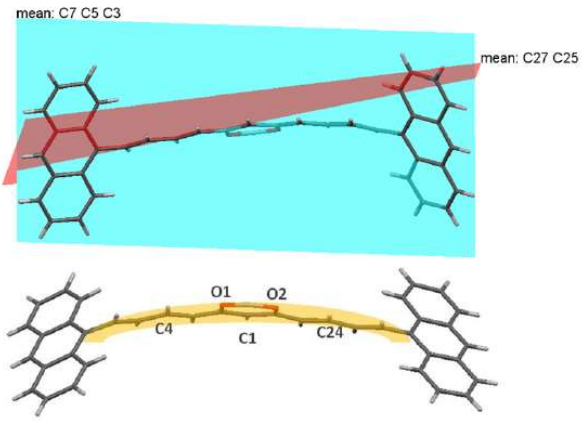

Figure A.2.4: ORTEP representation of 9ALCCMoid showing the gentle bending of the molecule.

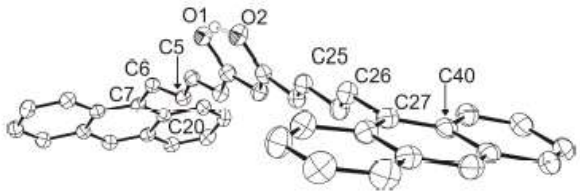

Figure A.2.5: ORTEP representation of 9ALCCMoid. Tilted anthracene groups. Torsion angles were found using C5-C6-C7-C20 (50.47 ˚) and C25-C26-C27-C40 (50.56 ˚).

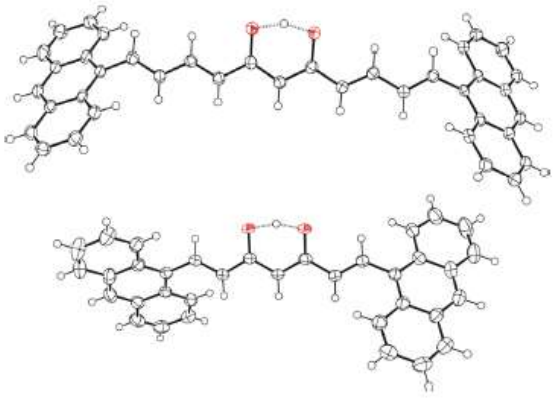

Figure A.2.6: Comparison between the 9ALCCMoid (up) and 9Accm (down) structures. Carbon and hydrogen are in grey and oxygen in red colors.

Annex 2.7: Scheme of graphene layer deposition on the silicon.

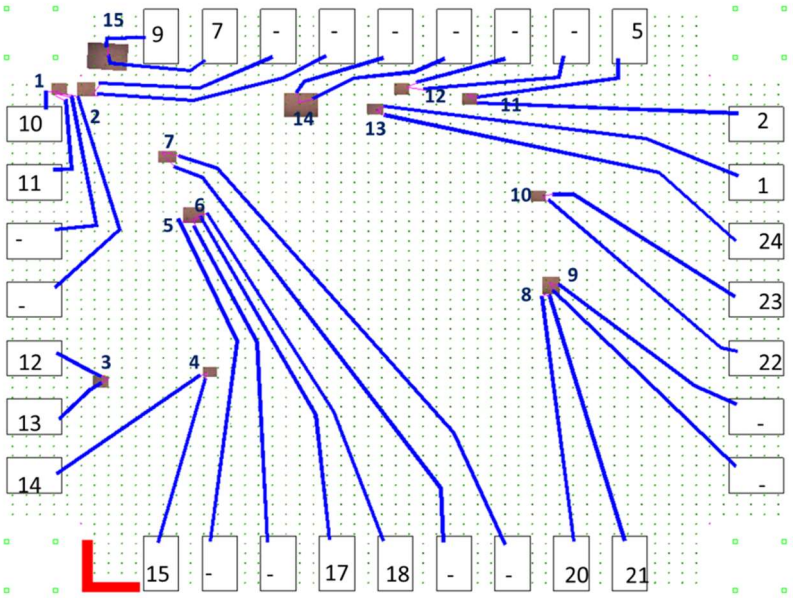

Figure A.2.7: Scheme of graphene layer deposition on the silicon.

Annex 2.8: Gate coupling calculation.

$$\beta = \frac{1}{{}^{1}/_{\alpha_+} + {}^{1}/_{\alpha_-}}$$

Annex 2.9: dI/dV color plot. Green lines marked the inelastic co-tunneling excitations and yellow line vibrational excitons.

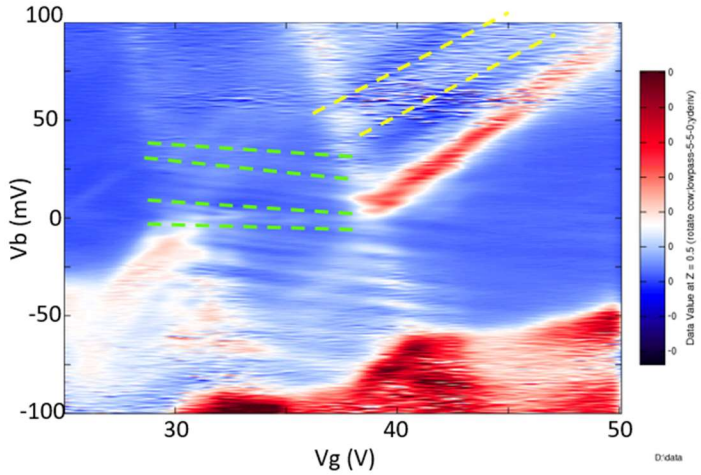

Figure A.2.8: dI/dV color plot. Green lines marked the inelastic co-tunneling excitations and yellow line vibrational excitations.

Annex 2.10: dI/dV-V_{gate} trace measured at V_{bias} = 25 meV.

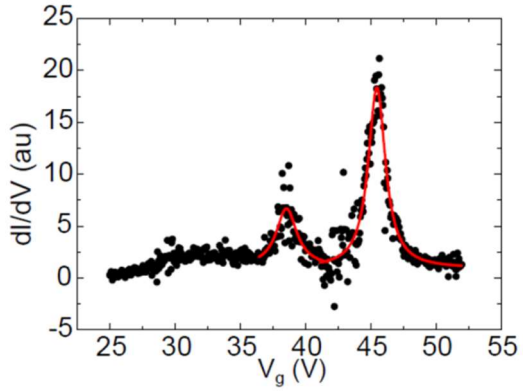

Figure A.2.9: dI/dV-Vg_{ate} trace measured at V_{bias} = 25 meV. The resonance are the edges of the diamond coulomb observed in the Figure A.2.8. The solid red line are Lorentzian fits to the peak. The value of Γ is estimed as β·FWHM.

Section III: Molecular Sensors

Annex 3.1: Mass spectrum of Pyr-acidCCMoid and Pyr-alkyneCCMoid.

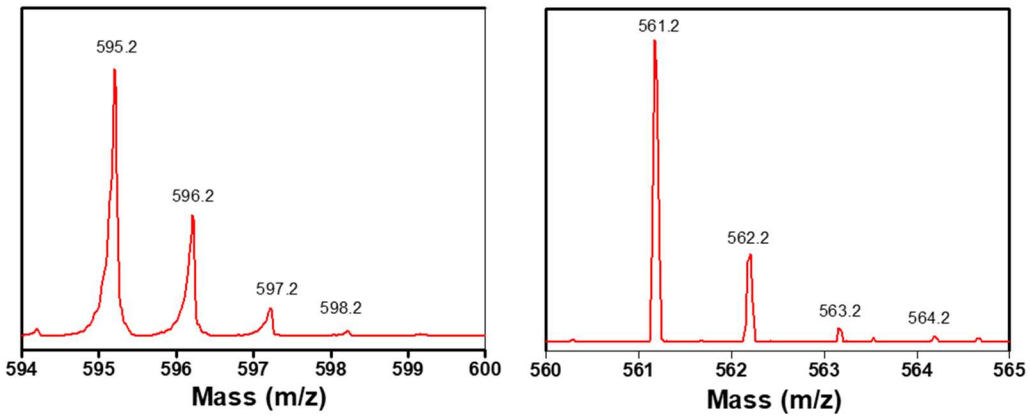

Figure A.3.1: Mass spectrum of Pyr-acidCCMoid (left) and Pyr-alkyneCCMoid (right).

Annex 3.2: Fluorescence microscopy images of Pyr-acidCCMoid with different CDI incubation times

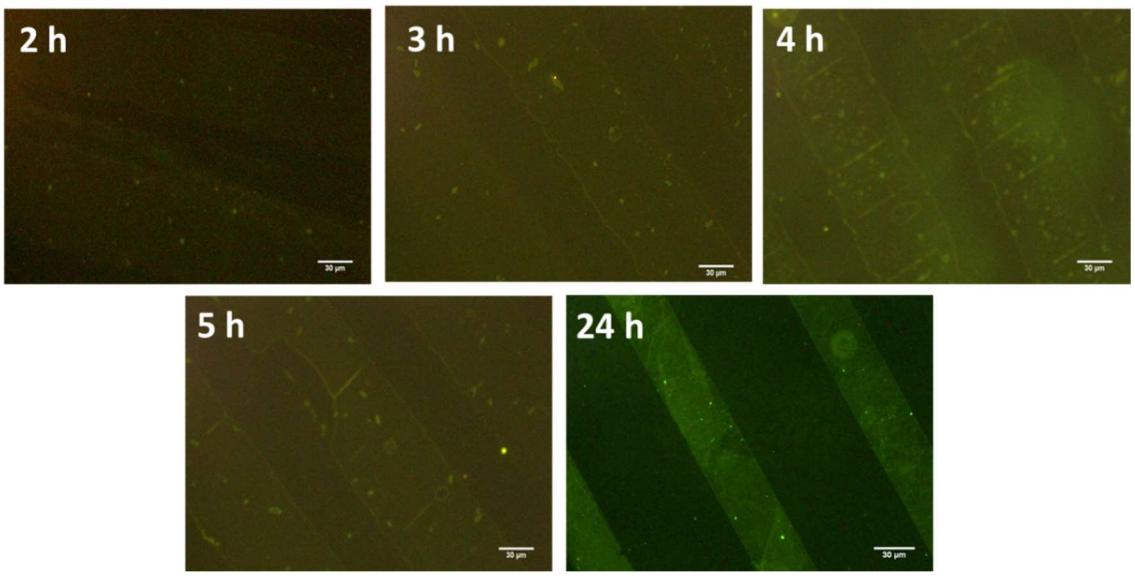

Figure A.3. 2: Fluorescence microscopy images of Pyr-acidCCMoid with different CDI incubation times.

Section IV: Molecular Host-Guest chemistry

Annex 4.1: Mass spectrum of FcCCMoid (left) and Fc9Accm (right).

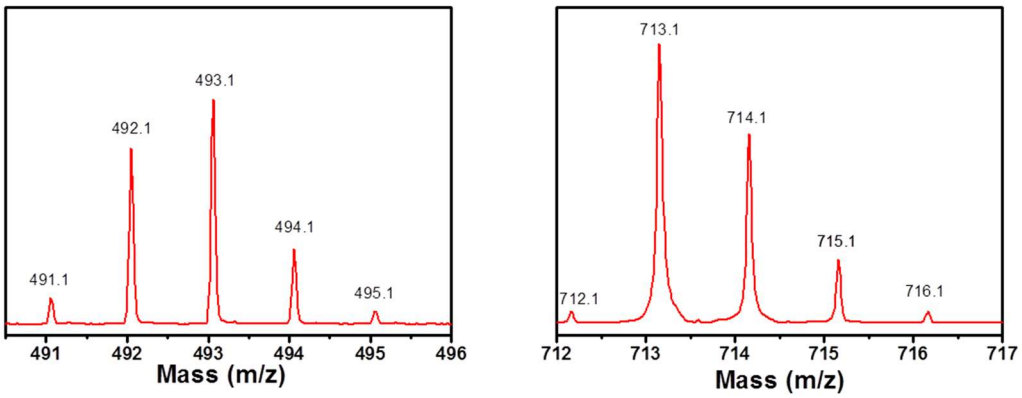

Figure A.4.1: Mass spectrum of FcCCMoid (left) and Fc9Accm (right).

Annex 4.2 ^{1}H NMR spectra of Fc9Accm in THF (up) and 9Accm in $CDCl_3$ (down)

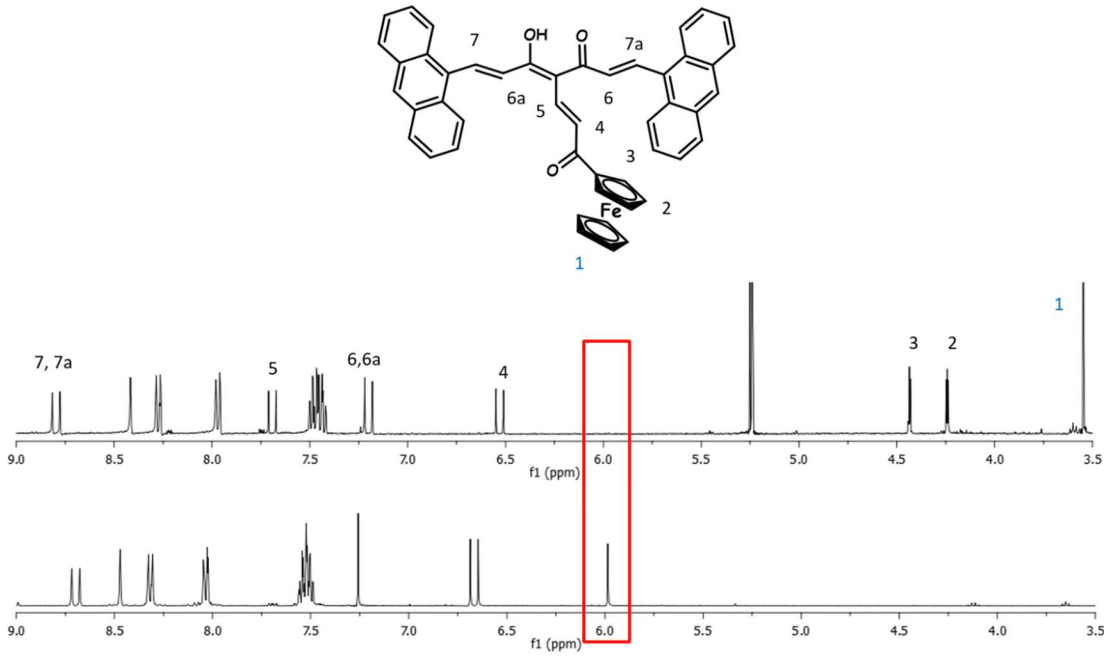

Figure A.4.2: ^{1}H NMR spectrum of Fc9Accm in THF (up) and 9Accm (down) in $CDCl_3$ (down).

Annex 4.3: Crystallographic data and refined structure for compounds FcCCMoid and Fc9Accm.

Table S1.1 Crystallographic data and refined structure for compound FcCCMoid.

	FcCCMoid
Formula	$C_{27}H_{24}Fe_2O_2$
M_r	492.15
Crystal system	monoclinic
Space group	P12/n 1
λ (Å)	0.71073
a (Å)	26.468(6)
b (Å)	5.8068(13)
c (Å)	26.895(6)
α (°)	90.00
β (°)	90.110(3)
ϒ (°)	90.00
V (Å^3)	4133.6(16)
T [K]	101(2)
Z	8
ρ (g/cm^3)	1.578
Shape and colour	plate red
Crystal size (mm^3)	0.25x0.3x0.3
Reflections	7845
Parameters	561
Restraints	0
R_{int}	0.1358
R_1 [a]	0.1239
wR2 [b]	0.1410
S	0.849

[a] $R_1 = \sum| |F_o| - |F_c| |/\sum|F_o|$, for I>2σ(I). [b] $wR_2 = \{\sum[w(Fo^2 - F_c^2)^2]/\sum[w(F_o^2)^2]\}^{1/2}$, for all data.

Annex 4.4: Control CV measurements of FcCCMoid@SAM-CB[7]/Au(111), FcCCMoid/Au(111), Fc9Accm@SAM-CB[7]/Au(111) and Fc9Accm/Au(111) in 0.1 M Na_2SO_4.

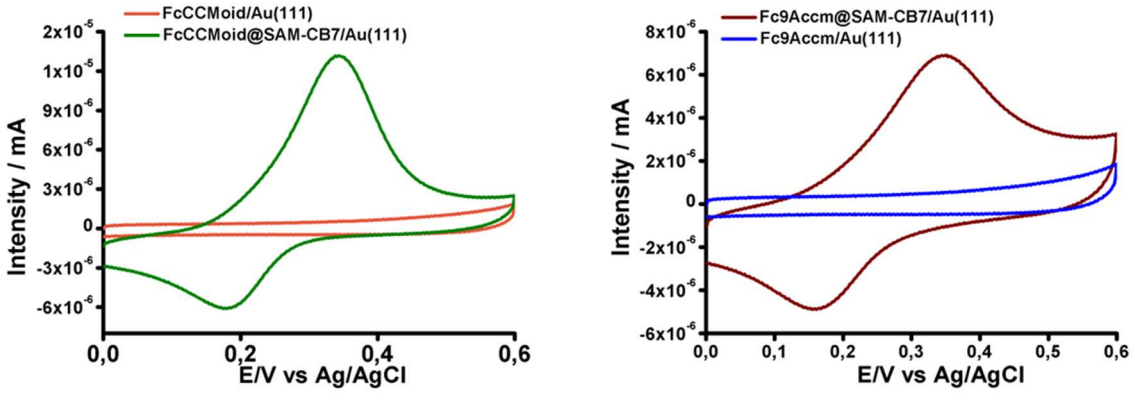

Figure A.4.3: CV measurements of (left) FcCCMoid@SAM-CB7/Au(111) and FcCCMoid/Au(111), (right) Fc9Accm@SAM-CB7/Au(111) and Fc9Accm/Au(111) in 0.1 M Na_2SO_4.

Annex 4.4: ^{1}H NMR spectra of FcCCMoid@CB[7], FcCCMoid, CB[7] and Fc9Accm@CB[7], Fc9Accm, CB[7].

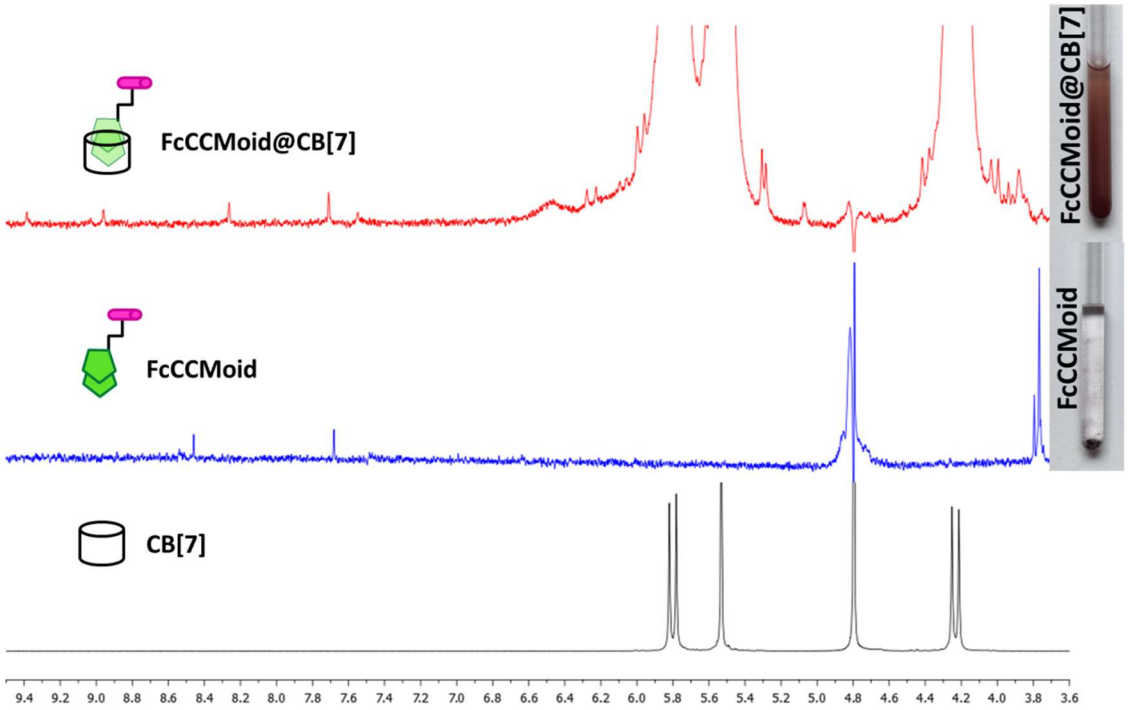

Figure A.4.4: ^{1}H NMR spectra of FcCCMoid@CB[7], FcCCMoid and CB[7] in D_2O.

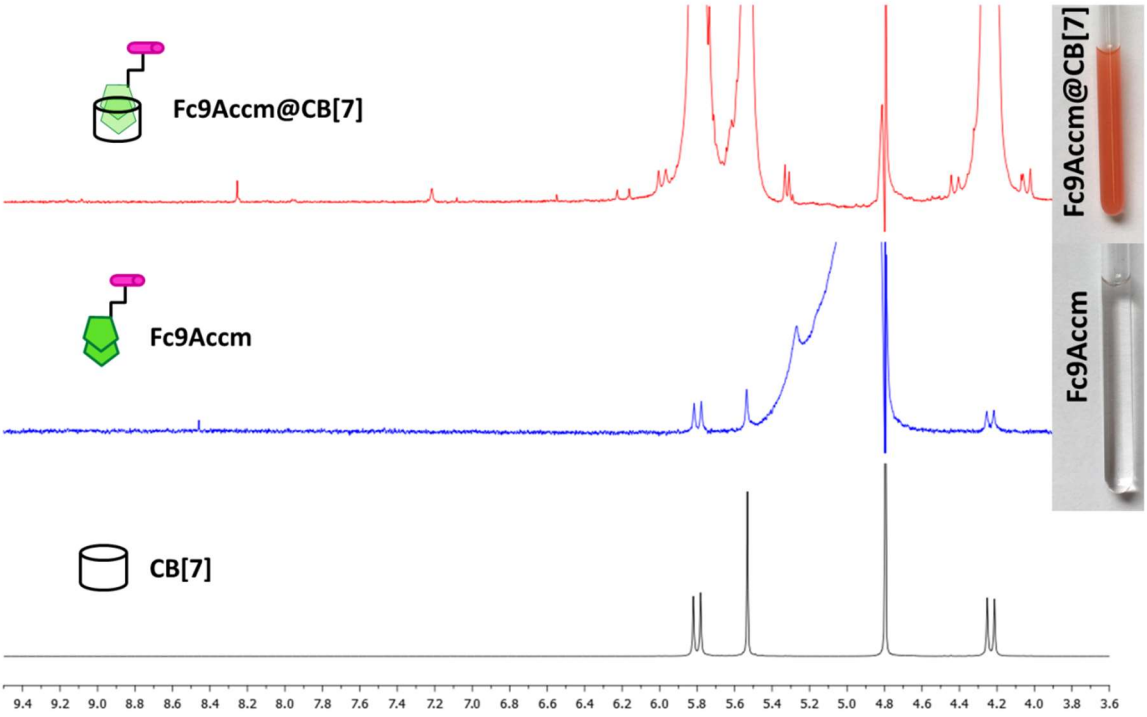

Figure A.4.5: ^{1}H NMR spectra of Fc9Accm@CB[7], Fc9Accm and CB[7] in D_2O

Annex 4.5: Representation of metal coordination with $[M_6L_4]^m$ stoichiometry

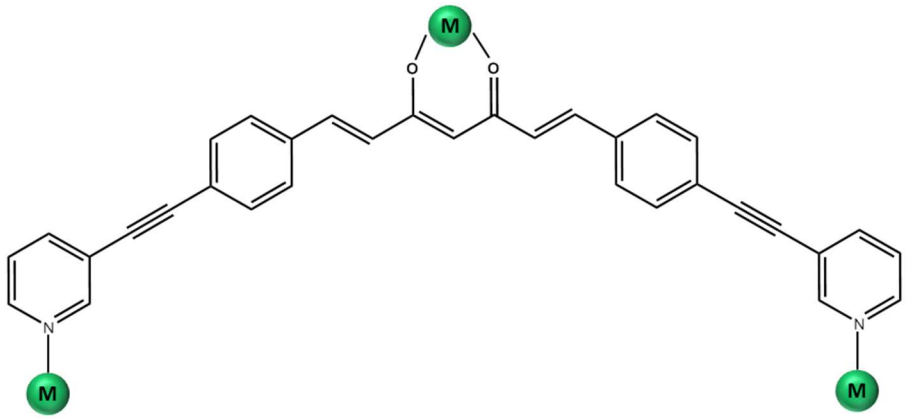

Figure A.4.6: Representation of metal coordination with $[M_6L_4]^m$ stoichiometry.

Section V: Molecular Donor-Acceptor chemistry

Annex 5.1: Crystal data and structure refinement for D1, D2, D3, D4 and A3

Table S1. Crystal data and structure refinement

	D1	D2	D3	D4	A3
Formula	$C_{33}H_{24}O_2$	$C_{33}H_{23}BF_2O_2$	$C_{37}H_{30}O_4$	$C_{75}H_{60}B_2Cl_2F_4O_8$	$C_{23}H_{18}N_4O_4S_2$
M_r	452.52	500.32	538.61	1257.75	478.53
C. System	orthorhombic	monoclinic	monoclinic	monoclinic	monoclinic
Space group	P b c a	C 1 2/c 1	P21/n	C 2/c	P21/n
λ (Å)	0.729	0.7470	0.8266	0.8266	0.86256
a (Å)	15.683 (3)	23.744 (3)	9.868 (2)	33.160 (7)	4.5600 (9)
b (Å)	5.666 (11)	12.834 (17)	29.609 (6)	7.7530 (16)	22.132 (4)
c (Å)	52.16 (10)	7.805 (11)	37.809 (8)	26.971 (5)	21.300 (4)
α (°)	90	90	90	90	90
β (°)	90	91.356 (7)	90.87 (3)	118.95 (3)	90.57 (3)
ϒ (°)	90	90.00	90.00	90	90
V (Å³)	4635.5	2378.1 (6)	11046 (4)	6067 (3)	2149.5 (7)
T [K]	293 (2)	100 (2)	293 (2)	293 (2)	100 (2)
Z	8	4	16	4	4
ρ (g/cm³)	1.297	1.397	1.296	1.377	1.479
Shape	yellow needle	Orange rod	plate orange	plate orange	plate orange
Reflections	66910	17518	25859	7445	5244
Parameters	317	173	1489	480	299
Restraints	0	0	0	206	0
R_{int}	0.1338	0.1100	0.0826	0.0828	0.0679
R_1[a]	0.1305	0.0603	0.0778	0.0816	0.0673
wR2[b]	0.3878	0.1333	0.2211	0.2259	0.1655
S	1.088	1.024	1.075	1.071	1.091

Annex 5.2: UV-Vis absorption spectra on solid state for D1, D2, D3, D4 and A1, A2, A3, A4.

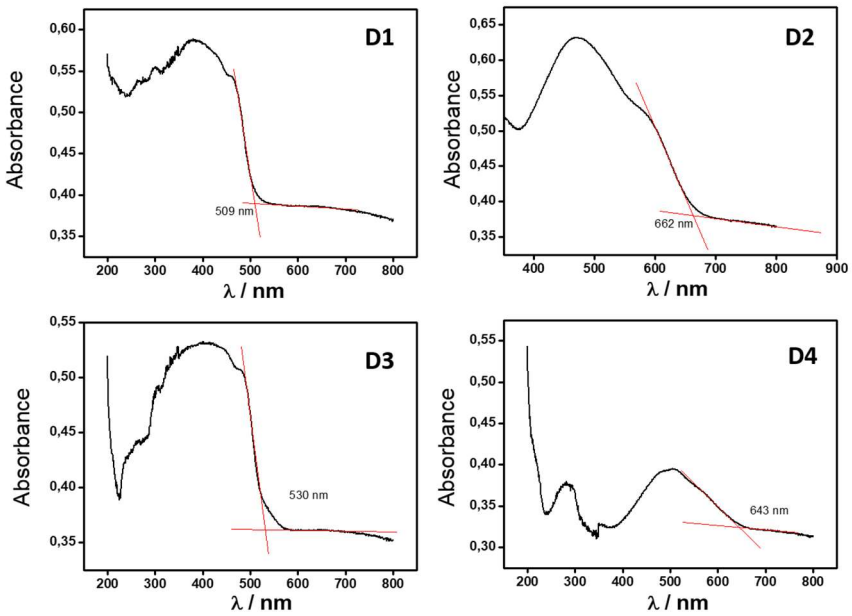

Figure A.5.1: UV-Vis spectra on solid state for D1, D2, D3, and D4.

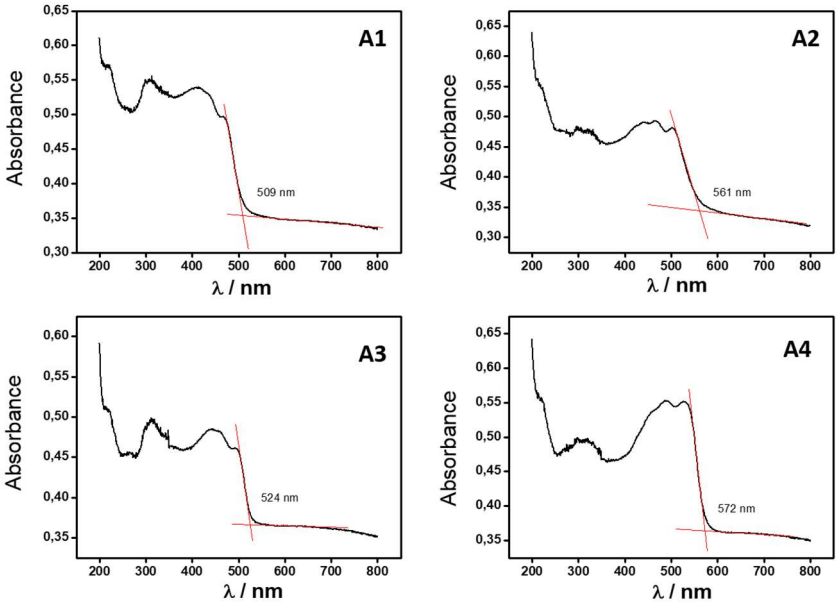

Figure A.5.2: UV-Vis spectra on solid state for A1, A2, A3 and A4.

Physical Techniques

Infrared Spectroscopy: IR spectra were obtained as KBr pellet samples on a Nicolet 5700 FTIR spectrometer at the Universitat de Barcelona (UB).

Elemental Analysis: (C, H, N) were performed on a Perkin-Elmer II Series CHNS/O Analyzer 2400, at the "Servei de Microanàlisi" of CSIC, Barcelona, Spain.

Magnetic measurements were performed using a Quantum Design MPMS SQUID magnetometer at the "Unitat de Mesures Magnètiques" of the Universitat of Barcelona or by Dr.Olivier Roubeau using a Quantum Design MPMS-XL Evercool SQUID at the SAI Physical Measurements of the Universidad de Zaragoza.

Electronic absorption: UV-Vis spectra in solution were recorded using a Varian Cary 100 UV/Vis spectrophotometer and on solid state on a UV-Vis-NIR Cary 5000 (190-3300 nm). The measurements were made with an integrating sphere as an Optical component and KBr pellets with 0.010 mg of CCMoid and 200 mg KBr.

Fluorescence emission: Fluorescence spectra were recorded using Horiba Jobin-Yvon SPEX Nanolog-TM and Cary Eclipse spectrofluorimeters.

^{1}H NMR paramagnetic: ^{1}H NMR spectra were recorded on Varian Gemini-300 spectrometer (300 MHz)

^{1}H NMR diamagnetic: ^{1}H NMR spectra were recorded on Avance VRX 400 instrument (400 MHz) using deuterated chloroform ($CDCl_3$) and dimethylsulfoxide (DMSO-d_6).

Mass spectrometry: ESI experiments were performed using a LC/MSD-TOF (Agilent Technologuies) with a dual source equipped with a lock spray for internal reference introduction and MALDI experiment using a 4800 Plus Maldi TOF/TOF Analyzer at the "Unitat d'Espectrometria de Masses" (SSR) of the Universitat de Barcelona.

X-ray data were collected with:

- Bruker APEX II CCD Advanced Light Source in Lawrerence, Berkeley National Laboratory

- Bruker APEX II QUAZAR diffractometer with $Mo_{K\alpha}$ radiation (λ = 0.71073 Å) and equipped with a microfocus multilayer monochromator

Force Atomic Microscopy: AFM images were captured in tapping mode using a Multimode AFM attached to Nanoscope IV electronics (Digital Instruments, Sara Barbara, CA) at the "Centros Científicos y Tecnológicos" (CCiT) of the Universitat de Barcelona.

Photoemission: Ultra-violet Photoemission Spectroscopy (UPS) and X-ray Photoelectron Spectroscopy (XPS) experiments were carried out by Dr. Jordi Fraxedas. The experiments were performed at a bare pressure of 10^{-10} mbar and room temperature using a SPECS PHOIBOS 150 hemispherical analyzer equipped with a 2D CCD detector and using monochromatic HeI (21.22 eV) and AlKα (1486.6 eV) radiation as excitation sources respectively, at the

Electrochemistry of the SAMs (CV, DPV and SW): The experiments on surface were performed with a Bio-Analytical Systems, BasI-Epsilon electrochemical work-station, using a conventional three-electrode electrochemical cell. The working electrode was a thin vapor deposited Au film deposited on glass (12 x 12 mm slides purchased from Arrandee, Germany). The reference electrode was $Ag/AgCl_{sat}$ and a platinum wire of 5 cm^2 geometrical area served as the counter electrode. All the CV, DPV and SW measurements were performed at room temperature under N_2 atmosphere and using scan rates of 50 mV/s.

Electrochemistry in solution (CV and DPV): The experiments in solution were acquired on an SP-150 (BioLogic) potentiostat modulated by EC-Lab V10.02 software. A three-electrode system with Pt reference electrode, Pt counter-electrode and C(graphite) working electrode; using tetrabutylammonium hexafluorophosphate [$TBA(PF_6)$] (0.1 M in 15 mL of dry CH_2Cl_2) served as an inert electrolyte. The curves were recorded at scan rate of 100 $mV \cdot s^{-1}$ using dry CH_2Cl_2 solution with a 10^{-4} M concentration of the compounds under N_2 atmosphere. Ferrocene was used as an internal standard.

Optical microscope: The images were captured using an Olympus RXSITRF Optical microscope with a USH-1030L mercury lamp.

Electron paramagnetic resonance (EPR): The measurements were collected in National High Magnetic Field Laboratory (FSU) by Stephen Hill, using EMR Homodyne 17T Spectrometer, using frequencies 50 to 450 GHz and temperatures between 5-10 K with magnetic field range 0-14.5 T.

Contact angle: The contact angle measurements were performed with a DSA 100. Water drops were deposited through a manual computer controlled system. MilliQ water drops were deposited, with a volume of 3.0 µL/min. The measurements were performed in the clean room of the Nanoquim platform available at the ICMAB.

Confocal microscope: The images were captured using a Leica TCS SP5 confocal microscope at the "Servei de Microscòpia" at the Universitat Autònoma de Barcelona (UAB).

List of Publications

1) Novel sandwich triple-decker dinuclear Nd^{III}-(bis-N,N-p-bromo-salicylideneamine-1,2-diaminobenzene) complex.
Ahmed M. Abu-Dief, Raúl Díaz-Torres, Eva Carolina Sañudo, Laila H. Abdel-Rahman, Núria Aliaga-Alcalde.
Polyhedron. 2013, 63, 203

2) Multiscale Study of Mononuclear CoII SMMs based on Curcuminoid Ligands
Raúl Díaz-Torres, M. Menelaou, A. Sorrenti, G. Brandariz, E. Sañudo, O. Roubeau, S. J. Teat, M. J. Esplandiu, J. Fraxedas, E. Ruiz, N. Aliaga.
Chemical Science. 2016, 7, 2793.

3) Sequential Electron Transport and Vibrational Excitations in an Organic Molecule to Few-Layer Graphene Electrodes.
Enrique Burzuri, Raúl Díaz-Torres, Joshua Island, Alexandra Fursina, Arántzazu González-Campo, Olivier Roubeau, Simon J. Teat, Núria Aliaga-Alcalde, Eliseo Ruiz and Herre S. J. van der Zant.
ACS Nano. 2016, 10, 2521.

4) Multiscale Approach to the Study of the Electronic Properties of Two Thiophene Curcuminoid Molecules.
Alvaro Etcheverry-Berríos, Ignacio Olavarría, Mickael L. Perrin, Raúl Díaz-Torres, Domingo Jullian, Ingrid Ponce, José H. Zagal, Jorge Pavez, Sergio O. Vásquez, Herre S. J. van der Zant, Diana Dulic, Núria Aliaga-Alcalde and Mónica Soler.
Chem. Eur. J 2016, 22, 12808.

5) Comparative Magnetic Studies in the Solid State and Solution of Two Isostructural 1D Coordination Polymers Containing CoII/NiII-Curcuminoid Moieties.
Raúl Díaz-Torres, M. Menelaou, Arántzazu González-Campo, S. J. Teat, E. Carolina Sañudo, Mónica Soler and Núria Aliaga-Alcalde.
Magnetochemistry. 2016, 2, 29.

Acknowledgements

Una vez acabada esta etapa me gustaría tener unas palabras de agradecimiento a todas las personas que han contribuido a que este trabajo fuera posible. Personalmente, considero esta etapa como una de las más enriquecedoras de mi vida, debido a que, aparte de los conocimientos científicos adquiridos, he tenido la oportunidad de madurar y crecer como persona, desarrollando una opinión más crítica.

Todo esto, no hubiera sido posible sin una persona, y a la cual van dirigidas mis primeras palabras. A ti Núria, por darme la oportunidad de realizar una tesis y por toda la confianza depositada en mí desde un principio. Gracias por el entusiasmo con cada resultado obtenido, por la motivación, por transmitirme tu pasión por la ciencia y hacerme disfrutar de la investigación, y por hacerme crecer como persona. Me gustaría agradecer también la parte personal durante todos estos años, tu comprensión y tu cercanía, que ha dado lugar que nuestra relación se encamine hacia una muy buena amistad; y siento que si soy como soy es en parte culpa tuya, gracias de verdad.

Por otro lado, me gustaría agradecer a Guillem Aromí, por mostrarse siempre tan cercano y por darme la oportunidad de formar parte y pertenecer al grupo GMMF.

Seguidamente, agradecer a las colaboraciones científicas que han ayudado de forma activa a la obtención de resultados. A Carolina y Olivier por la resolución de las estructuras cristalinas, a Nuria Clos por las medidas magnéticas realizadas y a Eliseo Ruiz por los cálculos teóricos.

Me gustaría agradecer a todas las personas que forman o han formado parte del ICMAB, y que les considero una de mis familias científicas. Primeramente, Arancha, muchas gracias por guiarme y enseñarme a analizar los resultados con rigor científico. A Sandra, por ser tan comprensiva y por cuidarnos tanto a todos, siendo una pieza indispensable para el grupo. A Marta y Ezhil, por ser tan espontáneas y divertidas, a Wenjie por su ayuda científica y a las “nuevas” incorporaciones, Laura y Dani, por traer esa alegría y aire fresco al grupo. Me gustaría agradecer especialmente a los estudiantes que he tenido la suerte de llevar y que han contribuido en esta tesis, especialmente a Dayana y Raquel, por haberme dejado aprender de ellos cuando se supone que yo les estaba enseñando.

A mi otra familia científica de la UB y a todos aquellos que están o han pasado por el departamento de Q. Inorgánica. Empezando por el máster, gracias Miki por las cervezas/calimochos en el Hao y estar siempre ahí y a ti Laia por ser como eres y por esos días en Escocia, os tengo un cariño muy especial a los dos. A los que ya acabaron, pero han dejado su huella y tengo la suerte de seguirles viendo cada fin de semana: Lluis por ser mi profesor de guitarra y estar tan loco, Alberto por ser mi confidente y por todas las risas, a Marta por todos los descansos a las 17 h y a Rosa por ser siempre tan positiva. A los que han vuelto: Saskia, por lo divertida que eres y las catas de vino y Beltzane por ser única y sacarme cada día una sonrisa. A los que aún están y han hecho que cada al mediodía fuera el mejor momento del día estos últimos meses: a Lidia y a Berta por aguantar mis bromas, a Mariona por darme galletas “gullon”, a Guillermito por ser compañero ceniciento y a Fran por la ayuda en los trámites finales. Me gustaría también agradecer a Arnald, por estar siempre

predispuesto a ayudar y por su humor tan característico, y a César y Ana, por convertirte en colchonera.

Me gustaría agradecer a la gente que está o ha pasado por el GMMF: a Leo por los momentos vividos y por enseñarme a dar mis primeros pasos en la Q. Orgánica, a Ivana por tu amistad y por contagiarme tu entusiasmo por la ciencia y al resto de miembros Carolina, Albert, Mohanad, Jorge, Gavin, MJ, Santi, Marta, etc, gracias a todos. Dentro de este grupo, me gustaría agradecer especialmente a tres personas, que se han convertido en tres grandes amigos: a David, porque fuiste y sigues siendo un espejo donde mirarme no solo a nivel científico sino también personal, a Vero por lo pasado y por toda la conexión que nos une y a Rosa por ser mi alma gemela.

Me gustaría tener unas palabras de agradecimiento a las personas que me han ayudado y me han abierto sus brazos en todas las estancias que he tenido la oportunidad y la suerte de vivir. A Enrique en Delft, gracias por tu paciencia y tu tiempo a la hora de explicarme todos los conceptos físicos. A Euan, en Edimburgo, por darme la oportunidad de trabajar en su grupo y poder coincidir con Julia, Sergio, Anders, Robin, Hector y Helena. A Zagal, Mónica e Ingrid en Santiago (Chile), por hacerme sentir como en casa durante esos meses. Agradecer también a todos los amigos chilenos, especialmente a mi "hermano chileno" Álvaro y a Lindley, Joseline (increíble viaje por Perú), Ítalo, Fabian, Felipe, Sara, Nataly, Pachi y todos y cada uno de ellos.

A mis amigos fuera de la universidad, empezando por los de "sants": Edu, Marc, Kiko, Arnau y especialmente a ti Gerard por estar siempre ahí y ser como un hermano para mí. A mis amigos del pueblo, (el sitio más bonito del mundo), que habéis conseguido que cada verano volviese con las pilas cargadas.

A mi familia los "paris", por todo el soporte y especialmente a mi primo Juanfran y mi amiga Rebeca que te cuento como familia. Gracias a los dos por los momentos de placita y por todo vuestro apoyo, os quiero tener siempre cerca.

Finalmente me gustaría dar las gracias a mi familia más cercana, a Vicky, a mi hermano Alex (y al pequeño Noah que está en camino), por todo vuestro apoyo durante estos años; no puedo ser más afortunado teniéndoos. Pero, sobre todo, quisiera dar las gracias a mis padres Santiago y M.ª Carmen por todo el sacrificio, por enseñarme cada día y por apoyarme incondicionalmente. Alcanzar esta meta no hubiera sido posible sin vosotros.

Raúl Díaz Torres